Structural Diversity in Metal-Organic Frameworks and Metal-Organic Polyhedra with 1,3,5-Triethynyl-Benzene Based Linkers

A thesis submitted to the University of Dublin for the degree of

Doctor of Philosophy

Joseph Eiffe

School of Chemistry

University of Dublin

2023

Declaration

I declare that this thesis has not been submitted as an exercise for a degree at this or any other university and that it is entirely my own work, except where otherwise cited, referenced, acknowledged or accredited.

I agree to deposit this thesis in the University's open access institutional repository or allow the Library to do so on my behalf, subject to Irish Copyright Legislation and Trinity College Library conditions of use and acknowledgement.

X

Joseph Eiffe

Summary

The study of metal-organic frameworks and metal-organic polyhedra is a rapidly evolving area of research. The research presented in this thesis serves to further our understanding of these advanced materials with the primary focus on the effects of linker symmetry and functionalisation. The newly synthesised materials were then examined using physical and computational techniques to study the influence of the material's structure on its properties.

Chapter 1 summarises the available literature related to this thesis's work. This chapter introduces the reader to the various concepts regarding metal-organic frameworks (MOFs) and metal-organic polyhedra (MOPs). The aims of the thesis are also outlined.

In **Chapter 2** using the newly synthesised amino functionalised organic linker 3,3',3"-((2-aminobenzene-1,3,5-triyl)tris(ethyne-2,1-diyl))tribenzoic acid ($H_3BTEB_{mmm}NH_2$) in combination with Cu^{2+} ions two MOPs, $[Cu_{36}(BTEB_{mmm}NH_2)_{24}(H_2O)_{28}(DMF)_8]$ (**1**) and $[Cu_{12}(BTEB_{mmm}NH_2)_8(H_2O)_{12}]$ (**2**) were synthesised. The two MOPs have the structures of a cuboctahedron and octahedron, respectively. This demonstrates the diverse range of possible structures by using the conformational flexibility of benzene-trisethynyl benzoate (BTEB) based linkers.

These newly synthesised MOPs were then implemented as structural units in the construction of MOFs. This was achieved by using the technique known as 'pillaring'. The pillaring method involves the addition of a bipyridyl ligand, in this instance 4,4'azobipyridine (Azpy), which coordinates to the apical position on $\{Cu_2\}$ paddlewheel SBUs within the MOPs framework. By controlling the amount of Azpy used in the synthesis, and its ratio to the $H_3BTEB_{mmm}NH_2$ linker, the dimensionality of the pillared MOF product can be selected. Using a low mole ratio of Azpy to $H_3BTEB_{mmm}NH_2$ led to the pillaring of **1** into a one-dimensional coordination polymer $[Cu_{36}(BTEB_{mmm}NH_2)_{24}(Azpy)(DMF)_{34}]$ (**3**), while a high mole ratio led to the three-dimensional framework $[Cu_{36}(BTEB_{mmm}NH_2)_{24}(Azpy)_6(DMF)_{30}]$ (**4**). However, attempting to pillar **2** into a framework leads to an unexpected result with the MOP disassembling in solution and reforming into a pillared two-dimensional framework, $[Cu_6(BTEB_{mmm}NH_2)_4(PPP)_2(Azpy)(H_2O)_2]$ (**5**).

In **Chapter 3** the effects of linkers with reduced symmetries on the MOFs framework are studied. A new family of BTEB-based linkers was first synthesised using various combinations of *para*-benzoate, *meta*-benzoate and isophthalate moieties. These new linkers are combined with Cu^{2+} ions to form a metal-organic framework. Cu^{2+} ions were chosen as they have a strong tendency to form the structural building unit known as a $\{Cu_2\}$ paddlewheel secondary building unit (SBU). This readily reproducible SBU allows for the effect of the organic linkers geometry on the structure of the MOF to be examined in isolation. A series of MOFs, **6** - **11** were then synthesised using the new symmetry reduced tritopic linkers and tetratopic linkers. The structures and properties were examined using both physical and computational techniques.

In **Chapter 4** we then focused on examining the influence of linkers with reduced symmetry on the structure and properties of the inorganic SBUs. To study these effects, metal ions that can form a broad range of inorganic SBUs in combination with the new symmetry-reduced linkers were studied. This chapter's first MOF to be discussed, $[NH_2(CH_3)_2]_6[Zn_9(BTEB_{ppi})_6]$ (**12**), provides an excellent example of the potential SBUs that could be synthesised using the new linkers. The MOF contains two SBUs that are uncommon in the literature, with the structure of one SBU, a 5-connected node, being reported only once before.

Using the same H_4BTEB_{ppi} linker with Co^{2+} ions led to the new MOF, $[Co_2(BTEB_{ppi})(DMF)_3]$ (**13**). The inorganic SBUS within the MOF was found to be dinuclear, with one Co^{2+} ion coordinated by three solvent molecules. This structural aspect of the SBU is a common feature in MOFs used in catalysis. Based on this structural feature and the literature reports of cobalt-based MOFs used for catalytic electrochemical water splitting, a preliminary investigation of the MOFs to act as a water-splitting catalyst was carried out. The MOF was determined to be an active catalyst for the oxygen evolution reaction t for extended periods of time.

The final MOF to be discussed in the thesis, and the only MOF in this work containing a pentacarboxylate organic linker, is a zinc-based MOF, $[Zn_7(HBTEB_{iip}^{4-})_3(DEF)_7](NO_3)_2$ (**14**). In the MOFs framework, only four of the linkers carboxylate groups coordinate with the metal ions, like the literature-known compound. Where the structure of the two MOFs diverges is the remaining carboxylate group. This carboxylate group remains uncoordinated and directed towards the pores of the MOF. This is a desirable feature in MOF chemistry that typically require post-synthetic modification to achieve serving to demonstrate the considerable potential that linkers with reduced symmetry have in MOF chemistry.

Chapter 5 describes the details of experimental procedures and characterisation data of any new compounds.

The thesis concludes in **Chapter 6** with a brief summary of its contained works alongside a discussion of possible avenues for further research that this work opens up.

Acknowledgements

First and foremost, I would like to thank my supervisor Prof. Wolfgang Schmitt. I am grateful for the opportunity to work with him and his research group. His continued guidance and support over the past few years was invaluable, without which this work would be a shadow of itself.

This research would not have been possible without the assistance and support from the following people in the Schmitt group. I would like to thank Dr. Nianyong Zhu (Jom) for his work on the single-crystal X-ray refinements and his previous work in the group, which lay the foundations for this project. Along with Dr. Joaquinn Soriano López, for his assistance with all electrochemistry-related aspects,including the catalysis measurements, and Mariah O'Doherty for EDX analysis.

To everyone in the Schmitt group, both past and present members, including Éadaoin, Muhamed, Seb, Kevin, Debo, Rory, Friedrich, Paul, Luana, Amal, Guanghua, Greg, Ako, Dean, Aoife and Geroid thank you for all your help and for keeping me sane over the years!

I would especially like to thank my Mam, Dad, sister, the rest of my family and friends for their continued support over the years both at home and PhD related.

I would like to thank the technical and support staff in the School of chemistry. In particular, I would like to thank Dr. John O'Brien and Dr. Manuel Reuther for their assistance with a number of techniques, especially in NMR. I would also like to thank Dr. Brendan Twamley for his assistance with all things crystallography and his assistance in measuring PXRD patterns.

Finally, I would like to thank the European Research Council (ERC) for the financial support which made this research possible.

Table of Contents

Abbreviations

BDC	benzene -1,4-diarboxylate
BET	Brunauer–Emmett–Teller
BTEB	Benzene-triethynyl-benzoate
CN	Coordination network
CP	Coordination polymer
cub	Cube
cuo	Cuboctaheron
CUS	Coordinatively unsaturated sites
DCM	Dichloromethane
DEF	Diethylfromamide
dia	Diamond
DMF	Dimethylformamide
DMSO-d	Deuterated dimethyl sulfoxide
DOE	US Department of Energy
EDX	Energy-dispersive X-ray spectroscopy
ESI	Electron spray ionisation
fcu	Face centered cubic
FT-IR	Fourier transform infrared spectroscopy
HER	Hydrogen evolution reaction
HKUST	Hong Kong University of Science and Technology
HRC	Hydrogen reduction catalyst
HR-MS	High resolution mass spectrometry
ico	Icosahedron
IRMOF	Iso-reticular metal-organic framework
MeOH	Methanol

MIL	Matériaux de l'Institut Lavoisier
MOCN	Metal-organic coordination network
MOF	Metal-organic framework
MOM	Metal-organic material
MOP	Metal-organic polyhedron
NMR	Nuclear magnetic resonance spectroscopy
oct	Octahedron
OER	Oxygen evolution reaction
PCN	Porous coordination network
PCP	Porous coordination polymer
pcu	Primitive cubic
PSD	pore-size distribution
PSM	Post-synthetic modification
pts	Platinum sulfide topology
PXRD	Powder X-ray diffraction
RBF	Round bottomed flask
RCSR	Reticular chemistry structure resource
S.A.	Surface area
SBU	Secondary building unit
SCXRD	Single crystal X-ray diffraction
tbo	Twisted boracite topology
tet	Tetrahedron
TGA	Thermogravimetric analysis
THF	Tetrahydrofuran
UiO	University of Oslo
UMC	Undercoordinated metal centre
WOC	Water oxidation catalyst

XRD	X-ray diffraction

Chapter 1

Introduction

1 Introduction

1.1 Porous inorganic and hybrid materials

Coordination compounds derive their name from the coordination bonds that occur in the structure.[1] A coordination bond is the bonding interaction between a ligand and a metal ion through the donation of electron pairs. Compounds that contain these bonds are commonly referred to as 'complexes'. This class of materials has been known to be used since ancient times.[2] These compounds are commonly found in pigments owing to their vibrant colours. The compounds' vibrancy and range of colours arise from the transition metals absorbing in the visible range of the electromagnetic spectrum through various mechanisms, including metal to ligand charge transfer, the ligand to metal charge transfer and d-d transitions. Notable examples of these compounds include Prussian blue ($Fe_7(CN_{18})$ and aureolin ($K_3[Co(NO_2)_6]$).

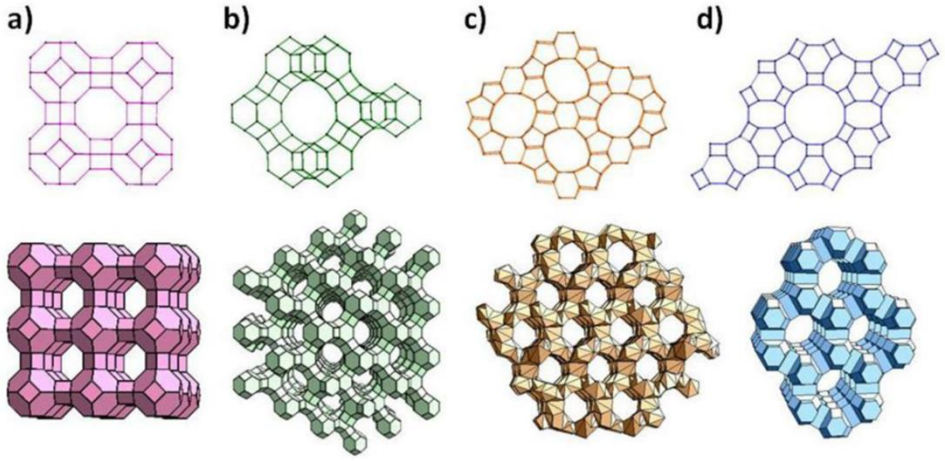

Figure 1.1: Representative zeolite frameworks showing pore openings). a) Zeolite A (3D, 4.2 Å pores), b) Zeolite Y (3D, 7.4 Å pores), c) Zeolite L (1D, 7.1 Å pores), and d) ZSM-5 (silicalite) (2D, 5.3 × 5.6 Å and 5.1 × 5.5 Å pores). Reprodueced from reference 3.

One of the widely used porous materials in industry was first identified in 1756 by Swedish mineralogist Axel Fredrik Cronstendt. He discovered the materials porous nature upon observing the production of steam when the material known as stilbite was heated. He named this group of porous aluminosilicate materials' Zeolites' from the Greek words' zeo' meaning to boil and 'lithos' meaning stone.[4,5] One of the attractive features of these materials is that they can be cheaply extracted from the ground or synthesised.[6] The materials have a series of properties that make them useful for a broad range of applications, particularly the highly porous material and charged surfaces. The surface area of these materials can be on the order of hundreds of m^2/g.[7] The structure of these aluminosilicates comprises SiO_4^{4-} and AlO_4^{5-} building units which can combine to form a near-infinite family of structures (**Figure 1.1**).

1.2 Porous coordination compounds

1.2.1 Metal-organic frameworks

The study and characterisation of porous hybrid organic-inorganic materials encompass the study of the rapidly developing class of material: Metal-Organic Frameworks (MOFs). IUPAC defines MOFs as "a coordination network with organic ligands containing potential voids".[8] This definition describes a class of coordination compounds that extend through repeating coordination units in two or three dimensions combining both inorganic and organic moieties through strong bonds.[8] An example for one of these structures can be seen in **Figure 1.2,** with MOF comprised of metal nodes containing Zn^{2+} ions linked by terephthalic acid organic linkers and is known as MOF-5.[9] In comparison to zeolites, which have been known to occur in nature since 1756, MOFs were believed to be exclusively synthetic materials until the discovery of $NaMgFe(C_2O_4)_3 \cdot 9H_2O$ a naturally occurring oxalate based MOF.[10]

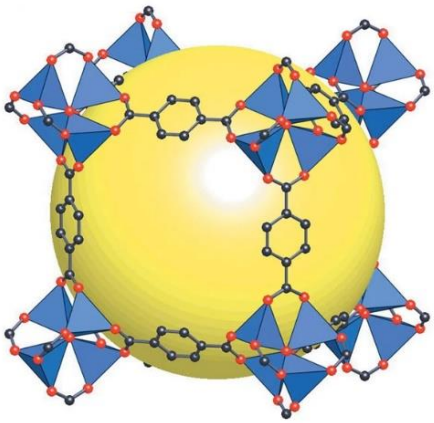

Figure 1.2 The single crystal structure X-ray structure of MOF-5 (isorenticular metal-organic framework – 5). The MOF is comprised of tetranuclear {Zn_4O} SBUs, which a connected by terephthalic acid ligands which act as linear linkers. The structure contains a series of voids. (C - black, O - red, Zn – blue tetrahedrons, internal void - yellow sphere). Reproduced from reference 9.

Hoskins and Robons first proposed the concept of linking metal nodes with organic linkers into extended networks in 1989.[11]. However, it was not until later that the design principles and synthetic procedures needed to synthesise the materials were developed that the first MOFs were synthesised.[12,13,14] These design principles and synthetic procedures expanded the concept of crystal engineering first proposed by Schmidt and Kitaigorodsky.[15,16] Through crystal engineering, it was now possible to predetermine the crystal structure based upon its constituent building blocks. This is done by reducing the complex nature of the structure to simple geometric shapes such as triangles, squares and hexagons, to name but a few. Each of the geometric shapes used in the structure is then assigned to either the inorganic building blocks, which consist of metal ions or clusters and are commonly referred to as secondary building units (SBUs) or the organic linkers, commonly known

as organic building units, organic SBUs or ligands.[17] An example of this reduction of the building units to triangles, squares and tetrahedrons can be seen in **Figure 1.3**. By carefully choosing ligand and metal ion combinations, it is possible to predictably produce a crystalline structure with a known arrangement of the building units within. The use of these simplified structural components is important in the description of MOFs where both the nature and geometry of the components and their three-dimensional arrangement impart strong influence on the properties of the resulting MOF.[18]

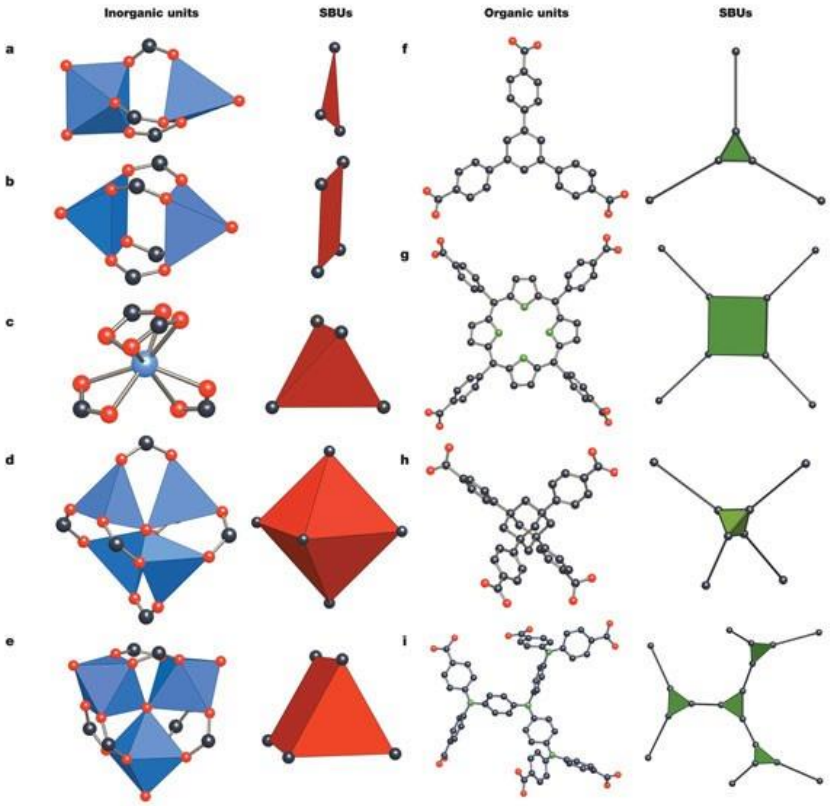

Figure 1.3 A series of examples of how the inorganic SBUs and linkers can have their geometric complexity reduced to simple polygons or polyhedra. In the inorganic units, the metal-oxygen polyhedra are blue, and their corresponding simplified polygons or polyhedra (red) are defined by the carboxylate carbon atoms. In the organic linkers, the polygons of polyhedrons to which linkers are attached are shown in green. (C – black, O – red, N – green, Metal – blue/blue polyhedra, simplified geometries – red and green) Reproduced from reference 17.

A vast number of inorganic SUBs have been discovered and used in the synthesis of MOFs, comprised of transition metals,[19,20,21] lanthanides,[21,22,23] actinides,[24,25] and main group metals.[26,27] In combination with a near-infinite number of linkers that can be used, an immeasurable number of MOFs can theoretically be synthesised. This large variety of MOFs and their ability to tune their properties have led to a rapid expansion of research into the area of MOFs. A search of journal articles with the 'MOF' unveils that more than 20,000 articles have been published in the last two decades in this field of science. Currently, each year up to 3000 new articles are published with a focus on

MOFs. In **Figure 1.4** this rapid growth in the area can be seen with an increase in the number of articles published year on year. The search of the term 'MOF' in both title and abstract, however, does not show the true scope of the field as a number of other names and descriptors have been used, including coordination networks (CN), metal-organic materials (MOMs), etc. Therefore, the actual number of articles in the field may be greater than this.

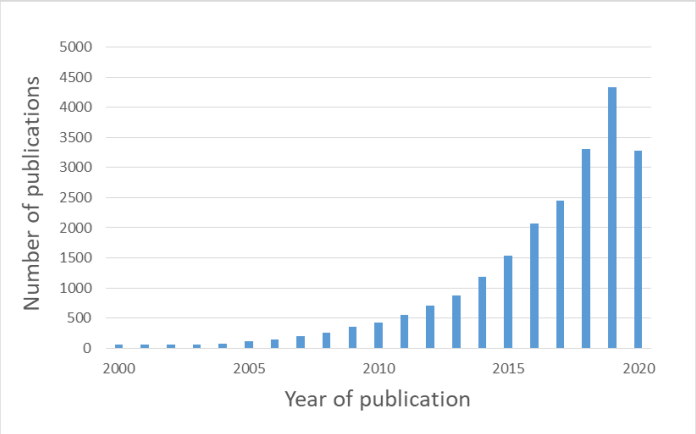

Figure 1.4 The number of publications containing the term MOF from the year 2000 to 2020. Source: Scientific citation index database Web of Science

1.2.2 Metal-organic polyhedrons

In recent years, a secondary class of porous hybrid materials that has seen rapid development is metal-organic polyhedrons (MOPs). Other standard terms for these materials include molecular coordination cages,[28,29,30] molecular containers,[31,32,33] and nano-balls.[34] MOPs and MOFs can be seen as a subset of metalo-supramolecular materials, with both being based upon the same fundamental principle of linking inorganic SBUs with organic linkers. The two materials are often constructed from similar SBUs and linkers but where the two classes of materials diverge in their structural design is the extent to which the building units are linked. In MOFs, the network can be treated as extending indefinitely, forming either a one, two or three-dimensional framework. In contrast, MOPs form when the extent of the linking of the network is limited to one supramolecular structure. MOPs, therefore, can be described as the zero-dimensional equivalent of MOFs. Shown in **Figure 1.5** two examples of MOPs can be seen with a) being a MOP comprised of palladium ions linked by pyridyl linkers and b) being comprised of copper ions linked by carboxylate-based linkers. Each MOP encapsulates a single pore that is accessible through the gaps in the framework, commonly known as "windows".[35,36] Due to MOPs acting as discreet molecular species, they can maintain their properties while dissolved in solution rather than acting as a suspension like MOFs. This property allows for the synthesis of highly tunable molecular species. Similarly to MOFs, the structure of MOPs can be reduced to the connectivity of both the inorganic SBUs and linkers.

Two of the most influential researchers in the field of MOPs are Fujita and Stang whose work lay the foundation of the development of MOPs with their work in the field being published as early as 1995.[35] Due to MOPs having similar properties to that of MOFs, the areas of application that they have been studied for overlap. Some of the most examined applications include gas storage,[37,38] chemical sensing,[39,40] catalysis,[41,42] and guest uptake/release.[40] The main driving interest that separates MOPs from MOFs in these applications is their ability to perform these applications homogenously rather than the heterogeneous nature of MOFs

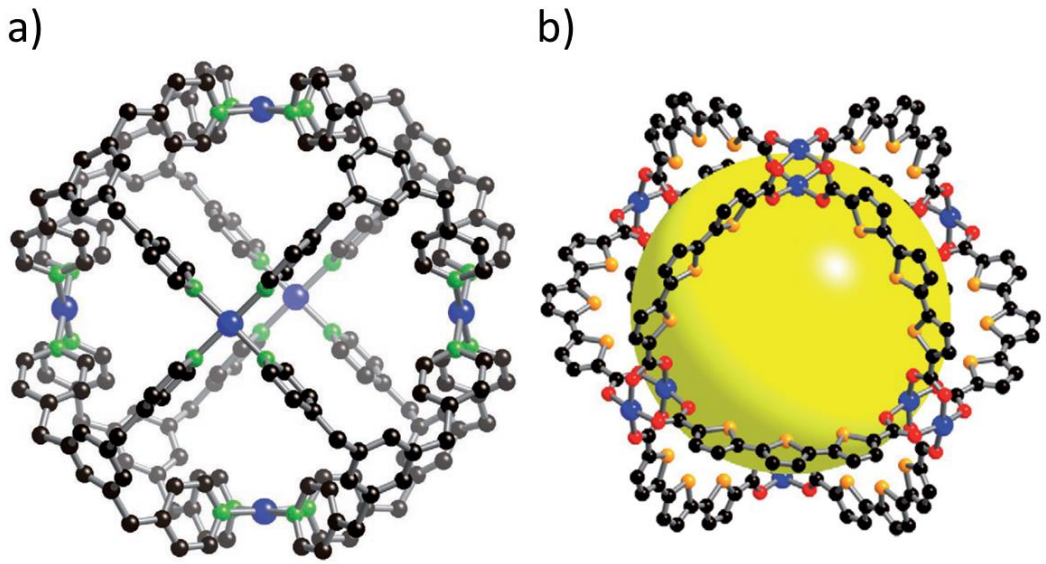

Figure 1.5 Two examples of MOPs. a) [Pd_6(1,3,5-tris(4-pyridylmethyl)benzene)$_8$] with its rhombic dodecahedral structure and b) [Cu_{12}(2,2':5',2''-terthio-phene-5,5''-dicarboxylate)$_{12}$] with its tetrahedral structure. Colour scheme. (C - black, O – red, N – green, S – orange, Pd – purple, Cu – blue, Internal void – yellow sphere) Reproduced from reference 43.

1.2.3 Classification of extended coordination compounds and terminology

The development of new materials requires the creation of a new convention on the classification and terminology related to these said materials. Disparity initially arose in the convention of these materials due to the convergent research of multiple groups worldwide. While the term MOFs has now been cemented as the name for this class of porous coordination frameworks, several independently coined names have/are used in the literature. These include but are not limited to coordination polymer (CP),[44,45,46] metal-organic material (MOM),[36] coordination network (CN),[47] porous coordination polymer (PCP),[48] porous coordination network (PCN),[49,50,51] microporous coordination polymer (MCP),[52,53] and metal-organic coordination network (MOCN).[54,55,56]

In order to establish a common language for the description of this new class of materials, a panel of experts was brought together by IUPAC in 2009. After years of deliberation, in 2013, the IUPAC panel gave a number of recommendations for the naming convention of the materials. The result of

the meeting was the creation of a hierarchal structure to clarify the different types of materials that have similar descriptors. The main categories that were defined were as follows. A coordination polymer is defined as 'a coordination compound continuously extending in one, two or three-dimensions through coordination bonds. A coordination network is 'a coordination compound extending, through coordination bonds in one dimension, but with cross-links between two or more individual chains, loops or spiro-links, or a coordination compound extending through coordination bonds in 2 or 3 dimensions. While a MOF is 'a coordination polymer with an open framework containing potential voids.' A diagrammatic representation of the hierarchy can be seen in **Figure 1.6**. It can be seen that MOFs are just a specialised subset of coordination compounds. While not explicitly stated in the recommendations from the panel, the standard terminology of MOP is seen as an extension of the definition of MOF with the limitation of the dimensionality of the framework to a single-encompassed pore.

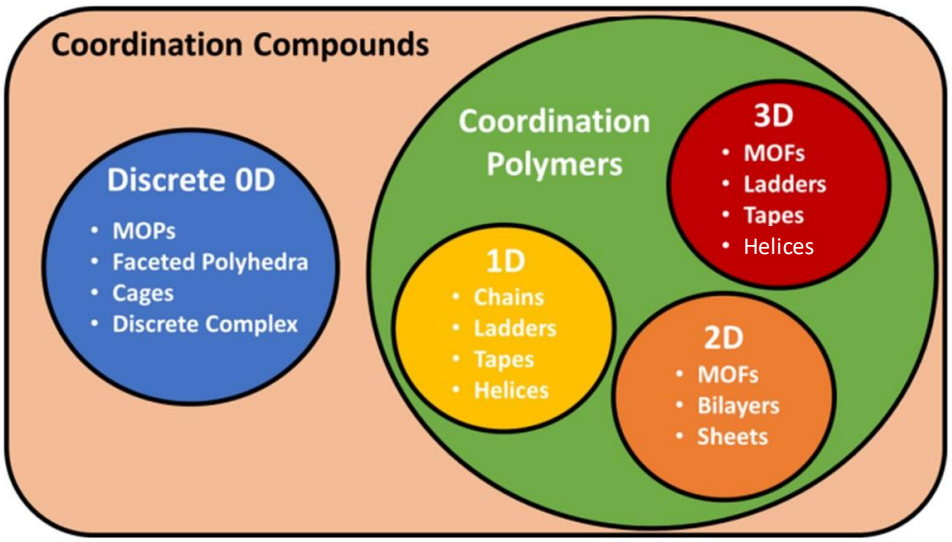

Figure 1.6: Venn diagram of the naming and classifications of coordination compounds commonly used in the literature. Adapted from reference 36.

1.2.4 Topology, the network approach and reticular synthesis

In mathematics, topology is the study of a geometric object's properties that are preserved under continuous deformations, such as stretching, twisting and bending but not tearing or glueing. This makes it an ideal tool for describing MOFs and other related network-containing materials (e.g. Coordination polymers, zeolites, etc.). The use of topological descriptors extends beyond just the recommendations for naming conventions from IUPAC. It brings several benefits when studying the structures of MOFs, including a) an understanding of the structure of the synthesised MOF, b) the ability to allow for straightforward comparisons between other MOFs that have been synthesised, c) a more concise way of communicating the structure in the literature and d) the ability to synthesise a MOF with a specifically targeted topology.

Wells initially developed a net approach to aid in the description of the structure of inorganic compounds.[57,58] His concept was to reduce the complex structure of a compound to a simplified net. A net is defined as an infinite array of nodes that are linked with aptly named 'linkers'. The two defining rules for determining the structure of a net is that each node must be connected to three or more nodes, and linkers must make only connections between two separate nodes. Using this system, the connectivity of the net could be described by using the general (*n*,*p*) notation. Where *n* represents the number of nodes in the smallest closed circuit in the net and *p* is the number of connections that each node at the vertices of the smallest circuit have. In **Figure 1.7** an example of a two-dimensional (6,3) net can be seen where 6 is from the "6-gon" that makes the smallest net and 3 arises from the number of connections at each vertex

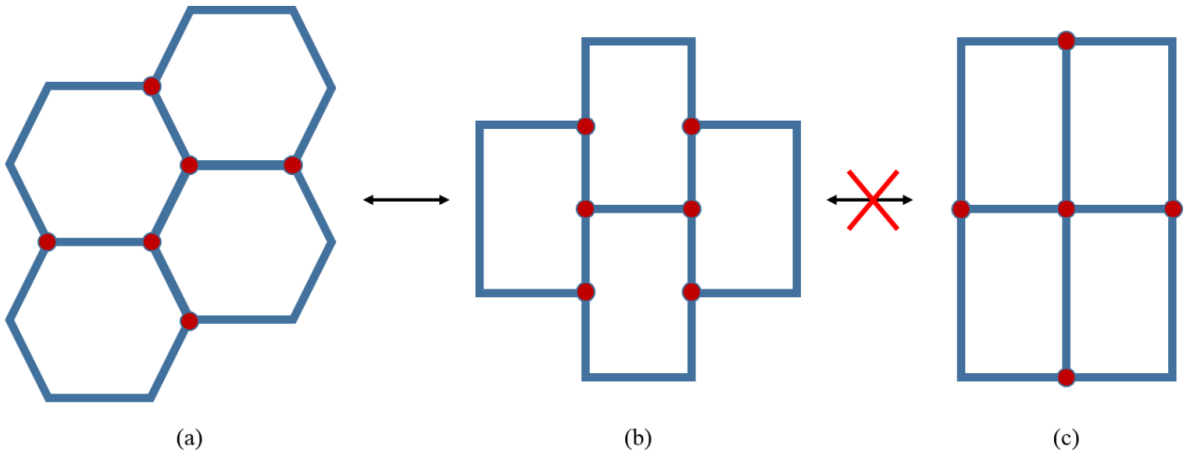

Figure 1.7: a) and b) represent two two-dimensional (6,3) nets. Although the shape of the two nets appears different, they are still formed by 3-connected nodes linked into 6 membered rings. c) is a two dimensional (4,4) net which is similar in appearance to b) but has a different topology.

Hoskins and Robson produced the first theory of a three-dimensional material based around the linking of metal "nodes" and organic "spacers" .[11] With their synthesis of a copper - 4,4',4",4'"-tetracyanotetraphenylmethane ($[Cu(C(C_6H_4CN)_4)]\cdot BF_4\cdot xC_6H_5NO_2$) they developed the first conceptual understanding of MOF geometry and topology based upon the constituent components that comprise the structure. The application of networks to describe the structure of these coordinated frameworks was first applied to MOFs, independently, with the simultaneous publications by the O'Keeffe and Férey groups in 2000.[59,60] This application of topology to MOFs served as the basis on which reticular chemistry was created.

Another descriptor is the use of the *k*-c notation, where *k* corresponds to the degree of connectivity of the vertices in a network.[18] Each vertex is commonly referred to as *k*-c in order to be distinguished from graph theory, where the term connected has a different meaning. When multiple vertices are present in a network, the *k* values a listed the use of (k_1, k_2, …)-c is used to describe a net. Care must

be taken to avoid confusing the k-c notation with Wells's (*n*,*p*) notation with both descriptors found commonly in the literature.

To bring order to these many descriptors, O'Keeffe et al. developed the searchable database called the Reticular Chemistry Structure Resource (RCSR).[61] Descriptors that previously had been used to specify zeolites were applied to the new porous coordination compounds. The descriptor consists of three bold lower cases characters with the codes being generated from the corresponding inorganic default network. For example, **dia** is derived from the network of diamond and **pts** derived from platinum sulphide. These codes are called reticular chemistry structure resource (RCSR) symbols and have commonplace as descriptors in the literature (**Figure 1.9**).[62]

In **Figure 1.8** two examples of well-known MOFs in the literature can be seen. The first is of MOF-5, which is comprised of six connected octahedral {Zn_4O} SBUs linked by linear diatopic ligands (benzene-1,4-dicarboxylic acid). The resulting structure is a 6-c net with the RCSR code **pcu** (primitive cubic). The secondary structure is of HKUST-1 (Hong Kong University of Science and Technology), which has a 3,4-c net with the RCSR code **tbo** (twisted boracite), with the 4-connected {Cu_2} SBUs being linked by 3-connected linkers (benzene-1,3,5-tricarboxylic acid).

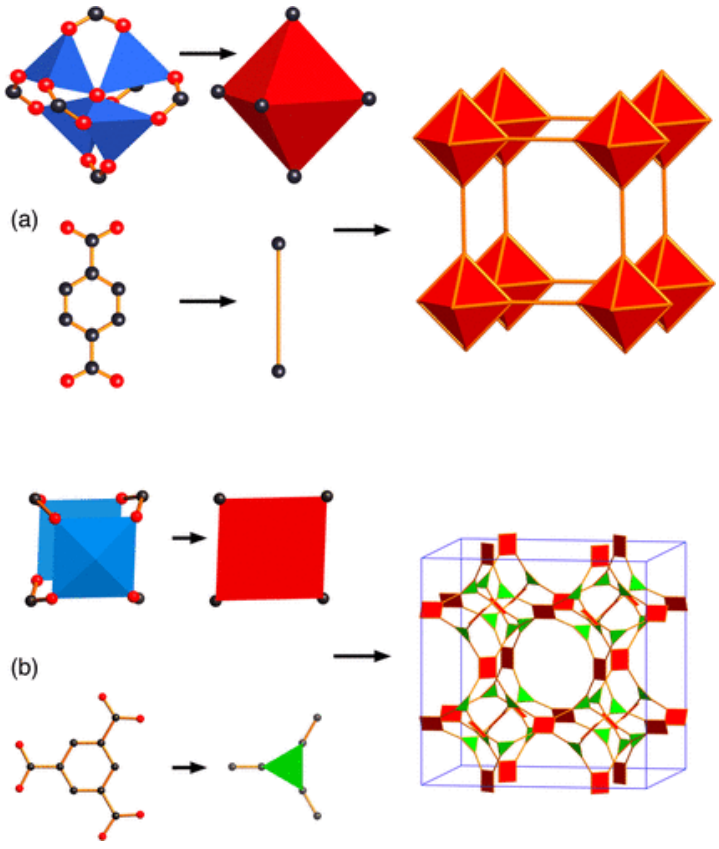

Figure 1.8: a) The building units of MOF-5 showing the abstraction of the {Zn_4O} SBU as a 6-c octahedron, the ditopic terephthalate linker as a rod and their assembly into the (6-c) pcu net. b) the building units of HKUST-1 showing the {Cu_2} paddlewheel SBU abstracted as a 4-c square, the tritopic linker as a 3-c triangle and their combination to form the (3,4-c) tbo net. Reproduced from reference 62.

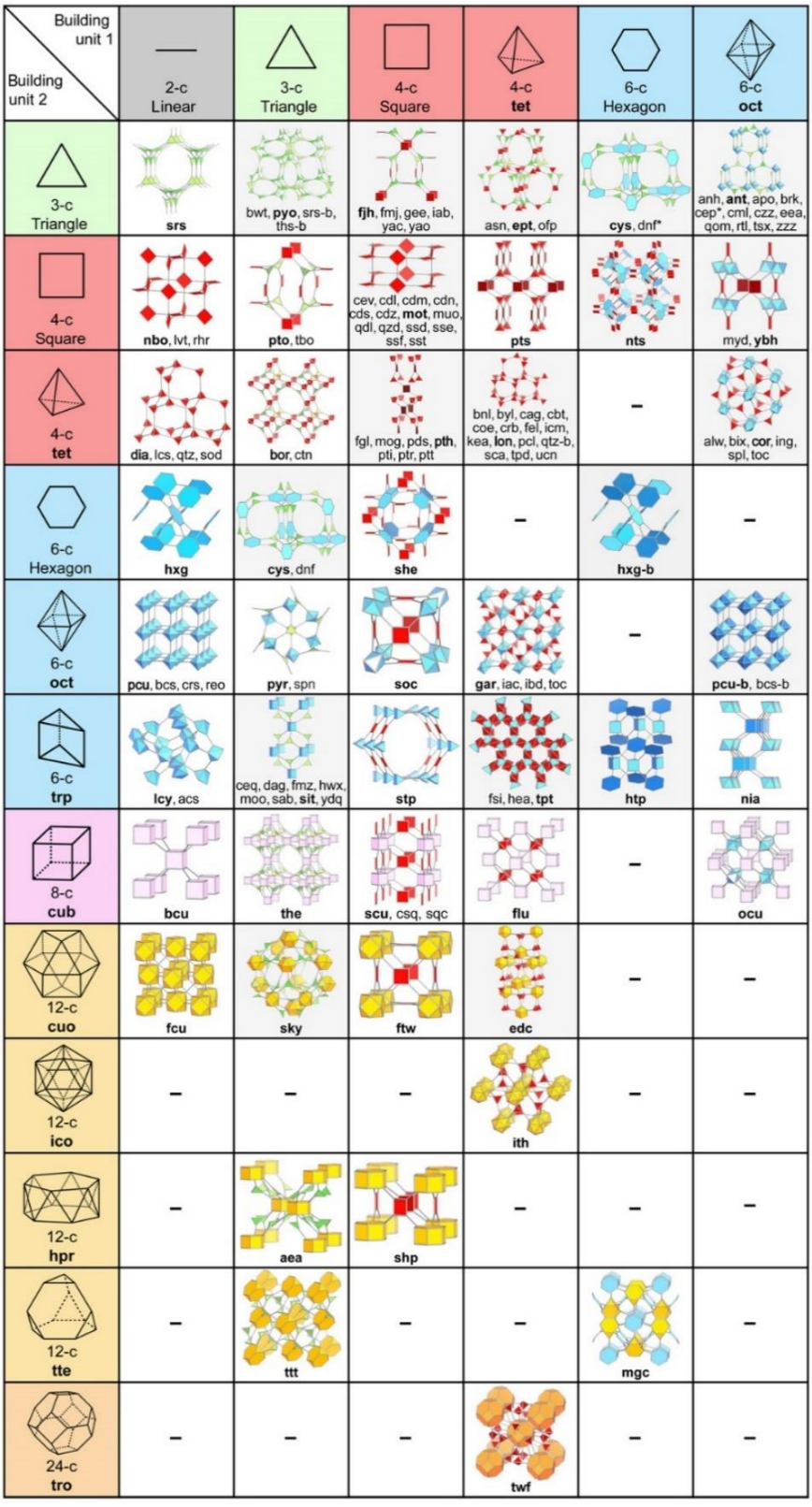

Figure 1.9: A table of possible binoidal nets representing binary frameworks made by reticular chemistry. If more than one net exists, then the identifier of the indicated net is shown in bold. In these cases, either the local symmetry of the building units (for example, torsion angles and dihedral angles) or the comparison of the maximum symmetry embedding and the topological density helps to decide which net is most likely to form from the given set of building units. Reproduced from reference 63.

In comparison to MOFs, which can form a near-infinite number of nets MOPs can form a far smaller number of structures. The topology of MOPs are often described by the shape and the structure of the SBUs and linkers that comprise them. In the description of MOPs, the inorganic SBUs are commonly treated as the vertexes of a polyhedron and the linkers are treated as the edges, for ditopic linkers, and the faces, for tritopic or greater linkers. Analogous to that of MOFs, several methods have been developed to describe the structure of a MOP. The simplest method of describing the MOPs is the ratio of the inorganic SBUs to linkers. This description method tends to be limited to MOPs, where the organic linkers occupy the edges of the polyhedron. The prominent researcher in the field of MOPs, Fujita *et al.* used this descriptor for his M_nL_{2n}-based MOPs.[64,65,30] These cages were comprised of square planar Pd^{2+} ions coordinated by four N-donor bispyridyl linkers. This helps simplify the complex formula for a MOP to just the ratio of the SBUs to linkers.

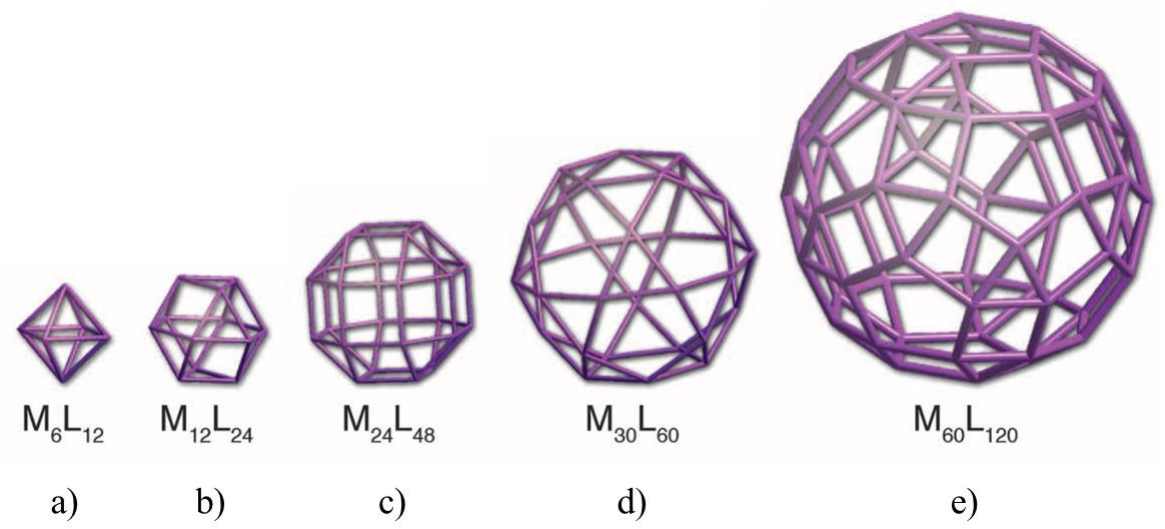

Figure 1.10: The family of M_nL_{2n} polyhedra where metals (M) and bridging ligands (L) are mapped onto the vertices and edges, respectively, of the polyhedra. a) octahedron, b) cuboctahedron, c) rhombicuboctahedron, d) icosidodecahedron, and e) rhombicosidodecahedron. Adapted from reference 64.

Based upon the RCSR codes given for the MOFs topologies, a similar set of codes was given for the various polyhedra that the MOPs form. Like the assignment for MOFs, the RCSR codes for the topologies are based upon the structure of previously known topologies, which are the Platonic and Archimedean solids. Examples include **tet** (tetrahedron), **oct** (octahedron), **cub** (cube), **cuo** (cuboctahedron), and **ico** (icosahedron) (**Figure 1.11**).

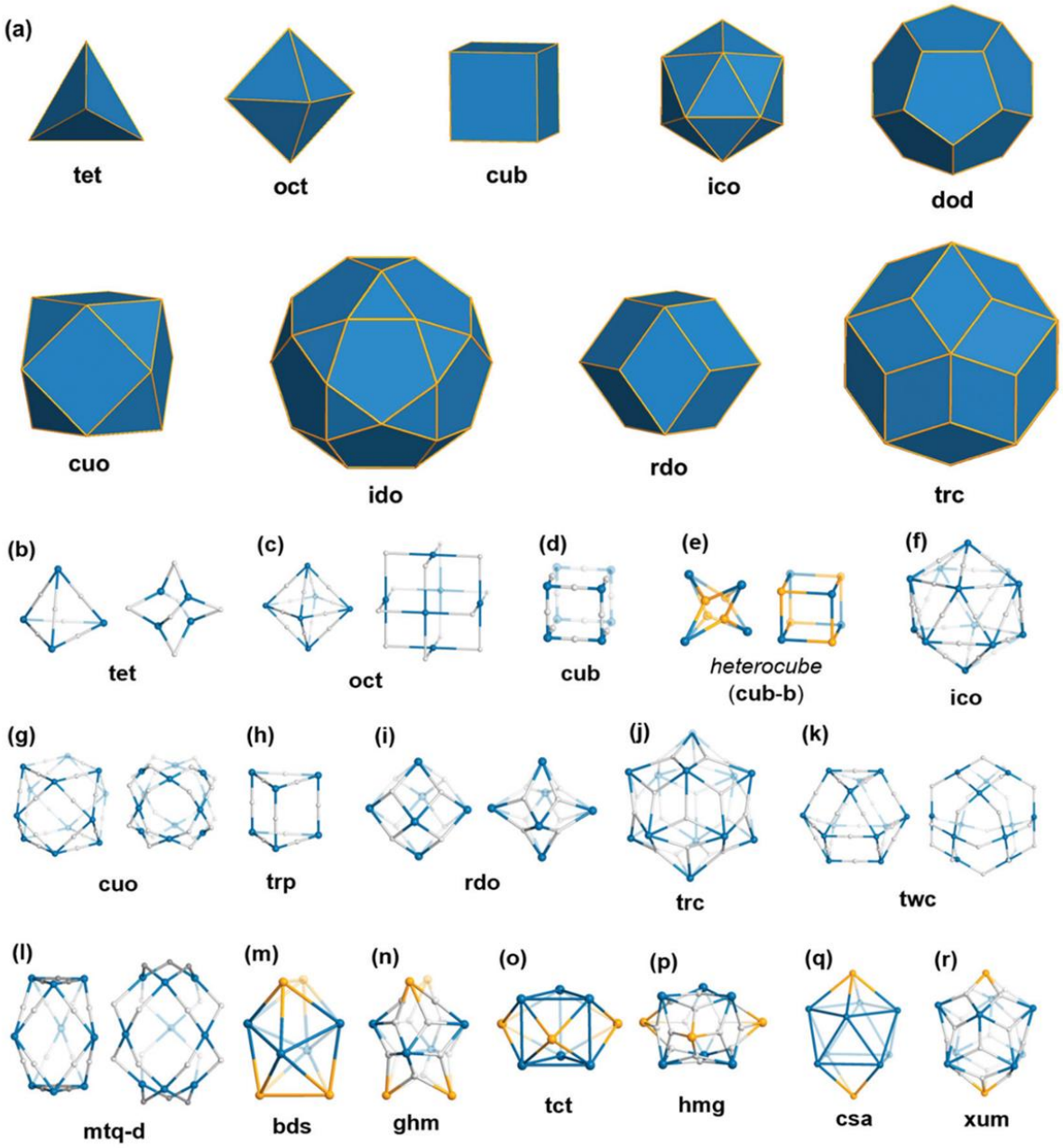

Figure 1.11: The three boldfaced letters (xyz) are the RCSR code for the polyhedra.[61,43] **(a) Nine edge- transitive polyhedra, specifically the five regular solids, i.e., tetrahedron (tet), octahedron (oct), cube (cub), icosahedron (ico), dodecahedron (dod), two quasi-regular solids, i.e., cuboctahedron (cuo), icosidodecahedron (ido), and Catalan solids as duals of the quasi-regular solids, i.e., rhombic dodecahedron (rdo) and rhombic triacontahedron (trc). (b)–(r) The skeletal view of 17 polyhedra including the heterocube (cub-b), triangular prism (trp), anticuboctahedron (twc), hendecahedron (mtq-d), snub disphenoid and face-capped snub disphenoid (bds, ghm), triaugmented triangular prism and face-capped triaugmented triangular prism (tct, hmg), and gyroelongated square bipyramid and face-capped gyroelongated square bipyramid (csa, xum). Reproduced from reference 66.**

1.3 Design and synthesis of MOFs and MOPs

1.3.1 Reticular synthesis

The terms ‘reticular’ and ‘reticular synthesis’ were defined by Yaghi et al. in a highly cited Nature paper in 2003.[67] The term ‘reticular’, derived from the Latin word ‘*reticulum’* meaning ‘net’, and was defined as “having a form of a net or netlike" and reticular synthesis defined as "the process of assembling judiciously designed rigid molecular building blocks into predetermined ordered structures (networks), which are held together by strong bonding". In reticular synthesis, the chosen inorganic SBUs and organic linkers are selected based upon their geometry and their ability to remain unaltered during the synthesis of the MOF. The geometries of the chosen SBUs and organic linkers are determined from the topology of the targeted framework. This same network can be synthesised with a range of inorganic SBUs and organic linkers so long as they maintain the geometrical requirements for the framework. This ability to substitute various building units is known as ‘iso-reticular synthesis’.[68] Using this method, the pore size and porosity of the material can be fine-tuned through the extension or shortening of the organic linkers. In **Figure 1.12**, examples of iso-reticular synthesis can be seen. Yaghi et al. distinguished this concept from supramolecular chemistry as the construction of the framework involve the formation of strong coordination bonds.[17]

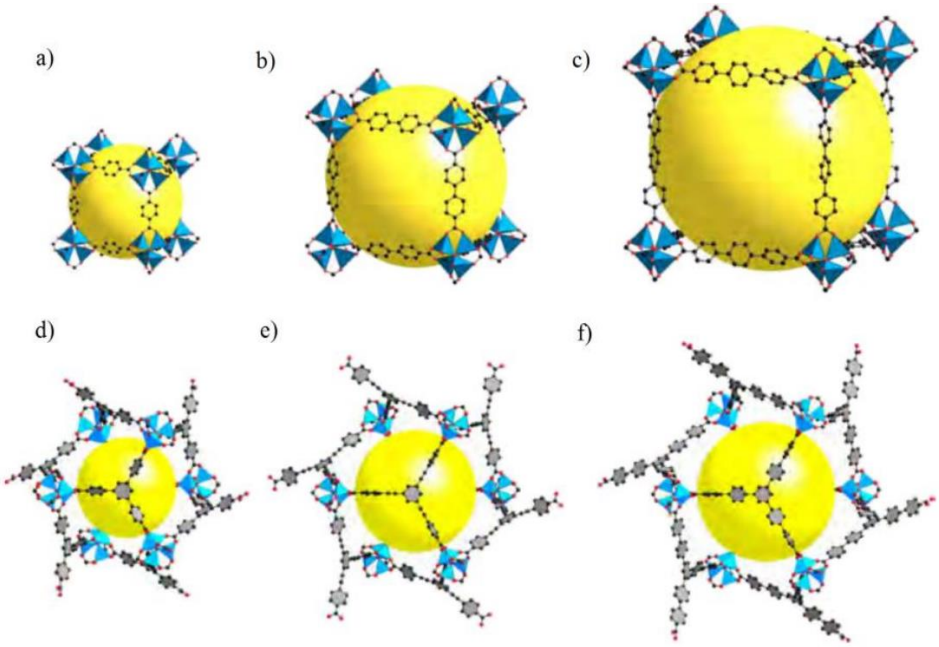

Figure 1.12: Representations of two different series of iso-reticular MOFs. a) IR-MOF-1 (also known as MOF-5),[9] b) IR-MOF-10,[69] c) IR-MOF-15,[69] d) MOF-177,[70] e) MOF-180,[71] f) MOF-200.[71] Adapted from references 69 and 71.

Similarly to MOFs isostructural methods can be applied to MOP design to tun the properties of the MOPs. In contrast to MOFs, however, MOPs can accept a broader range of angles in both the inorganic SBUs and organic linkers while maintaining an iso-structural MOP. To determine the

limits of these angles, O'Keeffe and Yaghi denoted these two angles as 'η' for the angle between the direct linkages of the inorganic SBU and 'θ' for the angle between the direct linkages of the organic linkers.[43] Using these two angles, they calculated the various combinations for these angles and sorted the MOPs into categories based upon their shapes. Representations of these groups and their topologies are shown in **Figure 1.13**.

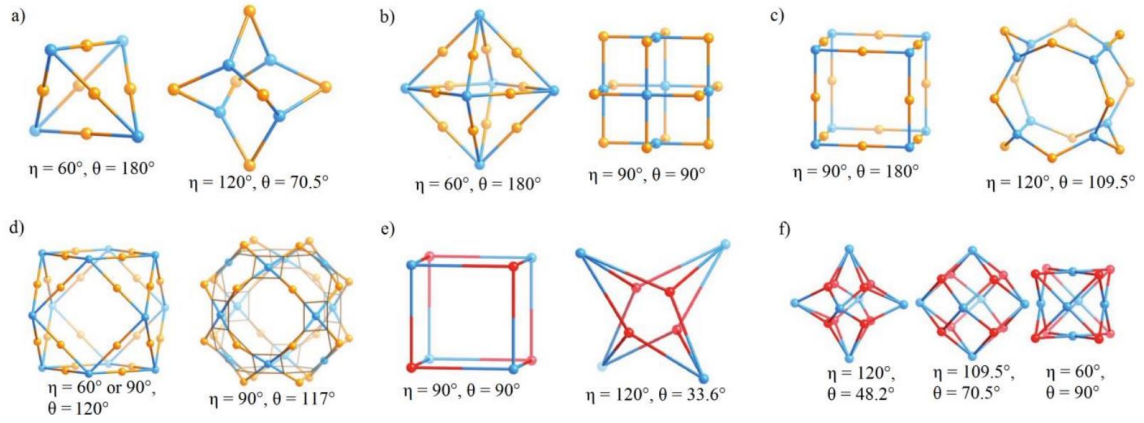

Figure 1.13: Representations showing structure topologies of MOPs. a) Tetrahedron: two different configurations of four trivalent SBUs (blue) with linkers (orange), b) Octahedron: two different configurations of six tetravaelnt SBUs (blue) with linkers (orange), c) Cude: two different configurations of eight trivalent SBUs (blue) with linkers (orange), d) Cuboctahedron: two different configurations of twelve tetravalent SBUs (blue) with linkers (orange), e) Heterocube: two different configurations of eight trivalent SBUs (red/blue), f) Rhombic dodecahedron: three different configurations of eight trivalent SBUs (red) linked to six tetravalent SBUs (blue). Adapted from reference 43.

While there are many MOPs in the literature that the descriptors used by O'Keeffe and Yaghi predict the formation of, there remains a significant amount where these descriptors fail. The reason for this failure is attributed to both deviation from the idealised bond geometries described by O'Keeffe and a rotation component present in some linkers, which leads to a twisting of the linker around a symmetry axis. Hay et al. further expanded on the works carried out by O'Keeffe to include a wider range of factors in the SBUs and organic linkers geometry, which allow for more significant deviation from the idealised geometry described by O'Keeffe and Yaghi.[72] Most notably, in the inclusion of a twist angle to an organic linkers description (**Figure 1.14**). This allows for the conformational flexibility of the organic linker to be factored into the MOPs predicted structure.

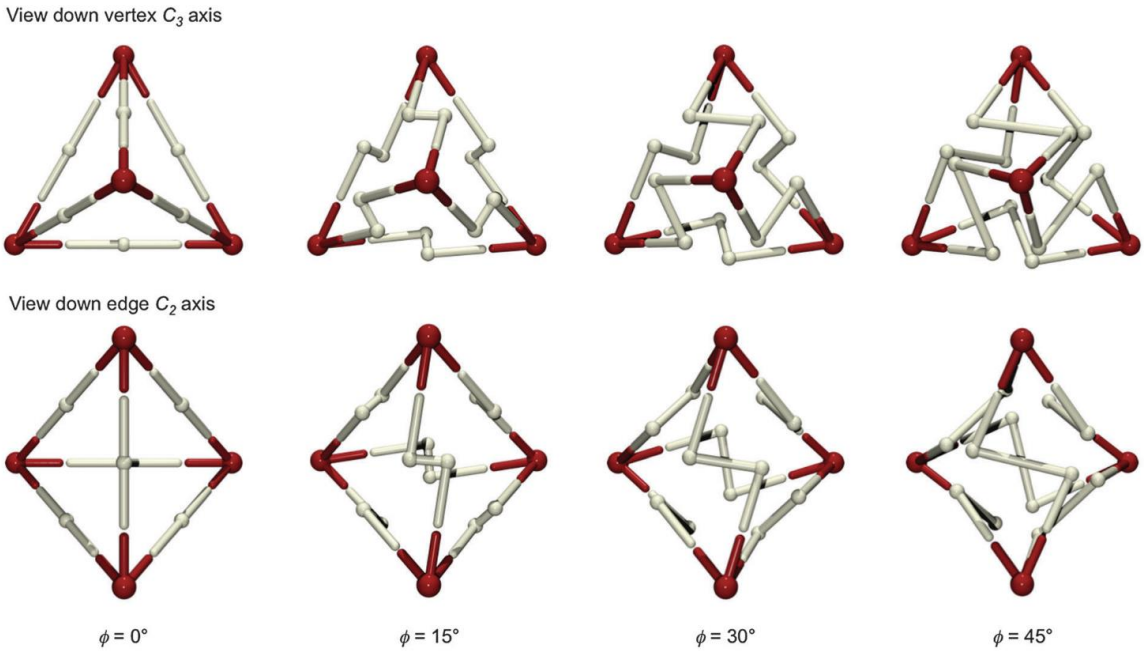

Figure 1.14: Progressing from left to right shows how the greater twist angle influences the structure of tetrahedral MOP. The organic linkers (white) is divided into two joints which become further separated as the twist angle increases. As the twist angle increases, the inorganic SBU (red) rotates around the C_3 axis of the tetrahedron. Reproduced from reference 72.

1.3.2 Functionalisation and post-synthetic modification

The functionalisation of a MOF or MOP is the incorporation of additional functional groups into the structure that serve to alter the properties of the compound.[73] These additional functional groups do not play a structural role in the formation of the framework but are merely present within the structure. This ability to add additional functionality to a MOF is possible through the isoreticular synthetic approach to MOF and MOP synthesis. The methods used in the literature to functionalise MOFs can be divided into two broad categories, pre-synthetic[74,75,76] and post-synthetic.[77,78,79]

In the per-synthetic functionalisation of a MOF the organic linkers used to construct a previously known MOF are replaced with linkers with the required functional group. With the application of iso-reticular synthesis, for as long as the geometry of the underlying organic linker remains unchanged, so will the MOF structure remain unaltered. Various versions of MOF-5 have been synthesised using functionalised organic linkers by Yaghi et al. (**Figure 1.15**).[74] From this set of organic linkers it is apparent that the list of functional groups introduced by this method is severely limited. Functional groups such as alcohols, aldehydes, carboxylic acids, nitriles, phosphines, plus others, are absent from this list of functionalised linkers. This is due to these functional groups being incompatible when used with the BDC scaffold as their presence complicates or even prevents the synthesis of the MOF. This is due to these functional groups either being thermally labile in the

solvothermal synthesis, limited by their solubility or coordination to the metal ions, thus altering the framework of the MOF.

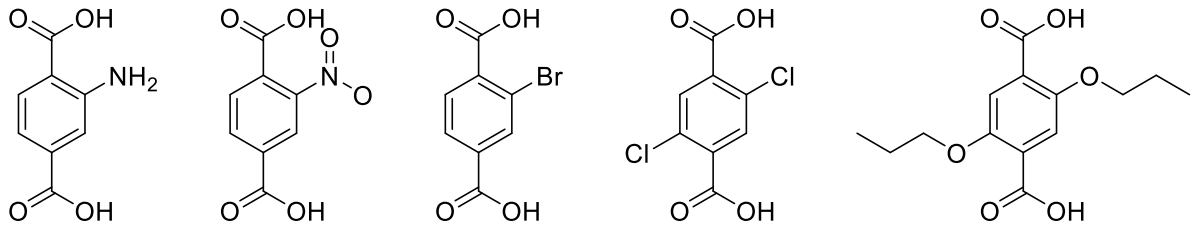

Figure 1.15: Examples of functionalised benzene-1,4-dicarboxylate (BDC) based linkers used by Yaghi et al. to synthesise MOF-5 derivatives.[74]

Due to these issues and the limited scope of pre-synthetic functionalisation, post-synthetic functionalisation has grown in favour of adding functionalisation to a MOF. Post-synthetic functionalisation is the chemical modification that is performed on a synthesised MOF rather than on the organic linker precursors. Using this method, the newly introduced functional groups need to be compatible with the final MOF, negating any incompatibility issues with the synthetic methods. For these post-synthetic reactions to occur, however, they often first require a pre-synthetic functionalised MOF, which contains functional groups that do not disrupt the synthesis of the MOf but that can be reacted with post-synthetically. An example of this is seen in **Scheme 1**where the amino group of an amino functionalised derivative of MIL-101(Fe) is reacted with a BODIPY derivative to give the material photoluminescent properties that are absent in the parent MOF.[80]

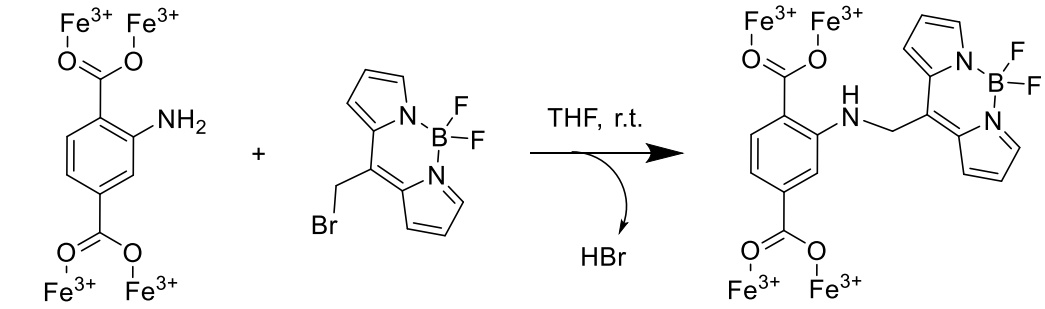

Scheme 1: Reaction for the post-synthetic functionalisation of an amino functionalised derivative of MIL-101(Fe) with a BODIPY photosensitiser. Adapted from reference 80.

Metal ion-exchange reactions can also be used to modify the properties of a MOF. These exchange reactions are often performed by simply allowing the MOF crystals to sit in a metal salt solution. In

both MOFs and MOPs heterometal can be introduced at chelating sites of the organic ligands,[81], and exchanged with the metal ions that comprise the inorganic SBUs.[63,82,83,84] The extent of this exchange, whether partial or quantitative, can be controlled through the conditions in which the exchange takes place.[85,86,87,88,85]

These same methods of functionalisation can also be applied to the MOPs. In contrast to MOFs however, the location of the functionalisation of the MOP has a considerable influence on the MOPs properties. These two sites are exo-hedral, where the exterior surface of the MOP is functionalised and endohedral, where the organic linkers are functionalised to modify the central pore (**Figure 1.16**).[89,90]

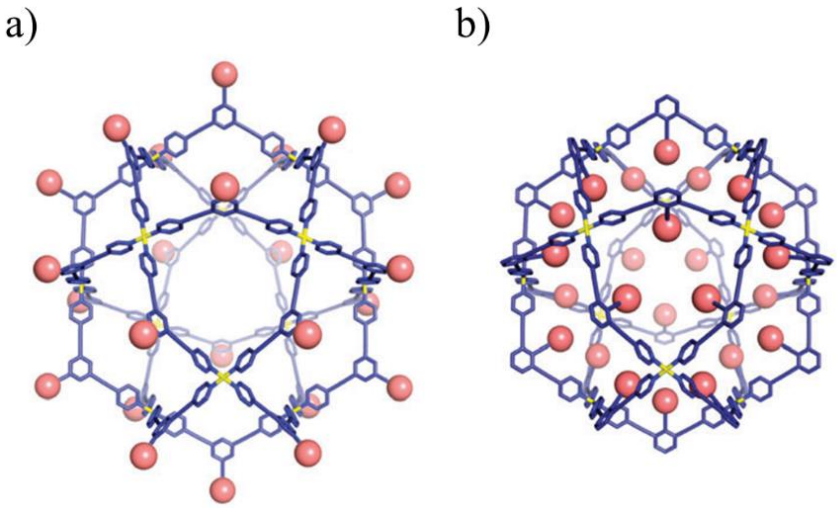

Figure 1.16: A bis(pyridine) ligand modified for the a) exo-hedral and b) endo-hedral functionalisation of a representative MOP. (bis(pyridine) ligand – blue, Pd – yellow, functional group – pink) Adapted from reference 89.

Fujita et al. synthesised a series of MOPs with a diverse range of functional groups both internally. For the exo-hedral functionalisation, he attached a series of bio-active materials, including saccharides,[91] peptides,[92] and nucleotides (**Figure 1.17 a, b and c**).[93] These bio-active groups are of great interest for biomedical applications.

Unlike the exo-hedral functionalisation, endo-hedral functionalisation is limited by the size of the MOP. In order to accommodate these functional groups, Fujita et al. synthesised a series of isoreticular MOPs through the expansion of the bis(pyridyl) linker. Even with the enlargement of the MOPs pore volume, the choice of functional groups is often still limited to groups that can pack dense enough not to disrupt the synthesis of the MOP. This packing requirement often limits the choice of endohedral functional groups to flexible chains as they can bend to adapt to the packing requirements. Some examples of these include poly(ethylene oxide) chains,[94] and perfluorinated chains, where the two functional groups altered the pore's polarity and hydrogen bonding affinity (**Figure 1.17 d and e**). These two functionalisation methods can happen simultaneously, allowing for functionalisation of the MOP through the various combinations of linkers (**Figure 1.17 f**).

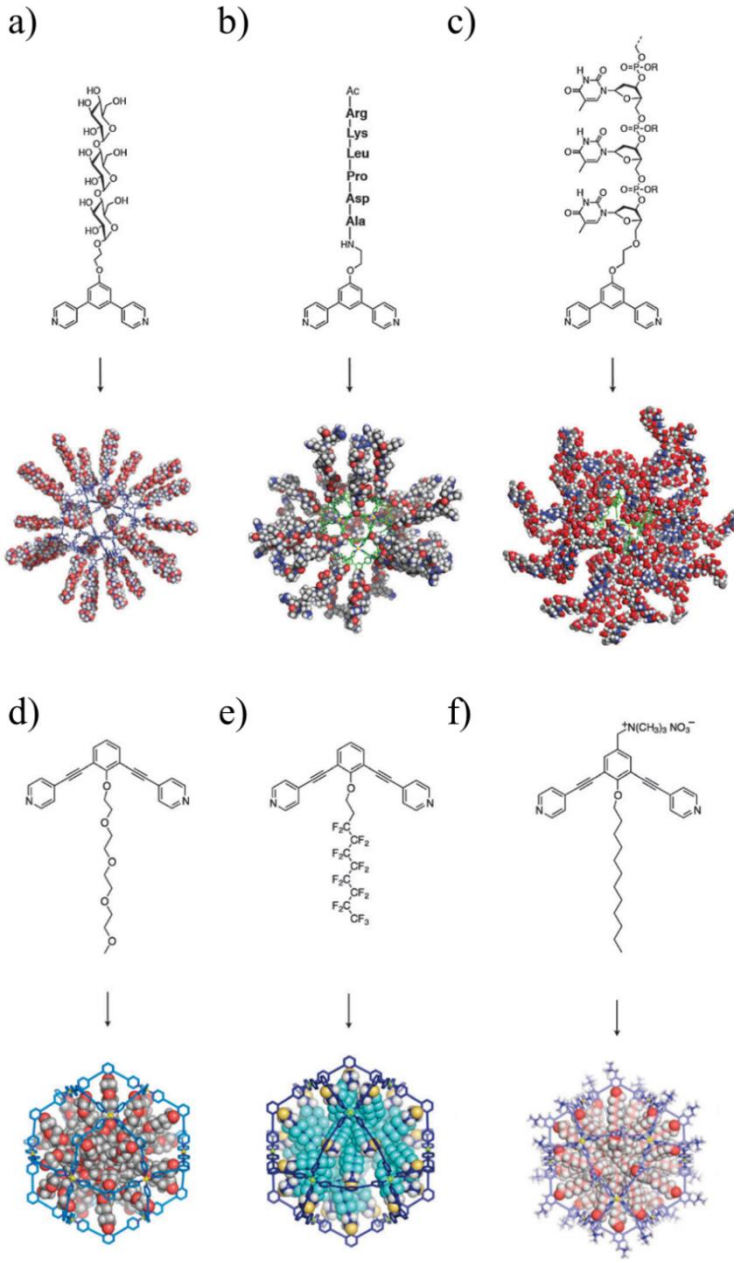

Figure 1.17: A series of exo-hedrally functionalised MOPs with a) saccharides, b) peptides, c) nucleotides and endohedral functionalised MOPs with d) poly(ethylene oxide) chains and e) perfluorinated chains. f) A MOP both endo- and exo-hedrally functionalised with ammonium cations externally to increase its solubility in aqueous solutions and alkane changes internally to increase that non-polar character of the pore. Adapted from reference 89.

1.3.3 Methods of synthesis

Several methods have been reported in the literature to synthesise MOFs and MOPs. The method in which the MOFs and MOPs have been prepared significantly impacts a number of aspects of MOF synthesis, including crystal quality, quantity, and purity. Synthetic methods that have been studied so far include microwave-assisted,[95,96,97] mechanochemical,[98,99] sonochemical,[100,101] electrochemical,[102,103,104,105,106] and vapour diffusion[107] (**Figure 1.18**).

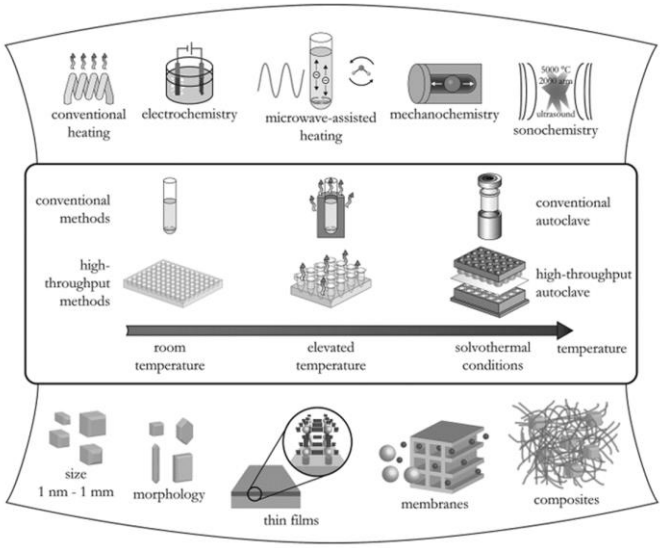

Figure 1.18: An overview of synthesis methods, possible reaction temperatures, and final reaction products in MOF synthesis. Reproduced from reference 108.

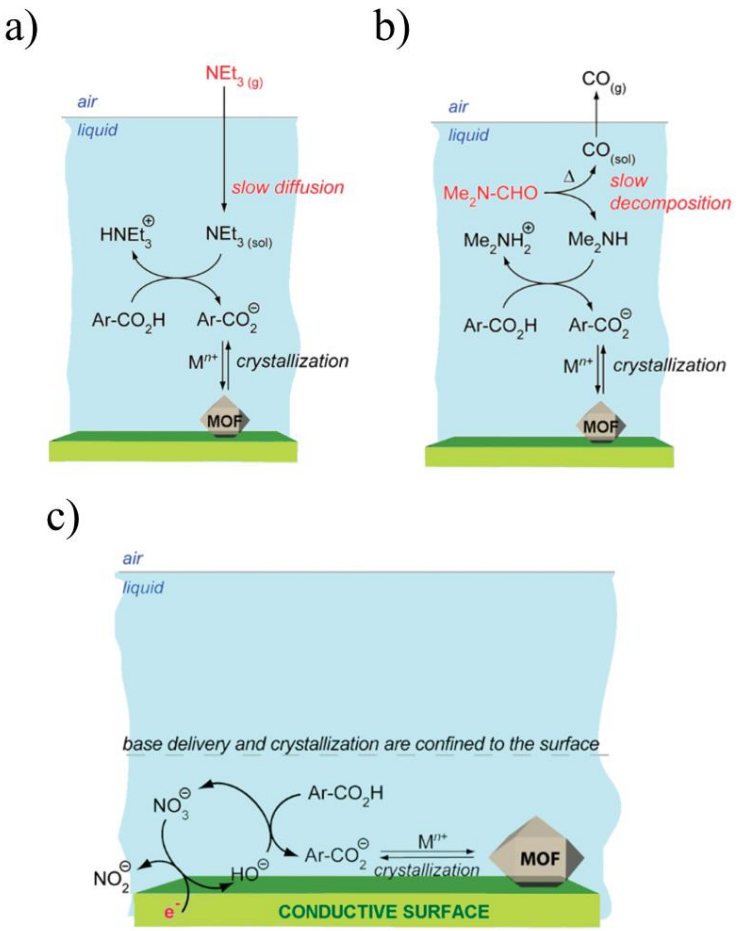

Figure 1.19: Typical crystallisation routes for the synthesis of MOFs: a) slow vapour diffusion of triethylamine, b) slow thermal decomposition of amide solvents under solvothermal conditions, and c) formation of hydroxide ions near the surface of an electrode. Adapted from reference 102.

Vapour diffusion was one of the first reported methods to synthesise crystals of MOF of sufficient size and quality to be studied using single-crystal X-ray diffraction. Through the slow diffusion of the base triethylamine into the reaction solution, the gradual deprotonation of the carboxylate-based ligand occurred, allowing for the slow growth of the MOF crystals (**Figure 1.19 a**). This procedure was used for the structural determination of one of the original archetypal MOFs, MOF-5.[108] The choice of synthetic method is dependent mainly on the desired compound, its morphology and potential application. Methods such as microwave-assisted, mechanochemical and sonochemical synthesis are more applicable for synthesising large quantities of MOF whose structure has been predetermined from other methods.

1.3.3.1 Solvothermal synthesis

Solvothermal synthesis is the most widely reported method of synthesising new MOFs. It allows for the reagents to overcome thermodynamic barriers associated with the formation of network structures and solubility issues of the reactants. The method tends to provide a balance of both producing reasonably-sized crystals required to characterise the resulting structures using single-crystal X-ray diffraction characterisation and high yields of the product. A solvothermal reaction takes place in a sealed pressure vessel in which the chosen solvent is heated above its boiling point generating autogenous pressure. [108,109,110]

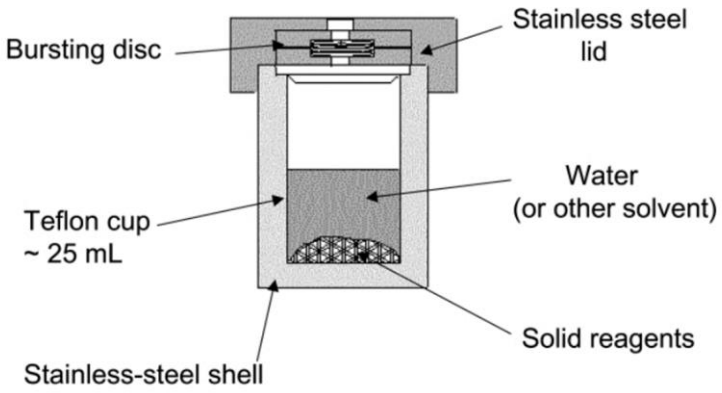

Figure 1.20: A schematic of a Teflon-lined, stainless steel autoclave typically used in the laboratory to perform subcritical solvothermal synthesis. Reproduced from reference 110.

The crystallisation of MOFs is an extremely sensitive process, with MOFs only being synthesised after an extensive trial and error approach. This approach is often the limiting factor for the discovery of new MOFs and MOPs. Although both automation[111,112] and computational methods[113,114,115,116] have recently been used to speed up the rate of discovery through mass sample preparation or by modelling theoretically possible structures. To further complicate matters, the synthetic approaches

often lead to the formation of unwanted side products. Manual separation of the desired product from the unwanted side products is often necessary.

One of the main strengths of solvothermal synthesis is the large number of synthetic variables that can be used to optimise the synthesis of the MOF. Temperature, pressure, pH, concentration, mole ratios, and time can be modified to a broad range of reaction conditions. These parameters can be altered for the selective growth of a MOF and the size and morphology of the crystals. The sheer number of variations and combinations of these parameters leads to the difficult task of discovering a new MOF.

One of the critical parameters for the synthesis is the choice of solvent. A range of solvents has been reported in the literature, including H_2O,[117,118,119] DMSO,[120,121] EtOH[122] and amide based solvents.[123] The dialkylamide solvents DMF, DMA and DEF are the most widely used solvents due to their high polarity, aiding the solubility of the metal salts and the organic linkers and their ability to impart stabilisation effects to reagents and intermediates. The use of dialkyl amide solvents are also known to experience slow decomposition during the synthesis. The resulting dialkylamine products that are formed *in-situ* gradually deprotonate the carboxylic acid-based ligands, aiding in the formation of SBUs and crystal growth (**Figure 1.19 b**). However, it is noted that the term solvothermal synthesis is often incorrectly used in the literature when associated with MOF synthesis. The strictest definition is the heating of a reaction solution within a pressure vessel to above the solvent's boiling point. [3,110] In literature, the term is more often used to refer to reactions that occur in sealed vessels at elevated temperatures but remain below the solvent's boiling point. [45,124]

1.4 Applications of MOFs and MOPs

1.4.1 Gas storage

Owing to the high porosity and tunable structure of MOFs and MOPs, they have found use in a range of applications where these two factors can be most exploited. Solid porous materials have become a significant area of research in chemistry and engineering, with their applications focused on capturing, releasing, and storing various gases.[125,126,127] In comparison to similar classes of solid porous materials such as carbon-based solids, zeolites, porous silica, porous polymers and covalent-organic frameworks, MOFs have been established as the most tunable and structurally diverse (**Table 1.1**).

Table 1.1: A comparison of classes of solid-state adsorbents. Adapted from reference 125.

	Metal-organic frameworks	Zeolites	Covalent-organic frameworks	Porous organic polymers	Porous molecular solids
Porosity	Microporous, mesoporous	Microporous, mesoporous	Microporous, mesoporous	Usually microporous	Usually microporous, rare mesoporosity
Pore size distribution	Sharp	Sharp	Sharp	Broad	Sharp
Crystallinity	High	High, occasionally amorphous	Moderate to high	Amorphous	High
Stability	Modest	High thermal stability, occasionally pH sensitive	low for borates, high for imines	Good, especially hydrothermal	Modest, Isolated examples of hydrothermal stability
Modularity	Very high	High, new structures can be based on known zeotypes	In principle high, growing occurrence	Very high	Rare, some co-crystals
Processability	Insoluble, composites and films well known	Insoluble, films, composites, pellets well developed	Insoluble, examples of surface growth	Low, except PIMs	Soluble – pro or con depending on the application
Designability	Excellent, well developed reticular chemistry	High but design of organic templates is often challenging	Reticular chemistry applies in principle	Control over composition well developed, control over 3D organisation limited	Control over functionality within the cage. Limited control over the assembly
Unique selling point	High structural and chemical control for specialised application	Stability, established use	Electronic properties	Extended conjugation possible	Physical properties intrinsic to cages, solubility
Summary	Established and highly active field, awaiting large-scale application	Major commercial importance, still growing	Early promise for organic electronics	Growing area, diverse chemistry, commercial application for PIMs	New area, early promise for specific separations

1.4.1.1 Hydrogen storage

With the advent of the adverse effects of climate change and efforts to minimise its impact on the planet, new technologies are required to reduce carbon emissions. One of the primary sources of worldwide emissions is transport. To eliminate these emissions, an alternative carbon-free energy material is required. One of the leading candidates to replace carbon-based materials is hydrogen. Hydrogen is a fuel source with the highest energy density by weight, producing nearly three times as much energy when burned compared to petrol (120 MJ/kg vs 44.5 MJ/kg).[128] The only by-product from its combustion in air is water. This makes it an attractive alternative to fossil fuels being both sustainable and eco-friendly.[129]

The main drawback hindering the widespread adoption of hydrogen for transport is its low volumetric energy density. New strategies are needed to be developed to store the gas such that they reduce this negative property. To encourage development in the field, the US Department of Energy (DOE) has funded research into the area with clear targets to reach for a range of aspects for the storage of the material.[130] These targets are regularly increased to drive further development.[9, 70,71,124, 131]

MOFs are a prime candidate for the storage of hydrogen. They can do this through two different methods. One method is through the simple physisorption of the gas molecules onto the large surface area of the MOF. Hydrogen uptake capacity approximately increases with the increased surface area of the MOF. This capacity is only limited by the maximum theoretical surface area possible with MOFs.[132,133] The second method for storing hydrogen in MOFs is by introducing unsaturated metal centres (UMCs). These UMCs can be generated in MOFs by removing coordinated solvent molecules under vacuum or high temperature.[134,135,136] These UMCs can result in increased uptake characteristics, especially at lower pressures where the stronger binding interactions between the UMCs and H_2 molecules are the dominant binding interaction.[137]

The first MOF reported in the literature that was found to be capable of storing a significant amount of hydrogen was MOF-5. In 2003 uptakes of 4.5 wt% (1 bar, 78 K) and 1 wt% (20 bar, 298 K) were reported for MOF-5.[9] Since then, extensive investigations into MOFs as hydrogen storage materials were conducted. Another significant benchmark was set in 2007 using a structurally related, high-surface-area ZnMOF, MOF-177, achieving an uptake of 7.5 wt% at 60 bar and 77 K.[70] Through further optimisation of the synthesis and activation procedures, this was later improved to 9.6 wt % at 77 K and 100 bar (**Figure 1.21**).[138]

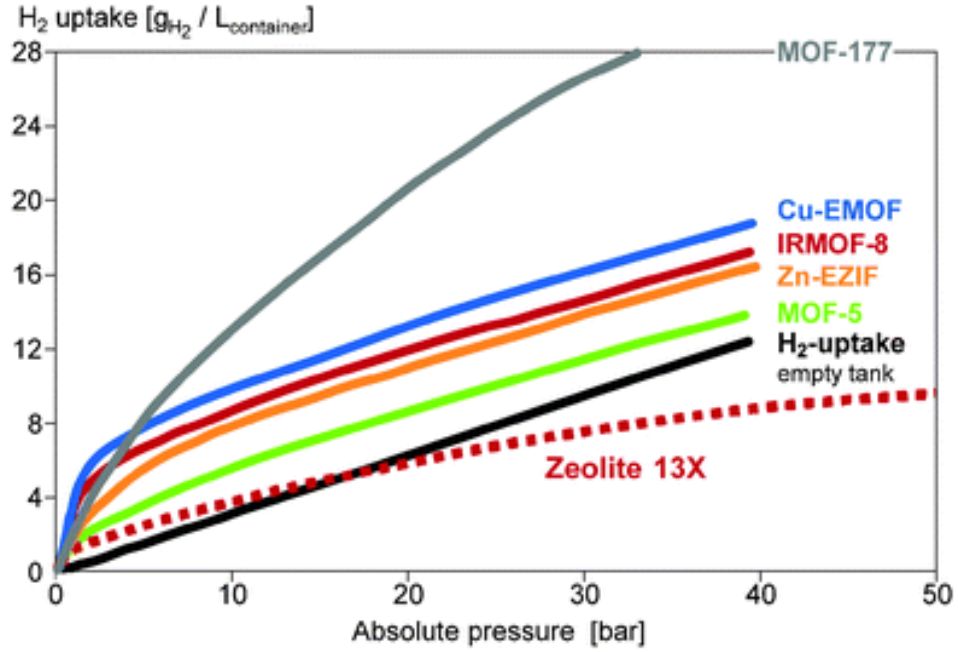

Figure 1.21: The hydrogen storage properties of some representative MOFs at high pressure in prototype trials. Reproduced from reference 139.

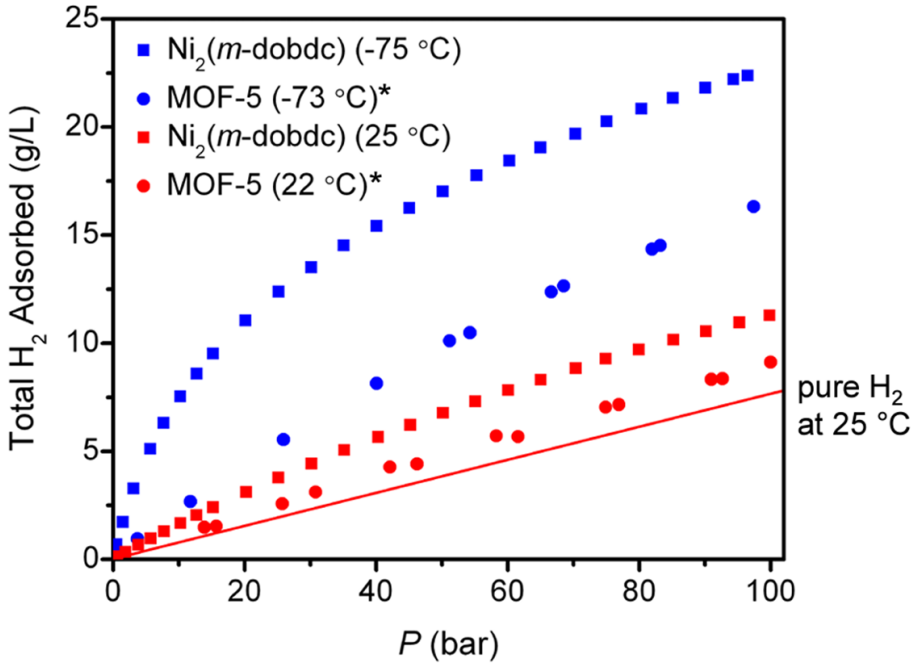

Figure 1.22: High-pressure H_2 adsorption using [Ni_2(*m*-dobdc)] compared to MOF-5 at both cryogenic and ambient temperatures. Reproduced from reference 140.

While these materials achieve the DOEs H_2 storage target of 5.5 wt% uptake they fail with regards to the other targets. Notably, a target density of 40 g/L and an operating temperature of 233 K or higher. Current research focuses on achieving these objectives. The cause of the previously mentioned materials not meeting these other goals is the weak binding interaction between the H_2 molecules and MOF. To increase the bonding interactions between the MOF and H_2 molecules MOFs

with UMCs were synthesised. These UMCs are known to increase the enthalpy of H_2-adsorbent interactions, which should approximately be above 15 kJ/mol to facilitate strong adsorption at higher temperatures.[141] One record-setting MOF that utilises UMCs is Ni_2(*m*-dobdc). The MOF was discovered to have an exceptional H_2 uptake of 12.1 g/L at 100 bar at 298 K . This is a significant increase compared to MOF-5 when it was first reported. It was capable of achieving this uptake due to the uncoordinated Ni^{2+} sites, which led to the polarisation of H_2 molecules upon sorption, resulting in a binding enthalpy of 13.7 kJ/mol.

1.4.1.2 CO_2 capture and storage

Another method in which MOFs are playing a role in combating rising CO_2 levels is through the capturing and storing of CO_2. Many methods have been proposed for carbon capture and sequestration (CCS).[142] Physical solvents such as SELEXOL® and Rectisol® have been used for over forty years to separate acidic gasses such as CO_2 and H_2S from feed gas streams.[143] Chemical solutions, such as aqueous alkanolamine solutions, react with the CO_2 to form carbamates and bicarbonates.[144,145,146] These chemical solutions tend to be more effective than physical solvents with increased selectivity and stronger bonding interactions. These strong bonding interactions can be seen as a double edge sword as the regeneration of the solution requires heating to elevated temperatures, consuming a lot of energy in the process.[142] Further drawbacks to this method include the corrosive nature toxicity of the solvents.

Several other methods are currently under investigation and development. These methods aim to minimise or eliminate the drawbacks of the previously discussed methods. Alkali metal hydroxides and $Ca(OH)_2$ are highly selective and economical routes to capture CO_2 from the air.[147,148,149] The regeneration of the hydroxides and isolation of CO_2 requires heating the carbonates above 800 ºC, making the process energetically inefficient.[149] A range of other porous materials, including zeolites, porous carbons and mesoporous silica, have been demonstrated to have excellent absorption of CO_2 at low pressures.[150,151,152] The selectivity, uptake and rate of adsorption can be improved through the functionalisation of the materials.[153,154,155,156,157] However, this that be chemically challenging and alters the method in which the materials absorb CO_2 from a physiorpitive to a chemisorptive process.

MOFs are attractive alternative materials for the capture of CO_2 due to their high gas uptake, tuneability of properties based upon their required needs, and high performance and recyclability. A broad range of methods has been applied to MOFs to improve their properties for CO_2 capture. The two properties of the CO_2 molecules that are most often used to separate them from other gas molecules is the kinetic diameter (3.30 Å) and its significant electric quadrupole moment.[158,159] MOFs containing both with[160,161,162,163] or without[164,165,166,167,168,169] UMCs have been used to capture CO_2. For the physisorption processes, the sizes of the pore can be tuned to preferentially bond to CO_2 through ligand design or through the strategic interpenetration of the framework. The linkers can be

further designed to contain -OH and -NH_2 functional groups that will chemically bond to the gas molecules.

One of the earliest MOFs used to capture CO_2 was developed by Zaworotko with the group of MOFs known as SIFSIX (**Figure 1.23**).[170] The MOFs were discovered to have excellent selectivity for CO_2 adsorption at low pressures (*ca.* 40 Pa). In the structure of the SIFSIX-3-M (M = Ni, Cu, Zn) MOFs, the pores have a diameter of *ca.* 3.3 Å, allowing for a single CO_2 molecule to interact with the walls of the pore. This pore diameter is too small to permit the uptake of N_2 with its kinetic diameter of 3.64 Å. The addition of the electronegative fluorine atoms on the SiF_6^{2-} anions allows for polarisation of the CO_2 molecules. The combination of these two effects leads to a high enthalpy of adsorption and high selectivity towards CO_2 at low pressures.[171]

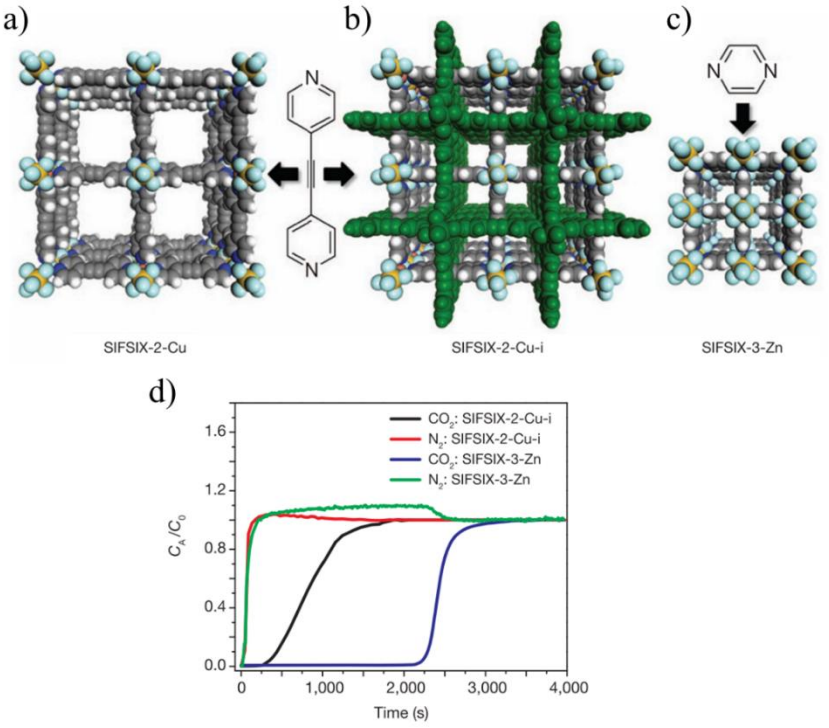

Figure 1.23: Three examples of MOFs belonging to the SIFSIX family of compounds. a)SIFSIX-2-Cu, b) SIFSIX-2-Cu-i and c) SIFSIX-3-Zn. The interpenetrated structure of SIFSIX-2-Cu-i allows for the reduced pore size compared to the structure of SIFSIX-2-Cu even though the two MOFs are synthesised from the same linker. d) the breakthrough curves of CO_2 and N_2 for the MOFs SIFSIX-2-Cu-I and SIFSIX-3-Zn. The longer breakthrough time for CO_2 for the two MOFs indicates the selective adsorption of CO_2 over N_2. Adapted from reference 171.

Two strategies for the implementation of UMCs in MOFs for CO_2 storage are found in the literature. One technique is similar to that of the storage of H_2 in a MOF. MOFs with large pore diameters that are lined with UMCs facilitate strong interactions and selectivity.[172] The MOFs can be further optimised such that two UMCs are located in the optimum distance and position such that an

adsorbed CO_2 molecule coordinates to the two UMCs. An example of this is found in the MOF PCN-88.[173] The MOF contains two copper paddlewheels that, when activated, contain UMCs that are separated by approximately 7 Å. With this separation, a single CO_2 molecule is capable of being trapped between the two UMCs. This method is known as the single-molecule trap (SMT) approach, which allows for highly selective uptake of CO_2.

Another approach to using the UMCs in the adsorption of CO_2 is in combination with diamine compounds (**Figure 1.24**). Through the adsorption of the diamine compounds into the MOF allows for the heterogenisation of the amine solvents. In chemically robust MOFs with well-separated UMCs, one amine of the diamine molecule can bind to a metal cation as a Lewis base, while the second amine remains available as a chemically reactive adsorption site. MOFs that have one-dimensional channels that UMCs line can adsorb CO_2 *via* a unique mechanism involving the formation of ammonium carbonate chains (**Figure 1.24 b**). The adsorption of CO_2 can be tuned through the selection of the diamine compound (**Figure 1.24 c**).

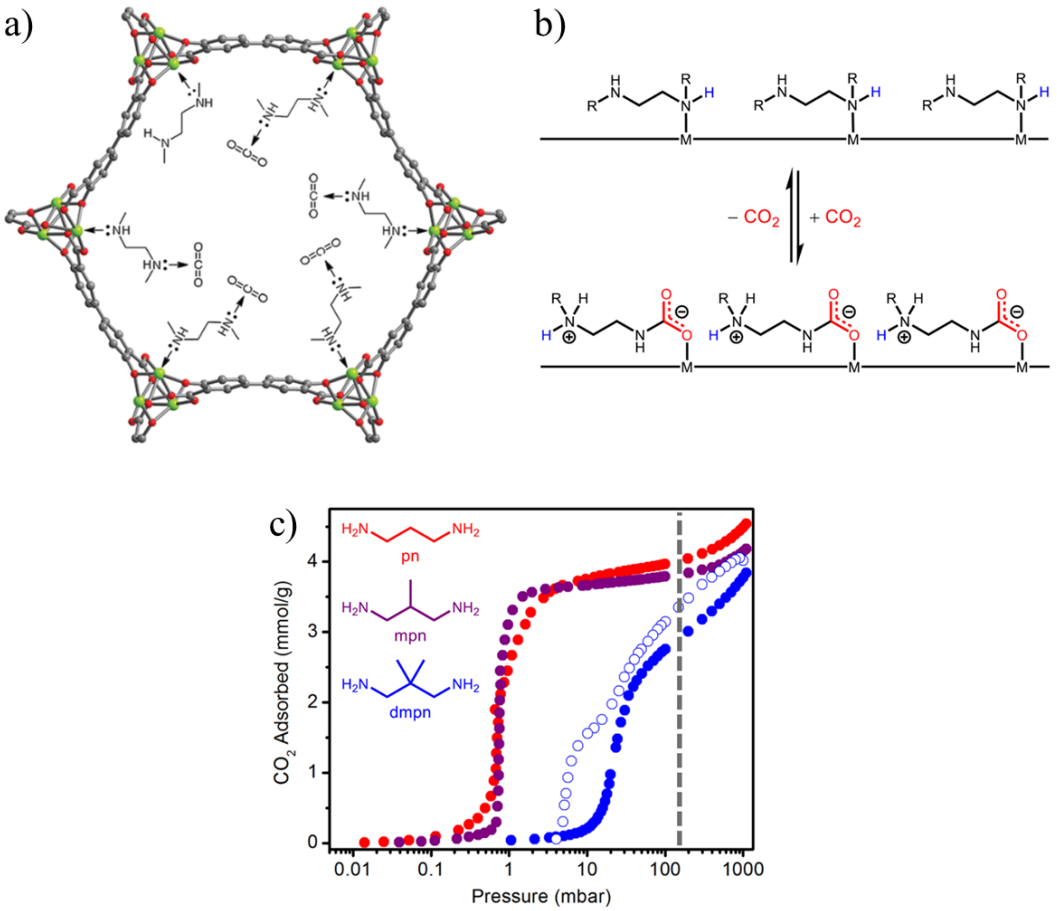

Figure 1.24: a) N,N′-dimethylethylenediamine coordinating to the UMCs on the Mg-ions found in Mg_2(dobpdc). b) Depiction of cooperative CO_2 insertion into a row of Mg^{2+}–diamine sites to form ammonium carbamate chains along the pore axis. c) Isoterms for the adsorption of CO_2 in Mg_2(dobpdc) with various diamine compounds. Adapted from references 174 and 175.

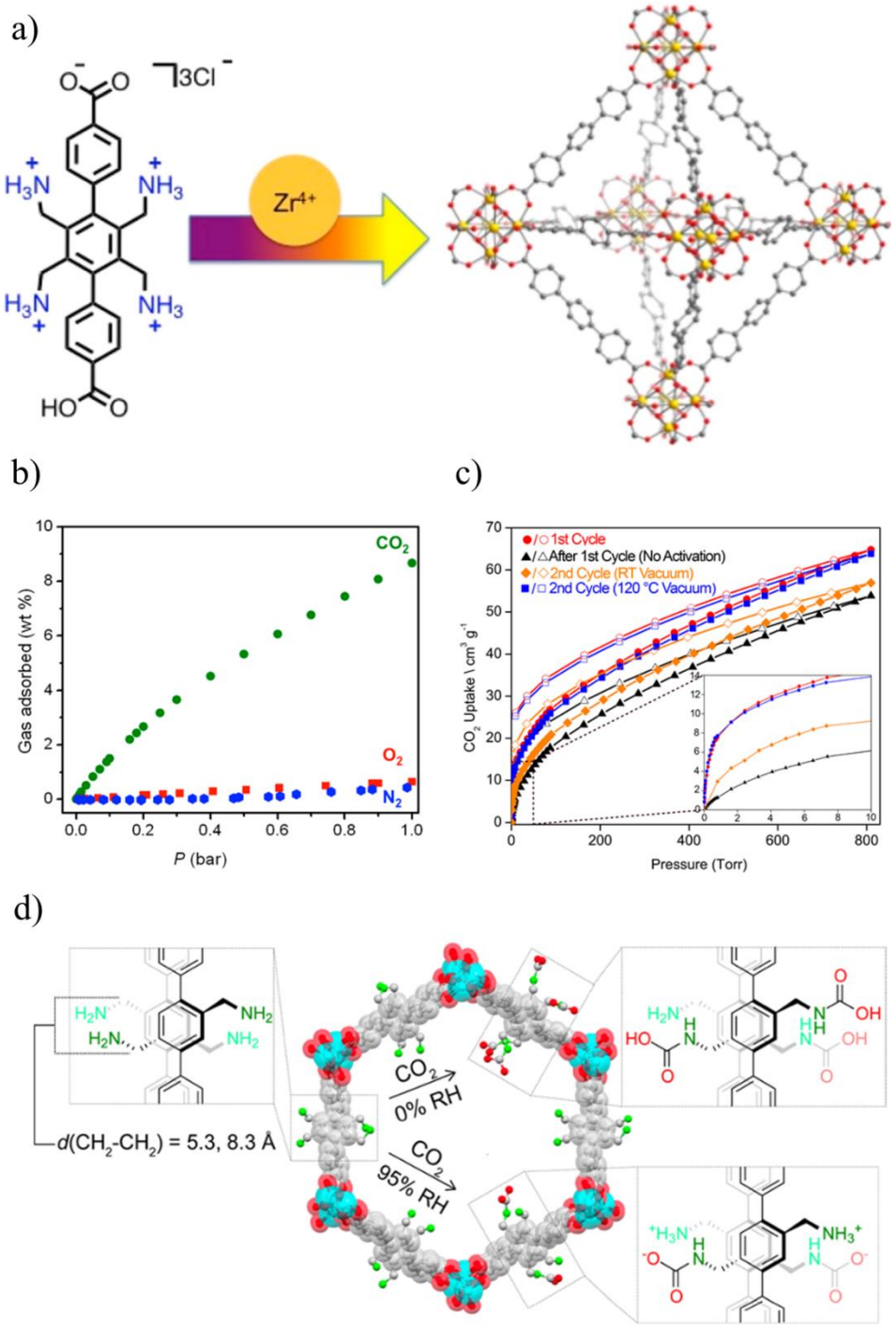

Figure 1.25: The MOF $Zr_6O_4(OH)_{2.1}F_{1.9}$(tpdc-4CH_2NH_2·3HCl)$_6$ with its four amino groups on the linker. The MOF is highly selective towards the adsorption of CO_2, as seen in the adsorption isotherm as shown in b). c) The CO_2 isotherm for IRMOF-74-III-(CH_2NH_2)$_2$ with various ways of activating the MOF. d) A modelled structure of IRMOF-74-III-(CH_2NH_2)$_2$ depicting the three possible pore environments before and after exposure to CO_2 under 95% relative humidity (bottom right pore wall) and dry (upper right pore wall) conditions. Adapted from references 176 and 177.

Another strategy for implementing amine groups into the framework of the MOF is to utilise linkers that contain basic N-donor groups. These N-donor groups come in the form of N-heterocyclic

groups,[178,179] aromatic amines[180,181] or alkyl amines(**Figure 1.25**) [176,182,177]. The N-donor groups follow this order in being the most effective in bonding with CO_2 due to their increased nucleophilic character of the amino group. The presence of the primary amino groups is found to increase the absorption of CO_2 for the MOFs in humid atmospheres.[183,184,185] Many MOFs have a high affinity for the adsorption of H_2O, which reduces their capacity for CO_2 adsorption. In the atmosphere, the concentration of H_2O is many orders of magnitude higher than CO_2 concentrations. H_2O, with its smaller kinetic diameter in comparison to CO_2 (2.65 Å vs 3.3 Å), has a strong tendency to rapidly adsorb into the MOF, where they bond strongly with the charged or polarisable structure of the MOF. Amine functionalised MOFs, which contain large pores, are capable of reducing this effect. Some MOFs have even been designed to utilise the H_2O molecules to aid in the capture of CO_2. The H_2O molecules assist in the formation of carbamates in the structure (**Figure 1.25 c) and d)**).[176,186]

1.4.2 Catalysis

One of the most widely studied areas in MOF chemistry is their use in catalysis. While there have been reports in the literature of using MOPs for catalysis, the dominant area of research is focused on the use of MOFs. Catalysts can be divided into two overarching categories: homogenous and heterogeneous catalysts. Homogeneous catalysts are usually small molecules containing metal ion coordinated complexes with either open metal sites or weakly bound solvent molecules. For the catalyst to be active in the reaction, it is dissolved in the reaction solution. This allows the catalyst to interact with the reagents and alter the reaction rate. In contrast, heterogeneous catalysts are either solid metals or metal oxides that do not dissolve in the solution or remain as a suspension.

Each type of catalysis has its advantages and disadvantages. Homogenous catalysts can be highly active for a range of reactions. Through the addition of auxiliary ligands to the reaction, the selectivity and yields for the reaction can be further improved. It is also possible to drastically alter the conditions in which the reaction is carried out. However, the catalysts tend to be unstable with limited turnover numbers and are difficult to recycle for further reactions. Heterogenous catalysts, however, are stable at elevated temperatures for extended periods of time. They are usually easy to separate from the reaction mixture and are highly recyclable. Due to the active sites for the catalyst being limited to the surface of the solid, they have reduced overall activity.

The interest in utilising MOFs as catalysts stems from their ability to combine the favourable properties of both types of catalysts. They combine the high surface area and selectivity of homogenous catalysts while also having the stability and recyclability of heterogeneous catalysts. Nearly all aspects of MOF design has been used to catalyse reactions. MOFs have been shown to catalyse reactions by keeping reactants close to each other within the MOFs pores[187,188] or by directly catalysing reactions using open metal sites contained within the MOFs.[189,190] The open metal sites can be located either on the inorganic SBUs or post synthetically functionalised organic linkers.[190]

MOFs and also MOPs have been used to catalyse a wide range or reactions, including multi-component coupling reactions,[191] Aldol-Tishchenko reactions,[192] amidation reactions,[193] bromination reactions,[194] allylic oxidations,[195] Diels-Alder cyclisations,[195] cyclopropanations reactions,[196] oxidation of alkanes and alkenes,[197,198] oxidative dehydrogenation,[199,200] oxidative coupling reactions,[201] acetylenic acid cyclisations,[41] as well as many other types of catalysis.

1.4.2.1 Water splitting

One area in catalysis that MOFs have been studied in recent years is in the electrochemical splitting of water into oxygen and hydrogen. The main targeted product for the reaction is hydrogen. As mentioned in previous sections, hydrogen is seen as an alternative energy storage material for both vehicle and grid energy storage applications. By coupling the electrochemical production of hydrogen from water with electricity from renewable sources, which are often intermittent, it offers the potential to store clean energy for later use. Hydrogen is also a commonly used chemical feedstock, with one of its main uses being the production of ammonia. Unfortunately, the current primary commercial method of producing hydrogen is through the steam reforming of natural gas.[202] Hydrogen from the electrolysis of water accounts for only 3-4% of total hydrogen produced globally.

The overall water-splitting reaction requires that electron transfer events are coupled to catalytic units. At the anode, the catalytic units are able to mediate the four-electron, four proton-coupled splitting of H_2O (oxidation) and that at the cathode, the catalysts mediate the rebonding of protons and electrons forming H_2 (reduction) (**Figure 1.26**). The water oxidation reaction is particularly challenging due to its high energy demand (ΔG = 4.92 eV) and is widely accepted as the bottleneck in water electrolysis.[203,204,205] Binding sites on both the water oxidation catalysts (WOC) and proton reduction catalysts (HRC) are essential to the catalyst design as they allow for the interaction between the catalyst and the substrates of the solution. The sites on the catalyst may contain weakly bound solvent molecules or sites in which labile organic ligands are attached, which get displaced during the initiation of the reaction. Precious metal-based catalysts, such as Pt-based catalysts, are still considered the best water oxidation and hydrogen reduction catalysts; however, their widespread use is hampered by their high cost and low abundance.[206,207] Research currently focuses on developing low-cost, earth abundant alternatives to these materials.

$$4H^+ + 4e^- \longrightarrow 2H_2 \qquad E^0 = 0.00\ eV$$

$$2H_2O \longrightarrow O_2 + 4H^+ + 4e^- \qquad E^0 = -1.23\ eV$$

Figure 1.26: Reduction and oxidation half-equations for the electrolysis of water at pH 0.

MOFs have been demonstrated as efficient catalysts, both half-reactions for water splitting. Generally, for the hydrogen evolution reaction, the experiments are carried out in acidic media to lower the energy requirements and improve the catalytic performance of the MOF.

Two examples of HER active MOFs are the two cobalt-based MOFs, MOS 1 and MOS 2. The MOFs are constructed from conjugated benzenehexathiol and triphenylene-2,3,6,7,10,11-hexathiolate organic linkers. Both MOFs were shown to have significant HER catalytic activity under a wide range of different pH conditions. MOS 1, the more active the two MOFs, has an onset potential of 280 mV vs. SHE and a Tafel slope of 149 mV/dec at pH 1.3.[208] This high catalytic activity is attributed to the high conductivity of the MOF, something that is often lacking in other MOFs. A more recent example is a 2D cobalt(II)-based MOF containing a pentanuclear {Co_5} SBU was shown to be catalytically active.[209] A composite were prepared using graphene and the cobalt MOF. Of the various composites examined, the best gave rise to an onset overpotential of 125 mV and a Tafel slope of 91 mV/dec in 0.5 M H_2SO_4. Remarkably, after 1000 catalytic CV cycles, the catalytic activity was unchanged.[209]

For oxygen evolution reaction (OER) many WOCs containing earth-abundant transition metals such as cobalt, iron, copper, and manganese have been reported in the literature. One of the earliest reports for using MOFs as WOCs was published in 2011 by Lin et al. They synthesised an iridium functionalised derivative of UiO-67.[210,211,212] They performed this functionalisation through incorporating an organic linker that contained an iridium WOC into the synthesis of the MOF. The resulting MOF showed catalytic activity with a turnover frequency of 4.8 h^{-1} vs. 37 h^{-1} for the free molecular catalyst as pH 1. The lower turnover frequency is due to the lower diffusion of reagnets through the MOF when compared to the free floating reagents found in the homogenous solution.

Since then, several improved MOF-based catalysts have been reported. In 2016, a Co(II)-based azolate framework, MAF-X27-OH was prepared from a precursor derivative MAF-X27-Cl via post-synthetic ion exchange. After the ion exchange, the electrochemical water oxidation activity of the new material drastically increased. MAF-X27-Cl reached an overpotential of 387 mV at 10 mA/cm2 at pH 14. The potential decreased to 292 mV at 10 mA/cm2 for MAF-X27-OH under the same conditions.301 It was proposed that the ion exchange alters the reaction mechanism to proceed intramolecularly via an intraframework coupling pathway, as shown in **Figure 1.27**.

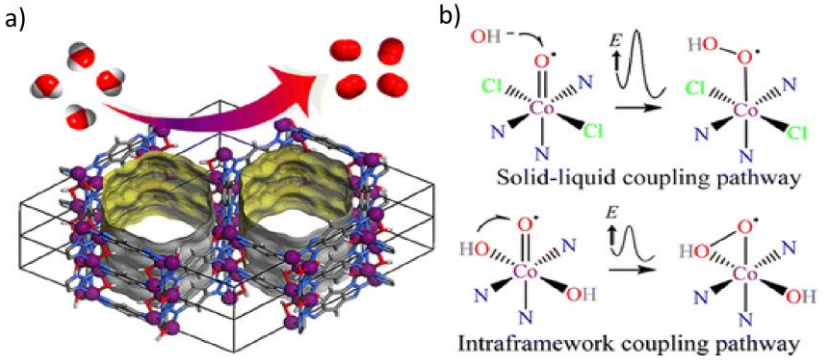

Figure 1.27: a) Three-dimensional coordination network and pore surface structures of MAF-X27-OH. b) Solid-liquid coupling pathway for MAF-X27-Cl and the intraframework coupling pathway for MAF-X27-OH. Reproduced from reference 213.

1.5 Aims and objectives

The objective of the work described in this thesis has been to synthesise and characterise novel metal-organic frameworks and metal-organic polyhedra in order to analyse the effects of linker flexibility and symmetry reduction on their structure and topologies. The term flexibility is used to describe the conformational freedom in the organic linkers used, and the term reduced symmetry derives from the symmetry of the organic linkers in this work being lower than the more commonly reported benzene-1,3,5triethynyl-benzoate (BTEB) based linkers.[39,214,71] Particular emphasis is given to the topological and supramolecular impact of these two factors on the crystal structures of the resultant coordination polymers.

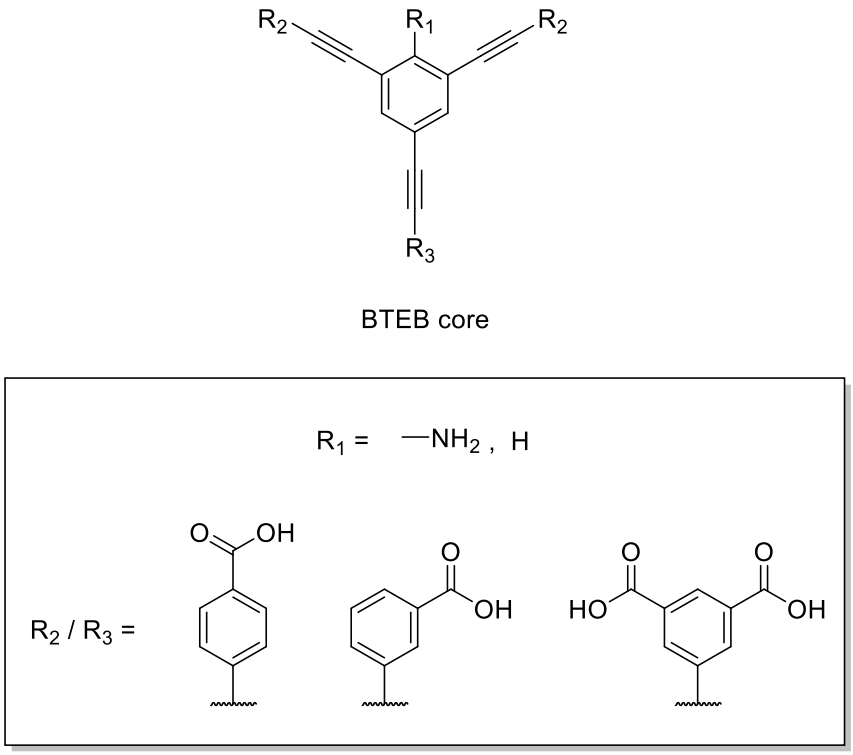

Figure 1.28: The core of the BTEB based linkers with the various methods of modification. R_1 allows for the addition of functionalisation of the linker without disruption to frameworks, while R_2 and R_3 allow for various combinations of moieties to be attached to the central core generating a large family of linkers with reduced symmetry.

BTEB based linkers have a number of structural aspects that make them an ideal ligand to study these aspects, as seen in **Figure 1.28**. The acetylene space units that connect the central phenyl ring to the moieties allow for the various conformations of the linker with its near-zero energy barrier for rotation around the axis of the triple bond. The spaces also allow a separation of the central phenyl from the influence of the moieties and *vice versa*. This allows for the functionalisation of the central phenyl without disruption to the framework formation in MOFs or MOPs. In this body of work, we chose the amino group to functionalize the linker as it was found to increase the tri-*meta*-benzoate-based BTEB linkers solubility in DMF. The increased solubility of the linker permits its use in

reactions at lower temperatures than would be typically possible with the non-functionalised linker. The lower temperatures may result in products that could not have been achievable at elevated temperatures. Using the new synthetic procedure discussed in **Chapter 3**, the linker's moieties can now be various combinations of different benzoates and isophthalate. The multitude of linkers that arise from these combinations can be viewed as variations of the BTEB linker but with reduced symmetry.

In **Chapter 2** we focus on developing an amino-functionalised organic linker to synthesise MOPs and their use as structural units in MOF design. MOPs containing the new linker are first synthesised, and their structures are studied. The variation in the structure of the two MOPs were found to arise from the various conformations of the organic linker. These new MOPs were then utilised in the synthesis of MOFs using a technique known as pillaring. With the addition of bipyridyl linkers, the MOP units were connected into a new framework. The first MOP synthesised, **1**, was connected into a one-dimensional polymer, **3**, and a three-dimensional framework, **4**. A new and dramatically different structure was formed while attempting to apply the same technique to the second MOP to be synthesised. The MOP unit was found to disassemble in solution and then reassemble into the commonly reported unit of a super paddlewheel. These units were then connected into two-dimensional sheets, which were then further pillared into the three-dimensional framework.

In **Chapter 3** we study the influence of BTEB linkers reduced symmetry on the structure of MOFs. A family of new linkers were first synthesised based upon the BTEB link core. Through a new synthetic procedure, the new linkers contained various combinations of *meta*-benzoate, *para*-benzoate and isophthalate moieties. Using these new linkers in combination with $\{Cu_2\}$ paddlewheel SBUs a series of MOFs were synthesised. Through maintaining the $\{Cu_2\}$ SBU as a common building unit in the MOFs design, the influence and effects of the linkers reduced symmetry on the MOF structure is isolated.

In **Chapter 4** we examine the effects of the organic linkers symmetry on the structure of the inorganic SBUs. By using ions that can form a more comprehensive range of SBUs, in this case, Zn^{2+} and Co^{2+} ions, the influence of the symmetry of the ligand on the SBUs is studied. The properties of the newly synthesised MOFs have then been examined, particularly the catalytic properties of the Co^{2+} based MOFs for the water oxidation reaction.

These experiments aim to offer an insight into the impact of the linkers flexibility and reduced symmetry on the design of MOFs and MOPs. These two effects are comparatively understudied in the literature compared to other aspects of linker design. This body of text aims to expand upon these two aspects, which represent an important development within the field. Understanding these factors will help build a more comprehensive theory of synthetic MOF chemistry and adds nuance to impart discussions pertaining to design and applications.

Chapter 2

Functionalised metal-organic polyhedra and their implementation into pillared frameworks

2 Functionalised metal-organic polyhedra and their implementation into pillared frameworks

2.1 Introduction

In this chapter we describe the successful synthesis of an amino-functionalised derivative of a BTEB based linker, 3,3',3''-((2-aminobenzene-1,3,5-triyl)tris(ethyne-2,1-diyl))tribenzoic acid ($H_3BTEB_{mmm}NH_2$). This new linker was then used to synthesise two {Cu_2} paddlewheel SBU based MOPs (**Figure 2.1**). The two MOPs were found to have vastly different structures attributed to the rotational flexibility of the extended, tri-functional $H_3BTEB_{mmm}NH_2$ linker. The first MOP synthesised using the new linker, $[Cu_{36}(BTEB_{mmm}NH_2)_{24}(H_2O)_{28}(DMF)_8]$ (**1**), has the structure of an inner octahedron that is surrounded by an outer cuboctahedral framework. The structure represents a highly augmented MOP whose complexity and topological characteristics compare to key structural attributes of MOFs. While the *anti*,*anti*-arrangement of two *meta*-benzoate moieties of the linker produces the 120º binding geometry that forms the outer cuboctahedral framework, the rotational flexibility of the remaining *meta*-benzoate moieties allows for the formation of the inner octahedron. This remaining moiety adopts two orientations in the structure. One is co-planar with one of the outer moieties in a *syn*,*syn*-arrangement while in the other, the moiety is perpendicular with respect to the rest of the linker.

The second MOP that was synthesised using the new linker, $[Cu_{12}(BTEB_{mmm}NH_2)_8(H_2O)_{12}]$ (**2**), has the topologically and structurally simpler construction of an octahedron. The MOP contains six {Cu_2} SBUs, located at the vertices of the octahedron, linked by eight $H_3BTEB_{mmm}NH_2$ linkers. The three *meta*-benzoate moieties of the linker adopt a perpendicular dihedral angle with the central phenyl ring. This allows the linker to occupy the eight triangular faces of the octahedron.

These new MOPs were then implemented in the construction of higher-dimensional MOFs. This method of connecting lower-dimensional materials into higher-dimensional materials through the additions of bipyridyl ligands is known as pillaring.[215,216,217] The labile coordination sites of the {Cu_2} SBUs facilitate the interconnect of the MOPs into a new framework with the bipyridyl ligands that coordinate to the {Cu_2} SBUs. Through experimentation of various pillaring ligand lengths, the ligand 1,2-di(pyridin-4-yl)diazene (Azpy) was the most successful in pillaring the MOPs. The degree of pillaring was controlled by carefully selecting the ratio between the bipyridyl ligand Azpy and the $H_3BTEB_{mmm}NH_2$ linker.

With a small ratio of the two ligands, **1** was successfully pillared into the one-dimensional coordination polymer $[Cu_{36}(BTEB_{mmm}NH_2)_{24}(Azpy)(DMF)_{34}]$ (**3**). In the structure, the Azpy ligands coordinate to two {Cu_2} SBUs located transversely on the outer cuboctahedral framework. By simply increasing the ratio of Azpy to $H_3BTEB_{mmm}NH_2$, the degree of pillaring was increased, leading to the

new MOF $[Cu_{36}(BTEB_{mmm}NH_2)_{24}(Azpy)_6(DMF)_{30}]$ (**4**). With the additional pillaring ligand, all of the external $\{Cu_2\}$ SBUs on the MOP was now coordinated by the Azpy ligand. This further degree of connectivity incorporates the MOPs into a dual interpenetrated framework, with each framework having the **fcu** topology.

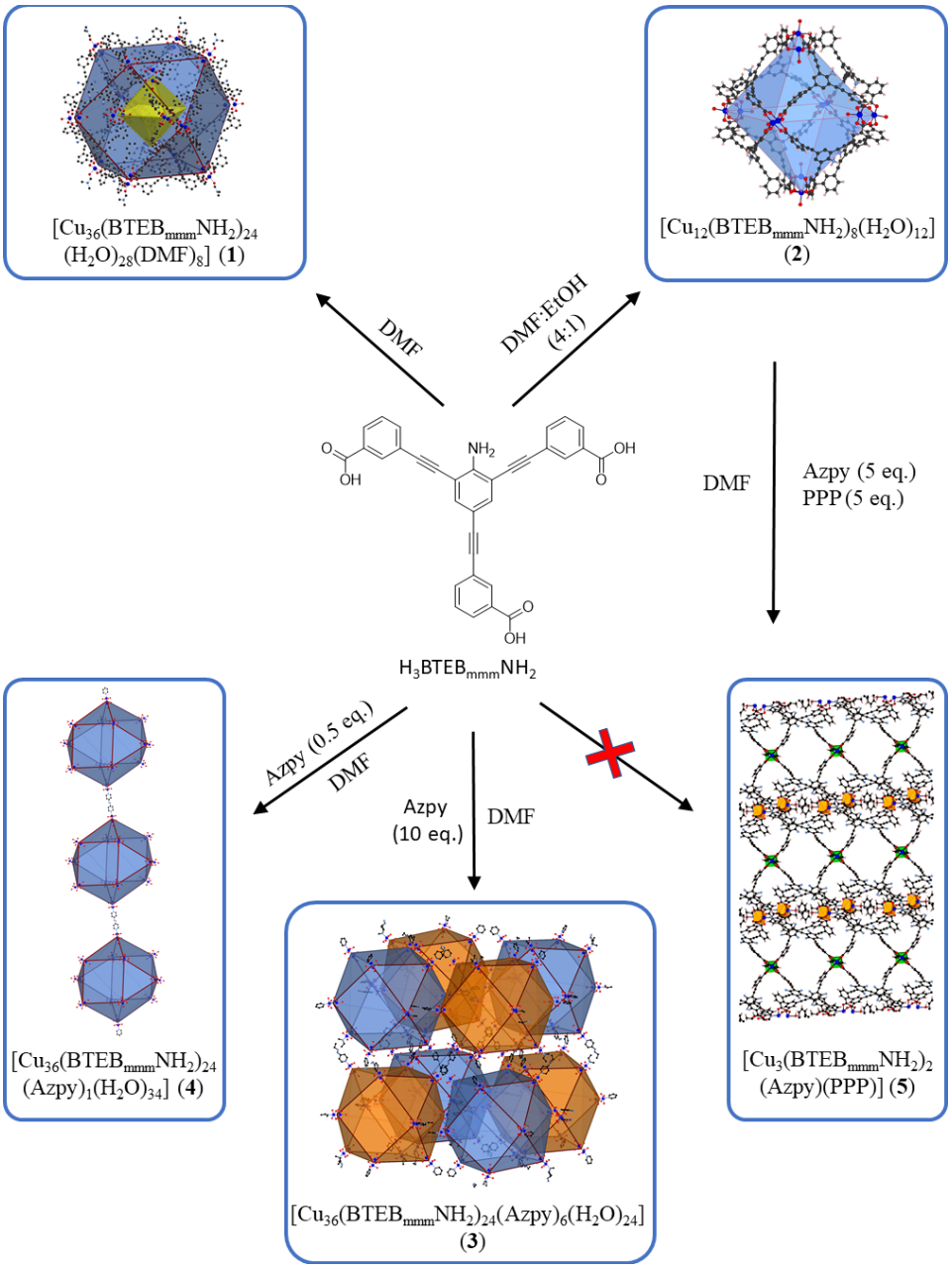

Figure 2.1: A graphical summary of the structures discussed in the chapter and their relation to each other. The two MOPs 1 and 2 were synthesised by reacting the linker $H_3BTEB_{mm}NH_2$ with $Cu(NO_3)_2{\cdot}3H_2O$ in various solvents. The pillaring of 1 is possible through the simple addition of the Azpy ligand to the reaction. The ratio of the Azpy to $H_3BTEB_{mm}NH_2$ controls the extent of the pillaring. A low ratio of the two ligands leads to the one-dimensional MOF 3, and a higher ratio leads to the three dimensional MOF 4. For the pillaring of 2 the MOP was first synthesised prior to the pillaring reaction. The resulting structure was a MOF comprised of two-dimensional sheets pillared rather than the expected pillaring of the 2.

When the same pillaring procedure was applied to the pillaring of **2** the synthesise was found to be incompatible with the synthesis of the MOP. To implement **2** into a pillared framework, a new approach was required. Due to EtOH, which is required to synthesise **2**, negatively affecting the pillaring reaction, a post-synthetic pillaring of the MOP was required. To increase the solubility of the MOP in the solution, a secondary pyridyl ligand with an aliphatic chain, 4-(3-phenylpropyl)pyridine (PPP), was added to the solution. The new MOF MOF, $[Cu_6(BTEB_{mmm}NH_2)_4(PPP)_2(Azpy)(H_2O)_2]$ (**5**), was synthesised. Rather than the expected pillaring of the MOP, the MOF comprises two-dimensional sheets that are pillared using the Azpy ligand offering a potential new way of synthesising MOFs.

2.2 Synthesis of $H_3BTEB_{mmm}NH_2$

The synthetic procedure for the amino-functionalised linker was initially based on similar BTEB based linkers that have previously been reported in the literature. [71,218, 219.] However, it was quickly discovered that several complications occurred when this procedure was applied to synthesise the $H_3BTEB_{mmm}NH_2$ linker. Apply to the literature reported procedure for the synthesis of BTEB to the amino functionalised ligand resulted in yields, approximately 20 mole%.[220] Much lower than that of the non-functionalised linker. A secondary negative effect was the formation of several side products leading to great difficulty in the purification of the ligand. The lower than expected yield of the Sonogashira coupling reactions are attributed to the amino functional group on the linker. The amino group is reported to alter both the steric and electronic interactions of the phenyl ring during the synthesis.[221,222]. A modified procedure was then developed to minimise the complications of the original synthesis and to improve yields. This new synthetic procedure is outlined in **Scheme 2** below.

The first step in the procedure was the Sonogashira coupling between trimethylsilylacetylene (TMSA) and 2,4,6-tribromo-aniline (TBA) (**Scheme 2 (i)**). TBA was first dissolved in a solution of triethylamine (TEA) and tetrahydrofuran (THF) in a 1:1 ratio by volume alongside 5% mole equivalents of $[PdCl_2(PPh_3)_2]$ and CuI. Where this synthesis diverges from the literature procedures, is in the rate of addition of TMSA and the length of time the reaction takes place. An initial quantity of 1.5-mole equivalents of TMSA was added to the solution, which was then heated under a nitrogen atmosphere for 72 h. An additional 1.5 equivalents of TMSA was added to the reaction mixture at 18 h and 36 h marks. It was found that this staggering of additions of TMSA significantly improved the yield of the reaction. It is believed that this is due to the gradual loss of TMSA during the extended reaction time. By spreading the addition of the TMSA over more extended periods of time, the loss of unreacted starting material minimised.

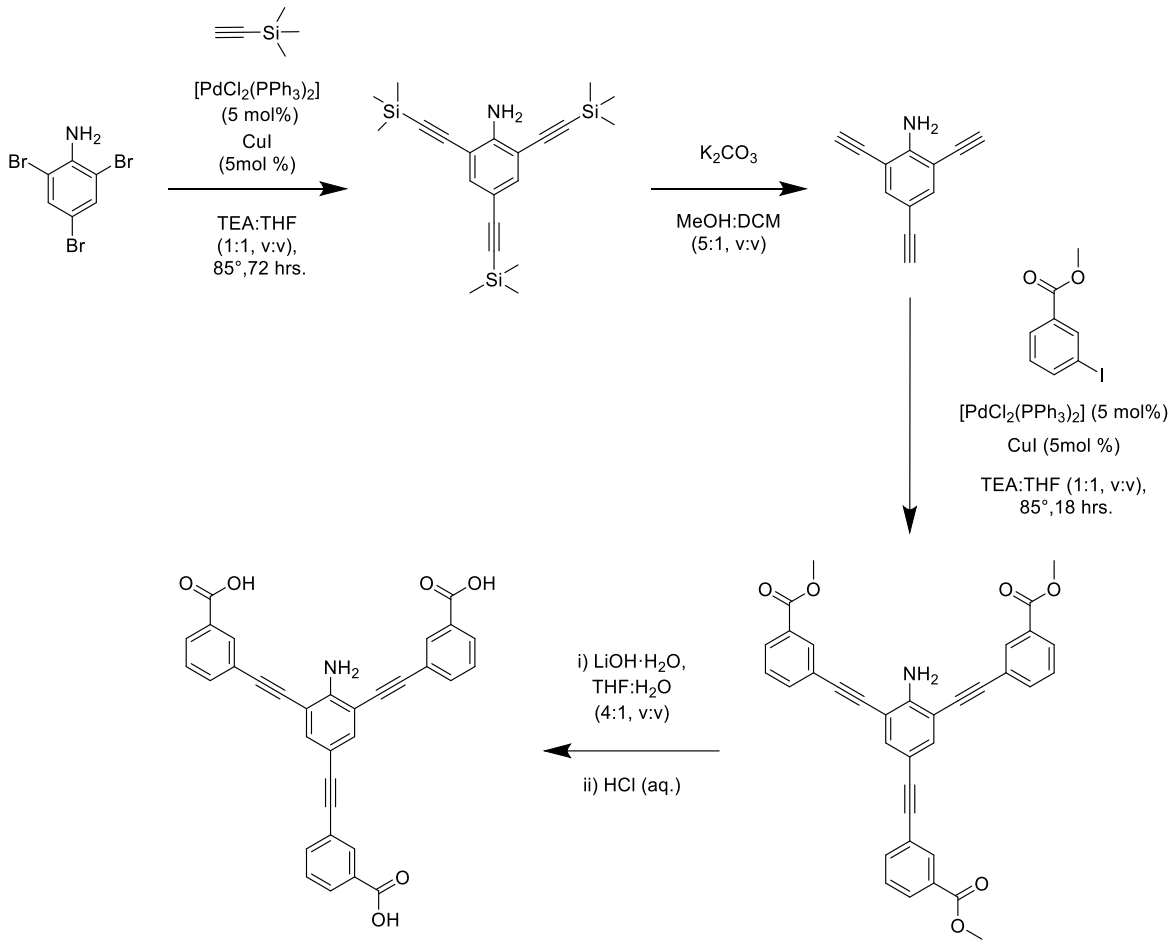

Scheme 2: Synthetic procedure for the synthesis of $H_3BTEB_{mmm}NH_2$

After the reaction had completed, the solvent was removed under reduced pressure to yield a crude black oily product. The crude product was then dissolved in CH_2Cl_2 and washed three times with a saturated aqueous solution of NH_4Cl, followed by a brine solution. This washing aids the extraction of metal ions from the organic layer. The organic layer was separated and dried using $MgSO_4$. Removal of the dried solvent under reduced pressure yielded a dark, yellow viscous liquid. The crude product was then purified using flash column chromatography, eluted with hexane to yield a viscous yellow oil with a yield of 93%.

The second step was the deprotection of the silyl protecting group (**Scheme 2 (ii)**). Firstly the protected compound was dissolved in a CH_2Cl_2 : MeOH (1:1, v/v) solvent mixture with an excess of K_2CO_3. The reaction mixture was then stirred at room temperature for 6 h. Progress of the reaction was monitored by thin-layer chromatography (TLC), eluting with CH_2Cl_2:Hexane (1:18). When the reaction had completed, deionised water was added to the reaction mixture. After separating the organic and aqueous phases, the organic layer was isolated and washed three times with a brine solution. The organic layer was then isolated, dried with $MgSO_4$. After the $MgSO_4$ had been filtered off using gravity filtration, the solvent was removed under reduced pressure to yield a lime green product with a yield of 78%.

A Sonogashira coupling reaction was then performed between the 2,4,6-triethynylaniline product from the previous step and methyl 3-iodobenzoate. This procedure follows a similar procedure to the previous coupling reaction between TMSA and TBA (**Scheme 2 (iii)**). The two reagents, 5% mole equivalents of $[PdCl_2(PPh_3)_2]$ and CuI, were first dissolved in a THF : TEA (1:1, v/v) solution. The solution was then heated to 85°C for 24 h. Upon completion of the reaction, the solvent was removed under a reduced pressure to leave behind a crude solid. The solid was dissolved in DCM and washed with a saturated aqueous solution of NH_4Cl, followed by a brine solution. The organic layer was separated and dried using $MgSO_4$. The solid was filtered off, and the solvent was removed under a reduced atmosphere to leave behind the crude product. The crude product was then purified by flash column chromatography eluting with CH_2Cl_2 to yield a bright yellow powder with a yield of 81%. This gives a total percentage yeild for the synthesis of the ligand at 47%.

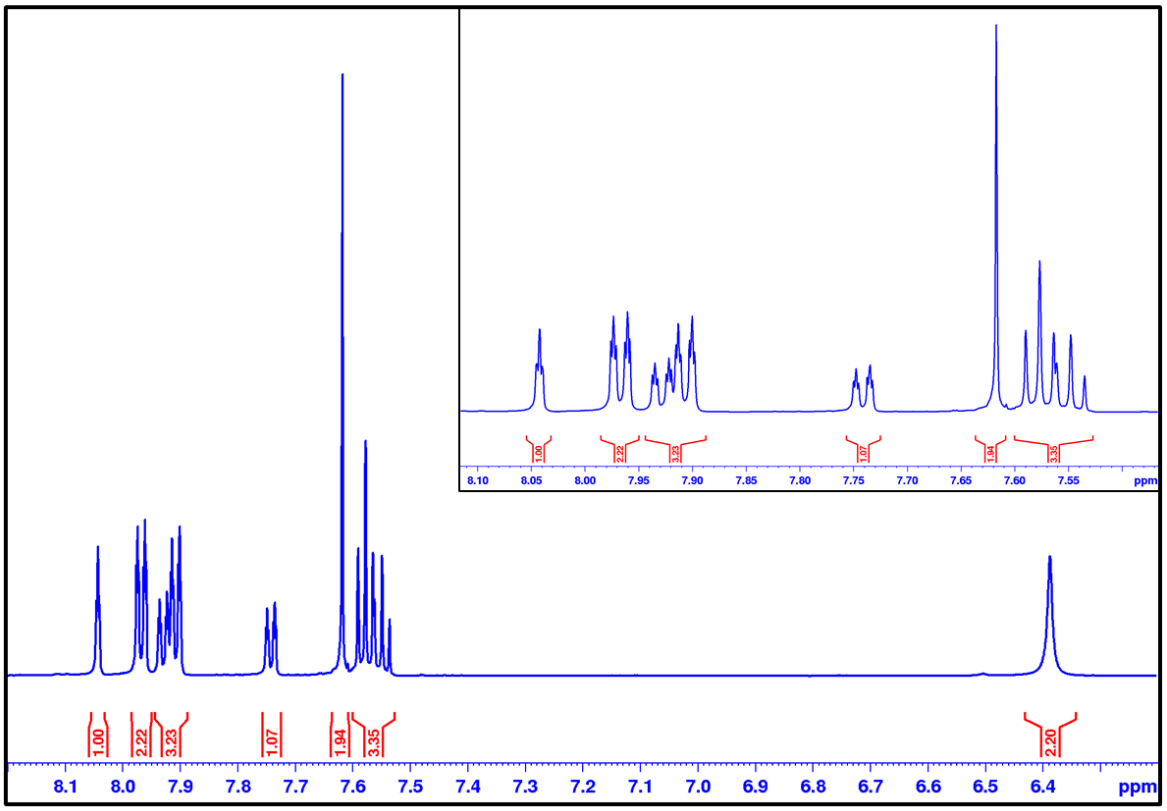

Figure 2.2: ^{1}H - NMR of $H_3BTEB_{mmm}NH_2$ linker

2.3 Metal-organic polyhedra

2.3.1 $[Cu_{36}(BTEB_{mmm}NH_2)_{24}(H_2O)_{28}(DMF)_8]$ (**1**)

1 was synthesised through heating a DMF solution of $H_3BTEB_{mmm}NH_2$ and $Cu(NO_3)_2 \cdot 3H_2O$, in a 1.5:1 mole ratio at 85 °C for 72 h. During the initial stages of the reaction, a large amount of yellow-brown amorphous material precipitated from the green solution. As the reaction progressed, green rhombohedral crystals grew on the walls of the reaction vial. The crystals were separated from the

insoluble precipitate and washed with a fresh DMF solution. The product was isolated as high-quality single crystals suitable for analysis by single-crystal X-ray diffraction. The crystals were measured, and the structure was solved in the monoclinic system with the space group *C2/m* with the unit cell parameters determined to be a = 54.9305(18) Å, b = 55.3715(18) Å, c = 44.3760(16) Å, $\alpha = 90^{o}$, β = 125.72(2)º, $\gamma = 90^{o}$.

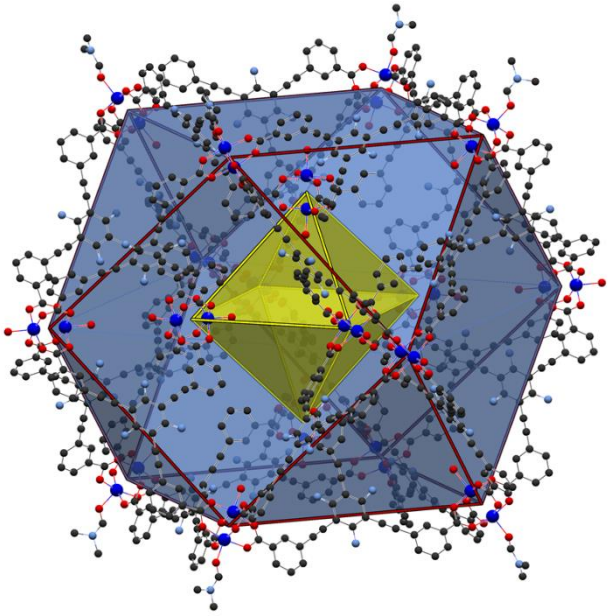

Figure 2.3: Structure of 1 with the outer cuboctahedron highlighted in blue and inner octahedron highlighted in yellow. (C-black, N-light blue spheres, O-red spheres, Cu-dark blue spheres)

The structure of **1** was determined to be a MOP with the chemical formula $[Cu_{36}(BTEB_{mmm}NH_2)_{24}(H_2O)_{28}(DMF)_8]$. The MOP is comprised of 24 $BTEB_{mmm}NH_2^{3-}$ linkers which coordinate to 36 Cu^{2+} ions. The MOP has the structure of an inner octahedron encircled by a cuboctahedral outer shell with an inner octahedron in an onion-type arrangement. The Cu^{2+} ions combine pairwise to generate $\{Cu_2\}$ paddlewheel SBUs. Twelve of theses $\{Cu_2\}$ SBUs are located at the vertices of the outer cuboctahedron, while the remaining six $\{Cu_2\}$ SBUs located at the vertices of the internal octahedron. The O-donor atoms on each deprotonated $BTEB_{mmm}NH_2^{3-}$ linker coordinate to the Cu^{2+} ions in a *syn,syn*-bidentate (μ_2-η^1:η^1) bridging mode. The O-donor atoms form the base of a square base pyramidal coordination environment around the central Cu^{2+} ion. The O-donor atoms from a H_2O or DMF solvent molecule coordinate to the apical position on each Cu^{2+} ion completing the square base pyramidal coordination environment The bond lengths and angles between the Cu^{2+} ion and the O-donor atoms are similar to those typically reported for $\{Cu_2\}$ SBUs.[223]

The $BTEB_{mmm}NH_2^{3-}$ linker has two conformations within the structure of **1**. In both conformations, the two outer *meta*-benzoates are in an *anti,anti*-alignment which generates the outer cuboctahedral framework of the MOP (**Figure 2.4 a)**). These two outer *meta*-benzoate moieties lie approximately

co-planar with respect to the central phenyl ring on the linker. The two conformations differ in the dihedral angle of the third, internal, *meta*-benzoate moiety (**Table 2.1**). In conformation **i,** the third *meta*-benzoate moiety adopts an approximately co-planar arrangement with respect to the central phenyl ring. This puts the internal moiety co-planar with one of the external *meta*-benzoate moieties, placing them in a *syn,syn*-arrangement. Four of the linkers in this conformation link two {Cu_2} SBUs generating a building unit known as a "super-paddlewheel" (**Figure 2.5 a)**).[196,224] The name of this building unit is derived from its structural similarity to the common {Cu_2} SBU. The two-building units contain the same degree of connectivity and symmetry. The difference between the units is the distance between the two external Cu^{2+} ions. The super-paddlewheel unit behaves like a {Cu_2} SBU that has been elongated along the Cu-Cu axis.

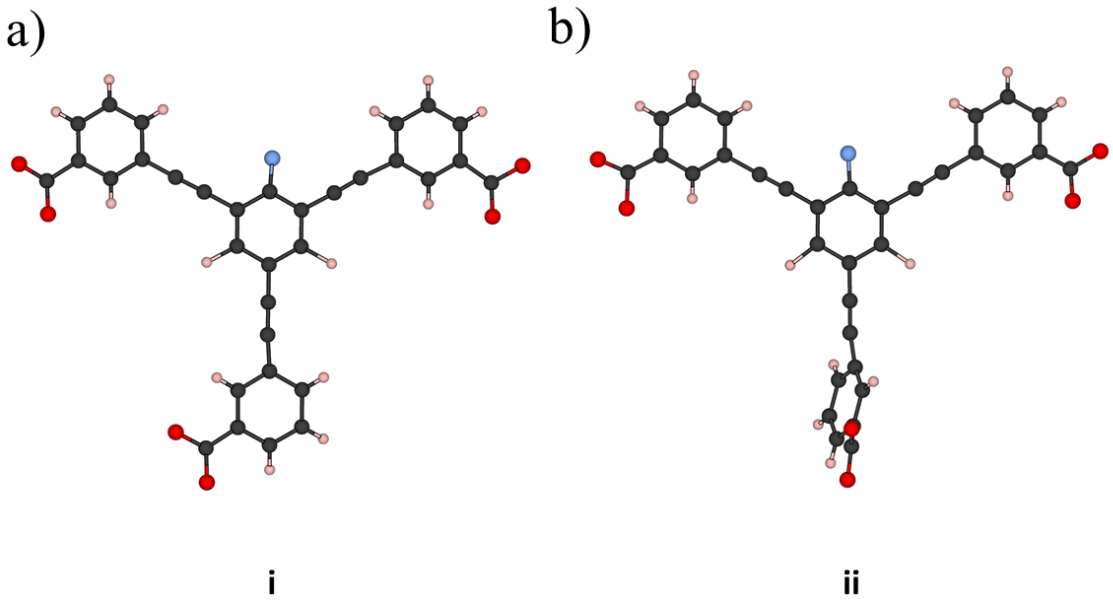

Figure 2.4: the conformations, i and ii, of the $BTEB_{mmm}NH_2^{3-}$ linker found in 1.

Table 2.1: Dihedral angle between the plane of the central phenyl ring and the plane of the benzoate moieties in the structure of 1.

Conformation	Dihedral angle between *meta*-benzoate (1) and the central phenyl ring	Dihedral angle between *meta*-benzoate (2) and the central phenyl ring	Dihedral angle between *meta*-benzoate (3) and the central phenyl ring
i	7.8707(10)º	8.5022(11)º	5.5652(10)º
ii	7.8707(10)º	8.5022(11)º	90.02(2)º

In the second conformation, the internal *meta*-benzoate moiety has a dihedral angle of 90º with respect to the central phenyl ring (**Figure 2.4 b)**). In this conformation, four linkers combine to create a square bowl-shaped unit. The four internal *meta*-benzoate moieties, which are perpendicular to the central phenyl ring, coordinate to a {Cu_2} SBU located on the internal structure of the MOP. This

central {Cu_2} SBU makes up part of the internal octahedral structure. The external *meta*-benzoate moieties coordinate to four external {Cu_2} SBUs forming the square face of the cuboctahedron (**Figure 2.5 b) & c)**).

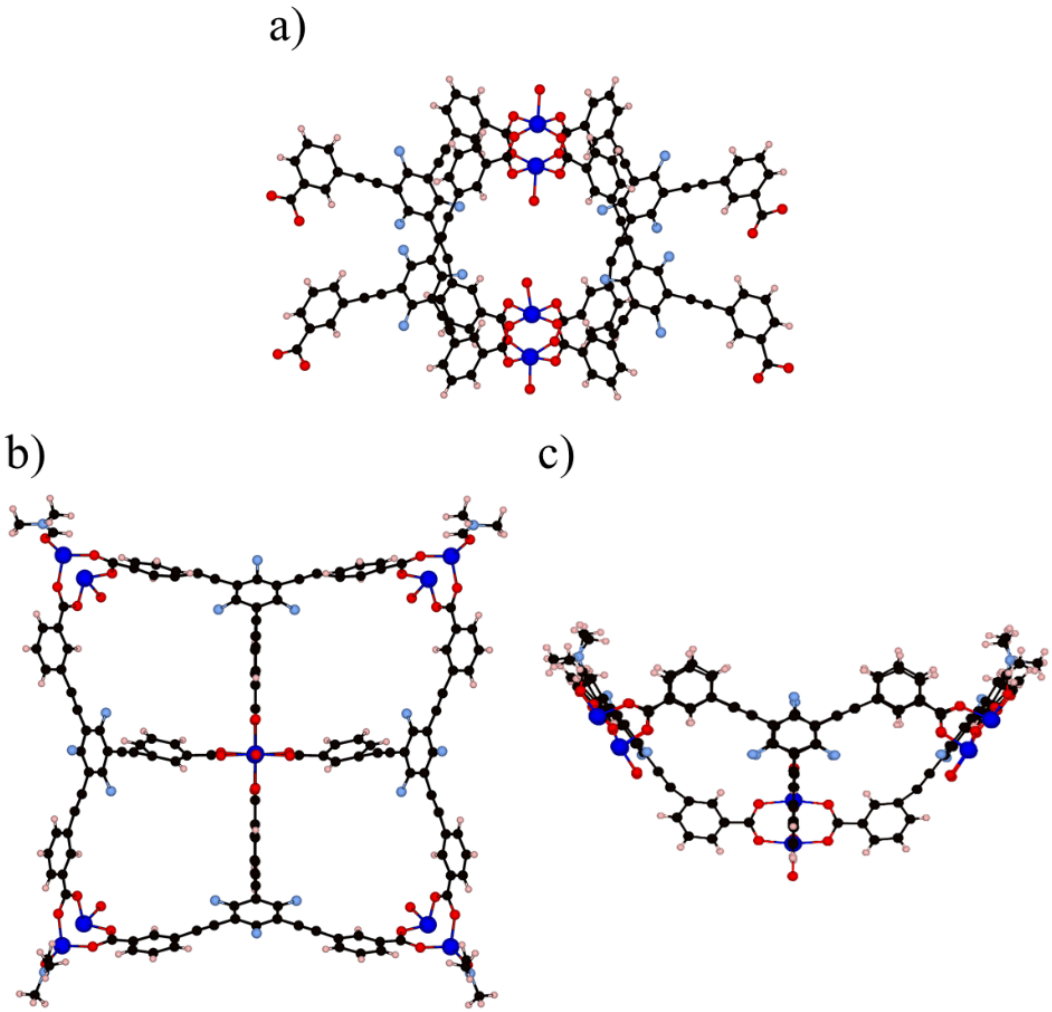

Figure 2.5: a) The super-paddlewheel unit is comprised of four $BTEB_{mmm}NH_2^{3-}$ linkers coordinating in a *syn, syn* arrangement to two {Cu_2} SBUs. b) The 'bowl shaped' unit viewed along the square face of the cuboctahedron and c) the 'bowl' like united viewed from the side. The unit contains one of the internal {Cu_2} SBUs connected to four of external {Cu_2} SBUs via four $BTEB_{mmm}NH_2^{3-}$. (C – black, O – red, H – pink, N -light blue, Cu – dark blue)

The overall structure of **1** contains four super-paddlewheel units and two bowl-shaped units connecting to create the MOP. The units are arranged such that the bowl-type building units occupy two opposite square faces of the resulting cuboctahedron. These occupied square faces block access to the pore located within the central octahedron (**Figure 2.6 a)**). The four remaining square faces of the cuboctahedron are open and allow access to the central octahedron (**Figure 2.6 b)**). Due to the symmetry of the outer cuboctahedron, the occupancy of the square faces is disordered across the three C_4 axes of the cuboctahedron in the crystal structure. This leads to the internal octahedron being disordered within the structure across the three C_4 axes of the cuboctahedron.

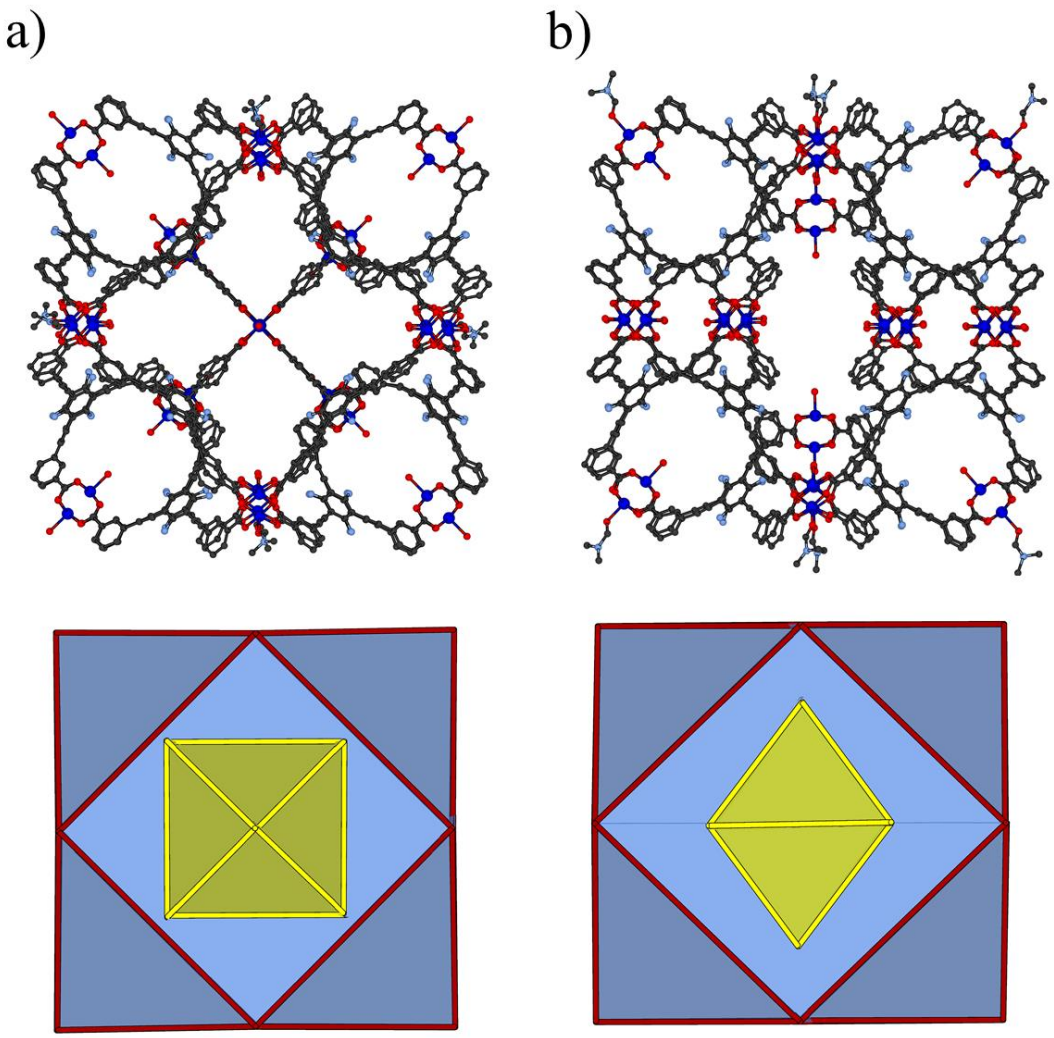

Figure 2.6: The a) closed and b) open square faces of 1 with graphical representations to highlight the structure. (C-black, N-light blue spheres, O-red spheres, Cu-dark blue spheres, outer cuboctahedral framework – blue cuboctahedron, inner octahedron – yellow octahedron)

The largest cross-sectional diameter of the MOP is the distance between the two exterior Cu^{2+} ions on opposite $\{Cu_2\}$ SBUs. This distance varies across the different pairs of external Cu^{2+} ions, ranging between 44.2 Å to 45.3Å. In the crystal structure of **1**, the coordination cages pack in a distorted hexagonal arrangement in the *ab*-plane. The hexagonal MOP arrangements stack parallel to the crystallographic *c*- axis (**Figure 2.7 a) & c)**). The MOPs are packed densely with a minimal void volume between the cages. Due to this, the sizeable accessible void volume is mainly attributed to the inner voids of the MOPs. This large void volume accounts for more than 73.3% of the unit cell volume.

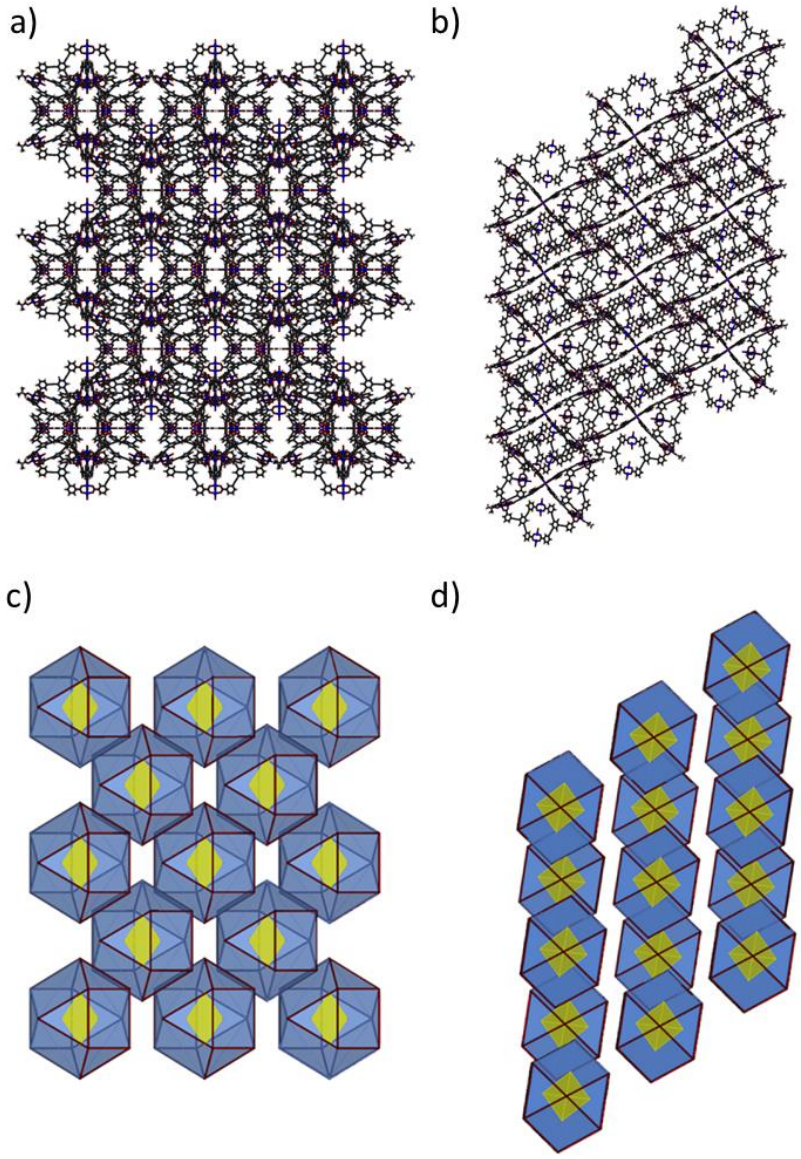

Figure 2.7: Packing diagrams and graphical representation for 1. a)& c) viewed along the crystallographic *c*-axis and b) &d) viewed along the crystallographic *b*-axis.

In order to assess the porosity of the structure, computational methods were employed due to the inherent instability of the MOP upon desolvation. The Poreblazer computational package was used to perform simulations to determine the pore-size distribution (PSD) and accessible surface area.[225] The compound was determined to have a He pore volume of 1.548 cm^3/g and an accessible surface area of 3718 m^2/g. The PSD was calculated using the method developed by Gelb and Gubbins, where progressively larger spheres are inserted into the structure.[226] From the PSD, it was found that the limiting, smaller pore diameter of the structure is 6.8 Å, and a maximum pore diameter of 16.8 Å is observed (**Figure 2.8**). Two well-defined pores are observed at 11.6 Å and 13.3 Å. The maximum pore diameter corresponds to the pore generated between two square faces of adjacent MOPs within the packed structure. The pore with a diameter of 13.3 Å corresponds to the pore within the central octahedron of the MOP.

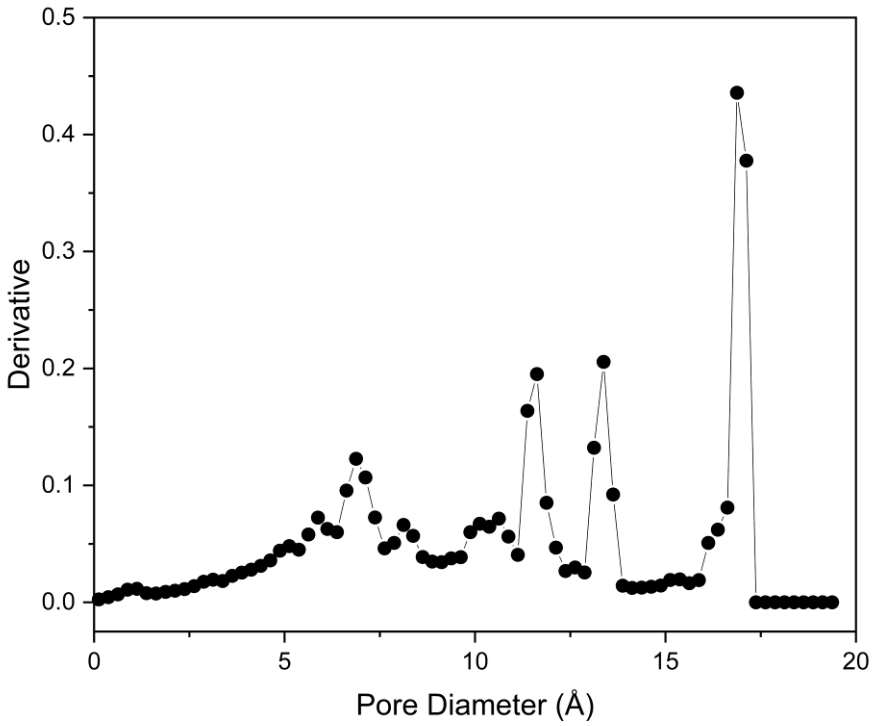

Figure 2.8: Simulated pore-size distribution of 1.

2.3.2 $[Cu_{12}(BTEB_{mmm}NH_2)_8(H_2O)_{12}]$ (**2**)

Through a simple modification to the synthesis of **1** a new secondary MOP, **2**, could be synthesised. The synthesis was similar to **1**, with the reaction between $Cu(NO_3)_2.6H_2O$ and $H_3BTEB_{mmm}NH_2$ carried out in the same 2:1 ratio as for **1**. However, the reaction was carried out in a solvent mixture of 20% EtOH and 80% DMF in this instance. After heating to 85 ºC for 48 h blue octahedral crystals were found to have grown on the glass surface of the reaction vial. The presence of the EtOH was found to be essential for the synthesis of **2**. Using these new reactions of increased metal to ligand ratio and shorter reaction time but with the absence of EtOH lead to formation of poor quality of crystals of **1** in low yields. With the use of EtOH in the synthesis the newly described crystals formed alongside an amorphous side product. Gentle agitation of the vial and decanting the reaction mixture facilitated the separation of the amorphous material. The crystals of **2** were isolated and found to be of sufficient quality for analysis by single-crystal X-ray diffraction. The crystal was measured, and the structure was solved in the tetragonal space group *I4/m* with the unit cell parameters a = 27.262(3) Å, b = 27.262(3) Å, c = 35.028(4) Å, α = 90º, β = 90º, γ = 90º.

The structure of **2** was discovered to be a MOP with the chemical formula $[Cu_{12}(BTEB_{mmm}NH_2)_8(H_2O)_{12}]$ (**Figure 2.9**). The twelve Cu^{2+} ions combine pairwise to generate six $\{Cu_2\}$ paddlewheel SBUs with each of the Cu^{2+} ions coordinated by four full deprotonated $BTEB_{mmm}NH_2^{3-}$ linkers. O-donor atoms of the carboxylate groups coordinate to the Cu^{2+} ions in a *syn,syn*-bidentate configuration and form the base of a square pyramidal coordination environment to the Cu^{2+} ion. An H_2O solvent molecule coordinates to each Cu^{2+} ion at the apical position. All

bond lengths and angles involving the Cu^{2+} ions are typical geometrical parameters for $\{Cu_2\}$ paddlewheel SBUs.[223]

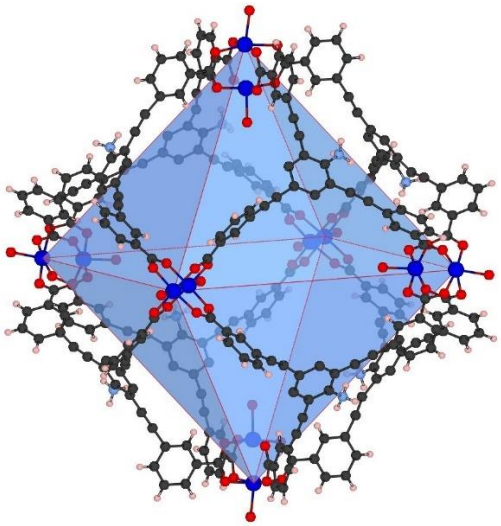

Figure 2.9: Crystal structure of 2 showing the six $\{Cu_2\}$ SBUs occupying the six vertices and the $BTEB_{mmm}NH_2^{3-}$ occupying the eight triangular faces of an octahedron. (Cu-deep blue, C-black, O-red, N-blue spheres, H-pink, representative octahedron-light blue octahedron.)

In **2**, the six $\{Cu_2\}$ SBUs occupy the six vertices of an octahedron while the $BTEB_{mmm}NH_2^{3-}$ linkers occupy the eight triangular faces. The dihedral angle between the three *meta*-benzoate moieties and the central phenyl ring range from *ca.* 81.4º to *ca.* 88.4º. The $BTEB_{mmm}NH_2^{3-}$ linkers are found in only one conformation within the structure of the MOP (**Figure 2.10**). The central phenyl ring is parallel with respect to the triangular faces of the octahedron (**Figure 2.9**).

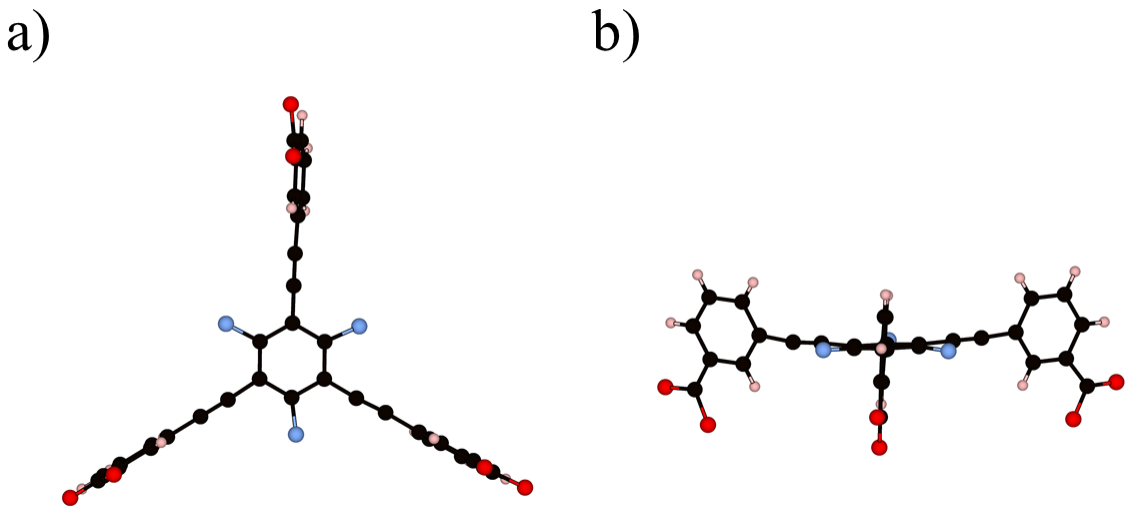

Figure 2.10: Conformation of $BTEB_{mmm}NH_2^{3-}$ linker viewed a) perpendicular and b) parallel to the mean plane of the central phenyl ring in Figure 2.10. The nitrogen atoms on the linker are disordered across three positions due to the C_3 symmetry of the linker. (Cu-deep blue, C-black, O-red, N-blue, H-pink)

Table 2.2: Dihedral angles between the *meta*-benzoate moieties and the central phenyl ring.

Conformation	Dihedral angle between *meta*-benzoate (1) and the central phenyl ring	Dihedral angle between *meta*-benzoate (2) and the central phenyl ring	Dihedral angle between *meta*-benzoate (3) and the central phenyl ring
i	81.4(7)º	82.6(7)º	88.4(6)º

A large pore is located within the centre of the octahedral structure. The distance between two opposite located Cu^{2+} ions of the resulting octahedron is approximately 21.4 Å, while the distance between opposite located central phenyl rings is approximately 22.3 Å. Considering the van der Waals radii of the atoms, the central pore is characterised by a diameter of approximately 14.5 Å. This central pore is accessible through twelve windows that are located along the edges of the octahedron. The windows' size depends on the orientation of the two $BTEB_{mmm}NH_2^{3-}$ linkers on either side of the window. Due to the C_3 symmetry of the $BTEB_{mmm}NH_2^{3-}$ linker gives rise to the amino group being disordered across three positions. This, in turn, gives rise to three different window sizes that allow access to the central pore. The window with the largest diameter occurs when no amino groups are directed towards the window. This causes a window diameter of 6.6 Å considering the shortest relevant interatomic distances. The window with the smallest diameter occurs when two amino groups are directed towards the window, giving a cross-sectional diameter of 5.4 Å.

In the crystal structure of **2**, the octahedral cages are arranged in a body-centred cubic packing agreement. (**Figure 2.11**) Van der Waals interactions weakly bond the MOPs. A series of inter-cage channels with a diameter of *ca.* 5.7 Å extend within the structure in the directions of the crystallographic *a* and *b*- axes. The calculated void volume accounts for 61.6 % of the unit cell. The majority of this void volume is due to the pore within the MOPwith only a minor volume located between the MOPs.

Simulations of the pore-size distribution and accessible surface area were carried out using the Poreblazer software.[225] The simulations reveal a He pore volume of 0.991 cm^3/g and a calculated surface area of 1925.38 m^2/g. The pore-size distribution was calculated using the method developed by Gelb and Gubbins.[227] The limiting channel diameter was determined to be *ca.* 5.28 Å, and the maximum pore diameter of *ca* 13.88 Å. These results strongly agree with the crystallographic estimations. The pore-size distribution is shown in **Figure 2.12**.

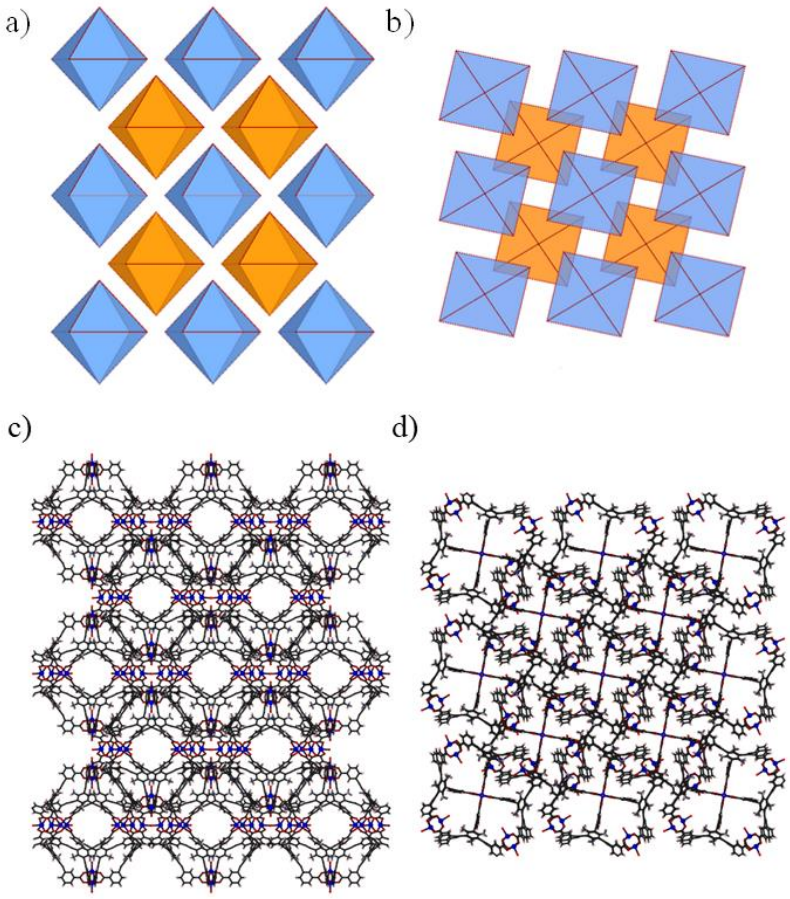

Figure 2.11: Packing diagram of 2 a)/c) viewed along the a/b- crystallographic axis. b)/d) viewed along the c-crystallographic axis. (Blue octahedron - layer a, orange octahedron - layer b).

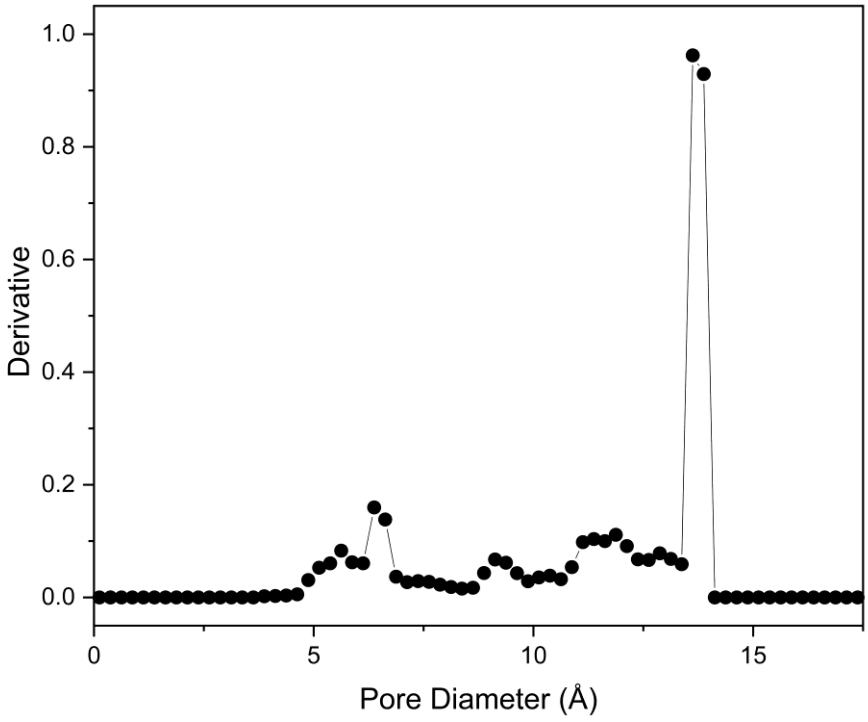

Figure 2.12: Simulated pore-size distribution of 2.

Table 2.3: Crystallographic parameters for 1 and 2.

Identification code	1	2
Empirical formula	$Cu_{36}C_{816}H_{496}N_{36}O_{180}$	$C_{240}H_{192}Cu_{12}N_8O_{60}$
Formula weight	15972.44	4910.65
Temperature / K	215(2)	215(2)
Crystal system	Monoclinic	Tetragonal
Space group	*C2/m*	*I4/m*
***a* / Å**	54.9305(18)	27.262(3)
***b* / Å**	55.3715(18)	27.262(3)
***c* / Å**	44.3760(16)	35.028(4)
***α* / º**	90	90
***β* /º**	125.72(2)	90
***γ* / º**	90	90
Volume / Å^3	109578(23)	26033(7)
Z	2	8
ρ_{calc}/ g/cm^3	0.482	0.658
μ / mm^{-1}	0.604	0.838
F(000)	16176	5240
Crystal size / mm^3	0.350 × 0.130 × 0.130	0.25 × 0.25 × 0.25
Radiation	1.54178 Å	1.54178 Å
θ range for data collection / º	1.272 to 38.615	2.053 to 52.646
Index ranges	-43 <= h <= 41 -44 <= k <= 44 -35 <= l <= 35	-25 <= h <= 26 -15 <= k <= 28 -34 <= l <= 35
Reflections collected	177406	35140
Independent reflections	30215 [R(int) = 0.1353]	7555 [R(int) = 0.0372]
Data/restraints/parameters	30215 / 3659 / 2571	7555 / 298 / 352
Goodness-of-fit on F^2	1.123	1.059
Final R indexes [I>=2σ (I)]	R1 = 0.1339, wR2 = 0.3638	R1 = 0.1176, wR2 = 0.3557
Final R indexes [all data]	R1 = 0.1844, wR2 = 0.3903	R1 = 0.2039, wR2 = 0.4002
Largest diff. peak/hole / e.Å^{-3}	0.554 and -0.511	0.395 and -0.354

2.3.3 Physiochemical characterisation of **1** and **2**

2.3.3.1 Powder X-ray diffraction

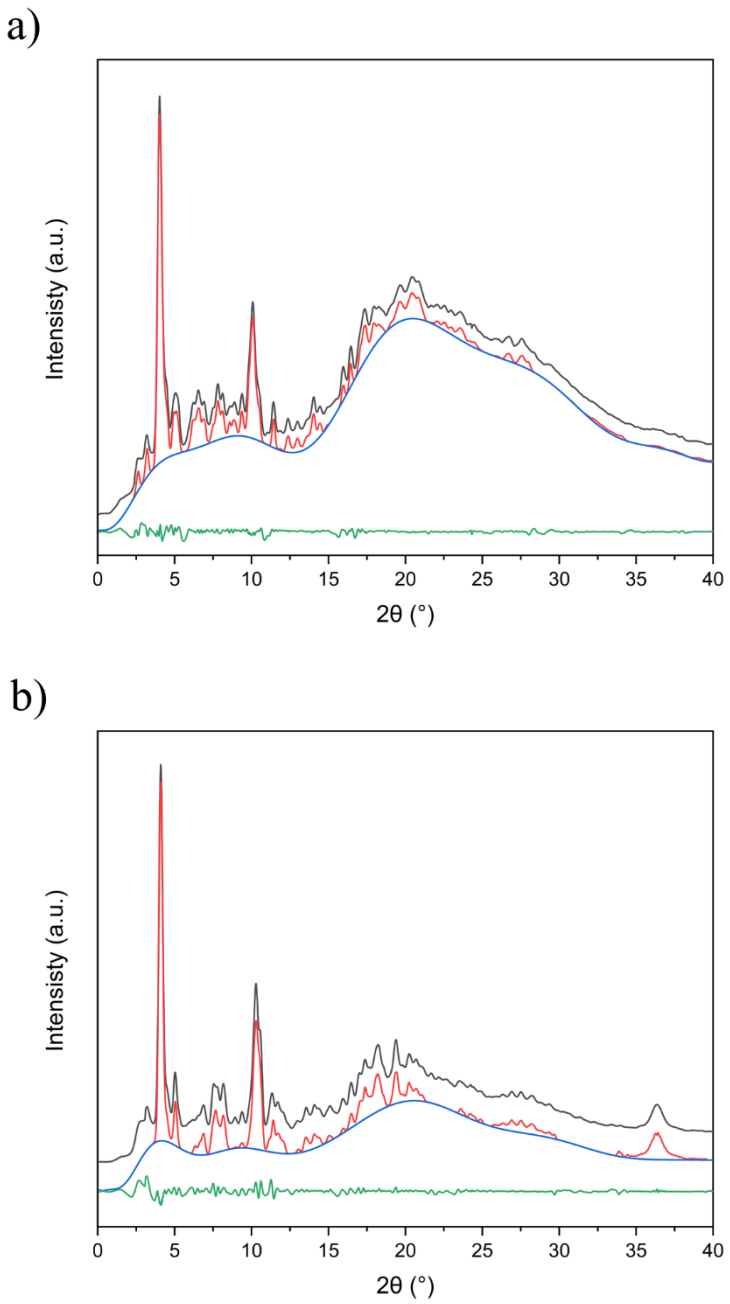

Figure 2.13: PXRD patterns for a) 1 and b) 2. (Measured diffraction – black, calculated background – blue, theoretical diffraction pattern – red, difference between measured and theoretical – green)

The two compounds, **1** and **2**, were characterised by X-ray powder diffraction to confirm their bulk purity. The two compounds were prepared by grinding the crystals in DMF before loading the samples into a quartz capillary. This method minimises the possibility of structural collapse of the two MOPs through desolvation or capillary forces. The powder patterns of the samples was measured

at 215 K, using a Bruker APEX II DUO X-ray diffractometer. The patterns were found to have a significant background signal due to diffraction from the quartz capillary.

The computational package Expo2014 was used to calculate the background signal and fit the experimental diffraction to the theoretical diffraction pattern.[228,229] Using the Rietveld method the weighted profile R-factor and the unweighted profile R-factor were calculated for the two diffraction patterns.[230] The two experimental diffraction patterns matched well with the theoretical diffraction patterns for the two compounds (**Figure 2.13 & Table 2.4**).

Table 2.4: Calculated unweight R-factor and weighted R-factor for 1 and 2.

Compound	Rp	Rwp
1	0.869	2.022
2	2.129	4.361

2.3.3.2 Thermogravimetric analysis

Thermogravimetric analysis (TGA) was carried out to examine the thermal stability of **1** and **2**. The two compounds were heated at a rate of 4 ºC per minute under a nitrogen atmosphere (**Figure 2.14 a) & b)**). For **1**, an initial rapid weight loss of *ca.* 38.6 % occurred between 20 ºC and 36 ºC. This initial loss in mass is due to the loss of solvent from the crystals. A further loss of 22.1 % mass occurred between 36 ºC and 124 ºC. This loss in mass is due to the removal of DMF and H_2O solvent molecules within the pores in the MOPs and the voids between the MOPs. Another mass loss occurred between 219 ºC and 370 ºC, which is calculated to be 8.5 %. This is due to the decarboxylation reaction of the $BTEB_{mmm}NH_2^{3-}$ used to construct the MOF and decomposition of the organic linker..

Upon heating, **2** experienced an initial weight loss of *ca.*43 % between 20 ºC and 120 ºC. This initial loss was attributed to the removal of DMF and H_2O solvent molecules within the pores in the MOPs and the voids between the MOPs. A secondary weight loss of *ca.* 29 % occurs between 200 ºC and 700 ºC, with this weight loss being attributed to the decomposition of the $BTEB_{mmm}NH_2^{3-}$ linkers. This step includes the decarboxylations and the carbonisation of the linkers.

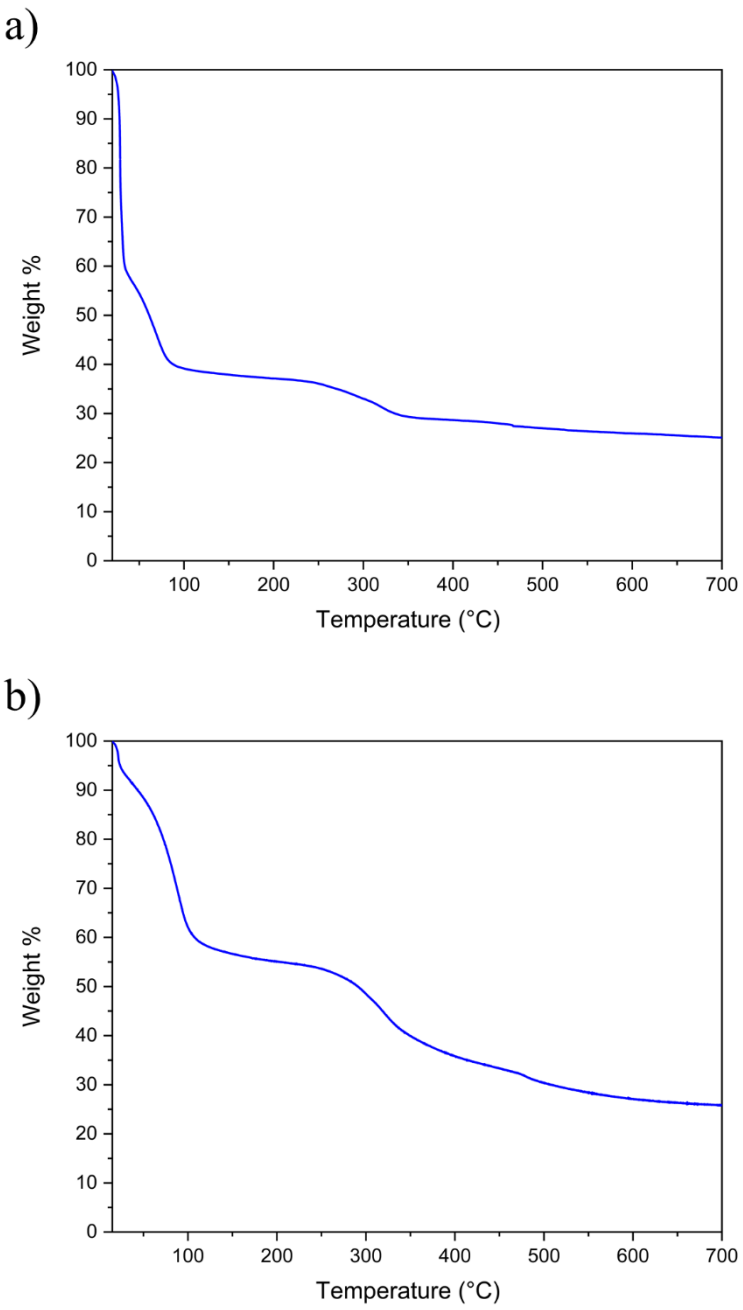

Figure 2.14:TGA of 2 heated at a rate of 4 ºC per minute under a nitrogen atmosphere.

2.3.3.3 Fourier transform infrared (FT-IR) and Raman spectroscopy

FT-IR and Raman spectroscopy were used to characterise **1** and **2**. The FT-IR and Raman spectra of the two compounds were found to be similar in nature, with the two spectra being dominated by the bands arising from the $BTEB_{mmm}NH_2^{3-}$ organic linkers. In the two FT-IR spectra, bands found at 3460 cm^{-1} and 3320 cm^{-1} associated with ν(N-H) stretching frequencies of the central amino group can be seen. A weaker band at 3074 cm^{-1} is associated with the aromatic ν(C-H) stretching involving sp^2 hybridised carbon atoms. Some of the latter bands coincide with broadened bands from hydrogen bonding to solvent molecules within the porous framework. The DMF solvent molecules' characteristic aldehyde ν(C-H) stretching frequencies can be seen at 2928 $cm^{-1,}$ and 2858 cm^{-1}.[231] At

2212 cm^{-1} a weak band associated with ν(C≡C) stretching of the organic ligands are observed. This band is indeed present in these structures due to the amino group located on the central phenyl ring, which imparts a degree of asymmetry to the alkyne bond. This asymmetry increases the intensity of the band in the IR spectrum.[232] At 1660 cm^{-1} in both spectra of **1** and **2**, strong bands correspond to the carbonyl stretching mode of coordinating DMF and constitutional DMF solvent molecules within the porous structure of the MOF. Bands found at 1620 cm^{-1} and 1430 cm^{-1} correspond to the asymmetric and symmetric ν(C=O) carboxylate stretches of the organic ligand. The difference between these bands, Δ =190 cm^{-1}, indicates that the carboxylate groups are in a bidentate bridging mode.[233]

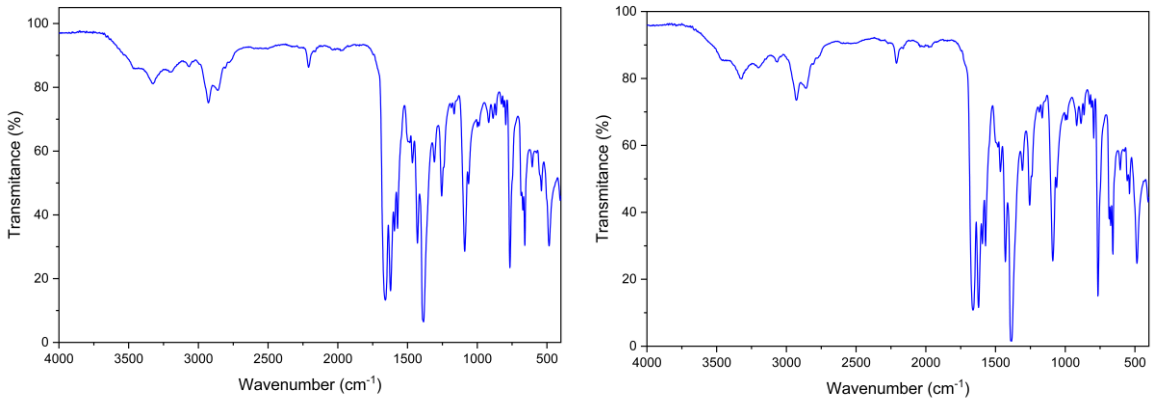

Figure 2.15: IR spectra of a) 1 and b) 2.

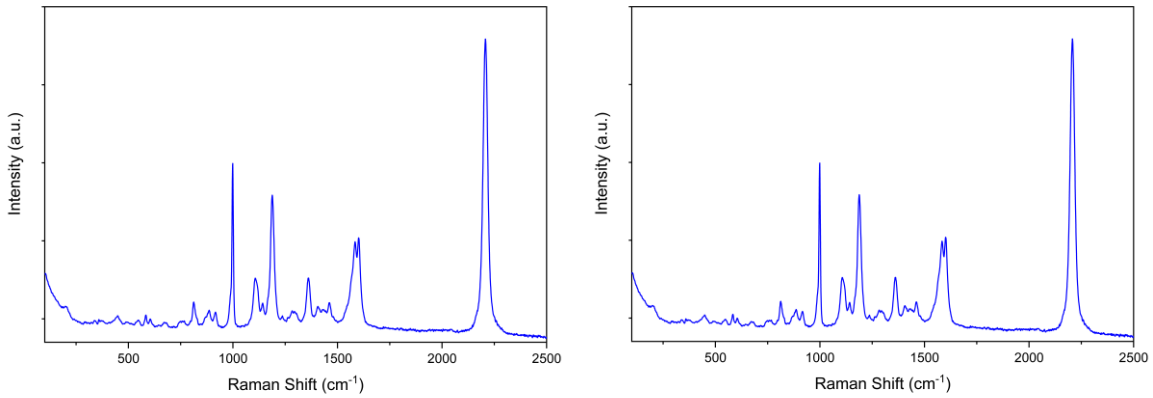

Figure 2.16: Raman spectra of a) 1 and b) 2

The Raman spectra of the two compounds, **1** and **2**, were also found to be very similar due to the two structures being constructed of the same $BTEB_{mmm}NH_2^{3-}$ linkers. A weak band found at 200 cm^{-1} corresponds to the δ(O-Cu-O) bending in the {Cu_2} SBUs.[234] In the region of 900 – 1200 cm^{-1} aromatic ν(C-H) bands are identifiable. The band at 998 cm^{-1} can be attributed to the ν(C-H) vibrations associated with the central phenyl ring.[235] The following three bands at 1107 cm^{-1}, 1143 cm^{-1} and 1187 cm^{-1} can be assigned to the ν(C-H) vibrations of the three *meta*-benzoate moieties.[235] Two aromatic δ(C=C) vibrations give rise to bands at 1582cm^{-1} and 1608 cm^{-1}. The most substantial

band in the two spectra is the band found at 2207 cm^{-1} and which is due to the acetylenic spacer units.[235]

2.3.4 Topological and structural analysis of **1** and **2**

2.3.4.1 Topological analysis

The structures of **1** and **2** are a subset of MOFs and MOPs with a *'A_3X_4'*-stoichiometry where 'A' and 'X' represent 4- and 3-connected nodes, respectively, where each 4-connected node is connected to four 3-connected nodes and *vice versa*.[236] The combination of these two nodes is then used to construct edge-transitive default topologies that are described by the RCSR symbols **tbo** and **pto.** Notable examples of structures that belong to this family include HKUST-1 and MOF-14.[237,238]

The topologies of **1** and **2** were analysed, and their simplified representations were constructed (**Figure 2.17**). The two structures were found to have (3,4,4)-sub-connectivities and (3,4)-sub-connectivities, respectively. In both structures, the 3-connected node corresponds to the $BTEB_{mmm}$-NH_2^{3-} linker while the 4-connected node corresponds to the $\{Cu_2\}$ SBUs. In the structure of **1** the two 4-connected nodes relate to the two topologically distinguishable $\{Cu_2\}$ SBUs, with these being the $\{Cu_2\}$ SBUs at the vertices of the outer cuboctahedron and the $\{Cu_2\}$ SBUs at the vertices of the inner octahedron. The two structures can be described by their unique set of point symbols. The point symbol for **1** was found to be $4^6{\cdot}\{4{\cdot}6^2{\cdot}8^3\}{\cdot}\{4^2{\cdot}6\}$, while the point symbol for **2** was found to be $\{4^3\}_4\{4^4{\cdot}6^2\}_3$.

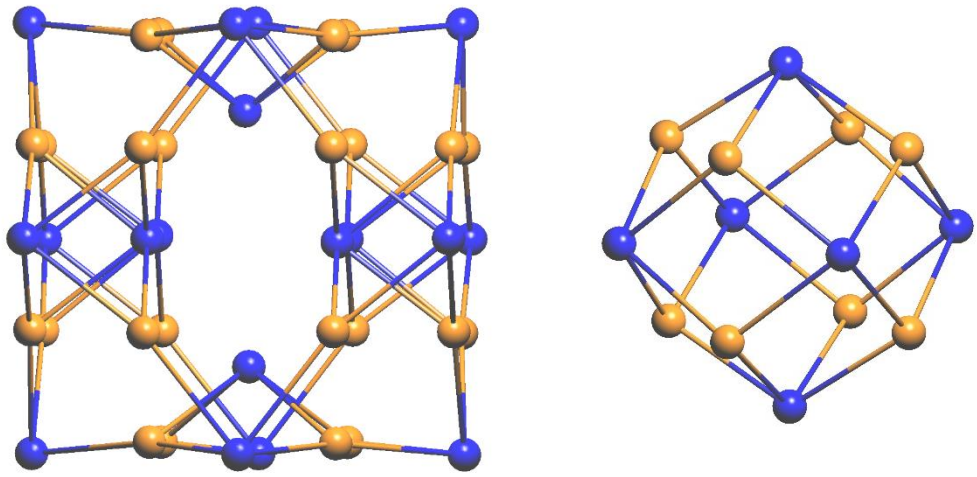

Figure 2.17: Topological representation of a) 1 and b) 2. (4-connected nodes – blue, 3-connected nodes - orange)

2.3.4.2 Structural analysis

The two MOPs, which were synthesised using the $BTEB_{mmm}NH_2$ organic linkers and $\{Cu_2\}$ SBUs, have the topology of the convex polyhedra, a cuboctahedron and octahedron, respectively. The two critical angles that determine the structure and topology of a MOP are the angles between the organic linkers and the inorganic SBU, and the angles between the coordinated functional groups on the organic linker, often denoted by the symbols η and θ, respectively.[43,239,72] The two MOPs, **1** and **2**, both contain $\{Cu_2\}$ SBUs, which sets the angle η in these structures to 90º. With this angle being set to 90º, the structures of the two MOPs are solely differentiated by the conformation of the $BTEB_{mmm}N_2$ organic linkers. Due to the acetylenic spacer units, the $BTEB_{mmm}NH_2^{3-}$ ligand can access a broader range of conformations than that would be possible using ligands in which phenyl moieties are directly connected..

The geometrical requirements for the construction of a cuboctahedron and octahedron were outlined in work by Yaghi *et al.*[43] It was calculated that for the construction of a cuboctahedron considering the geometries of planar $\{Cu_2\}$ SBUs, the optimal linker geometry forms an angle of 117º between two carboxylate groups. In the structure of **1**, the two external *meta*-benzoates moieties are in an *anti-anti* arrangement with respect to each other. This arrangement creates an angle of 120º, considering idealised bond geometries which is proximate to the mathematically described angle (**Figure 2.18 a)**). The small discrepancy is compensated by slight distortions in the structure of the coordination cage, most notable in the bending of the acetylenic spacers.

In the structure of **2**, the *meta*-benzoate moieties lie perpendicular to the central phenyl ring. This gives the ligand a typical tripod geometry. (**Figure 2.18 b)**) In this geometry, the angle between the carboxylate groups is approximately 52º. This is a deviation of 8º from the mathematically calculated optimal angle of 60º. This deviation is compensated by the bending of the acetylene-type spacer units.

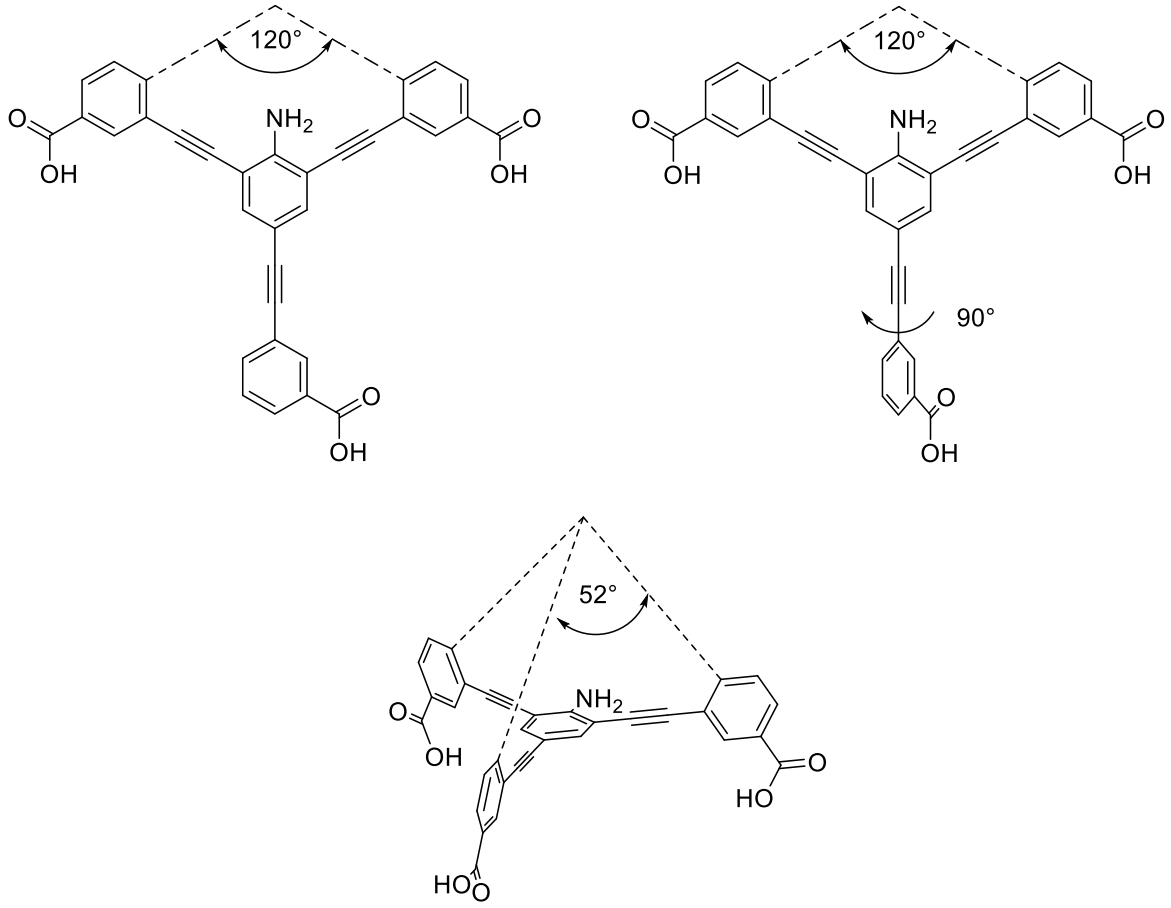

Figure 2.18: The three conformations that the $BTEB_{mmm}NH_2^{3-}$ linker is found within the structures of a) 1 and b) 2. The *anti*-arrangement of the external *meta*-benzoate moieties found in the structure of 1 creates an angle of 120º between the two carboxylate groups. With the *meta*-benzoate moieties rotated perpendicular with respect to the central phenyl, it creates an angle of 52º between the carboxylate groups.

2.4 Pillaring

With the successful synthesis of **1** and **2** we now focused on utilising these MOPs to construct higher dimensional MOFs. To construct the MOFs from the newly synthesised MOPs, a method known as pillaring was utilised.[215,240,217] Pillaring is the method of using for instance, bipyridyl ligands to coordinate to the labile sites on inorganic SBUs, in this instance, the apical position on two different $\{Cu_2\}$ SBUs. The pillaring ligand then acts as a connection between the two inorganic SUBs. In this work, several pillaring ligands were used. These ligands were chosen based on the intramolecular distance between their coordinating nitrogen atoms (**Figure 2.19**). It was predicted that by varying the length of the pillaring ligand, it would be possible to create a family of iso-structural MOFs with a range of porosities.

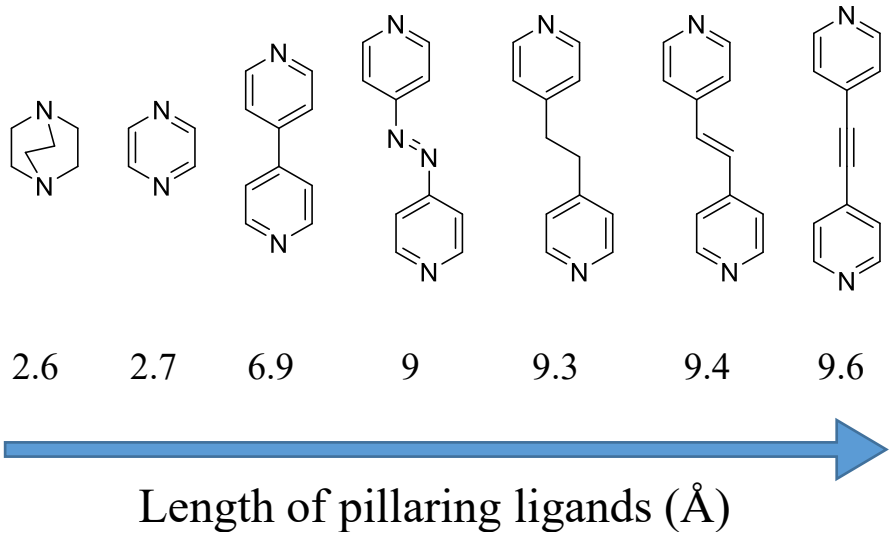

Figure 2.19: The bipyridyl ligands used in the pillaring reaction using 1 and 2 as SBUs; arranged with increasing distance between N-donor atoms.

Of the chosen ligands, two were found to have the most significant effect on the reaction. The two ligands were 1,4-diazabicyclo[2.2.2]octane (DABCO) and 4,4'azobipyridine (Azpy). When DABCO was used as the pillaring ligand, rather than pillaring the MOPs, a high yield of **2** was obtained. The high yield of **2** occurred even without the addition of EtOH, as was required in the previous synthesis of **2**. It is believed that selectivity to **2** and high yield is due to the basic nature of the two tertiary amine functionalities in DABCO. Previous reports in the literature note that the addition of a base is found to aid the synthesis of carboxylate base MOPs. This effect is due to the base deprotonating the carboxylic acid groups and thus increasing the coordination rate and propensity between the carboxylate and metal ions. [241,242,243] The absence of **2** when the remaining pillaring ligands are used in synthetic approaches is due to the weaker basic character of the pyridyl moieties.

Azpy was most successful in the pillaring of the MOPs. With its addition into the reaction mixture, it was found that two new MOFs could be synthesised. These are the result of pillaring **1**. By altering the ratio of the Azpy to $BTEB_{mmm}NH_2^{3-}$ linkers, it was possible to synthesise one MOF over the other selectively. The syntheses and the structures of these two MOFs are outlined in the next sections.

2.5 Pillaring of **1**

2.5.1 $[Cu_{36}(BTEB_{mmm}NH_2)_{24}(Azpy)(DMF)_{34}]$ (**3**)

3 was synthesised using the same mole ratio of $Cu(NO_3)_2.6H_2O$ to $H_3BTEB_{mmm}NH_2$ (2:1) as applied for the synthesis of **1**. However, in this instance, 1-mole eq. of the Azpy ligand is added to the reaction mixture. The mixture was then heated to 85 ºC for 72 h in DMF. From the solution, **3** crystallised as elongated, dark green, rhombohedral crystals alongside crystals of **1**. The distinctive colour and morphology allowed for the manual separation of the newly synthesised product from the side

product **1** and a co-precipitating amorphous material. The crystals were then cleaned through washings using DMF to remove any amorphous material adhered to the crystals' surface. The crystals were of suitable size and quality for analysis by single-crystal X-ray diffraction. The structure was solved in the triclinic space group $P\bar{1}$; the unit cell parameters were determined to be a = 37.58(3) Å, b = 40.16(3) Å, c = 43.33(4) Å, α = 113.930(9)º, β = 112.575(14)º, γ = 95.399(11)º.

The compound entails a one-dimensional MOF with the chemical formula $[Cu_{36}(BTEB_{mmm}NH_2)_{24}(Azpy)(DMF)_{34}]$. The one-dimensional chains are comprised of a series of MOPs connected by the Azpy ligands. The MOP SBUs have the structure of **1**, with six $\{Cu_2\}$ SBUs forming the internal octahedron, which is encapsulated by an outer cuboctahedral framework containing twelve $\{Cu_2\}$ SBUs. Each Cu^{2+} is coordinated by four O-donor atoms from $BTEB_{mmm}NH_2^{3-}$ linkers which form the base of a square base pyramidal coordination environment. The occupancy of the remaining coordination site on the Cu^{2+} ions varies from ion to ion within the structure of the MOP. For all, with the exception of two of the Cu^{2+} ions, an O-donor atom from a DMF solvent molecule coordinates to the apical position, completing the square base pyramidal coordination geometry.

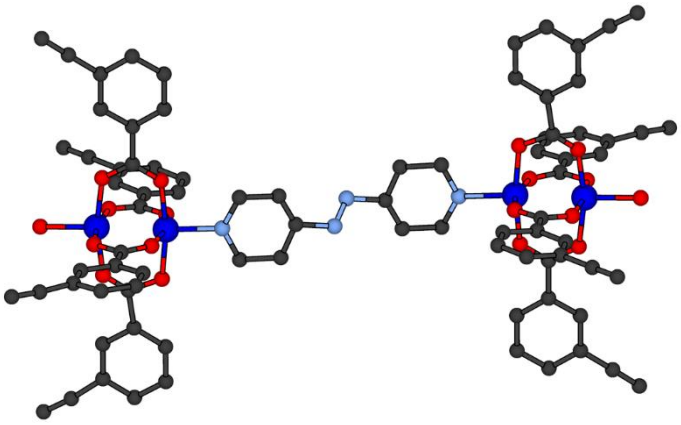

Figure 2.20: Azpy ligand coordinating to the apical sites on two $\{Cu_2\}$ SBUs through the N-donor atoms. (C -black, O – red, N – light blue, Cu – dark blue)

The remaining two Cu^{2+} ions located on the external cuboctahedral structure are coordinated by an N-donor atom from a connecting Azpy ligand (**Figure 2.20**). The corresponding N-Cu bond lengths are identical, within the measurement error, to those of the coordinating O-donor atoms from the DMF solvent molecules. The distance between the two N-donor atoms with the Azpy ligand is *ca.* 9.0 Å while the distance between the two Cu^{2+} ions coordinated by an Azpy ligand is *ca.* 13.3 Å. The two $\{Cu_2\}$ SBUs coordinated by the Azpy ligands are located on opposite vertices of the outer cuboctahedral structure (**Figure 2.21 a & b**). The internal octahedron of the **1** MOP unit is highly disordered due to the high symmetry of the external cuboctahedral framework and the rotational flexibility of the organic carboxylate ligands.

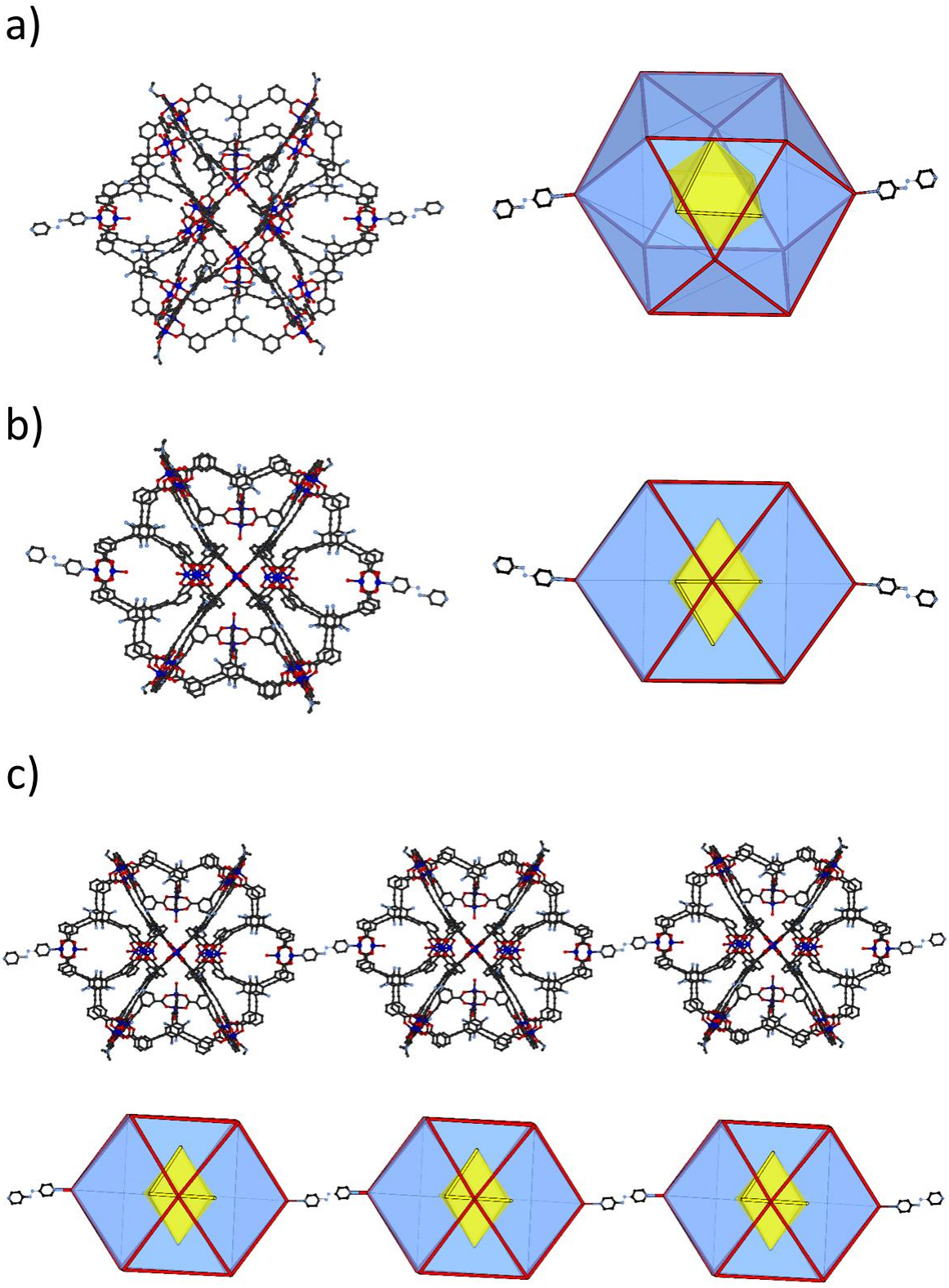

Figure 2.21: a) and b) show two Azpy ligands coordinating to two {Cu_2} SBUs located transverse to each other on the outer cuboctahedral structure along with a graphical representation. c) Linkage of 1 by Azpy ligands to form a one-dimensional chain seen both as found in the crystal structure and a graphical representation. (C -black, O – red, N – light blue, Cu – dark blue, inner octahedron – yellow, outer cuboctahedron – light blue with red edges)

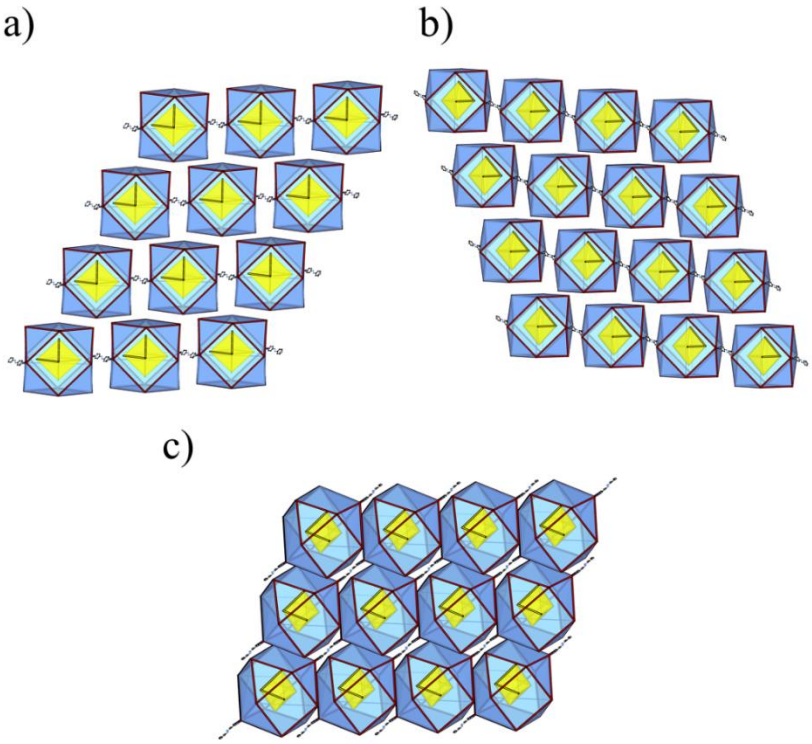

Figure 2.22: Graphical representation of the packing of the one-dimensional chains in 3 viewed along the crystallographic a) a-axis, b) b-axis, and c) c-axis. The framework of the MOP units is removed for clarity. (C – black, N – blue, outer cuboctahedral framework – blue cuboctahedron, inner octahedron – yellow octahedron)

The one-dimensional chains pack co-linearly in the crystal (**Figure 2.22**). Each chain is shifted with respect to each other along the axis of the chain to maximise the packing density between the chains. In **Figure 2.22 c**), the MOPs are seen to pack in an *a-b-a* packing arrangement in the direction of the crystallographic c-axis. The majority of the void volume in the structure derives from within the MOP units.. The largest void volume between the chains is located between two square faces of adjacent MOP units. This face to face packing generates a pore with a diameter of ca. 16.6 Å, considering atom-to atom distances.

The product rapidly loses crystallinity upon desolvation of the crystals. The potential porosity of the sample was therefore examined computationally using the Poreblazer software package. The compound was calculated to have a He pore volume of *ca.* 1.687 cm^3/g and a calculated surface area of *ca.* 4600 m^2/g. The limiting channel diameter was determined to be *ca.* 6.9 Å, while maximum pore diameter was calculated to be *ca.* 16.0 Å. These results agree with the crystallographic estimations whereby the largest pore diameter corresponds to pores that are formed between the square faces of adjacent MOP SBUs. The calculated pore-size distribution is shown in **Figure 2.23**.

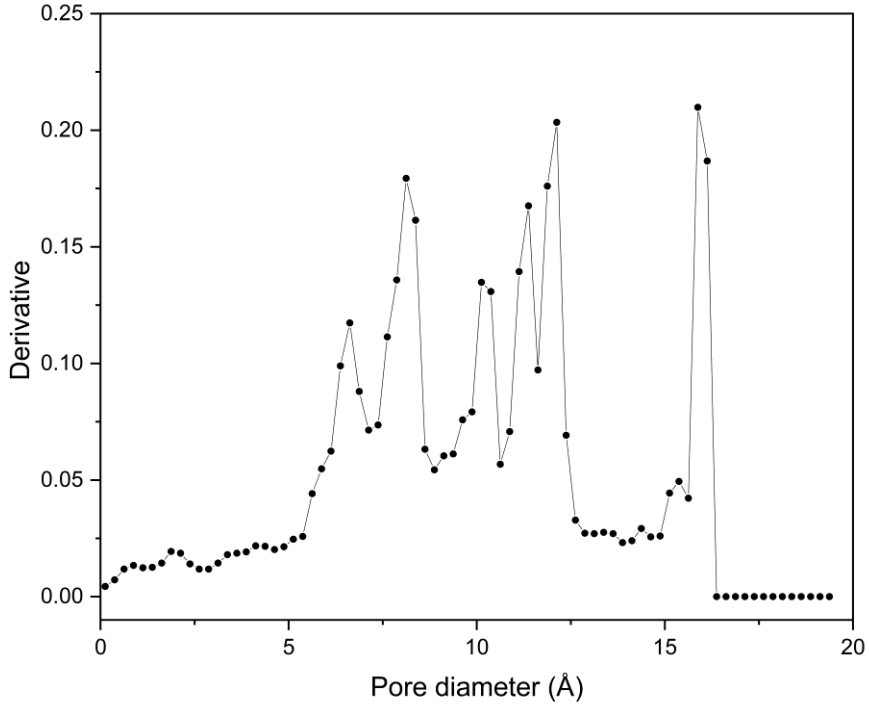

Figure 2.23: Simulated PSD of 3.

2.5.2 Powder X-ray diffraction

To verify the phase purity of the manually separated crystals PXRD analysis of the sample was carried out. Due to the large crystal sizes, the material was ground to a fine powder. The grinding was carried out within the mother liquor to minimise solvent loss and the associated capillary forces. The sample was then loaded into a quartz capillary and measured at 215 K using a Bruker APEX II DUO X-ray diffractometer. The fitting parameters of the theoretical diffraction pattern to the measured pattern were calculated using the computational package Expo2014 (**Figure 2.24**).[228,229] Using the Rietveld method, the weighted and the unweighted R-factor were calculated for the two diffraction patterns. The two R-factors were calculated to be Rp = 0.877 and Rwp = 1.941, respectively. These values indicated an agreement between the theoretical diffraction pattern and the measured pattern.

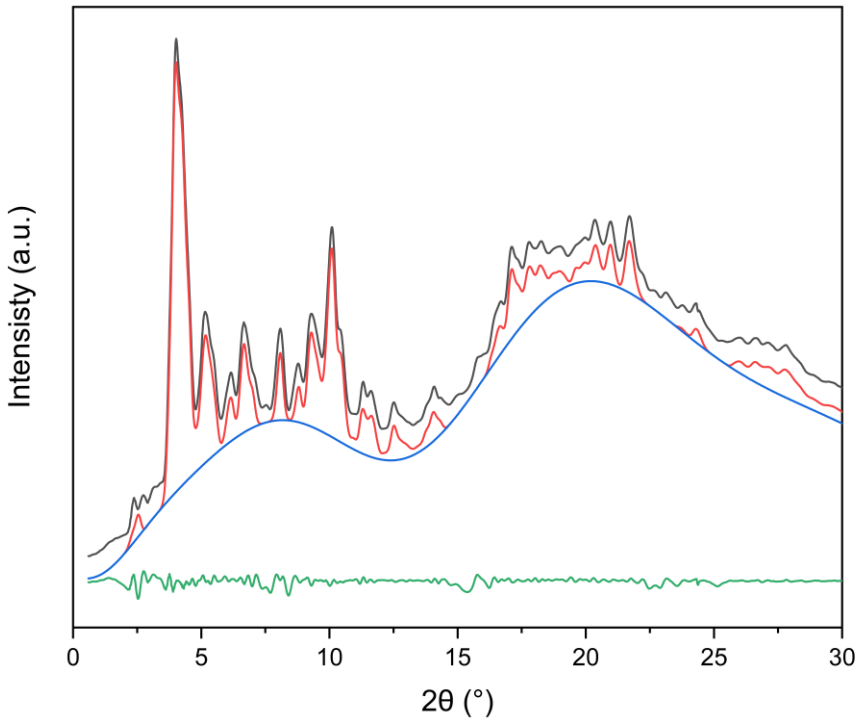

Figure 2.24: PXRD pattern of 3. (Measured diffraction pattern – black, theoretical diffraction pattern – red, calculated background – blue, difference between measured and theoretical diffraction pattern – green)

2.5.3 Thermogravimetric analysis

To examine the thermal stability of **3**, a thermogravimetric analysis of the material was carried out. Crystals of **3** were isolated and washed with DMF and dried between two sheets of filter paper to remove surface solvent residues. The compound was then heated at 4 ºC per minute under a nitrogen atmosphere. An initial loss in mass of *ca.* 50.9 % occurred between 20 ºC and 167 ºC. This loss in mass is due to the removal of DMF and H_2O solvent molecules from the pores of the MOF. A second distinctive mass loss of 22.8 % occurred between 235 ºC and 398 ºC. This weight loss is attributed to the decarboxylation reaction and degradation of the $BTEB_{mmm}NH_2^{3-}$ linkers. A final thermogravimetric step occurred between 405 ºC and 700 ºC, which may be associated with the degradation of Azpy moieties.

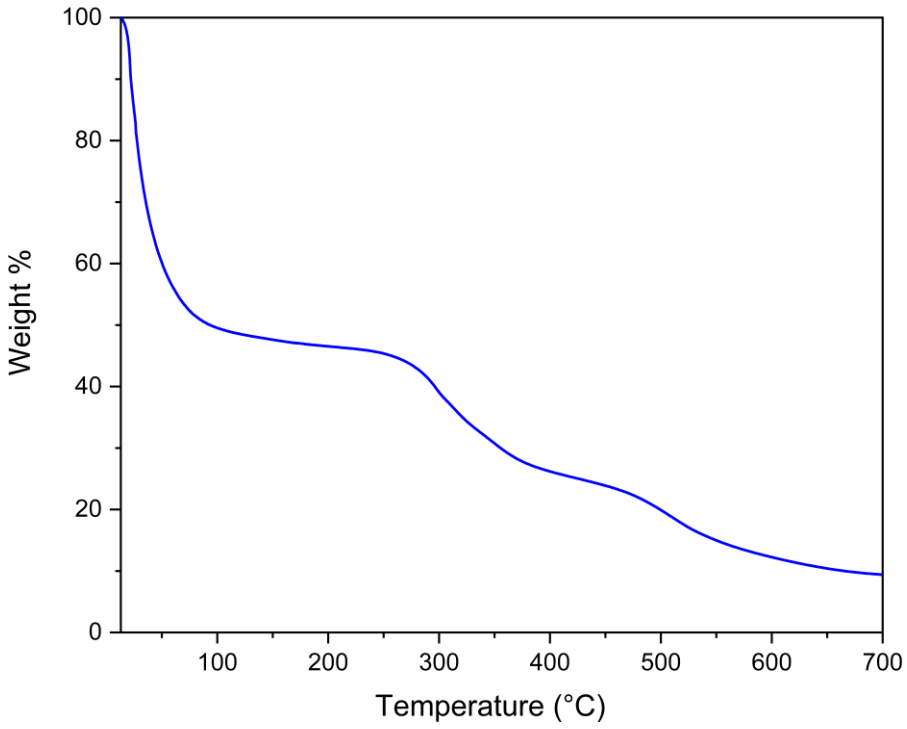

Figure 2.25 TGA of 3 measured under a nitrogen atmosphere at a rate of 4 ºC per minute

2.5.4 FT-IR and Raman spectroscopy

In the FT-IR spectrum of the compound, a series of broad bands are located at 3453 cm^{-1}, 3405 cm^{-1} and 3230 cm^{-1}. These bands can be attributed to the ν(N-H) stretching frequency of the amino-functional group on the $BTEB_{mmm}NH_2^{3-}$ linker and hydrogen-bonded solvent molecules located within the pores of the MOF (**Figure 2.36 a)**). The DMF solvent molecules' characteristic aldehyde ν(C-H) and methyl ν(C-H) stretching frequencies can be seen at 2931 cm^{-1} and 2856 cm^{-1}.[231] A strong band associated with the DMF ν(C=O) mode is located at 1666 cm^{-1}. Bands found at 1605 cm^{-1}, and 1442 cm^{-1} correspond to the asymmetric and symmetric ν(C=O) carboxylate stretches of the organic ligand. The difference between these bands, Δ =180 cm^{-1}, indicates that the carboxylate groups are in a bidentate bridging mode.[233]

Like the FT-IR spectra, the Raman spectrum of the compound predominately contains signals that derive from the $BTEB_{mmm}NH_2^{3-}$ linker. The most significant band in the spectrum is attributed to the ν(C≡C) acetylene spacer units of the linker and is centred at 2243 cm^{-1}. Two bands associated with the aromatic ν(C=C) stretches occur at 1607 cm^{-1} and 1584 cm^{-1}. Bands located at 1412 cm^{-1} and 1363 cm^{-1} are attributed to ν_s(C=O) stretching vibrations of the carboxylate groups. In-plane C-H bending modes that arise from the *meta*-benzoate moieties can be seen at 1207 cm^{-1} and 1121 cm^{-1}. The δ(C-H) vibrational mode associated with the central phenyl ring gives rise to a distinctive signal that occurs at 998 cm^{-1}.[235,244]

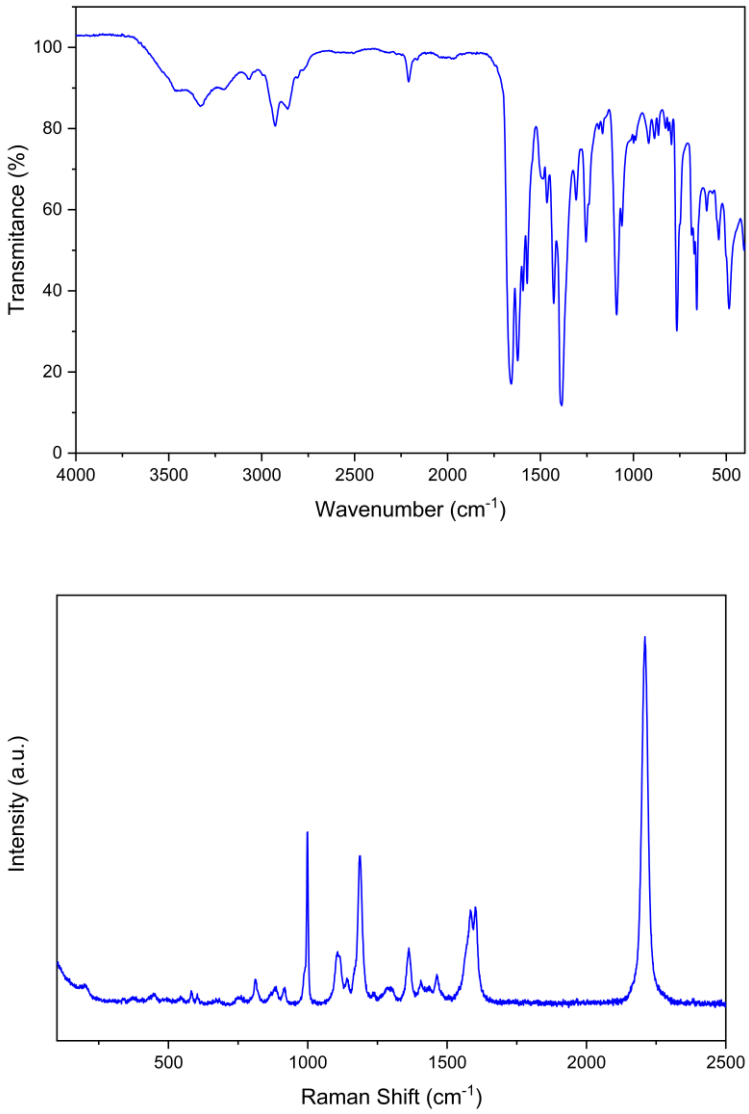

Figure 2.26:FT-IR and Raman spectra of 3.

2.5.5 $[Cu_{36}(BTEB_{mmm}NH_2)_{24}(Azpy)_6(DMF)_{30}]$ (**4**)

By further increasing the Azpy to $H_3BTEB_{mmm}NH_2$ linker ratio, a second type of MOF containing the Azpy ligand, **4**, was synthesised. The ratio of $Cu(NO_3)_2{\cdot}6H_2O$ to $H_3BTEB_{mmm}NH_2$ remained the same as for the synthesis for **1** (1.5:1 mole ratio). In this instance, 4-mole equivalents of Azpy were added to the reaction mixture. The DMF solution was then heated at 85 ºC for 72 h. During this time period which large, dark green cubic crystals grew on the glass surface of the reaction vial. The crystals were single-crystalline and of suitable quality for single-crystal X-ray analysis. The crystals were measured and solved in the cubic space group $Ia\bar{3}$;the unit cell parameters were determined to be $a = b = c = 81.374(8)$ Å, $\alpha = \beta = \gamma = 90^{o}$.

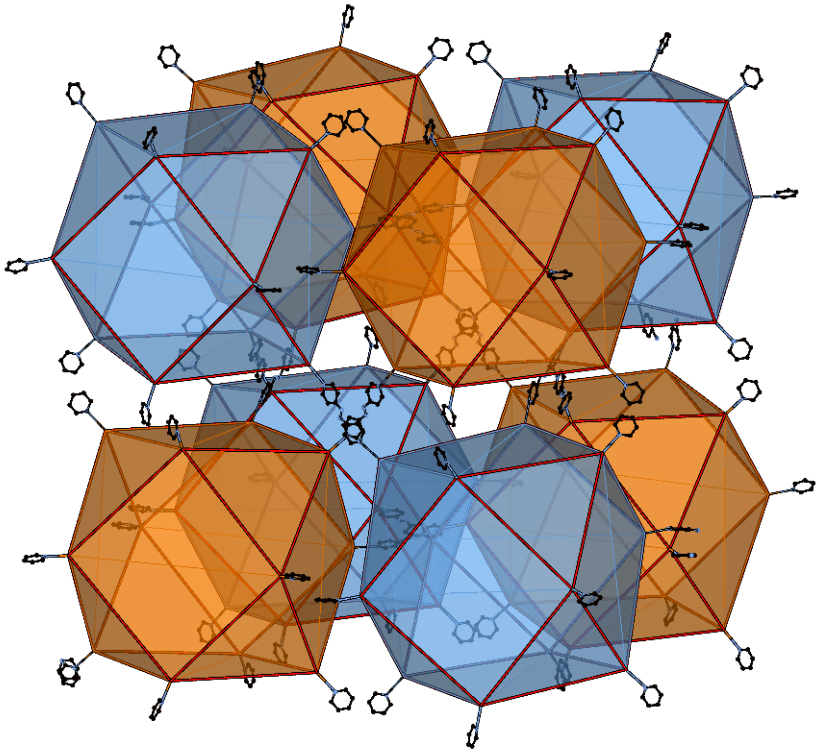

Figure 2.27: Structure of 4 containing two interpenetrated frameworks comprised of MOPs that have the structure of 1 linked into three-dimensional frameworks by Azpy ligands. For clarity, the MOPs are represented by cuboctahedra which depict the outer topology of the MOPs. (C – black, N – blue sphere, framework a – blue cuboctahedra, framework b – orange cuboctahedra)

The compound is composed of dual interpenetrated, three-dimensional frameworks; it has the chemical formula $[Cu_{36}(BTEB_{mmm}NH_2)_{24}(Azpy)_6(DMF)_{30}]$. The framework is constructed from MOPs that are interconnected by Azpy ligands. The MOP units have the structure of **1**, with only minor structural deviations involving the bond lengths and bond angles for the $\{Cu_2\}$ SBUs and the coordinating $BTEB_{mmm}NH_2^{3-}$ linkers. Like in the previously described MOF **3**, the internal octahedral structure of the MOP is disordered due to the rotational flexibility of the carboxylate ligand and the symmetry of the outer cuboctahedral framework. In comparison to **3**, where Azpy ligands coordinate only to two externally located Cu^{2+} ions, in **4**, all twelve external Cu^{2+} ions are coordinated by Azpy ligands. The Azpy ligands coordinate to the apical position of the Cu^{2+} ions *via* the N-donor atoms of the pyridyl rings. Between four adjacent MOP units, two Azpy ligands stack in a cross configuration, with the two ligands being part of two different frameworks (**Figure 2.28**). π-π Interaction occurs between two pyridyl rings of two adjacent Azpy ligands. The two pyridyl rings have a typical intermolecular distance of *ca.* 3.4(1) Å, a shift of *ca.* 2.06(2) Å and a tilt angle of *ca.* 0.2(4)º. These values match literature reported values for similar π-π bonding interactions.[245]

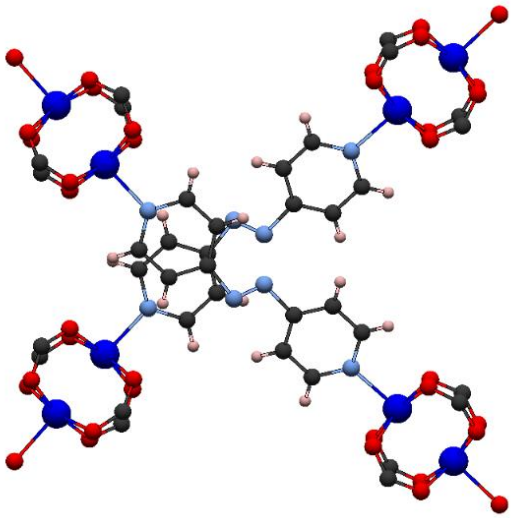

Figure 2.28: Stacking arrangement of two Azpy pillaring ligands in 4. Two pyridyl rings experience a π-π interaction. (C – black, O – red, N – light blue, H – pink, Cu – dark blue)

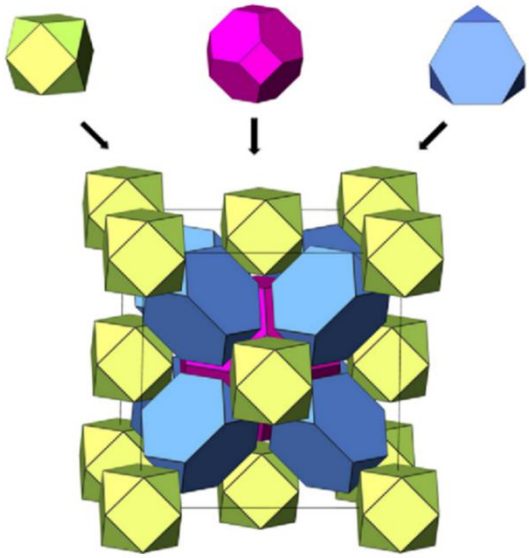

Figure 2.29: The structure of an individual fcu framework. The cuboctahedra (yellow) represent the MOPs in the structure of 4, with the truncated octahedral pore located between six cuboctahedra (pink) and tetrahedral pore (blue) located between 4 cuboctaheda. Adapted from reference 246.

Each of the two independent frameworks within the MOF has an **fcu**-type topology, with the MOP SBUs acting as 12-connected nodes that are connected by Azpy linkers (**Figure 2.29**). Each of the **fcu** frameworks contains two large pores; however, due to the interpenetration, these pores are absent within the structure of **4**. In **Figure 2.22 a & b,** the larger of the two pores associated with the individual **fcu** frameworks correspond to truncated octahedral void spaces highlighted in pink in **Figure 2.29**. These truncated octahedral pores are rendered by 6 MOP units located at the six vertices and twelve Azpy ligands, which reside on the edges of the pore. This pore has a diameter of *ca.* 55.7 Å, measured between the square faces of two opposite located MOPs. Due to the interpretation of

two frameworks, a MOP unit from the secondary framework occupies this octahedral void space (**Figure 2.30 c**).

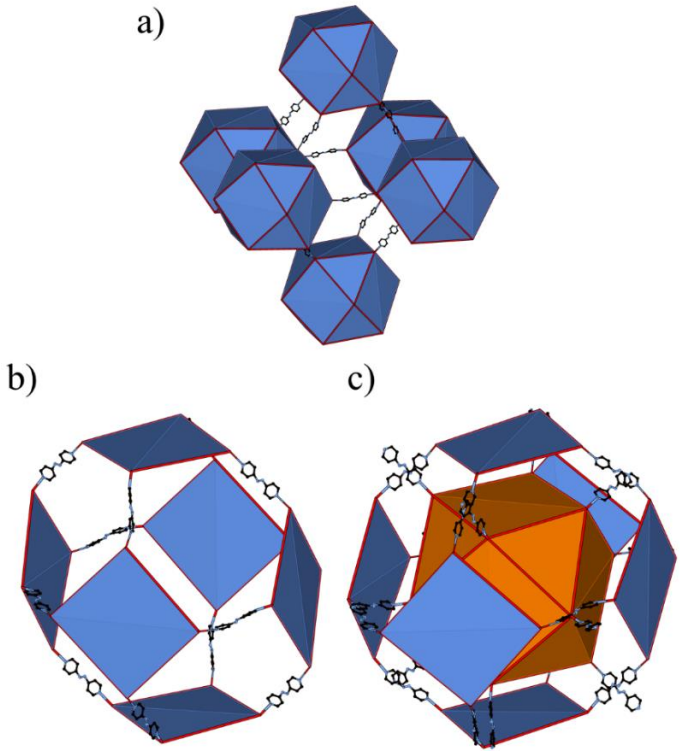

Figure 2.30:a) The octahedral pore found in one fcu framework between six MOP units. b) The octahedral pore with the MOP units removed for clarity. c) The occupied octahedral pore as found in 4 with a MOP unit from the secondary fcu framework located at the centre of the pore. (C – black, N – blue, MOP units – blue and orange cuboctahedra)

A second type of pore within the individual **fcu** framework has a tetrahedral topology. As for the octahedral void space, the vertices of this pore are provided by MOP units (**Figure 2.31**). This pore is smaller than the previously described octahedral pore; its characteristic cross-sectional distance measured between a triangular face and the opposite-located window has a value of *ca.* 31 Å. Within the interpenetrated structure of **4**, tetrahedral pores of both frameworks overlap(**Figure 2.32 a**). This overlap due to the interpenetration restricts access to these pores as the windows to the pore of one framework are blocked by MOP units of the second framework. When considering the overall two-fold interpenetrated structure, the largest void space locates in located at the centre of the unit cell, as shown in **Figure 2.32**.

The pore is rendered by eight adjacent MOP units, as shown in **Figure 2.32 b & c**. The pore has an octahedral topology, with the triangular faces of the MOP units acting as the triangular faces of the octahedron. Due to the π-π stacking of the Azpy ligands, direct access to these inner voids is restricted, with access solely through MOP units. This indirect pathway may somewhat be hindered by the disorder of the inner octahedral assembly in the MOP units, possibly resulting in slow diffusion of adsorbed molecules into the central MOF pores.

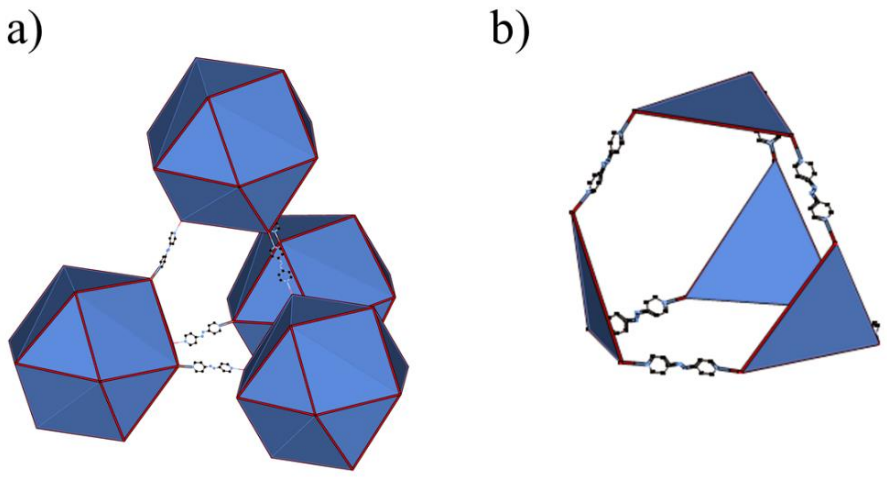

Figure 2.31: a) The tetrahedral pore within a single fcu framework and b) the pore with the MOPs removed for clarity.

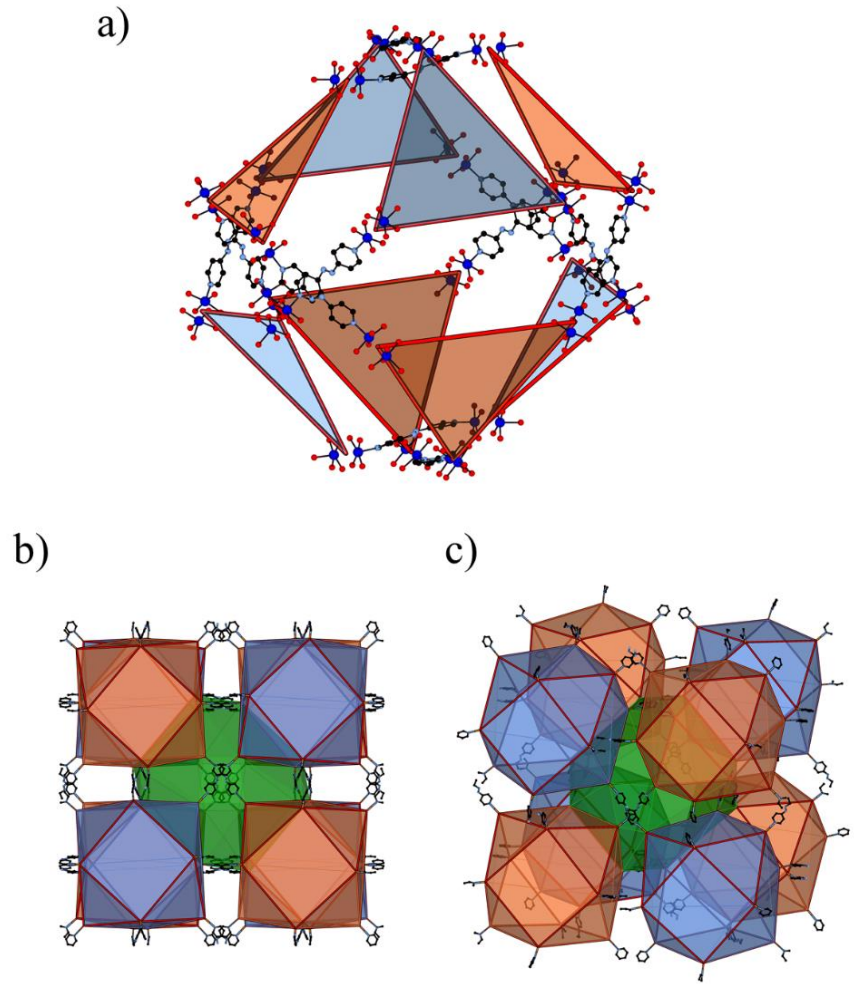

Figure 2.32: a) The octahedral pore formed between the two independent fcu frameworks. The triangular faces of the MOP units from one framework block the octahedral windows to the form from the second framework. b) & c) The octahedral pore (green) located between the eight adjacent MOP units of the two independent fcu frameworks highlighted. (C – black, N – blue, MOP units – blue and orange cuboctahedra, octahedral pore – green octahedron)

Further, a series of smaller pores are formed between the square faces of adjacent MOP units between the two frameworks. These pores are similar in shape to the pores observed in **3**, which also arise from the square faces of adjacent MOP units. The pores have a diameter of *ca.* 16.3 Å based on inter-atomic distances. This latter pore type is found to be the most numerous within the interpenetrated **fcu** MOF structure. Each MOP unit forms this type of pore between each of its six adjacent MOP units.

In summary, a single framework in **4** can be described as a cubic 'close' packed assemble of cuboctahedral MOP units. This packing gives rise to octahedral holes or interstices with similar dimensions to the MOPs that form the packing. The number of holes/interstices corresponds to the number of MOP units that make up the packing. The assembly gives further rise to smaller tetrahedral holes/interstices (approximately half the size of the octahedral holes). For every MOP unit, two tetrahedral voids exist in the structure. Upon 2-fold interpenetration, all available octahedral interstices become occupied by MOP units of the second framework. Hence the overall structure can be described as a cubic 'close' packing of MOPs in which MOPs of the second net occupy all resulting octahedral holes. Hence the structure of **4** topologically resembles a simple NaCl-type structure.

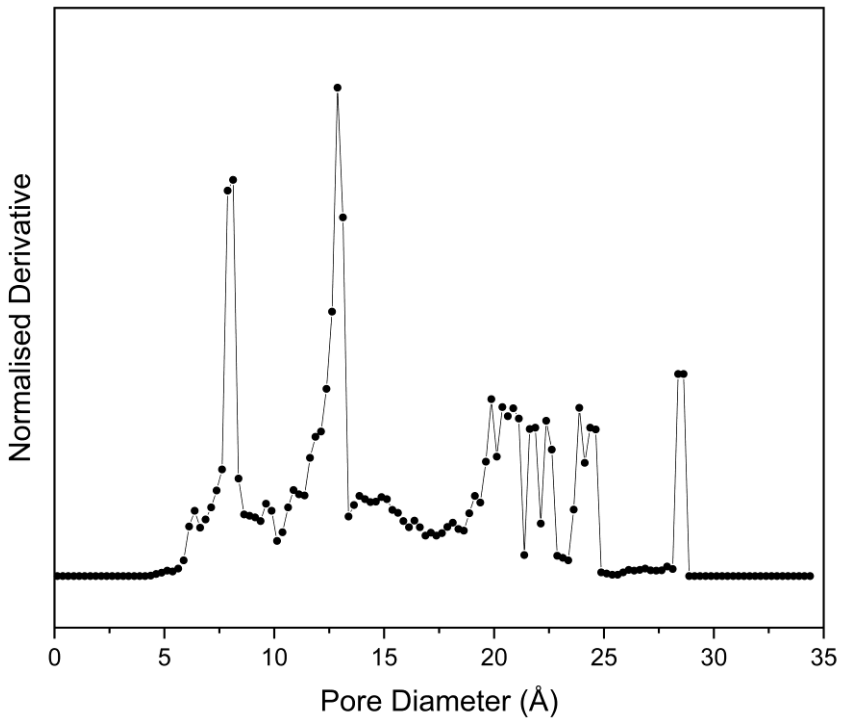

Figure 2.33: PSD simulation for 4.

To further examine the pore-size distribution in the MOF, computational studies using the Poreblazer computational package were carried out. The simulations reveal that the MOF has a theoretical He pore volume of *ca.* 1.97 cm^3/g and a potential surface area of *ca.* 4440 m^2/g. The pore-size distribution was calculated using the method developed by Gelb and Gubbins.[227] The limiting channel diameter was determined to be *ca.* 7.4 Å, and the maximum pore diameter was calculated to

be *ca.* 28.7 Å. These results strongly agree with the crystallographic analyses. The calculated pore-size distribution is shown in **Figure 2.33**. Considering this analysis, two distinct pores are found in the structure centred at 7.8 Å and 12.8 Å. The smaller pore is due to the void volume located at the centre of each MOP unit. The larger of these pores derives from the pore formed between adjacent MOP units. The largest pore diameter centred at 28.8 Å is associated with the void space in the centre of the unit cell, as shown in **Figure 2.32 b) & c)**.

2.5.6 Powder X-ray diffraction analysis

The phase purity of the synthesised bulk material was verified using PXRD analysis. The sample was prepared in the usual method involving grinding crystals of **4** in the mother liquor and loading the sample into a quartz capillary. The sample was then measured at 215 K using a Bruker APEX II DUO X-ray diffractometer. The PXRD pattern was found to have broad signals which are attributed to the weakly diffracting material and a significant background signal due to diffraction from the quartz capillary. Using the Expo2014 software package, the background signal and the fit of the experimental diffraction to the theoretical diffraction pattern were calculated.[228,229] Using the Rietveld[230] method, the weighted profile R-factor and the unweighted profile R-factor were calculated to be Rp = 1.105 and Rwp = 2.487 for the diffraction patterns. These values indicate a good agreement between the experimental diffraction pattern and the predicted pattern.

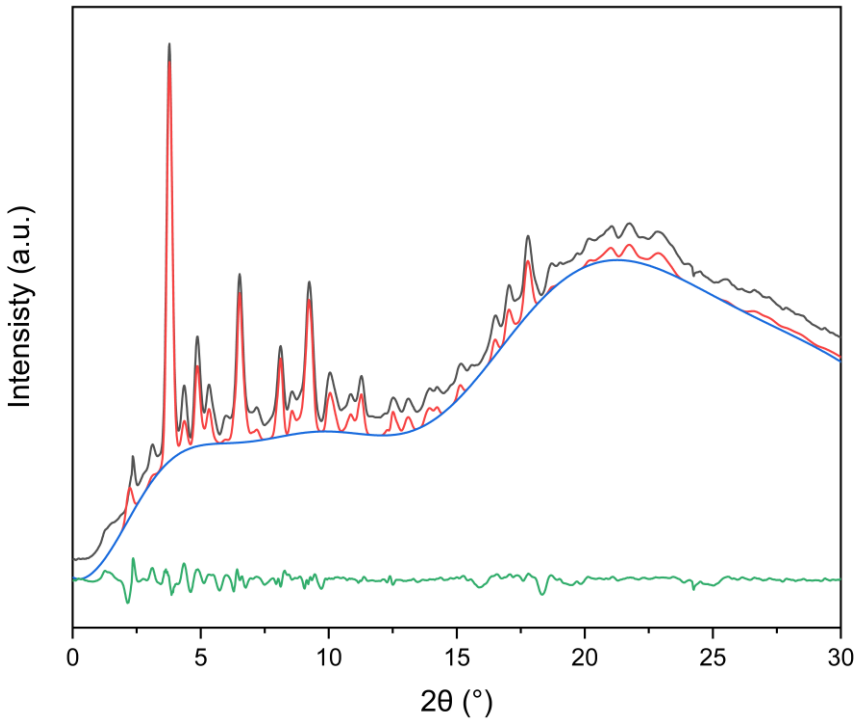

Figure 2.34: PXRD pattern of 4.

2.5.7 Thermogravimetric analysis

Thermogravimetric analysis was carried out to examine the thermal stability of **4**. The compound was heated under a nitrogen atmosphere at 4 ºC per minute from 20 ºC to 700 ºC. Upon heating, **4** experienced an initial weight loss of *ca.* 58.3 % between 20 ºC and 150 ºC. This initial loss is attributed to DMF and H_2O solvent molecules located within the porous framework and more strongly bound solvent molecules coordinated to the Cu^{2+} ions. Further weight loss of *ca.* 29 % occured between 200 ºC and 350 ºC. This weight loss is attributed to the decarboxylation reaction of the $BTEB_{mmm}NH_2^{3-}$ linkers and ligand degradation. The residual material was then found to be relatively stable at higher temperatures. A minor thermogravimetric step is centred at 476 ºC and is associated with a weight a loss of 4.6 %.

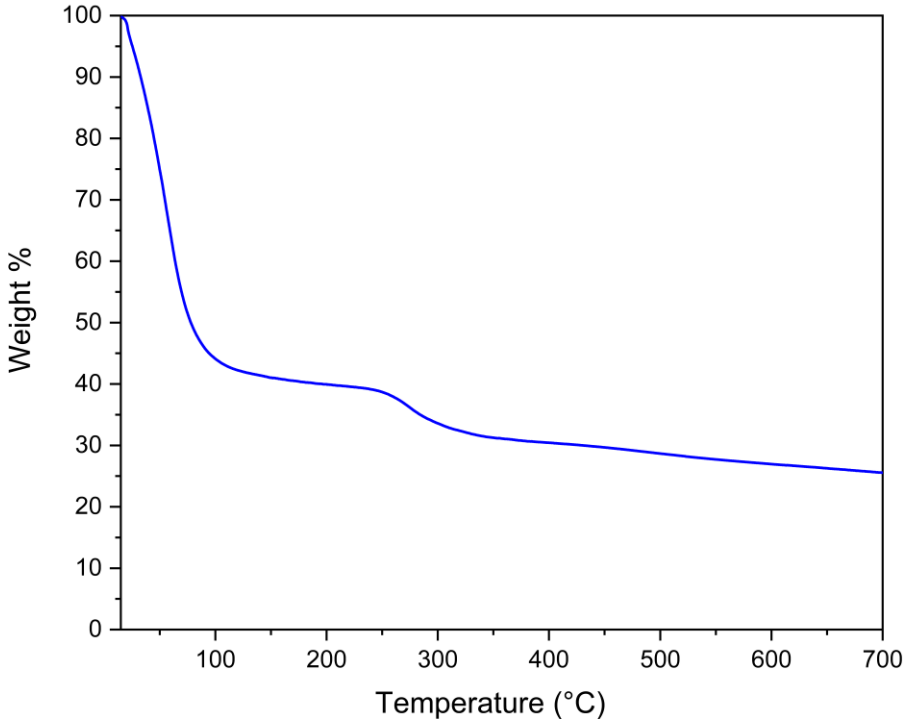

Figure 2.35: TGA of 4 heated at a rate of 4 ºC per minute under a nitrogen atmosphere.

2.5.8 FT-IR and Raman spectroscopy

In the FT-IR spectrum of **4** a broad band at 3454 cm^{-1} is attributed to the ν(N-H) stretching frequency of the amino- group on the $BTEB_{mmm}NH_2^{3-}$ linker (**Figure 2.36 a)**). A pair of bands located at 2933 cm^{-1} and 2878 cm^{-1} are attributed to the aldehyde ν(C-H) and methyl ν(C-H) stretching from DMF molecules within the porous structure. The DMF solvent molecules' characteristic aldehyde ν(C-H) and methyl ν(C-H) stretching frequencies give rise to signals at 2931 cm^{-1} and 2856 cm^{-1}.[231] The strong band associated with the DMF ν(C=O) mode is located at 1661 cm^{-1}. Bands found at 1625 cm^{-1} and 1445 cm^{-1} correspond to the asymmetric and symmetric ν(C=O) carboxylate stretches of

the organic ligand. The difference between these bands, Δ =180 cm^{-1}, indicates that the carboxylate groups adopt bidentate bridging mode.[233]

The Raman spectrum of **4** was measured from 100 cm^{-1} to 2500 cm^{-1}. The most prominent band in the spectrum occurs at 2235 cm^{-1}, corresponding to the symmetric ν_s(C≡C) stretch of the $BTEB_{mmm}NH_2^{3-}$ linkers. Two strong bands at 1611 cm^{-1} and 1583 cm^{-1} correspond to aromatic ν(C=C) stretches of the phenyl rings of the organic linkers. Bands at 1412 cm^{-1} and 1363 cm^{-1} are attributed to ν_s(C=O) bands of the carboxylate groups. In-plane δ(C-H) bending modes associated with the *meta*-benzoate moieties can be seen, while slightly lower wavenumbers of 1136 cm^{-1} and 1125 cm^{-1} correspond to the δ(C-H) bending modes associated with the *meta*-benzoate moieties. A strong band attributed to the central phenyl in-plane δ(C-H) bending vibrations occurs at 993 cm^{-1}.

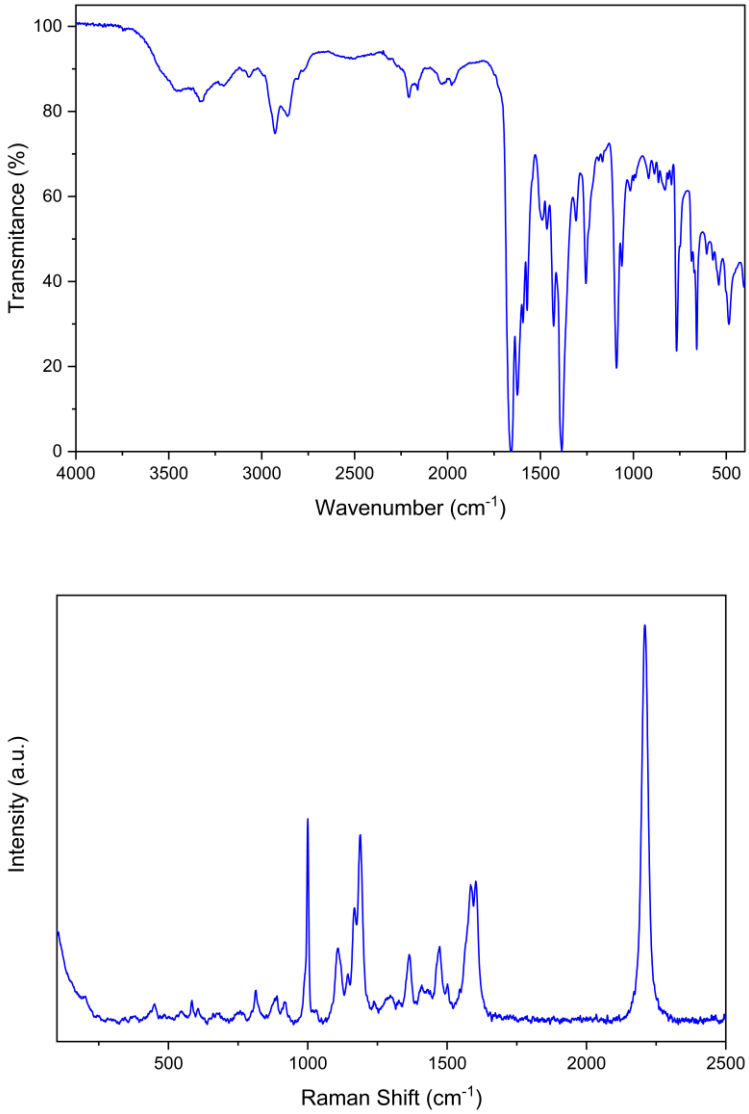

Figure 2.36: FT-IR and Raman spectra of 4.

2.5.9 Disassembly of pillared frameworks

Through the synthesis of **3** and **4** we successfully demonstrated the ability to assemble molecular species of **1** into higher dimensional frameworks. Following, we demonstrate the reversibility of the pillaring procedure resulting in the controlled disassembly of the MOFs. To the best of our knowledge, the ability to disassemble a MOF back to MOP units has been reported only once before in the literature.[247] In a previous report, the addition of pyridine as an N-coordinating solvent resulted in the disassembly of a MOF that was constructed from MOPs linked by 4,4'-bipyridine ligands.

Applying this same procedure to crystals of **4** was unsuccessful. The procedure was further modified using various concentrations of pyridine in a range of organic solvents (MeOH, EtOH, acetone, acetonitrile, DMF, DMA). Generally, upon the addition of crystals of **4** to the pyridine solutions, the crystals became opaque over the course of 6 hours. With additional time to react, the solution became clear and green in colour. No crystals or amorphous materials could be isolated from the solutions. Hence, it was impossible to verify the structural integrity of the MOPs upon dissolution in the presence of pyridine.

Based on these observations, we developed a new strategy to extract and isolate the MOPs from the pillared framework. Rather than adding competitive N-donor molecules to coordinate to the Cu^{2+} ions, additional metal ions were added to the reaction mixture to extract the connecting Azpy ligands. This technique may be regarded as the inverse to the literature procedure; in this instance, additional metal ions would initiate the disassembly and provide coordination sites for the organic ligands. It was anticipated that the Azpy ligands could preferentially coordinate to the additional metal ions in the solution. This procedure for this reaction to be carried out is similar to a known metal doping technique in MOF using second metal ions.[248,249,250,251,252] The secondary metal ion in the reaction solution exchanges with the ions used to construct the MOF, thus altering its properties. For this exchange to occur, crystals of the MOF are dispersed for extended periods in a concentrated solution containing the metal ion. Over time, an exchange between the ions in the framework and ions in the solution occurs. In this work, the metal exchange in **4** was regarded as a possible side reaction.

A series of Cu^{2+}, Co^{2+} and Zn^{2+} ions were chosen as reagents due to their similar biding strengths to N-donor ligands but varying prefered coordination geometries.[253,254] The nitrate salts of the metal ions were used as the NO_3^- anions are weakly coordinating ions. MOPs **1** and **2** are known to be stable in the presence of NO_3^- anions considering that $Cu(NO_3)_2{\cdot}3H_2O$ is used in the synthesis of the MOPs.

Of these three examined metal salts, only Co^{2+} could disassemble the MOF resulting in the crystallisation of MOP units to form **1**. The Co^{2+} ions have a tendency to adopt octahedral coordination environments and are less likely to form dinuclear paddlewheel assemblies.This is expected to reduce the tendency for ion exchange between the MOF and the Co^{2+} solution to occur.

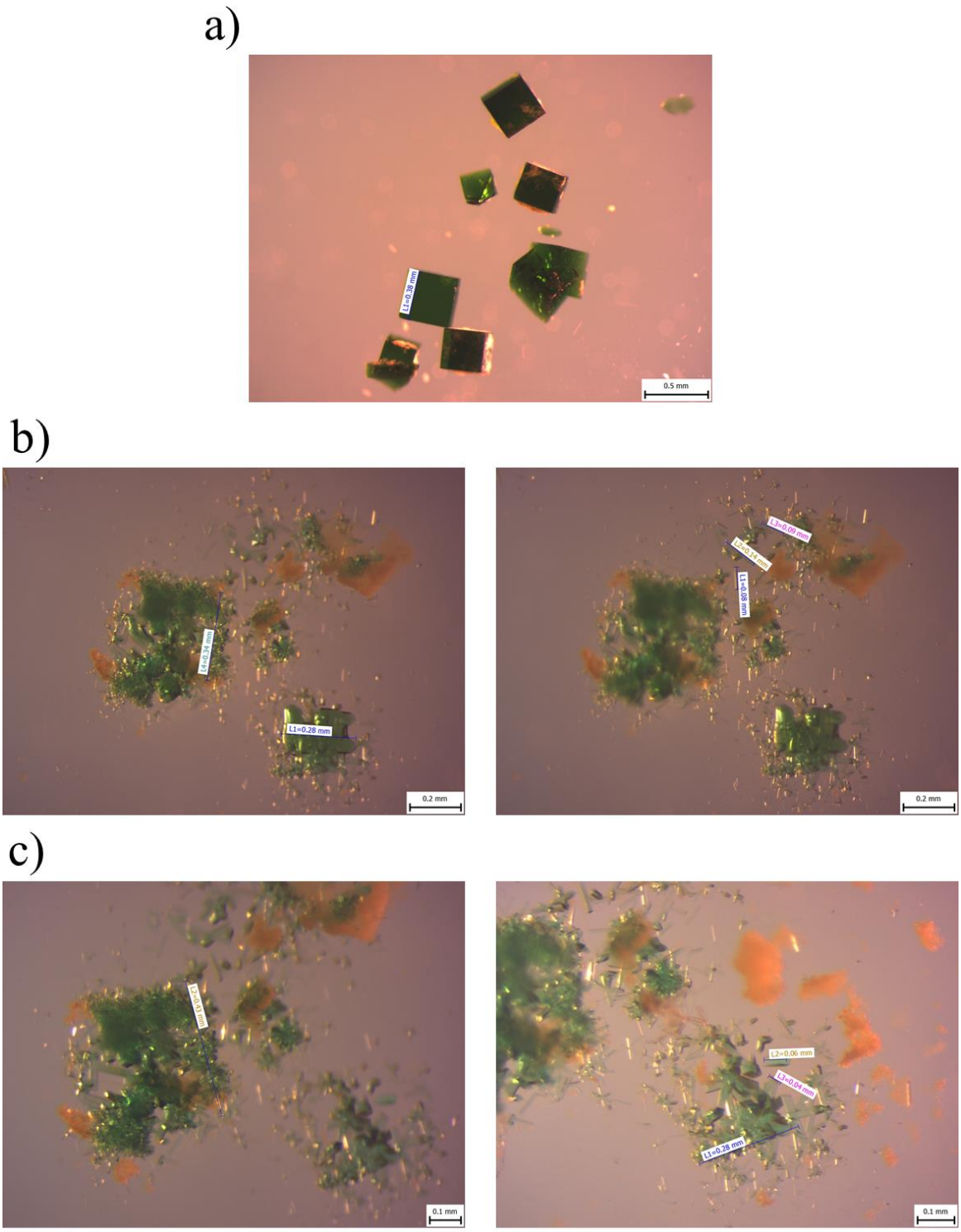

Figure 2.37: Crystals of 4 were placed into a dilute solution of $Co(NO_3)_2 \cdot 6H_2O$. The degradation of the crystals was monitored, and pictures were taken at a) 0 h, b) 24 h, and c) 48 h. At 0 h the crystals had clearly defined edges. After 24 h had elapsed, the breakdown of the crystal had begun, with the total breakdown occurring after 48 h.

The disassembly was carried out by dispersing freshly synthesised crystals of **4** in 1 ml of a 10 mM solution of $Co(NO_3)_2 \cdot 6H_2O$ in DMF. The crystals were then left to stand at room temperature and were monitored periodically (**Figure 2.37 a**). After 24 hours, cubic crystals were found to begin to

disassemble, forming new small green crystals (**Figure 2.37 b**). After 48 hours, the cubic crystals were found to be fully disassembled, and the new green, rod-shaped crystals were produced. The new crystals grew from within the cubic crystals and in close proximity to the cubic crystal. The spatial proximity of the crystallisation can be attributed to the low solubility of the MOP in DMF. The MOPs rate of dissolution is limited by diffusion, which leads to a high concentration gradient that facilitates the crystallisation of the MOP units at a solid-liquid boundary.

PXRD analysis of the newly formed crystals was carried out to facilitate the identification of the compound. As with the previous PXRD samples, the crystals were loaded into a quartz capillary to avoid any solvent loss. No griding of the crystals was required as the submillimetre size of the crystals was sufficient for the measurement. The PXRD patterns of the crystals were then compared to the measured PXRD patterns for **4** and **1** (**Figure 2.38**). From **Figure 2.38**, it is evident that the newly measured pattern matches the PXRD pattern of **1**. Using the Rietveld method, the theoretical diffraction pattern of **1** was fitted to the measured PXRD pattern of the new, resulting in R-factors of Rp = 0.775 and Rwp = 1.733. for the data, confirming the formation of **1** upon disassembly of **4**.

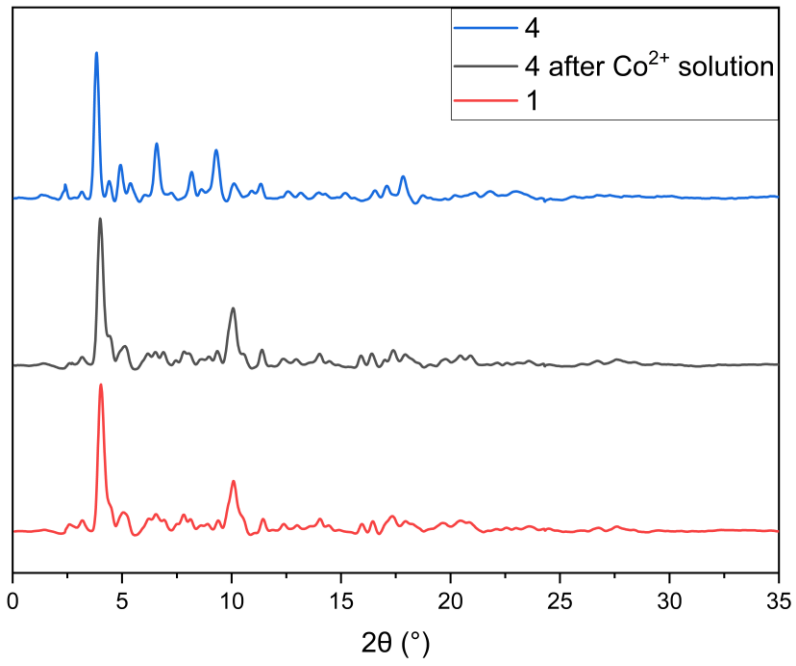

Figure 2.38: PXRD pattern of the crystalline material after dispersing crystals of 4 in a Co^{2+} solution. (PXRD of 4 – blue, PXRD of material after cobalt solution - black, PXRD pattern for 1 – red)

EDX analysis of the crystals was carried out to determine the degree of ion exchange between the Co^{2+} and Cu^{2+} ions. The sample was initially prepared by dispersing the cubic crystals of **4** in a 10 mM DMF solution of $Co(NO_3)_2 \cdot 6H_2O$. After 48 hours, the solvent was exchanged for fresh DMF. This was then repeated every 24 hours for three days. This ensures that all of the metal ions dissolved in the DMF solution were removed from the crystal's pores. The sample was then dried under a high vacuum for 24 hours to remove the DMF solvent. The EDX measurement was then performed, and

Cu:Co atomic ratio of approximately 50:1 was determined. This minimal quantity of Co^{2+} ions detected within the crystals confirms that the metal ion exchange is extremely slow and unfavourable.

The use of Cu^{2+} and Zn^{2+} ions were found to have a negative effect on the stability of the MOF. Under identical experimental conditions, Cu^{2+} ions led to rapid decomposition of the crystals within 24 h leading to clear solutions. Two possible mechanisms may contribute to the decomposition of the crystals. One mechanism is that the MOP units were liberated from the MOF framework and dissolved within the solution. However, this is unlikely to be the predominant process due to the low solubility of the charge-neutral MOP units in the DMF solution. However, no solid material was observed in the reaction vial. This gives credence to the decomposition of the MOP units alongside the deconstruction of the MOF. This process may lead to the presence of $BTEB_{mmm}NH_2^{3-}$ linkers that coordinate too the excess Cu^{2+} ions in solution, causing the formation of soluble structures.

Repeating the experiment with $Zn(NO_3)_2{\cdot}6H_2O$ also leads to the decomposition of **4**. After the dispersion of the crystals in a Zn^{2+}/DMFsolution for 12 h, yellow spherical particles were found in the reaction vial (**Figure 2.39**). The substance was analysed using FT-IR spectroscopy to verify that it contained the $BTEB_{mmm}NH_2^{3-}$ linker. PXRD analysis confirmed the amorphous nature of the material. Hence the material may likely be an amorphous coordination polymer.

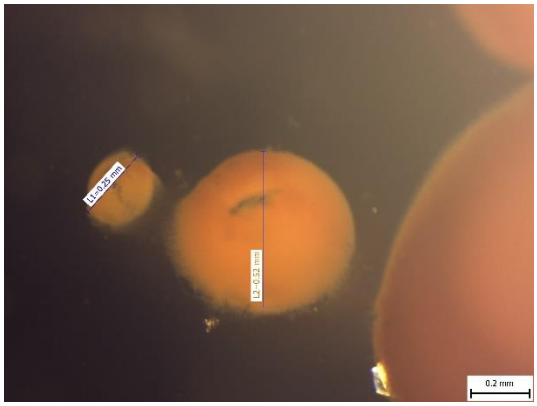

Figure 2.39: The use of Zn^{2+} ions leads to the decomposition of 4 and the formation of a yellow amorphous coordination polymer.

Table 2.5: Crystalographic parameters for 3 and 4.

Identification code	3	4
Empirical formula	$Cu_{36}C_{820}H_{496}N_{40}O_{180}$	$Cu_{36}C_{852}H_{480}N_{48}O_{168}$
Formula weight	16076.51	16364.25
Temperature / K	215(2)	215(2)
Crystal system	Triclinic	Cubic
Space group	*P-1*	*Ia-3*
***a* / Å**	37.766(11)	81.374(8)
***b* / Å**	40.142(11)	81.374(8)
***c* / Å**	43.466(12)	81.374(8)
***α* / º**	113.887(2)	90
***β* /º**	112.634(3)	90
***γ* / º**	95.437(3)	90
Volume / Å^3	53101(26)	538840(159)
Z	38	8
ρ_{calc}/ g/cm^3	1.317	0.403
μ / mm^{-1}	1.298	0.495
F(000)	21204.0	66528.0
Crystal size / mm^3	? × ? × ?	? × ? × ?
Radiation	1.54178 Å	1.54178 Å
θ range for data collection / º	29.604 to 91.556	2.66 to 94.804
Index ranges	-34 <= h <= 34 -37 <= k <= 37 -40 <= l <= 39	-33 <= h <= 77 66 <= k <= 76 -77 <= l <= 64
Reflections collected	159932	514100
Independent reflections	79183 [R(int) = 0.1715]	40780 [R(int) = 0.1779]
Data/restraints/parameters	79183 / 2486 / 4114	40708 / 1130 / 1503
Goodness-of-fit on F^2	0.867	1.785
Final R indexes [I>=2σ (I)]	R1 = 0.1088, wR2 = 0.2597	R1 = 0.2431, wR2 = 0.5134
Final R indexes [all data]	R1 = 0.2067, wR2 = 0.3314	R1 = 0.3420, wR2 = 0.5622
Largest diff. peak/hole / e.Å^{-3}	0.48 and -0.45	3.04 and -0.67

2.6 Pillaring of **2**

After the preparation of **3** and **4**, the focus shifted to synthesising a pillared structure containing the MOP of **2** as SBU. Initial attempts to synthesise pillared structures using the conditions that led to **3** and **4,** were ineffective. The presence of the Azpy ligand was found to disrupt the formation of **2** during the reaction, with the sole product being a copious amount of amorphous material. In order to circumvent the inhibition of the synthesis of **2**, the MOP was synthesised prior to the pillaring reaction.

To aid in the dissolution of the crystals and increase the solubility of the MOPs, EtOH was removed from the solvent mixture. The presence of EtOH in the reaction solution led to a dramatic reduction in the solubility of the MOP. To further increase the solubility of the MOP, the ligand 4-(3-phenylpropyl)pyridine (PPP) was used as an auxiliary reagent. The pyridyl compound was chosen due to its previously reported ability to coordinate to the {Cu_2} SBUs, increasing the solubility of the MOP in solution.[255,39] The ligand is known to bind to MOPs through the pyridyl ring, which coordinates to the labile coordination sites of the {Cu_2} SBUs. The presence of aliphatic chains on a MOP has previously been reported to increase the solubility of MOPs in organic solutions. [240,255, 256]

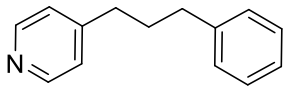

Figure 2.40: 4-(3-Phenylpropyl)pyridine (PPP) ligand used to help dissolve 2 in the DMF solution

2.6.1 Synthesis of [Cu_6($BTEB_{mmm}NH_2$)$_4$($PPP)_2$(Azpy)($H_2O)_2$] (**5**)

Crystals of **2** were first synthesised using the procedure discussed in **Section 2.3.2.** The crystals were isolated and washed with DMF three times to remove unreacted ligand and metal salts. Azpy and PPP were then added to the reaction vial containing the crystals of **2** in DMF. The reaction vial was gently agitated to help break up the crystals of **2**. Following the reaction mixture was heated to 85 ºC for 48 h. After the elapsed time, a mixture of two crystalline materials was found on the bottom of the reaction vial. One crystal type was determined to be unreacted **2**. Distinctively different, larger green plate-like crystals grew in clusters. The latter were manually separated and found suitable for analysis by single-crystal X-ray diffraction. The crystals were measured and solved in the triclinic space group $P\bar{1}$. The unit cell dimensions were determined to be a = 15.978(5) Å, b = 17.394(5) Å, c = 28.081(8)Å, α = 93.28(2)º, β = 92.84(2)º γ = 101.54(2)º.

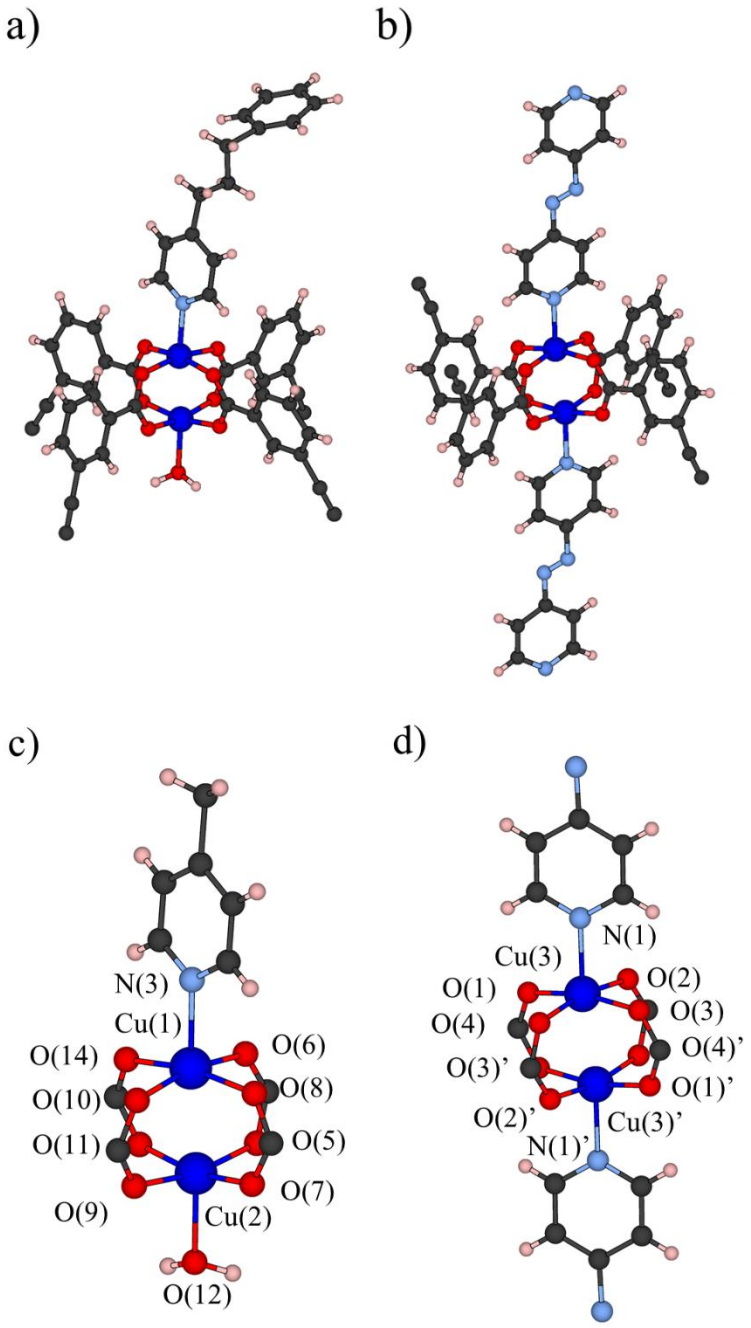

Figure 2.41: The two structurally distinct {Cu_2} SBUs found in 5 a) {Cu_2} coordinated by a PPP and H_2O molecule and b) {Cu_2} coordinated by two Azpy ligands at the apical positions. The labels for the coordinating N and O-donor atoms are shown in c) and d). (C - black, O - red, H - pink, N – light blue, Cu – dark blue)

5 was found to have the chemical formula $[Cu_6(BTEB_{mmm}NH_2)_4(PPP)_2(Azpy)(H_2O)_2]$ and has the structure of a series of pillared two-dimensional sheets. Each sheet contains two non-structurally equivalent {Cu_2} paddlewheel SBUs (**Figure 2.41**). Each Cu^{2+} ion is coordinated by O-donor atoms from four fully deprotonated $BTEB_{mmm}NH_2^{3-}$ linkers. These O-donor atoms create the base of the square base pyramidal coordination environment around each Cu^{2+} ion. The $BTEB_{mmm}NH_2^{3-}$ linkers coordinate to the Cu^{2+} ions in a *syn,syn*-bidentate (μ_2-η^1:η^1) bridging mode. The occupancy of the

apical position of the Cu^{2+} ion differs across the three crystallographically distinct Cu^{2+} ions. In one $\{Cu_2\}$ SBU, which contains Cu(1) and Cu(2), Cu(1) is coordinated by an N-donor atom that originates from a PPP ligand located at the apical position. Cu(2) is coordinated by the O-donor atom of an H_2O molecule (**Figure 2.41 a)**). The second $\{Cu_2\}$ SBU, which is comprised of Cu(3) and its symmetry equivalent Cu(3)'; here the apical positions on the two Cu^{2+} ions are coordinated by N-donor atom from bridging Azpy ligands (**Figure 2.41 b)**).

Table 2.6: selected bond lengths and angles found in 5.

Atoms	Distance	Atoms	Angle
Cu1-O6	1.987(8) Å	O6-Cu1-O8	89.5(4) º
Cu1-O8	1.961(10) Å	O6-Cu1-O14	89.7(4) º
Cu1-O10	1.969(11) Å	O10-Cu1-O14	88.6(4) º
Cu1-O14	1.974(12) Å	O6Cu1-N3	92.5(5) º
Cu1-N3	2.159(11) Å	O5-Cu2-O7	89.3(5) º
Cu2-O5	1.968(13) Å	O5-Cu2-O11	88.44) º
Cu2-O7	1.944(12) Å	O7-Cu2-O9	90.2(4) º
Cu2-O9	1.953(10) Å	O5-Cu2-O12	100.1(5) º
Cu2-O11	1.972(14) Å	O5-Cu2-O7	90.1(5) º
Cu2-O12	2.176(14) Å	O1-Cu3-O2	89.8(5) º
Cu3-O1	1.954(3) Å	O1-Cu3-O4	89.4(5) º
Cu3-O2	1.952(3) Å	O2-Cu3-O3	88.08(4) º
Cu3-O3	1.958(3) Å	O1-Cu2-ON1	98.1(4) º
Cu3-O4	1.950(3) Å		
Cu3-N5	2.168(4) Å		

The $BTEB_{mmm}NH_2^{3-}$ linker is found in two conformations within the structure of the MOF. The two conformations, while crystallographically distinct, may be regarded as topologically equivalent, whereby small variations of approximately 5º are observed for the dihedral angles between the *meta*-benzoate moieties and central phenyl rings (**Table 2.7**). In both conformations of the $BTEB_{mmm}NH_2^{3-}$ linker, the two *meta*-benzoate moieties are approximately co-planar, while the third *meta*-benzoate moiety adopts a larger dihedral angle with respect to the central phenyl ring. The two *meta*-benzoate moieties that are approximately co-planar coordinate to two $\{Cu_2\}$ SBUs in a *syn,syn*-arrangement. Four $BTEB_{mmm}NH_2^{3-}$ linkers link two $\{Cu_2\}$ SBUs generating a "super-paddlewheel" unit (**Figure 2.42**).

Table 2.7: Dihedral angle between the *meta*-benzoate moieties and central phenyl ring in 5.

Conformation	Dihedral angle between *meta*-benzoate (1) and central phenyl ring	Dihedral angle between *meta*-benzoate (2) and central phenyl ring	Dihedral angle between *meta*-benzoate (3) and central phenyl ring
i	24.9(2)º	27.2(3)º	35.2(2)º
ii	21.0(2)º	21.1(2)º	40.5(3)º

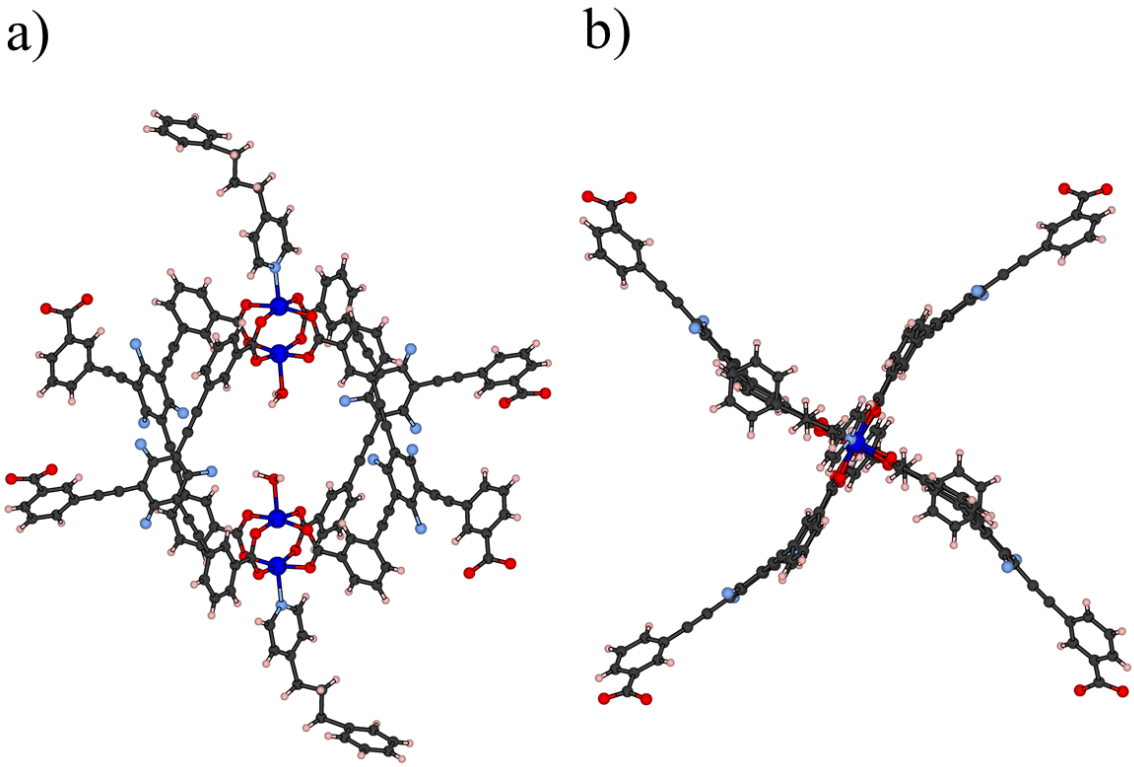

Figure 2.42: Structure of super-paddlewheel unit, which contains four $BTEB_{mmm}NH_2^{3-}$ linkers bridging two {Cu_2} SBUs, in 5. Two PPP ligands coordinate to the apical position on the two outer Cu^{2+} ions while two H_2O ligands coordinate to the two interior Cu^{2+} ions. (C – black, O – red, H – pink, N – blue, Cu – dark blue)

PPP ligands coordinate to the apical position on the two exterior Cu^{2+} ions that make up the super-paddlewheel (**Figure 2.42 a)**). Two H_2O solvent molecules coordinate to the apical positions of the two inner Cu^{2+} ions of the unit. The super-paddlewheel unit is distorted compared to the super-paddlewheel unit found in **1**. Rather than being planar like in **1**, two coordinating *meta*-benzoate moieties in **5** are bent *ca*. 26º with respect to the super-paddlewheel unit. This imparts a twist to the overall super-paddlewheel unit (**Figure 2.42 b)**).

These third *meta*-benzoate moieties have dihedral angles of *ca.* 35º or *ca.* 40º with respect to the central phenyl ring (**Figure 2.42 b)**). In the super-paddlewheel unit, the four *meta*-benzoate moieties are found in a *syn,syn,anti,anti*-arrangement. This arrangement of the moieties allows for the super-paddlewheel unit to connect to other super-paddlewheel units in a planar fashion as required to form the two-dimensional sheets. This is in direct comparison to the super-paddlewheel units in **1**, where the remaining *meta*-benzoate moieties are in a *syn,syn,syn,syn*-arrangement. The latter arrangement gives the unit the required concave shape needed to form the MOP. The relatively large dihedral angles between the four *meta*-benzoate moieties and the central phenyl allow the linker to compensate for the structural limitations imposed by the *meta* position of the carboxylate group.

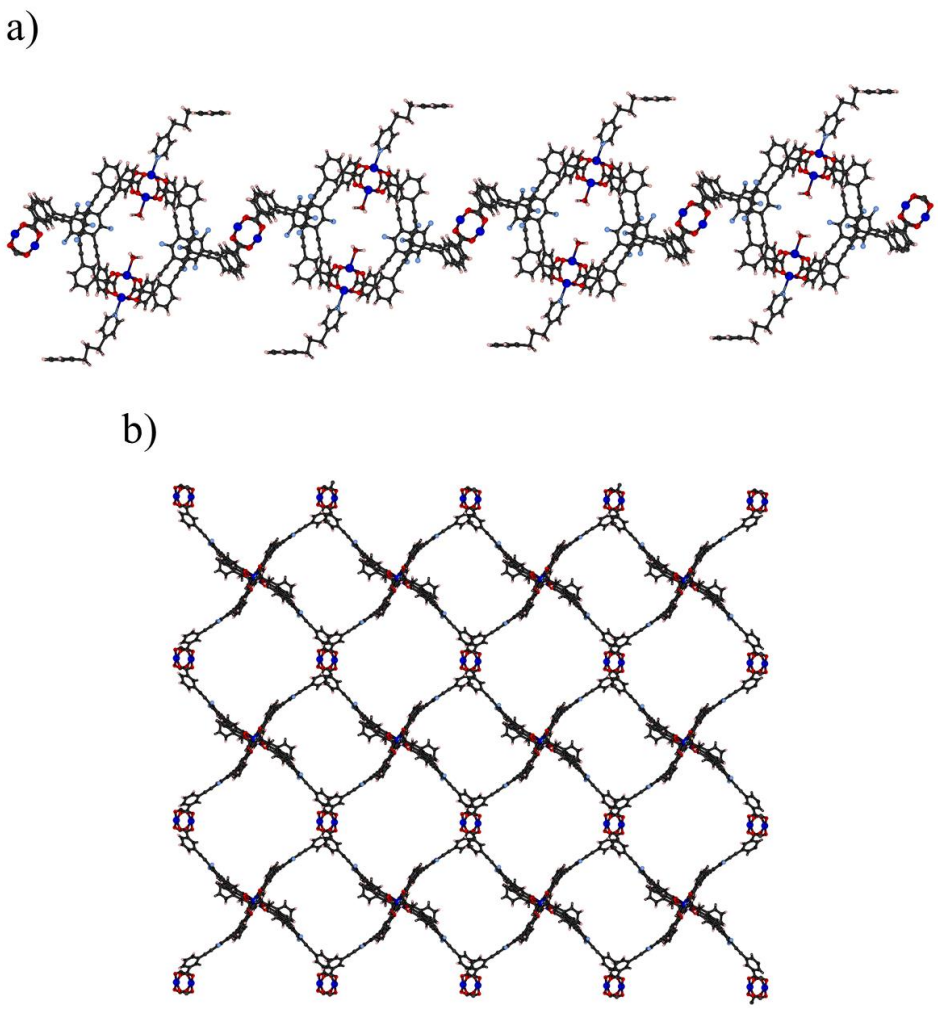

Figure 2.43: The structure of an individual two-dimensional sheet For clarity, the Azpy ligands which coordinate to the second {Cu_2} SBUs have been omitted. (C – black, O – red, H – pink, N – blue, Cu – dark blue)

The super-paddlewheel units connect through the second {Cu_2} SBUs to generate two-dimensional sheets (**Figure 2.43**). The {Cu_2} SBUs and super-paddlewheels connect in an alternating checkerboard-like pattern to form the sheets. Due to the structural restraints imposed by the *meta*-benzoate moieties, the {Cu_2} and super-paddlewheel units are tilted with respect to the mean plane

of the sheet (**Figure 2.43 a)**). The super-paddlewheel units are tilted at an angle of *ca.* 70 º, and the {Cu_2} SBUs are titled at an angle of *ca.* 35º. A series of distorted square pores are generated within the sheets with the {Cu_2} and super-paddlewheel units located at the vertices of the pores (**Figure 2.43 b)**). Due to the tilt of the super-paddlewheel units, the pores are found to have two different diameters. The smaller pore has a diameter of *ca.* 13 Å, and the larger pore has a diameter of *ca.* 17 Å.

Azpy ligands coordinate to the apical positions of the two Cu^{2+} ions in the {Cu_2} SBUs, acting as the connections between the sheets. The sheets are pillared along the crystallographic *a*-axis. The Azpy ligands and {Cu_2} SBUs form a series of chains that extend into the structure along the crystallographic *a*-axis; this can be seen in **Figure 2.44**.

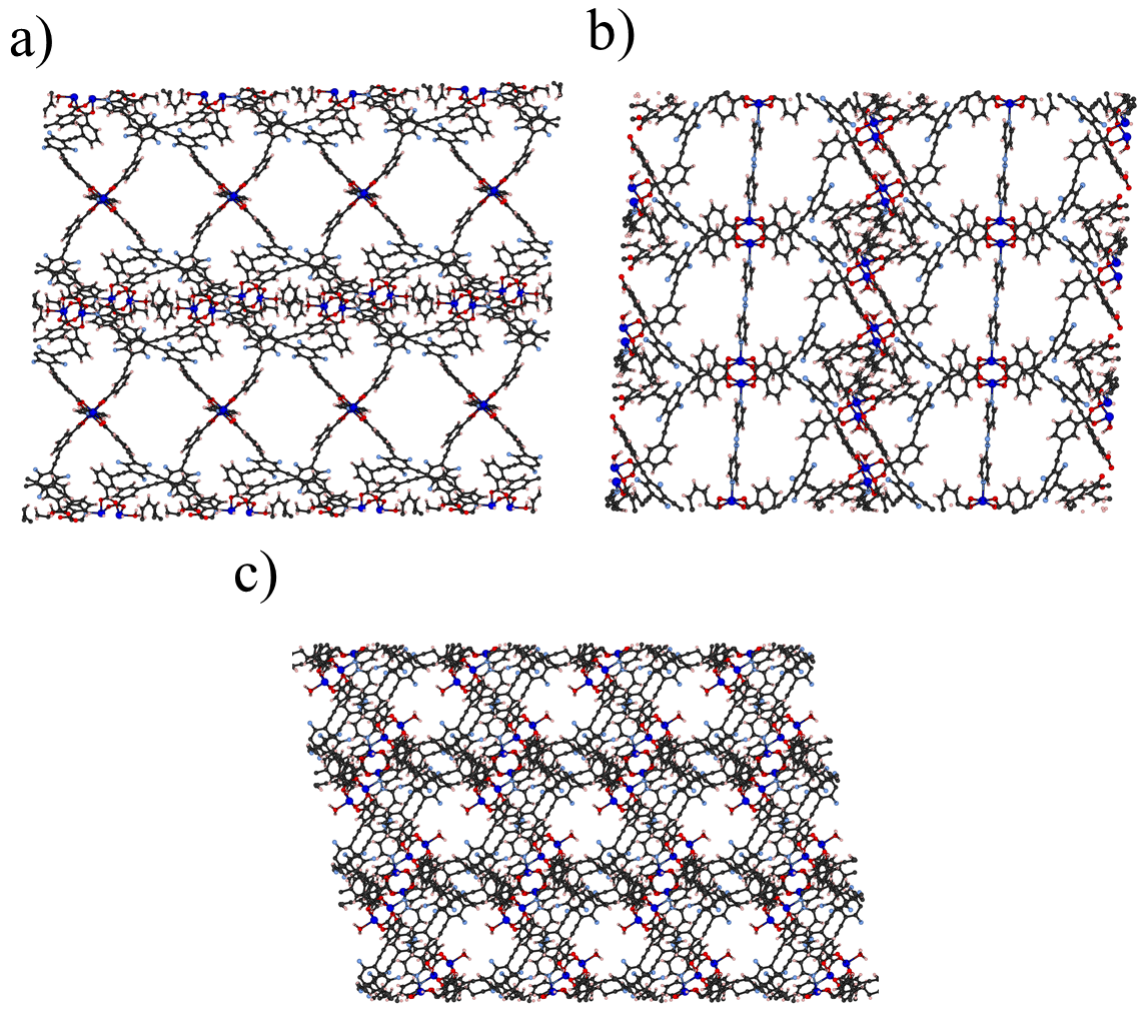

Figure 2.44: The extended structure of 5 viewed along the crystalographic a) *a*-axis, b) *b*-axis, and c) *c*-axis. (C – black, O – red, H – pink, N – blue, Cu – dark blue)

In the pillared structure of the MOF, a series of pores are generated between the sheets. Larger channels can be seen to extend into the structure along the crystallographic *a*-axis. The channel has an approximate diameter of *ca.* 11.6 Å. The second set of channels, with a diameter of *ca.* 4.8 Å

extend into the structure along the crystallographic *b*-axis. The final pore that can be seen within the structure is a pore located at the centre of the super-paddlewheel unit. These pores are found to align along the crystallographic *c*-axis generating a channel which, when the coordinated solvent molecules are removed from the structure, has a diameter of *ca.* 6.0 Å.

Using the Poreblazer computational package, the material's potential surface area and pore-size distribution were analysed. The desolvated structure was calculated to have a He pore volume of *ca.* 0.946 cm^3/g. The theoretically accessible surface area was determined to be *ca*. 2070 m^2/g. The limited pore diameter was calculated to be *ca* 4.6 Å. The maximum pore diameter was calculated to be *ca*. 10.2 Å. These results correspond to the channels that extend into the structure along the crystallographic *a*-axis. The simulated pore-size distribution is shown in **Figure 2.45**.

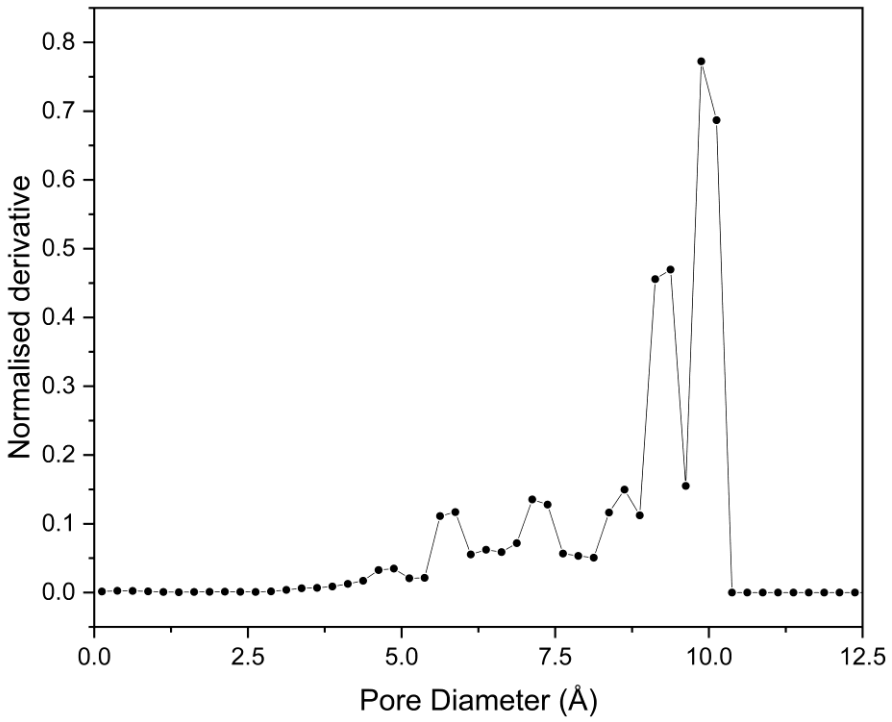

Figure 2.45: Simulated pore-size distribution of 5.

2.6.2 Topology

Using the computational package, ToposPro, a topological analysis of **5** was carried out.[257] The net topology for **5** was determined to be a trinodal, (3,4,6)-connected net. The overall point symbol was ascertained and found to be $\{4.8^2\}_4\{4^6\}_2\{8^4.10^8.12^3\}$. In the topological reduction of the framework, the 3-connected node corresponds to the $BTEB_{mmm}NH_2^{3-}$ linker. The two remaining 4-connected nodes correspond to the two $\{Cu_2\}$ SBUs found in the super-paddlewheel unit. The remaining 6-connected node corresponds to the $\{Cu_2\}$ SBUs, which are coordinated by the $BTEB_{mmm}NH_2^{3-}$ and Azpy ligands.

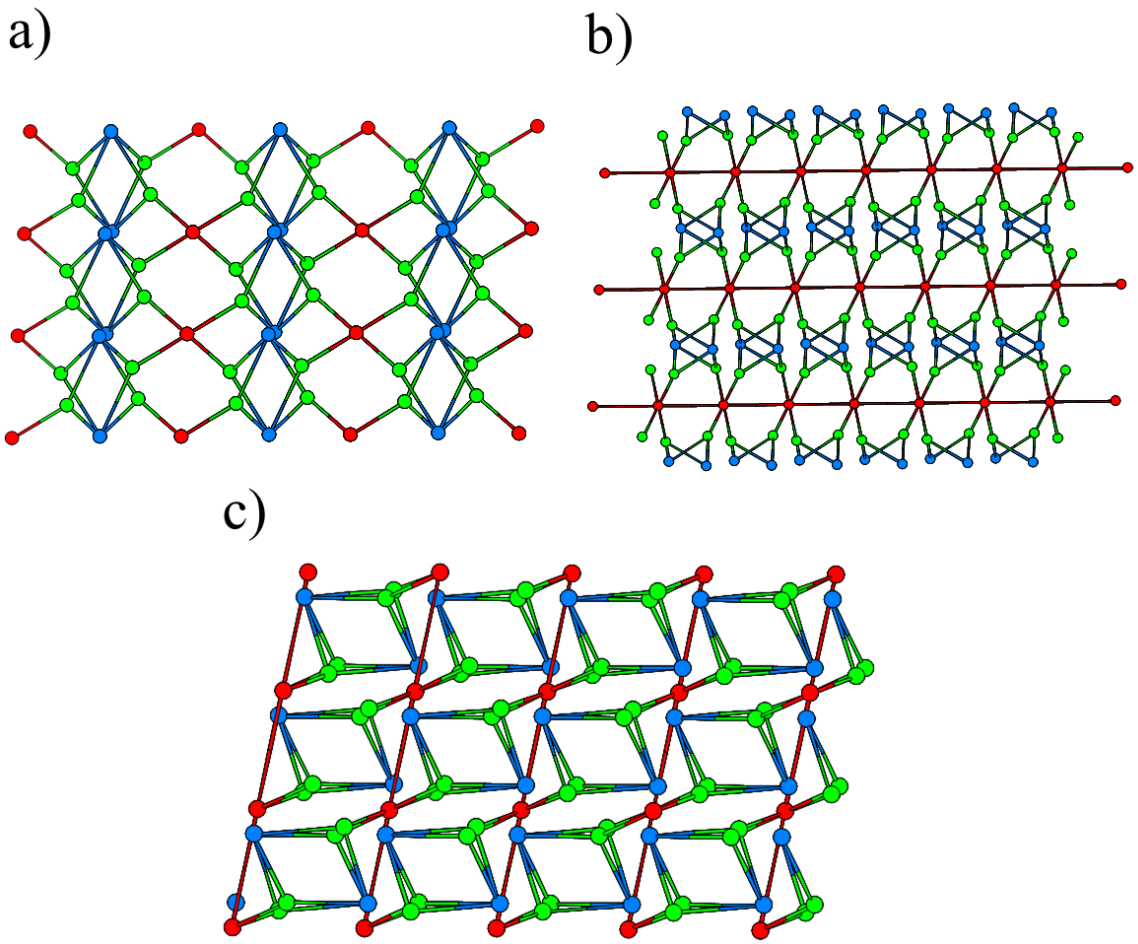

Figure 2.46: Topological reduction of 5 viewed along the crystalographic a) *a*-axis, b) *b*-axis, and c) *c*-axis. (3-connected nodes – green, 4-connected nodes – blue, 6-connected nodes – red)

2.6.3 Powder X-ray diffraction

PXRD analysis was performed to determine the phase purity of the isolated crystals. The crystalline product was manually separated from the undissolved reagent **2** and an amorphous side product. The sample was prepared in the previously described manner and loaded into a quartz capillary to avoid any loss of crystallinity. The sample was measured at 215 K, using a Bruker APEX II DUO X-ray diffractometer. The Expo2014 computational package was used to account for the background signal and to fit the experimental diffraction pattern to the theoretical, calculated diffraction pattern.[228,229] The large background signal in the measurement is attributed to the weak diffraction of the crystals. Using the Rietveld method, the unweighted profile R-factor and the weighted profile R-factor were calculated for the diffraction pattern.[230] The two factors were determined to be Rp = 1.256 and Rwp = 2.230, respectively. This indicates a good agreement between the experimental diffraction pattern and the calculated, expected diffraction pattern (**Figure 2.47**).

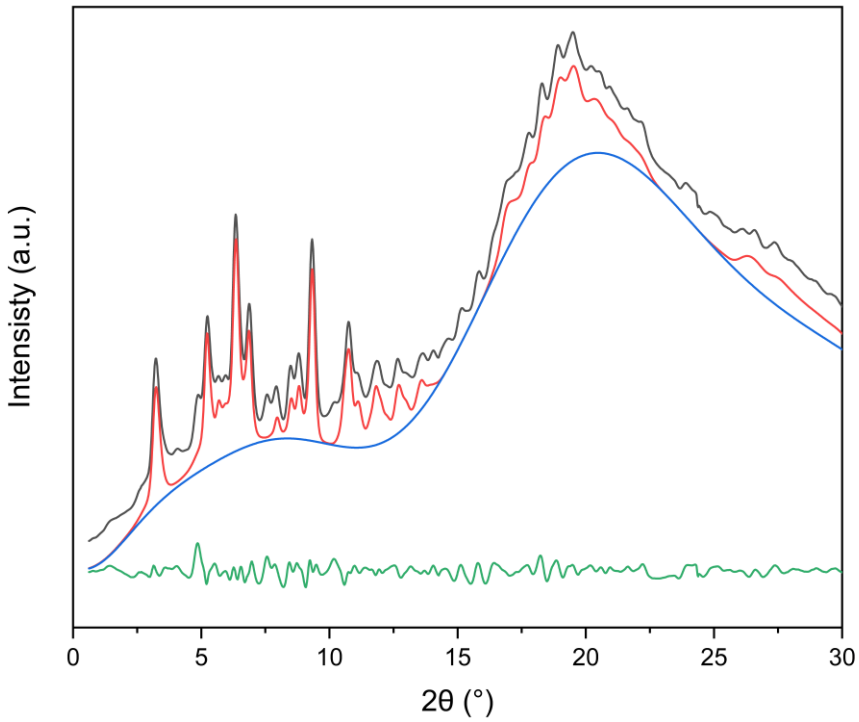

Figure 2.47: PXRD of 5. ((Measured diffraction pattern – black, the calculated background signal – blue, predicted diffraction pattern – red, the difference between measured and predicted – green.)

2.6.4 Thermogravimetric analysis

The thermal stability of the material was determined using thermogravimetric analysis. Crystals of **5** were removed from the mother liquor and gently dried with filter paper to remove any surface solvent residues. The crystals were then heated at 4 ºC per minute under a nitrogen atmosphere. An initial mass loss, *ca.* 56.3 wt.%, was found to occur between 20 ºC and 143 ºC. This solvent loss is due to the removal of solvent molecules from within the porous framework of the MOF. The material was to remain thermally stable up to *ca*. 240 ºC. At the second thermogravimetric step, between 240 ºC and 332 ºC, resulted in a weight loss of *ca.* 9.2 wt%. This is due to the initial thermal degradation of the $BTEB_{mmm}$-NH_2^{3-} linkers. From 372 ºC to 700 ºC, a further 18.2 % weight loss occurs, most likely due to the loss of N-donor ligands from the structure (**Figure 2.48**).

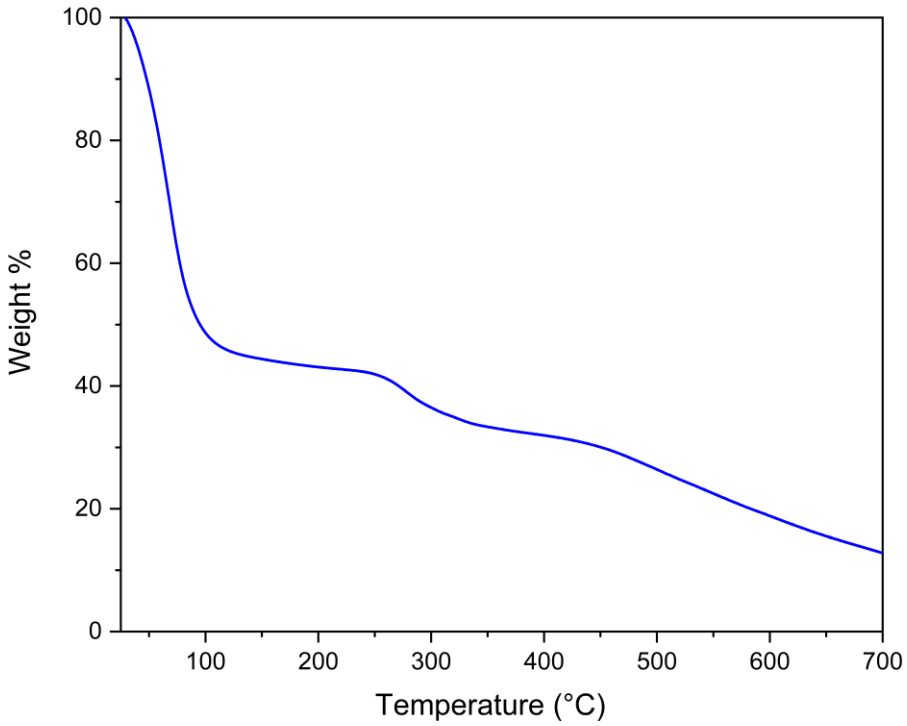

Figure 2.48: TGA of 5 measured at a rate of 4 ºC per minute under a nitrogen atmosphere.

2.6.5 FT-IR and Raman spectroscopy

The FT-IR and Raman spectra of the compound were found to be similar in nature to two corresponding spectra of **3** and **4**. A broad band centred at 3466 cm^{-1} is associated with ν(N-H) stretching frequencies of the central amino group on the $BTEB_{mmm}NH_2^{3-}$ linkers. A weaker band at 3074 cm^{-1} is associated with the aromatic ν(C-H) stretching vibrations involving sp^2 hybridised carbon atoms. The DMF solvent molecules' characteristic aldehyde ν(C-H) and methyl ν(C-H) stretching frequencies give rise to signals at 2931 cm^{-1} and 2856 cm^{-1}.[231] At 1660 $cm^{-1,}$ a strong band arises form to the ν(C=O) vibrational modes of coordinating DMF molecules and DMF solvent molecules located within the porous structure of the MOF. Bands found at 1623 cm^{-1} and 1432 cm^{-1} correspond to the asymmetric and symmetric ν(C=O) carboxylate stretches of the organic ligand. The difference between these bands, Δ =191 cm^{-1}, indicates that the carboxylate groups adopt bidentate bridging modes.[233]

In the Raman spectrum of the compound, the characteristic ν(C≡C) vibration gives rise to the most prominent band,at 2253 cm^{-1} (**Figure 2.49**). Two strong bands corresponding to aromatic ν(C=C) stretches of the phenyl rings are located at 1605 cm^{-1} and 1582 cm^{-1}, respectively. Bands at 1412 cm^{-1} and 1363 cm^{-1} are attributed to ν_s(C=O) vibrational bands of the carboxylate groups. A pronounced band that can be attributed to the in-plane δ(C-H) bending vibration of the central phenyl ring occurs at 992 cm^{-1}.

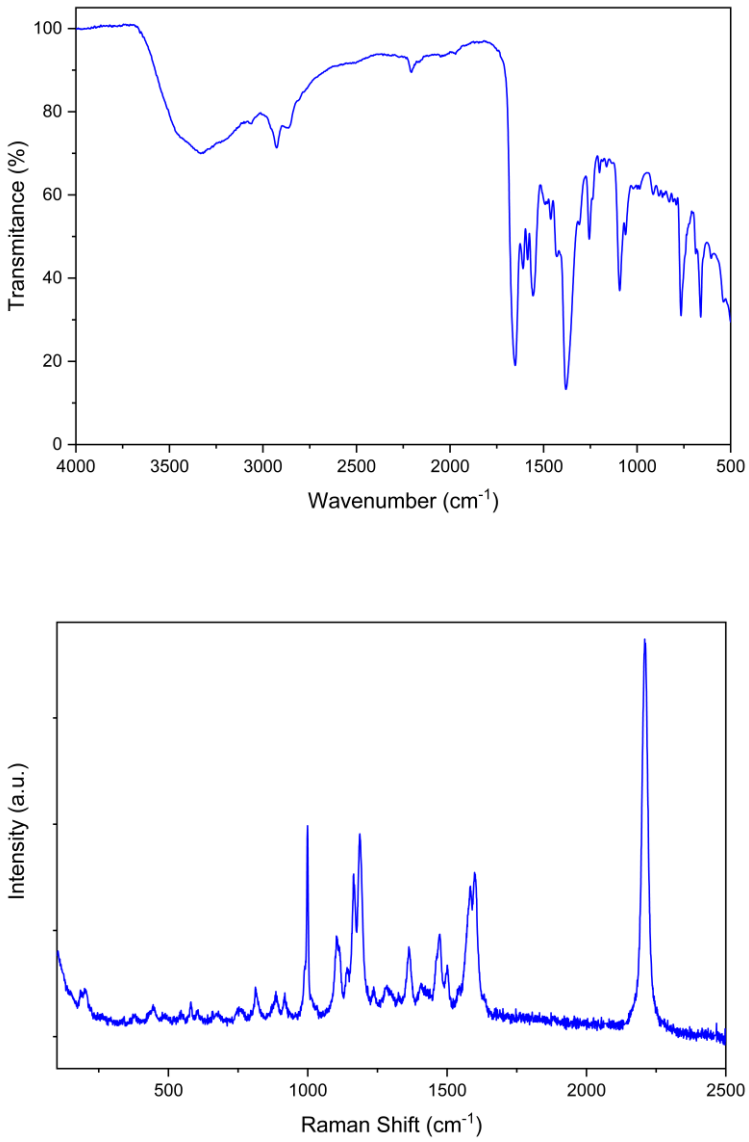

Figure 2.49: FT-IR and Raman spectra of 5.

Table 2.8: Crystallographic parameters for 5.

Identification code	5
Empirical formula	$C_{170}H_{92}N_{18}Cu_6O_{26}$
Formula weight	3183.85
Temperature / K	215(2)
Crystal system	Triclinic
Space group	*P-1*
***a* / Å**	15.978(5)
***b* / Å**	17.394(5)
***c* / Å**	28.081(8)
***α* / º**	93.28(2)
***β* /º**	92.84(2)
***γ* / º**	101.54(2)
Volume / Å^3	7619(4)
Z	1
ρ_{calc}/ g/cm^3	0.694
μ / mm^{-1}	0.450
F(000)	1620
Crystal size / mm^3	? × ? × ?
Radiation	MoKα (λ = 0.71073Å)
θ range for data collection / º	1.456 to 41.708°
Index ranges	-15<=h<=15, -17<=k<=17, -28<=l<=28
Reflections collected	66940
Independent reflections	15933 [R(int) = 0.1302]
Data/restraints/parameters	15933/60/1027
Goodness-of-fit on F^2	1.003
Final R indexes [I>=2σ (I)]	R1 = 0.0754, wR2 = 0.2225
Final R indexes [all data]	R1 = 0.1108, wR2 = 0.2483
Largest diff. peak/hole / e.Å^{-3}	0.47 and -0.40

2.7 Conclusion

In this chapter, the synthesis of an amino-functionalised BTEB-type organic linker is described. The synthetic procedure involved slight modifications of a literature method for the synthesised non-amino functionalised ligands. These modifications to the literature procedures were required due to the alterations of electronic and steric effects associated with the amino group. The new approach required a higher mole percentage loading of the palladium catalyst and the gradual addition of TMSA throughout the reaction. These simple steps led to a dramatically improved yield of the final product. The newly synthesised linkers were then successfully used in the synthesis of a series of MOPs and MOFs.

Two MOPs were synthesised by reacting the new linker with $Cu(NO_3)_2 \bullet 3H_2O$. The MOPs could be selectively synthesised by simple modification of the reaction conditions. Using DMF, **1** was synthesised while the simple addition of EtOH afforded **2** to be as synthesised. While the two compounds have different levels of metal-to-ligand ratio, 1.5:1 for **1** and 2:1 for **2**, and different reaction times, 72 hrs for **1** and 48 hrs. for **2**, it is the addition of EtOH for the synthesis of **2** that allows for the formation of the new cage. This is backed up through the application of synthesis of **2** but with the absence of EtOH. These reaction conditions simply lead to the formation of low-quality crystals of **1** in poor yields. The synthesis used in this text for the synthesis of **1** is the conditions needed to produce the best quality crystals in the highest yield. It was also found that using the same reaction conditions for **1** but with the addition of EtOH led to the formation of poor-quality crystals of **2**. As mentioned above, the conditions described in this text lead formation of the highest quality crystals suitable for single-crystal X-ray analysis.

The two MOPs have vastly different structures, with the differences arising from the various conformations of the $BTEB_{mmm}NH^{3-}$ linker. The MOP **1** has the endohedral structure of an inner octahedral unit encapsulated within an outer cuboctahedral framework. The MOP is composed of 24 $BTEB_{mmm}NH_2^{3-}$ linkers connecting 18 $\{Cu_2\}$ SBUs. Twelve of the $\{Cu_2\}$ paddlewheel SBUs act as the vertices of the outer cuboctahedron, while the remaining six act as the vertices of the inner octahedron. The $BTEB_{mmm}NH_2^{3-}$ linkers are found in two conformations within the framework. In the two conformations, two *meta*-benzoate moieties are in an *anti,anti*-conformation. These moieties coordinate to the twelve outer $\{Cu_2\}$ SBUs forming the outer cuboctahedral shell. The two conformations differ in the dihedral angle of the third remaining moiety on the linker. In one conformation, the remaining moiety is in a *syn,syn*-arrangement in relation to an exterior moiety. Four linkers link two $\{Cu_2\}$ SBUs, generating the literature known "super-paddlewheel" building unit. In the remaining conformation, the third moiety is perpendicular to the central phenyl ring. Four of these conformations combine to form a bowl-like unit. These two units combine to create the MOP. The second MOP that was synthesised adopts a structure of an octahedron. In this case, the

$BTEB_{mmm}NH_2^{3-}$ linker is found in only one conformation. In this conformation, the three moieties are perpendicular to the central phenyl ring. The linkers act as the triangular faces of the octahedron.

These MOP units were then utilised in the synthesis of MOFs using a well-established technique known as pillaring. **1** was created *in situ* and linked by pillaring Azpy ligands. A wide range of lengths for the potentially pillaring ligands was chosen for the reaction attempts. However, only the Azpy ligand was capable of pillaring the MOPs. By carefully selecting the ligand-to-linker ratio, it was possible to control the degree of pillaring.

The pillared structure **3**, is a one-dimensional coordination polymer comprised of MOPs with the structure of **1** linked by Azpy ligands. The polymer was synthesised using a 1:1 mole ratio of Azpy to $H_3BTEB_{mmm}NH_2$ ligands. In the structure, Azpy ligands were found to coordinate to two $\{Cu_2\}$ SBUs, which make out the outer cuboctahedron of the MOP. The two$\{Cu_2\}$ SBUs were located opposite to each other, allowing them to connect MOPs into one-dimensional chains.

Simply upon increasing the Azpy to $H_3BTEB_{mmm}NH_2$ ratio in the synthesis to 2:1, the cuboctahedral MOP was connected into a three-dimensional framework. In this structure, all of the outer $\{Cu_2\}$ SBUs are coordinated by Azpy ligands. These Azpy ligands connect the MOPs into a dual interpenetrated framework; Each framework adopts a **fcu** topology Whilst the topology of the rather complex MOF structure relates to a simple NaCl structure. It is remarkable that the 3D structure of **3** can reversibly be disassembled to its MOP SBUs upon dispersing **3** in a Co^{2+} /DMF solution.

Due to the low solubility of **2** a different approach was required to pillar these molecular entities. Rather than synthesising the MOP *in-situ,* a new approach required the MOP to be pre-synthesised. Using the normal synthesis of **2** crystals of the MOP were first isolated. The crystals were then added to a DMF/Azpy solution. The pyridyl ligand PPP was added to the solution to aid in the solubility of the MOP. Crystals were then found to have grown in the reaction vial. An unexpected result was obtained. The crystals were found to be two-dimensional sheets comprised of super-paddlewheel units pillared by the Azpy ligand. The PPP ligand was found to coordinate to the two $\{Cu_2\}$ SBUs that make up the super-paddlewheel. This result was unexpected as it meant that the MOPs were unstable in the reaction solution and transformed into super-paddlewheel units. The PPP ligand may have stabilised the super-paddlewheel unit in the solution allowing it to assemble into two-dimensional sheets that are pillared by Azpy moieties.

In summary, we have successfully synthesised two new MOPs and utilised these in the synthesis of MOFs through pillaring. We demonstrate that the resulting 3D MOF can be disassembled. An unexpected result was obtained when **2** was used to synthesise a MOF resulting in pillared two-dimensional sheets. The described approach offers a new way of synthesising complex metal-organic materials using complex MOPs as supramolecular reagents.

Chapter 3

The influence of BTEB based linkers with reduced symmetry on MOF structures and networks

3 The influence of BTEB based linkers with reduced symmetry on MOF structures and networks

3.1 Introduction

In MOF research, highly symmetrical linkers are prevalent and relatively common throughout the literature due to several factors. Two of these factors that contribute to their dominance in the literature are:

a) their ability to form highly symmetrical structures that are easier to predict using reticular synthesis concepts and synthesise and crystalise.[258,259,260] The resulting MOF topologies relate to default nets of purely inorganic archetype structures.
b) the convenience of their more straightforward synthetic procedures for their synthesis through the requirement of fewer synthetic steps. These simpler synthetic procedures allow for higher yields and ease of scalability, which are also essential factors for the development beyond academic research.[260]

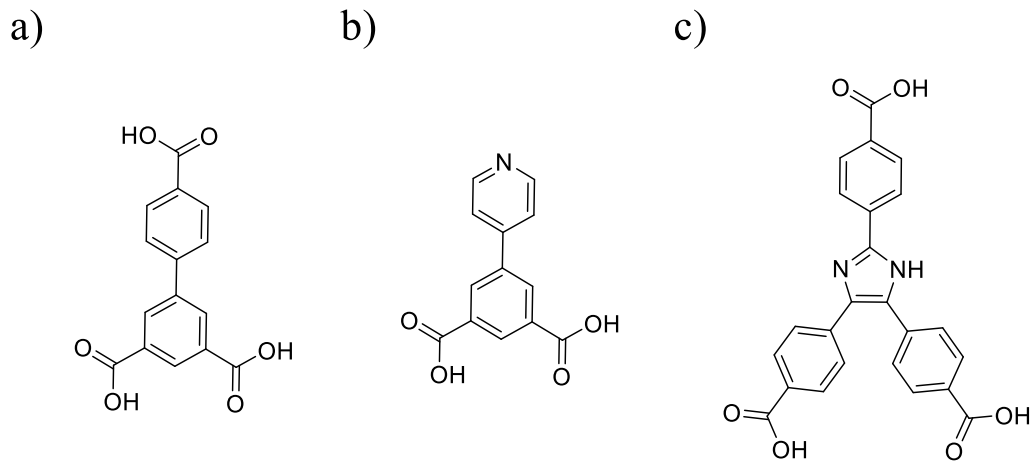

Figure 3.1: Examples of linkers that reduce the C_3 symmetry of classical trifunctional carboxylate linkers by a) introduction of a spacer to extend one axis of the linker,[261,262,263] b) introduction of secondary functional groups which coordinate to the inorganic SBUs [264,265,266] and c) introduction of heterocyclic compounds to modify bond angles of the linker.[267,268,269]

This preference for symmetrical linkers has left a vastly unexplored area in the study of linkers for MOFs. While some progress has been made in the research of rigid linkers with reduced symmetry, research has primarily focused on three different methods of reducing symmetry. These include but are not limited to a) the elongation of one axis of the linker through the introduction of spacer units, b) the introduction of two or more different functional groups onto the linker, and c) the addition of hetero-cyclic compounds which modify the geometry withing the linker (**Figure 3.1**). These three

methods of introducing asymmetry into the linkers cause a significant structural deviation from the original linker.

In the presented body of work, a new family of rigid linkers based on an underlying tripodal 1,3,5-benzene-trisethylbenzoate (BTEB) core was developed (**Figure 2.50**). This family of linkers was chosen for many reasons. Firstly, due to their relation to linkers that have previously been studied in the literature; hence, these linkers can be used to synthesise many MOFs, giving a library of structures to which comparisons can be drawn from the new structures.[39,220,270] Secondly, the ligands were synthesised due to the ability to draw comparisons between linkers within the ligand family considering a) the number of carboxylate groups present on the linker and b) the relative positions of the coordinating carboxylate groups forming isomeric MOFs. Finally, the use of ethynyl spacer units for the three spacer units in the linker allows for the distance between the benzoate/isophthalate moieties, and the central phenyl ring is the same. This eliminates the effect of different distances between the moieties and central phenyl on the MOF structure. The ethynyl space unit has the added benefit of eliminating the steric interactions that can occur in other commonly used spacer units. [271,272,273,274,22]

While there are many commonly found inorganic SBUs in the literature, MOFs are often synthesised from metal ions that are capable of creating a wide range of inorganic SBUs through variation in their coordination number and geometry [275,276,277] It is often observed that the reduction of the symmetry of the linker induces a structural change in the inorganic SBUs to compensate for the induced steric strains and structural limitations imposed by the linker. [22,266,278,279,280] The structural diversity of specific metals ions that can form a number of SBUs, increases the difficulty in analysing the influence of geometrical and functional factors of linkers on the framework structures. In this body of work, the attention was directed towards {Cu_2} paddlewheel SBUs to establish a library of comparable MOFs.

The {Cu_2} paddlewheel SBU found within the literature represents 4-connected nodes.[277] The SBU also has the geometrically simple structure of a planar square unit, a standard building block used in designing MOFs.[62,281,282] The low connectivity and square topology limit steric hindrance between the coordinating linkers to the SBU.[283] Focusing on this newly developed family of linkers and {Cu_2} paddlewheel SBUs, structurally comparable MOFs are expected to the synthesised.

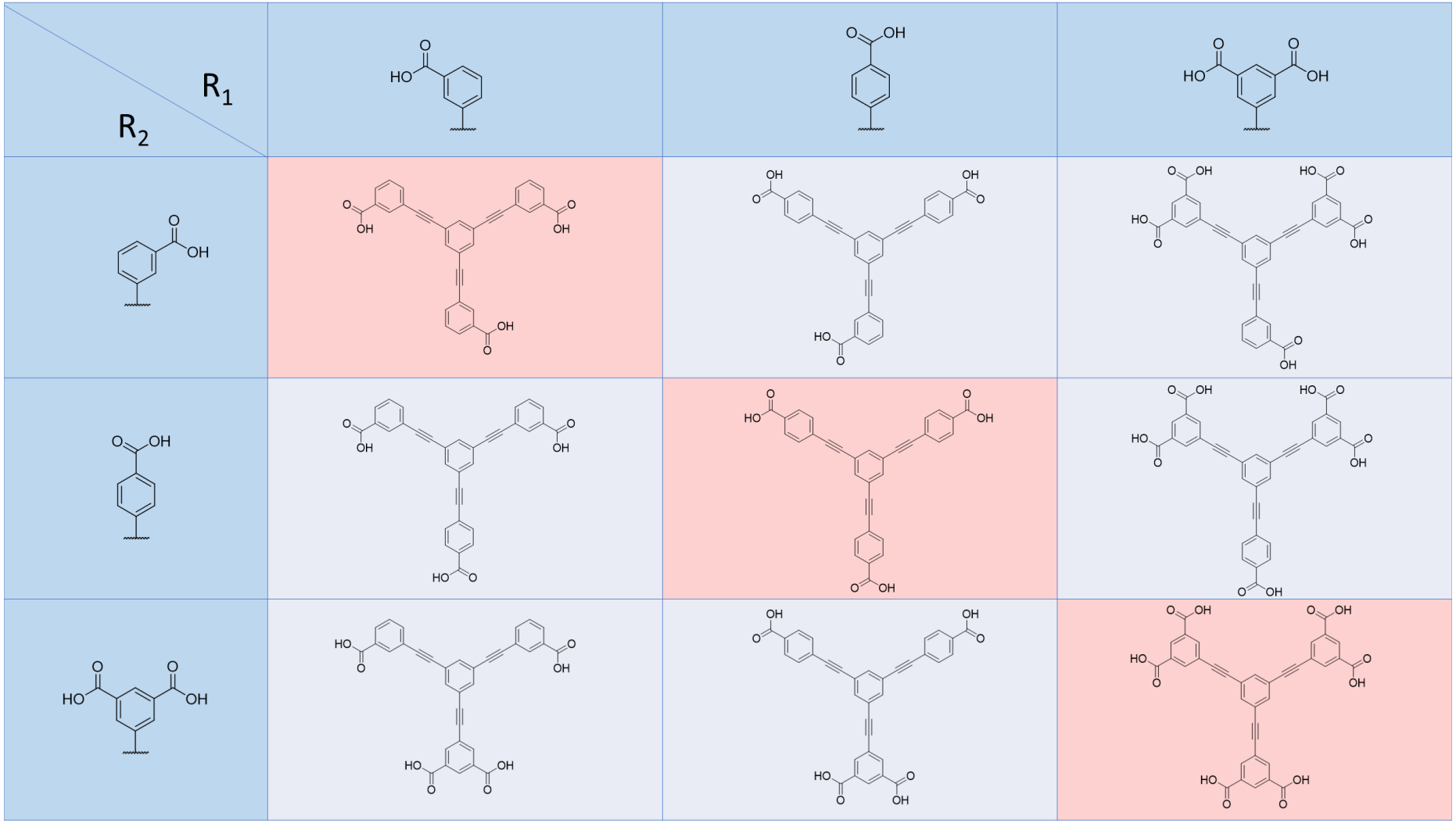

Figure 3.2: The family of BTEB-derived linkers used in this body of work. Possible combinations of *para*-benzoate, *meta*-benzoate and isophthalate moieties are shown. The linkers along the diagonal of the table represent the parent symmetrical linkers that have been previously described in the literature.

3.2 Synthesis of BTEB-derived linkers

The synthesis of related linkers with reduced symmetry can be achieved through various methods. Synthetic methodologies to rigid polycarboxylate ligands typically involve C-C coupling reactions to a central unit that can react at multiple sites. Little control is given to the degree of coupling to the central unit, often resulting in product mixtures containing partially reacted species and ligand derivatives. The targeted product can then be isolated during the purification step. This method, while simple in theory, is frequently plagued by difficult purification as a result of a wide range of possible products and/or suffering from low yields.[278]

Another commonly applied method to these rigid ligand types involves the coupling between two units that have different symmetries. This is most commonly used for bi-phenyl based linkers as these can easily be synthesised through cross-coupling between commercially available reagents.[262,265,274,284] Another noteworthy method involves the use of different functional groups, which behave orthogonally during the synthesis, influencing the functionality and/or the symmetry of the linker.[285,286] The latter method often increases the number of synthetic steps but has the benefit of increased selectivity for the targeted product.

For the synthesis BTEB-derived ligands, 1,3,5-tribromobenzene can be used as the core unit to which various spacer units and moieties can be attached. [39,214,287,288,289] The use of 1,3,5-tribromobenzene as a reagent, however, provides limited control on the degree of reaction when different moieties are intended to be attached. The use of molar ratios to control the degree of reaction often leads to a variety of products being synthesised.[278] For this project, we developed a synthetic procedure for the synthesis of the outlined BTEB-derived ligands (**Scheme 3**). The synthetic strategy utilises the reactivity difference between chloride and iodide leaving groups in Sonogashira cross-coupling reactions. Iodide leaving groups are commonly applied, facilitating reactions capable of that proceed in good yields at room temperature.[290,291,292] The chloride group, however, is found to be inert under these conditions. It is only relatively recently that Sonogashira couplings using chlorides as leaving groups have been developed.[293,294,295,296] For the Sonogashira coupling to the aryl chloride to take place the addition of a bulky, electron-rich *ortho*-bisphenylphosphane ligand is required. In this instance, the commercial ligand 2-dicyclohexylphosphino-2′,4′,6′-triisopropylbiphenyl (X-Phos) can be used. The use of this ligand activates the palladium catalyst facilitating the reaction with a chloride moiety. For the outlined purposes, 3,5-dichloro-1-idodbenzene can be used to establish the central phenyl ring to which the benzoate or isophthalate moieties are attached.

The alkyne benzoate/isophthalate moieties are synthesised before coupling to the central phenyl ring. The synthesis of the alkyne benzoates involves a two-step procedure. The first step involves a Sonogashira coupling of trimethylsilane-acetlyene (TMSA) to the selected bromo-benzoate/isophatlate.[297] For this, the $[PdCl_2(PPh_3)_2]$ catalyst, CuI, followed by the selected bromo-

benzoate/isophthalate, were dissolved in a THF/TEA mixture. TMSA is then added to the reaction mixture under an inert atmosphere *via* a syringe. The reaction mixture was then heated to 80 °C for 24 h under an inert atmosphere. After completion of the reaction, the solvent was removed under reduced pressure. The remaining crude solid was redissolved in CH_2Cl_2 and washed three times with a saturated aqueous solution of NH_4Cl and a brine solution. The NH_4Cl solution aids in the removal of copper and palladium salts through the formation of an aqueous Cu^{2+} phase and an insoluble palladium complex. Following this, the organic layer was separated, dried with anhydrous $MgSO_4$ and the solvent was removed under reduced pressure. The crude product was then purified by flash column chromatography eluted hexane:CH_2Cl_2 (18:1, v/v) to give pure products, with yields ranging between 80-94% for the three compounds.

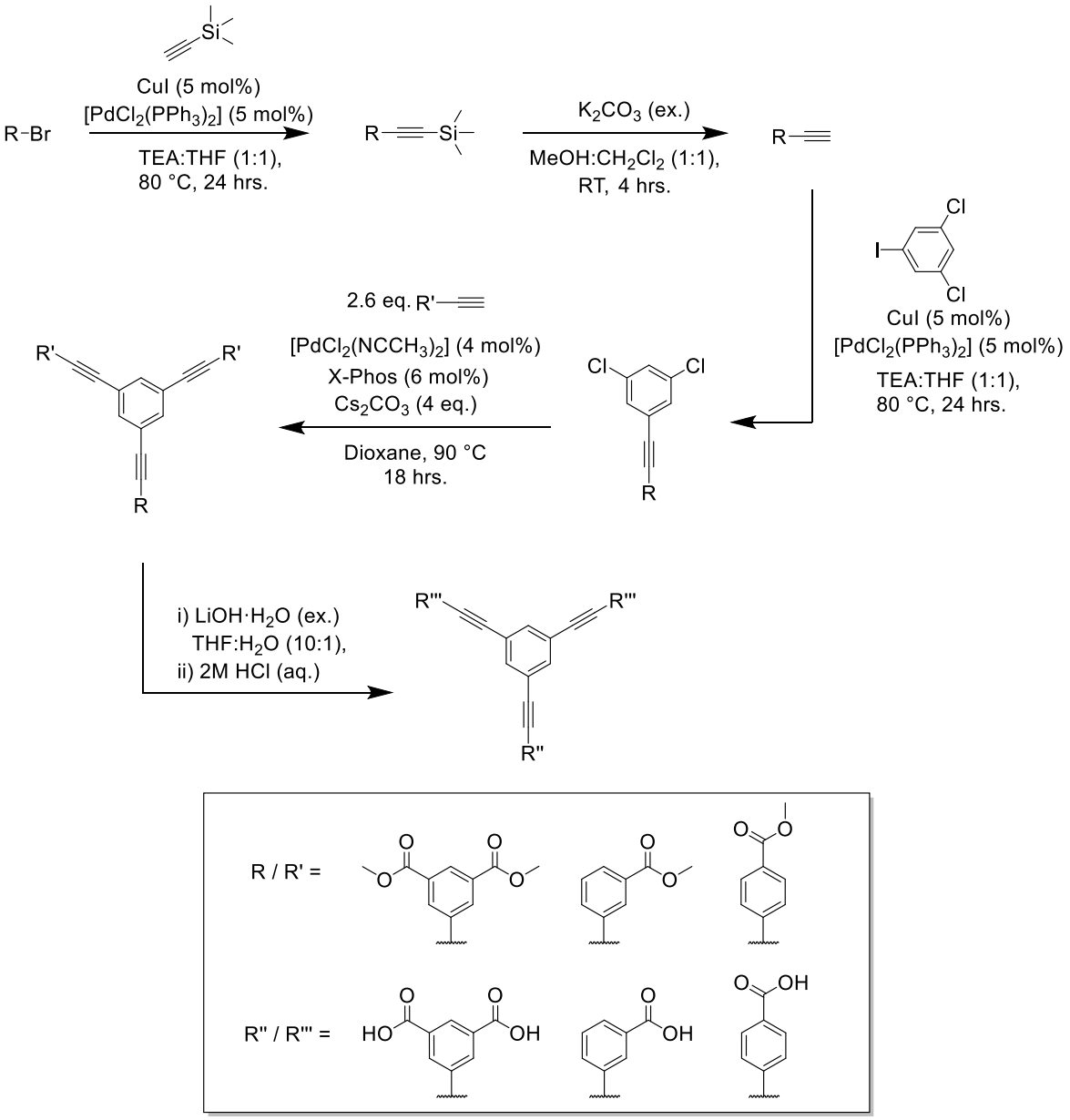

Scheme 3: Synthetic procedure for the synthesis of the reduced symmetry BTEB based linkers.

The second step is the deprotection of the trimethysilane protecting group. The chosen trimethylsilyl protected product was dissolved in a CH_2Cl_2:MeOH solvent mixture containing excess K_2CO_3. The solution was stirred at room temperature for 4 h. Upon completion of the reaction, the solvent was removed under reduced pressure and the crude product was purified by flash column chromatography eluting with hexane:CH_2Cl_2 (18:1, v/v) to give the deprotected alkyne product at a yield of 90%.

Step three of the synthetic procedure constitutes the coupling of the initial ethynyl-benzoate to 3,5-dichloro-1-idodbenzene. For this purpose, the chosen ethynyl-benzoate or isophthalate and 3,5-dichloro-1-idodbenzene were first dissolved in a THF:TEA (1:1, v/v) mixture. $[PdCl_2(PPh_3)_2]$ and CuI (both at 5% mol loading) were added under an inert atmosphere. The solution was then heated to 35 °C for 24 h. Upon completion of the reaction, the solvent was removed under reduced pressure. The crude product was purified by flash column chromatography, which was eluted with CH_2Cl_2. Upon removal of the solvent the purified product was found as a white crystalline powder with high yields of *ca.* >90% for the three products. In **Figure 3.3** the aromatic region of the NMR spectra of the three methyl esters of ((3,5-dichloro)ethynyl)-benzoates and isophthalate can be seen. The triplet signal at 7.35 ppm and the doublet at 7.41 ppm correspond to the two protons located on the dichloro-phenyl rings. These signals appear at closely similar positions for all three compounds.

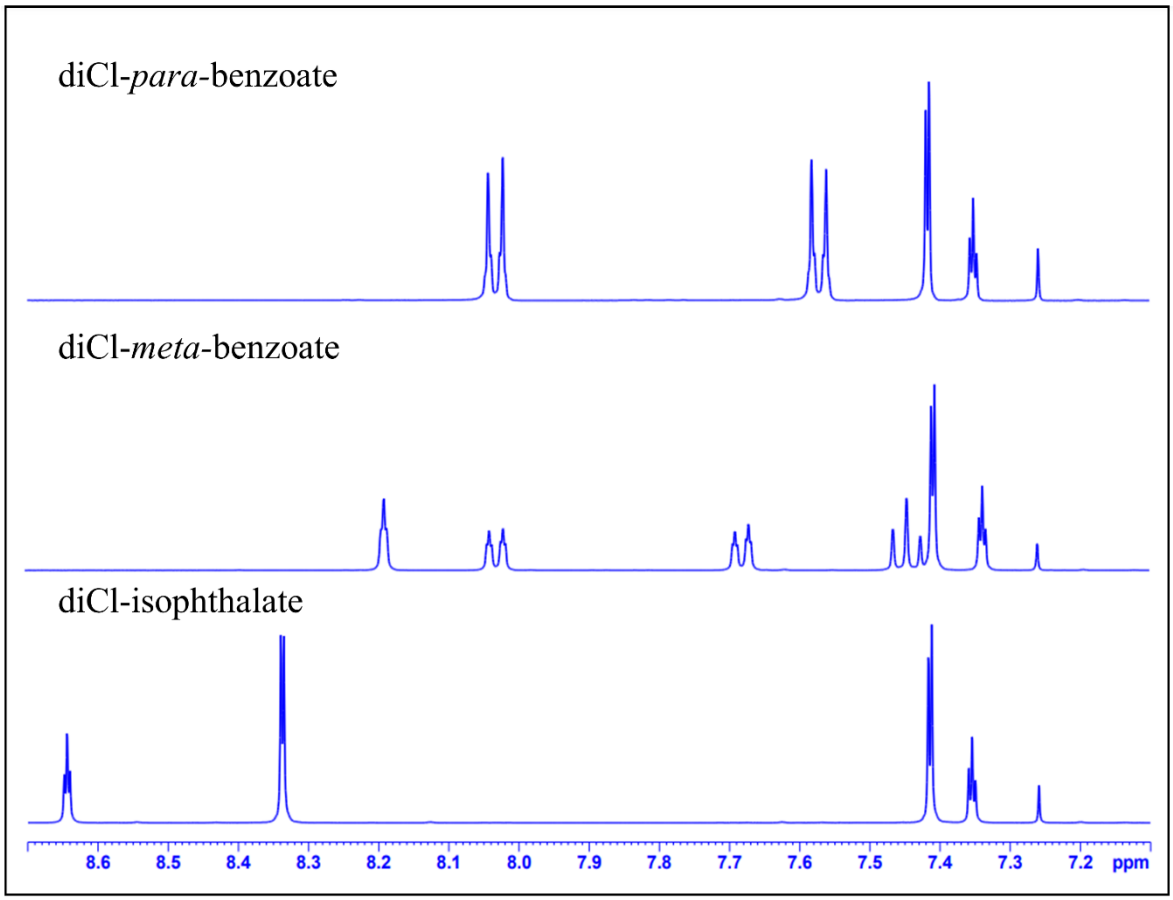

Figure 3.3: NMR spectra of the three intermediate compounds shown in the range from 7.1 ppm to 8.7 ppm

The following step involved the Sonogashira coupling reaction between the secondary ethynyl-benzoate or isophthalate moieties and the methyl ((3,5-dichloro)ethynyl)-benzoates or isophthalate. The applied procedure is a modification of a procedure reported by Buchwald *et al.*[296] The methyl ((3,5-dichloro)ethynyl)-benzoate product from the previous step was combined with $[PdCl_2(NCCH_3)_2]$, X-Phos and Cs_2CO_3 in dioxane. The solution was then stirred at 50 °C under an inert atmosphere for 1 h to activate the catalyst. Following this initial heating, the temperature of the solution was raised to 90 °C, and a solution containing 2.6 eq. of the secondary ethynyl benzoate in dioxane was added. The ethynyl-benzoate solution was added to the reaction mixture dropwise over six hours. It was found that if the ethynyl benzoate is added to the reaction mixture too quickly, a secondary reaction, analogous to the Glaser coupling reaction, occurs.[298] This side reaction leads to a dramatically lower yield of the desired product due to the consumption of ethynyl benzoate and the deactivation of the palladium catalyst. After the aryl alkyne solution was added, the reaction mixture was allowed to react for a further 12 hrs. Upon completion of the reaction, the solvent was removed under reduced pressure. The crude product was then taken up in CH_2Cl_2 and washed twice with deionised water and brine. The organic phase was separated and dried with $MgSO_4$ followed by the removal of the solvent under reduced pressure. The crude product was then purified by flash column chromatography eluted with EtOAc:CH_2Cl_2 (1:18, v/v). The products were obtained in high yields that ranged from *ca.* 76-84%.

The final step constitutes the removal of the protecting methyl ester groups. For this, the ester-protected products and excess of LiOH are dissolved in a solution of THF:H_2O (10:1, v/v) and stirred at room temperature for 8 hrs. The reaction progress was monitored by thin-layer chromatography, which was eluted with EtOAc. It was found that performing the reaction at elevated temperatures to increase the reaction rate leads to rapid degradation of the THF solvent through a ring-opening reaction. Lower reaction temperatures and longer reaction times were required to minimise this side reaction. Once the reaction was completed, the solvent was removed under reduced pressure. The crude product was dissolved in deionised water. The resulting solution was acidified to pH 1 with a 2 M aqueous HCl solution. The resulting white gelatinous solid was filtered off. When the majority of the water had been removed, the product was redissolved in dry THF. The solution was then dried over $MgSO_4$ to remove the remaining water from the product. The $MgSO_4$ was then filtered off, and THF was removed under reduced pressure to leave a white solid. The yield for these deprotection reactions ranged from *ca*. 75-89%. This gave a total percentage yield for the synthesis to range between 44% to 56%. The variation in yield can manly be attributed to compounding minor errors in the synthesis of each ligand rather than an inherent variation in the chemistry of each ligand.

The resulting compounds were characterised using a combination of ^{1}H-NMR and ^{13}C-NMR spectroscopy and mass spectrometry. In **Figure 3.4** the ^{1}H-NMR spectra of the aromatic regions for the products can be seen.

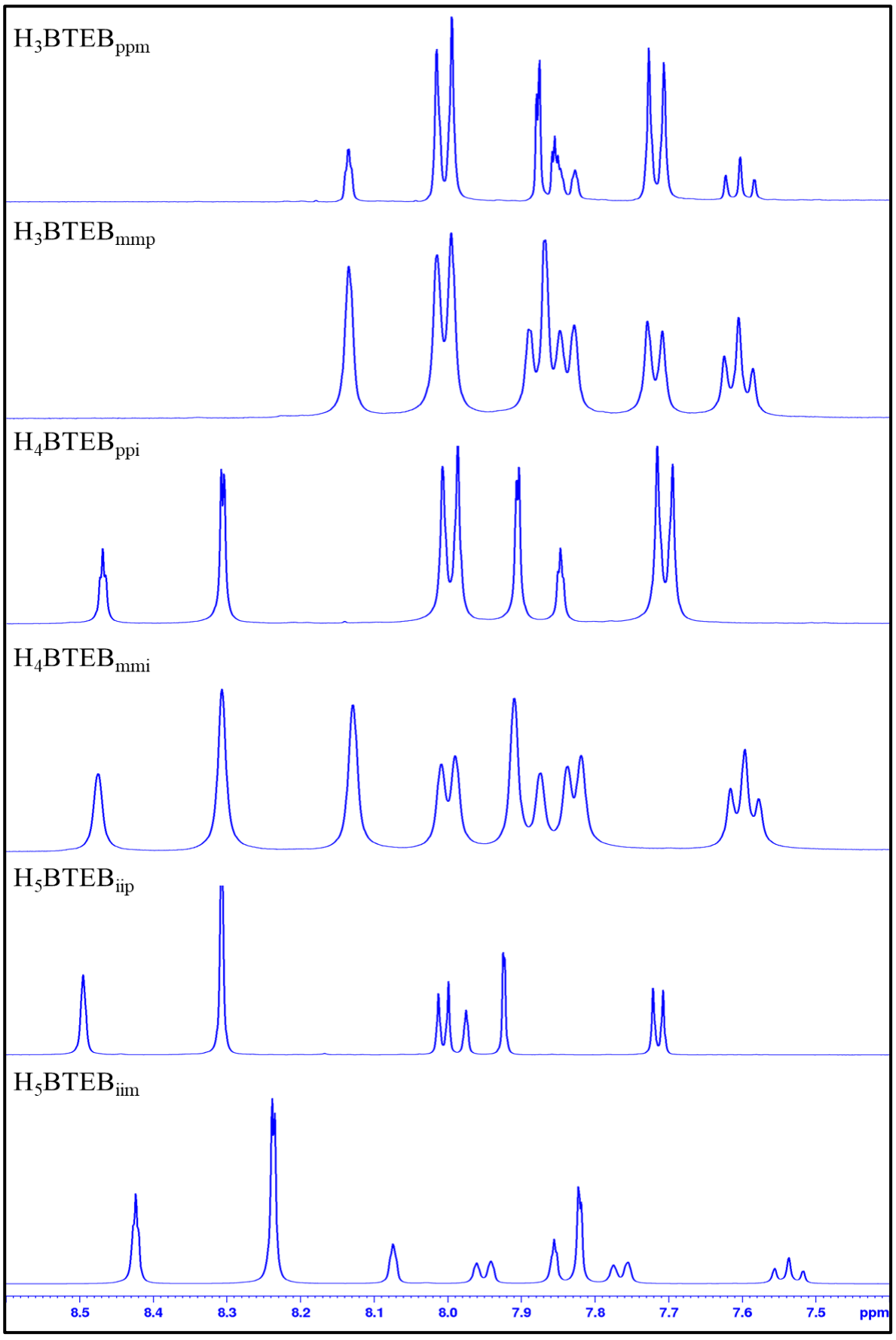

Figure 3.4: NMR spectra of the synthesised linkers; spectra are shown in the range from 7.4 ppm to 8.6 ppm.

3.2.1 Explanation of new terminology

In MOFs that contain highly symmetric linkers, each carboxylate group is structurally indistinguishable from its symmetrical equivalent. However, in linkers that have some degree of asymmetry the carboxylate groups are no longer symmetrically equivalent. Due to this disparity in the symmetrical equivalence of the carboxylate groups the connectivity of the linker, within the structure of the MOF, is highly dependent on how it is orientation and the arrangement of the carboxylate groups around the inorganic SBU. The connectivity of the inorganic SBUs is dependent on how the coordinating carboxylate groups are arranged around the SBU. By treating the non-symmetrically equivalent carboxylate groups as separate moieties, it is possible to characterise the various inorganic SBUs within the MOF based upon the arrangement of the moieties. The number of possible arrangements for the carboxylates to coordinate to the SBU is dependent on the number of non-symmetrically equivalent carboxylates on the linker and the number of carboxylates that coordinate to the SBU.

By limiting this body of work to the family of linkers found in **Figure 3.2** only two different non-symmetrically equivalent carboxylates are present in the linker. The choice of using $\{Cu_2\}$ paddle wheel SBUs limits the number of coordinating carboxylates to the SBU to four. The $\{Cu_2\}$ SBU has the added simplicity of a square planar SBU which removes some of the rotational requirements for the inorganic SBU in the structure. In **Figure 3.5** a list of the possible arrangements for the coordination that can occur with a linker containing two non-symmetry related carboxylates coordinated to a $\{Cu_2\}$ SBU is shown. In this body of work, we assign a Greek letter as an identification symbol to distinguish the different arrangements from one another.

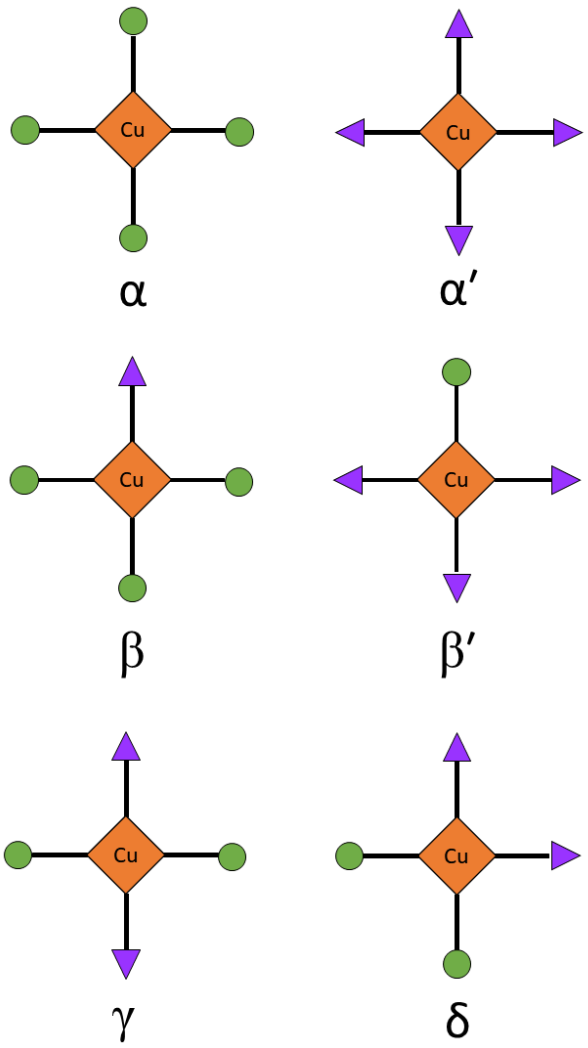

Figure 3.5: The six possible arrangements of two structurally distinct carboxylates coordinating to a {Cu_2} paddle wheel. The arrangements of α and β have the potential to form an inverted arrangement in which the secondary carboxylate is the main carboxylate that coordinates to the Cu^{2+} ion. These are denoted by the symbols α′ and β′. Due to symmetry, the arrangements of γ and δ do not have an inverted arrangement. Colour scheme: Copper ion (orange square), Primary carboxylate (green circle), secondary carboxylate (purple triangle).

In this nomenclature, the carboxylate that is the most numerous of the moieties is designated as the primary carboxylate, while the carboxylate that is found on the least numerous moiety is classified as the secondary carboxylate. In **Figure 3.6** the linker H_4BTEB_{ppi} contains two carboxylates from the *para*-benzoate moieties and two carboxylates from the isophthalate moiety. In this instance, the *para*-benzoate is the most numerous of the moieties and its carboxylate are designated as the primary carboxylate. With the linker containing one isophthalate moiety, its carboxylate groups are designated the secondary carboxylate groups. Note that although there are an equal number of *para*-benzoate carboxylates and isophthalate carboxylates, the greater number of *para*-benzoates designates them as the primary carboxylates

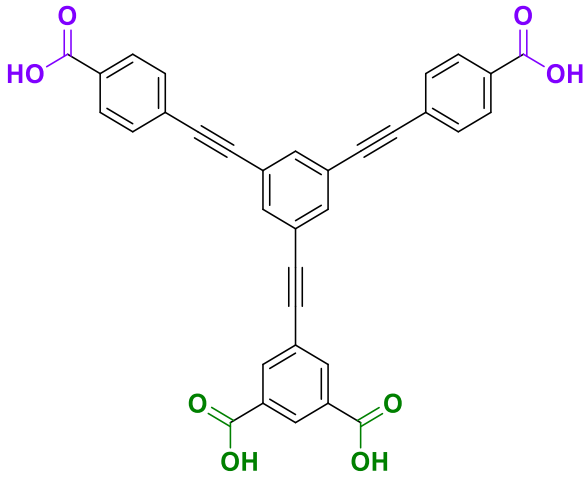

Figure 3.6: The linker H_4BTEB_{ppi} contains two primary carboxylates, derived from the *para*-benzoate moieties (purple), and two secondary carboxylates, derived from the isophthalate moiety (green).

In **Figure 3.7** an example of a coordination arrangement for the carboxylates coordinating to the $\{Cu_2\}$ SBU can be seen. In this instance, the linker used to synthesise the MOF is H_4BTEB_{ppi}, therefore designating the *para*-benzoate carboxylates as the primary carboxylates and the isophthalate carboxylates the secondary carboxylates. The two different carboxylates coordinated to the two Cu^{2+} ions in a *cis* like arrangement. This arrangement is then given the symbol **δ**.

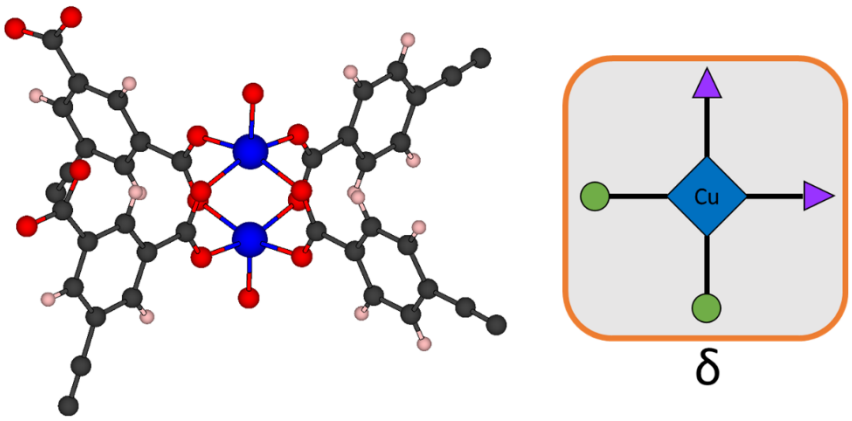

Figure 3.7:An example of the possible arrangements. Two *para*-benzoate and two isophthalates coordinate to the two Cu^{2+} ions in a *cis* like arrangement. A graphical example of the arrangement is also shown. This arrangement is denoted by the symbol δ. (C -black, O – red, N – light blue, Cu – dark blue)

3.3 Prediction of arrangement combinations

A secondary benefit of using the nomenclature discussed in the previous section is the ability to predict possible combinations of arrangements that can occur within the MOF. By using a few

assumptions, it is possible to determine which combinations are possible. The assumptions are as follows:

1. The linker remains unchanged over the course of the reaction. This is assumed that the linker doesn't experience any chemical alterations, whether by degradation due to the reaction environment (oxidation, decarboxylation etc.), or reacting with other reagents in solution (acidity regulators etc.).
2. All carboxylates on the linkers are fully deprotonated and coordinate to two Cu^{2+} ions in a *syn,syn*-bidentate bridging fashion. This assumption is so that there are no non-coordinating carboxylates within the structure of the MOF. This would alter the ratio of the carboxylates on the linker which form part of the connected framework and the degree of connectivity for the linker to be changed. For example, a tetra-carboxylate linker with a non-coordinating carboxylate would behave like a tri-carboxylate linker within the structure of the MOF if one of its carboxylate groups does not coordinate to a $\{Cu_2\}$ SBU.
3. All inorganic SBUs that are found within the MOF takes the form of the dimeric $\{Cu_2\}$ paddlewheel SBUs. This assumes that no other inorganic SBUs are present within the structure of the MOF which would alter the ratio of SBU to linkers.

Using these three assumptions a wide range of possible combinations for the arrangement of benzoates moieties coordinating to a $\{Cu_2\}$ SBU. (**Table 3.1**) This also allows for the elimination of any non-possible combinations. These combinations will also greatly simplify the different structures that will be synthesised. By using simple combinations, it is possible to compare the influence of the linker on the structure of the MOF.

Table 3.1: Examples of possible combinations of coordination arrangements of carboxylates to $\{Cu_2\}$ SBUs based upon the ratio of the moieties present in the linker.

Primary benzoate moiety	Secondary benzoate moiety	Ratio of carboxylates	Examples of possible combination of arrangements
para-	*meta-*	2:1	$\alpha_2\alpha'$, $\alpha\gamma_2$, $\alpha\delta_2$, $\alpha\gamma\delta$, $\beta_2\gamma$, $\beta_2\delta$, $\alpha\beta\beta'$, $\beta_5\beta'$, $\alpha_3\beta'_2\gamma$, …
meta-	*para-*	2:1	
para-	isophthalate	1:1	$\alpha\alpha'$, γ, δ, $\gamma\delta$, $\beta\beta'$, …
meta-	isophthalate	1:1	
isophthalate	*para-*	4:1	$\alpha_4\alpha'$, $\alpha_3\delta_2$, $\alpha_3\gamma_2$, $\alpha_3\delta\gamma$, $\alpha_2\beta_2\gamma$, $\alpha_2\beta_2\delta$, …
isophthalate	*meta-*	4:1	

3.4 Tris-carboxylate BTEB linkers

3.4.1 $[Cu_3(BTEB_{ppm})_2(DMF)(H_2O)_2]$ (**6**)

$[Cu_3(BTEB_{ppm})_2(DMF)(H_2O)_2]$ (**6**) was synthesised by reacting $Cu(NO_3)_2{\cdot}6H_2O$ and H_3BTEB_{ppm}, in a mole ratio of 1.5:1, in 0.5 mL DMF at 70 ºC for 96 h. After the reaction had finished, large blue, rhombohedral crystals were found to have grown on the walls of the reaction vial. The crystals were collected and were found to be of sufficient size and of suitable quality to be analysed by single-crystal X-ray crystallography. The crystal structure was measured and solved in the monoclinic crystal system and the *P2₁/C* space group. The unit cell dimensions were determined to be a = 21.759(7) Å, b = 20.043(7) Å, c = 40.745(13) Å, $\alpha = \gamma = 90^o$, $\beta = 94.52(2)^o$.

The structure of **6** was determined to be a porous three dimensional MOF with the molecular formula $[Cu_3(BTEB_{ppm})_2(DMF)(H_2O)_2]$. The asymmetric unit was found to contain three Cu^{2+} ions coordinated by two fully deprotonated $BTEB_{ppm}^{3-}$ linkers, and solvent molecules. The Cu^{2+} ions generate the distinctive dimeric $\{Cu_2\}$ paddlewheel SBUs. One paddlewheel SBU is composed of Cu(1) and Cu(2), while the second is composed of Cu(3) and its symmetry equivalent, Cu(3)'. Each Cu^{2+} ion is coordinated by four carboxylate groups and a DMF or H_2O solvent molecule *via* O-donor atoms thus, giving each Cu^{2+} ion a square-based pyramidal coordination environment. The O-donor atoms from the four carboxylate groups form the base of the square base pyramid with the solvent molecule located at the apical position. The carboxylate groups bridge two Cu^{2+} ions in a *syn,syn*-bidentate (μ_2-η^1:η^1) mode forming the $\{Cu_2\}$ paddlewheel SBUs. All bond lengths and angles found in the SBU are similar to literature known $\{Cu_2\}$ SBUs or compounds discussed in **Chapter 2**.[223] The nature of the solvent molecules which coordinate to the apical site varies across the three Cu^{2+} ions. Cu(1) and Cu(2) are coordinated by H_2O solvent molecules while Cu(3) and its symmetry equivalent are coordinated by DMF solvent molecules.

Each of the $\{Cu_2\}$ SBUs is coordinated by four $BTEB_{ppm}^{3-}$ linkers, with each $BTEB_{ppm}^{3-}$ linker connected to three $\{Cu_2\}$ SBUs. Due to the $BTEB_{ppm}^{3-}$ linker containing two different benzoate moieties, *para*-benzoates and *meta*-benzoate, two different coordination arrangements of the benzoate moieties to the $\{Cu_2\}$ SBUs are generated. For the $\{Cu_2\}$ SBU which contains Cu(1) and Cu(2), the Cu^{2+} ions are coordinated by three *para*-benzoate moieties and one *meta*-benzoate moiety. The benzoate moieties coordinate to the $\{Cu_2\}$ SBU with the **β** arrangement, considering the nomenclature described in **Section 3.2.1** (**Figure 3.8 a)**). The other unique $\{Cu_2\}$ SBU in **6** featuring Cu(3) and its symmetry equivalent Cu(3)' is stabilised by two *para*-benzoate and two *meta*-benzoate moieties. The different benzoate moieties coordinate to the $\{Cu_2\}$ SBU in a trans configuration giving the arrangement denoted as **γ** (**Figure 3.8 b)**). The two arrangements are found in the ratio 2:1ratio represented by the notation $\boldsymbol{\beta_2\gamma}$ which is in line with charge considerations and the possible combinations outlined in **Table 3.1**.

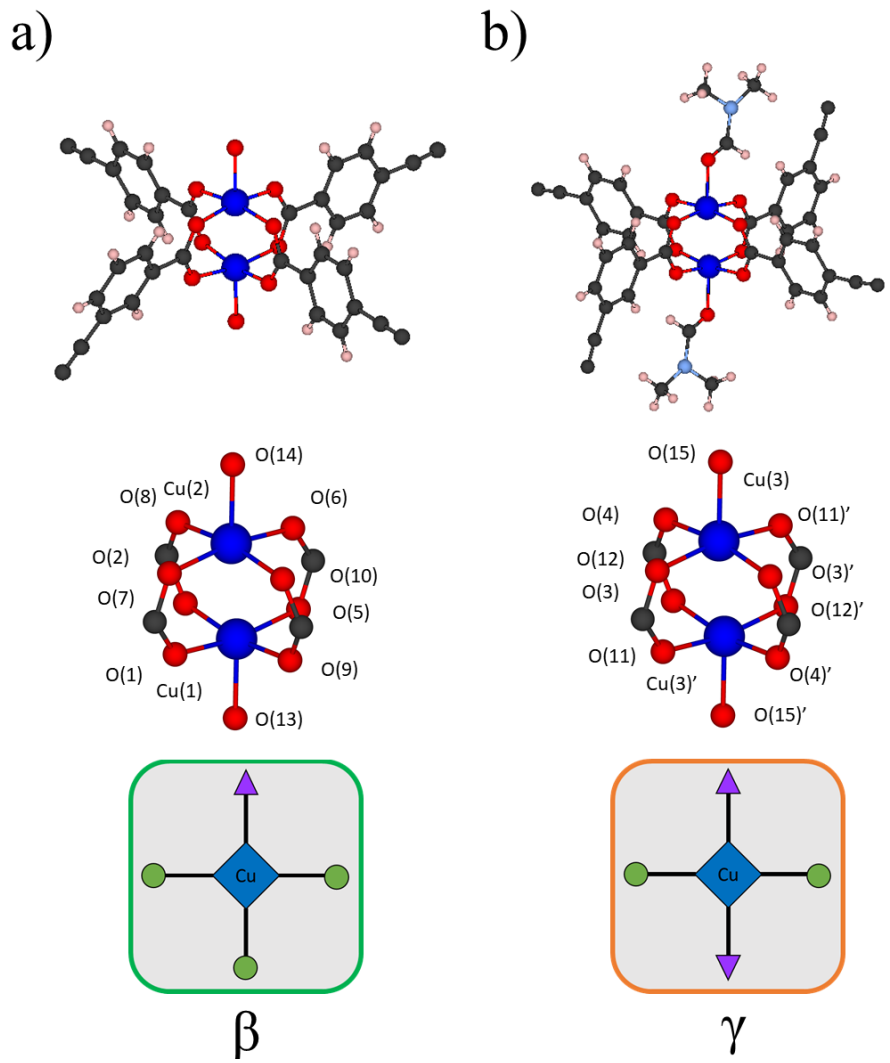

Figure 3.8: The two arrangements of the *para*-benzoate and *meta*-benzoate moieties coordinating to the Cu^{2+} ions in the $\{Cu_2\}$ SBUs in 6. a) Three *para*-benzoates and one *meta*-benzoate coordinate to Cu^{2+} ions in the β arrangement. b) Two *para*-benzoate and two *meta*-benzoate coordinates to the Cu^{2+} ions in the γ arrangement. c) the schematic representation of the arrangement of the benzoate moieties coordinating to the Cu^{2+} ions. (O - red, C- grey, H - pink, N - light blue, Cu - dark blue)

The $BTEB_{ppm}^{3-}$ linker is found in two conformations within the structure of **6** (**Figure 3.9**). In **Table 3.2** the dihedral angles of the benzoate moieties to the central phenyl ring are listed. In the first conformation, **i**, it can be seen that the *para*-benzoate moieties have a large dihedral angle with respect to the central phenyl ring while the *meta*-benzoate moiety is approximately co-planar with the central phenyl ring. In the second conformation, **ii**, the opposite case is true, the *meta*-benzoate has a large dihedral angle with respect to the central phenyl ring while the *para*-benzoates lie approximately coplanar to the central phenyl ring. It can be seen that the dihedral angles are spread over a broad range of values. These dihedral angles and the variety in angle size would be inaccessible without the presence of the acetylene spacer moieties within the linker.

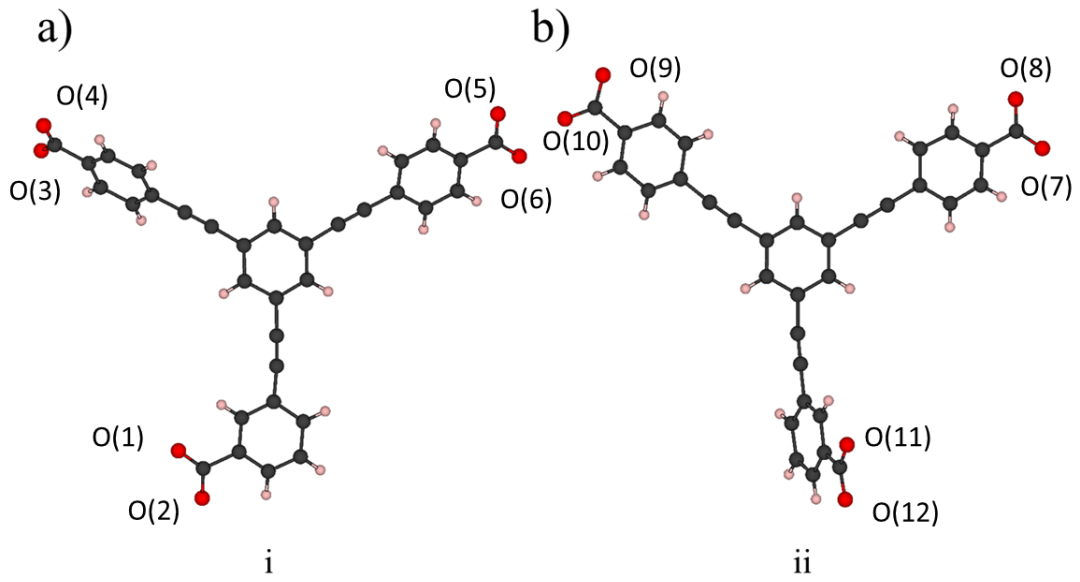

Figure 3.9: Conformations a) i and b) ii of the linker $BTEB_{ppm}^{3-}$ found in 6. (C-black, O -red, H – pink)

Table 3.2: Dihedral angles between the plane of the central phenyl ring and the plane of the benzoate moieties in 6.

Conformation	Dihedral angles involving *para*-benzoate moiety (º)	Dihedral angles involving *para*-benzoate moiety (º)	Dihedral angles involving *meta*-benzoate moiety (º)
i	56.1 (2)º	32.6 (2)º	6.3 (5)º
ii	1.3 (6)º	19.3 (8)º	64.1 (9)º

The structure of the MOF is of a three-dimensional framework with channels that extend along the crystallographic *b*-axis. The framework is similar in appearance to archetype MOF frameworks which are comprised of pillared two-dimensional sheets, with large voids located between the sheets.[299,300,217] However, in this instance, there is no secondary linker used to achieve the pillaring effect (**Figure 3.10 b)/c)**). The sheet-like units are interconnected by the $BTEB_{ppm}^{3-}$ linkers which adopt **i** conformation**.** The linker in **ii** conformation is located on the external faces of each sheet-like unit. The $\{Cu_2\}$ SBU with the **γ** arrangement is located at the centre of the sheet-like unit while the $\{Cu_2\}$ SBUs with the **β** arrangement are located on the external surface of the sheet-like unit. Large voids, with diameters of *ca*. 7.5 Å, are located within the sheet unit. Larger voids within the MOF are facilitated by the channels that are located between the sheet-like units. The channels extend through the structure along the crystallographic *b*-axis and are characterised by an edge to edge diameter of approximately 12 Å.

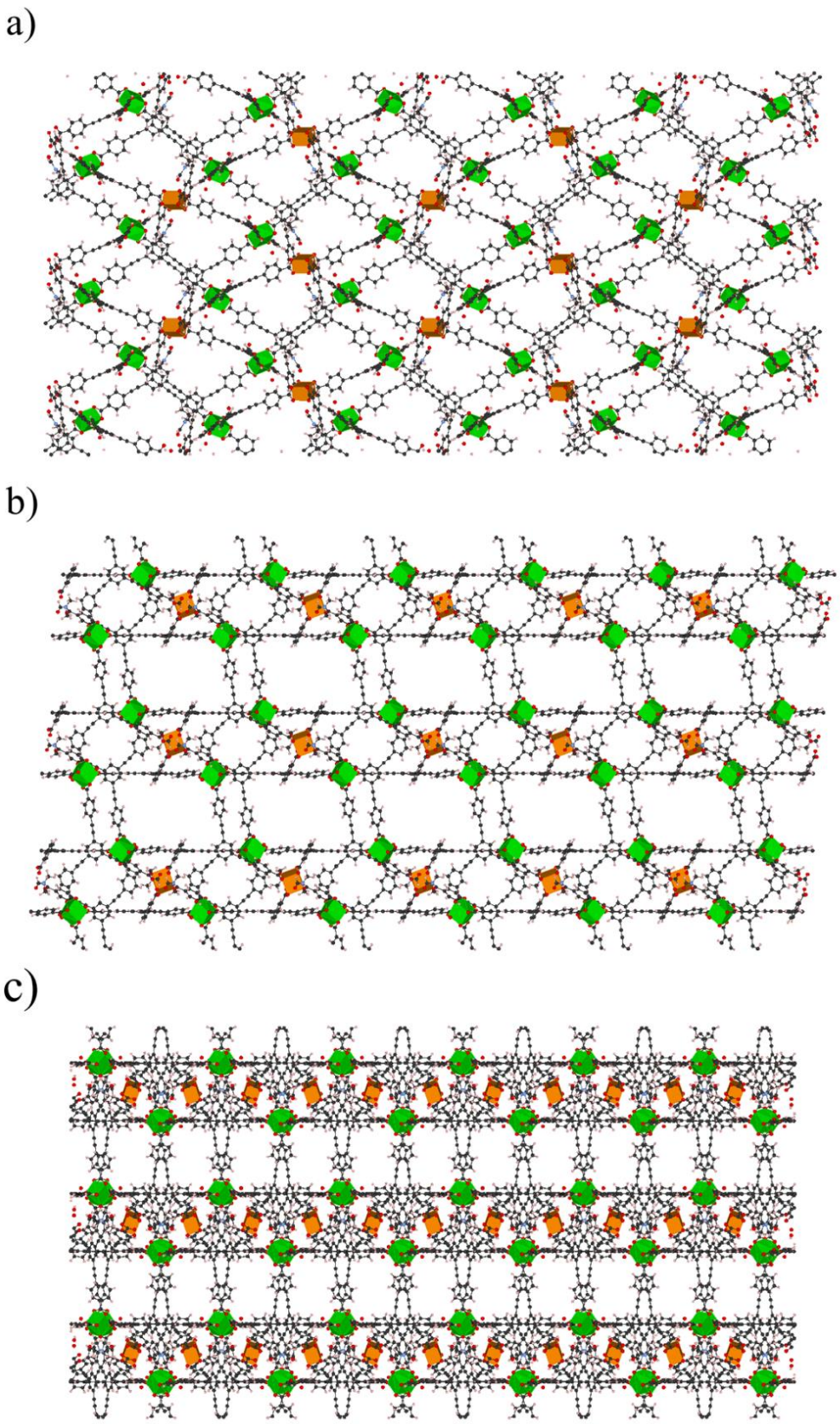

Figure 3.10: Packing diagram of 6 viewed along the crystallographic a) *a*-axis, b) *b*-axis and c) *c*-axis. (Green cubes – {Cu_2} SBUs with β arrangement, orange cubes – {Cu_2} SBUs with γ arrangement, O - red, C - grey, H - pink)

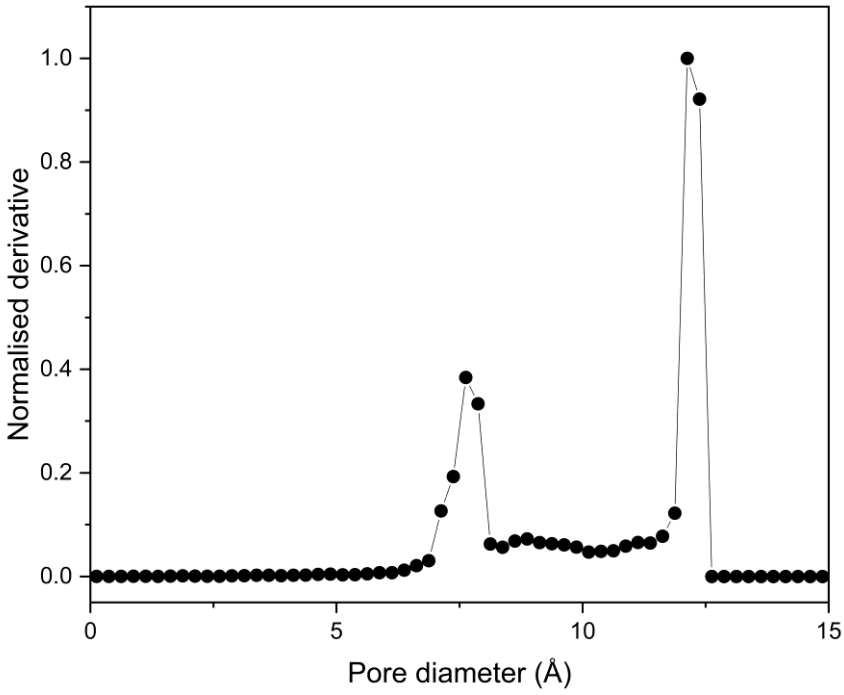

Figure 3.11: Simulated pore-size distribution for 6.

Computational methods were used to analyse the potential porosity of the desolvated framework. The Poreblazer software package was used to analyse the pore-size distribution and accessible surface area.[225] It was calculated that the desolvated structure has a He pore volume of 1.604 cm^3/g, and an accessible surface are of 4240 m^2/g. The MOF was found to have a limiting channel diameter of 8.1 Å and a maximum pore diameter of *ca.* 12.3 Å. As shown in **Figure 3.11**, the calculated pore-size distribution clearly highlights the two predominating pores in the structure. The smaller pore, with a pore diameter of *ca.* 7.6 Å, corresponds to the pores found within the sheet-like units of the structure. The larger pore has a medium pore diameter of *ca.* 12.1 Å corresponding to the channels between the sheet-like units which extend into the structure in the crystallographic *b*-axis (**Figure 3.10 b)**).

3.4.1.1 Powder X-ray diffraction

PXRD analysis was performed on a sample of **6** to verify the phase purity of the compound. The sample was prepared by grinding the crystalline sample to a fine powder while kept in the mother liquor. The sample was then loaded into a quartz capillary to avoid any loss of crystallinity of the sample due to solvent loss and associated capillary forces. The sample was measured at 215K, using a Bruker APEX II DUO X-ray diffractometer. Using the Expo2014 software package the background signal and fit the experimental diffraction to the theoretical diffraction pattern was calculated.[228,229]

Using the Rietveld method the unweighted profile R-factor and the weighted profile R-factor were calculated for the diffraction pattern.[230] The two factors were determined to be Rp = 1.970 and Rwp = 3.335 respectively. It was found that the experimental diffraction pattern matches well with the theoretical diffraction pattern (**Figure 3.12**).

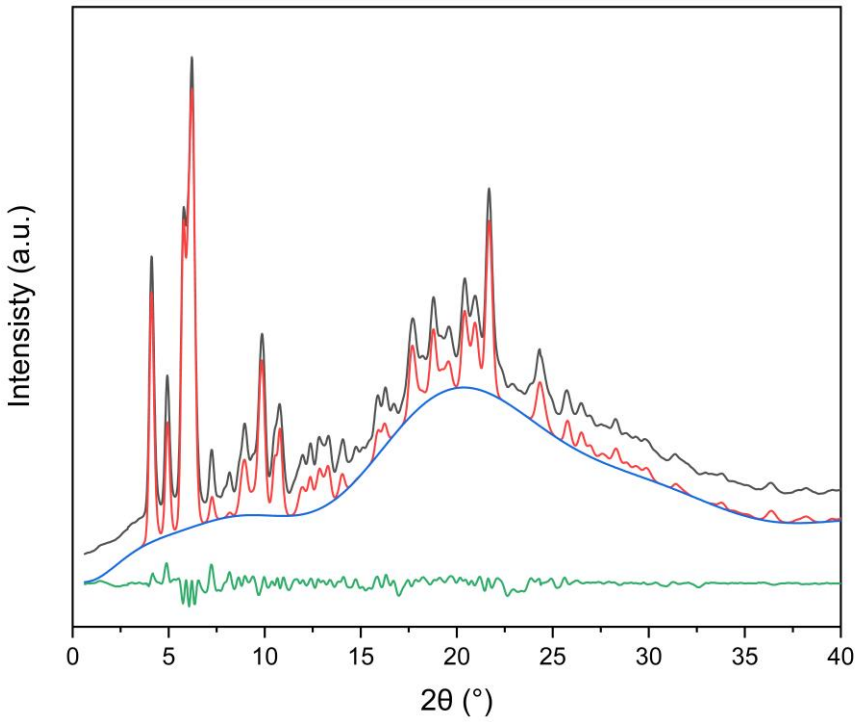

Figure 3.12: PXRD of 6 (Measured diffraction pattern – black, calculated background signal – blue, predicted diffraction pattern – red, the difference between measured and predicted – green.)

3.4.1.2 Thermogravimetric analysis

The thermal stability of the compound was examined using thermogravimetric analysis. The compound was prepared by removing crystals from a DMF solution. The crystals were then dried using filter paper to remove surface solvent residues from the crystals. The sample was then analysed by heating it from 20 ºC to 700 ºC at a rate of 4 ºC per minute under a nitrogen atmosphere (**Figure 3.13**). An initial loss of *ca.* 59 wt% was found to occur between 20 ºC to 114 ºC. This initial loss of mas is attributed to the loss of solvent molecules located within the pores of the structure. A second thermogravimetric step of *ca.* 7.7 wt% between 114 ºC to 298 ºC is due to the loss of strongly bound solvent molecules which coordinate to the $\{Cu_2\}$ SBUs. A further loss of *ca.* 6.03 wt% is found to occur between 298 ºC and 365 ºC. This is due to the degradation of the $BTEB_{ppm}^{3-}$ linkers.

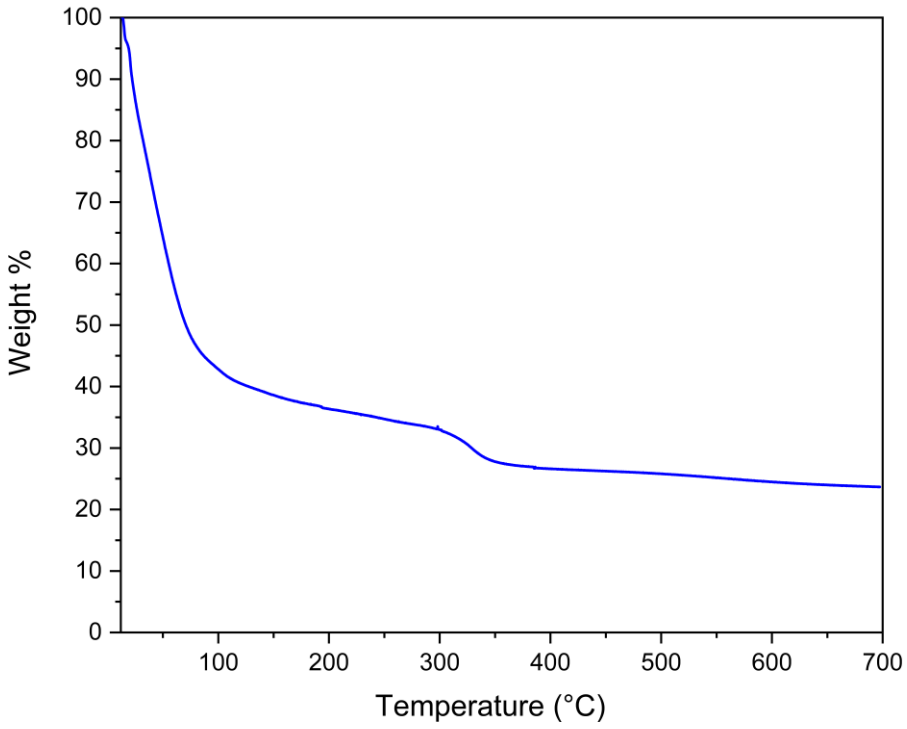

Figure 3.13: TGA of 6 heated from 20 ºC to 700 ºC at a rate of 4 ºC per minute.

3.4.1.3 FT-IR and Raman spectroscopy

FT-IR and Raman spectroscopy was used to characterise **6**. The two spectra were dominated by the signals from the $BTEB_{ppm}^{3-}$ linker. This confirms the presence of the $BTEB_{ppm}^{3-}$ linker within the structure of the MOF. In the FT-IR spectrum, a broad signal is found at 3459 cm^{-1} which is due to the presence of H-bonded solvent molecules located within the pores of the MOF or coordinated to the apical position on the Cu^{2+} ions. A pair bands at 2932 cm^{-1} and 2857 cm^{-1} is attributed to the C-H from DMF molecules both within the porous structure and coordinated to Cu^{2+} ions within the framework of the MOF. A strong signal due to the O=C stretching in the DMF molecule is found at 1664 cm^{-1}. The asymmetric carboxylate ν_{as}(COO) stretching mode of the $BTEB_{ppm}^{3-}$ linker is found at 1616 cm^{-1}, and the corresponding symmetric ν_s(COO) mode is found at 1435 cm^{-1}. Based upon the criterion outlined by Deacon and Philips the Δ value corresponding to the coordination mode, in this instance, is found to be 184 cm^{-1}, corresponds to the observed bidentate bridging mode.[233]

The Raman spectrum of **6** is mainly composed of signals from the $BTEB_{mmp}^{3-}$ linkers. The spectrum was measured from 100 cm^{-1} to 2500 cm^{-1}. A strong signal as 2209 cm^{-1} corresponds to the symmetric ν(C≡C) stretch. Two strong signals are found at 1604 cm^{-1} and 1580 cm^{-1} which correspond to aromatic ν(C=C) vibrations of the phenyl rings. Three peaks corresponding to aromatic C-C bonds are found at 1174 cm^{-1}, 1134 cm^{-1} and a shoulder at 1124cm^{-1}. The strong band found at 992 cm^{-1} is attributed to C-H bending from the central 1,3,5 trisubstituted phenyl ring.[235]

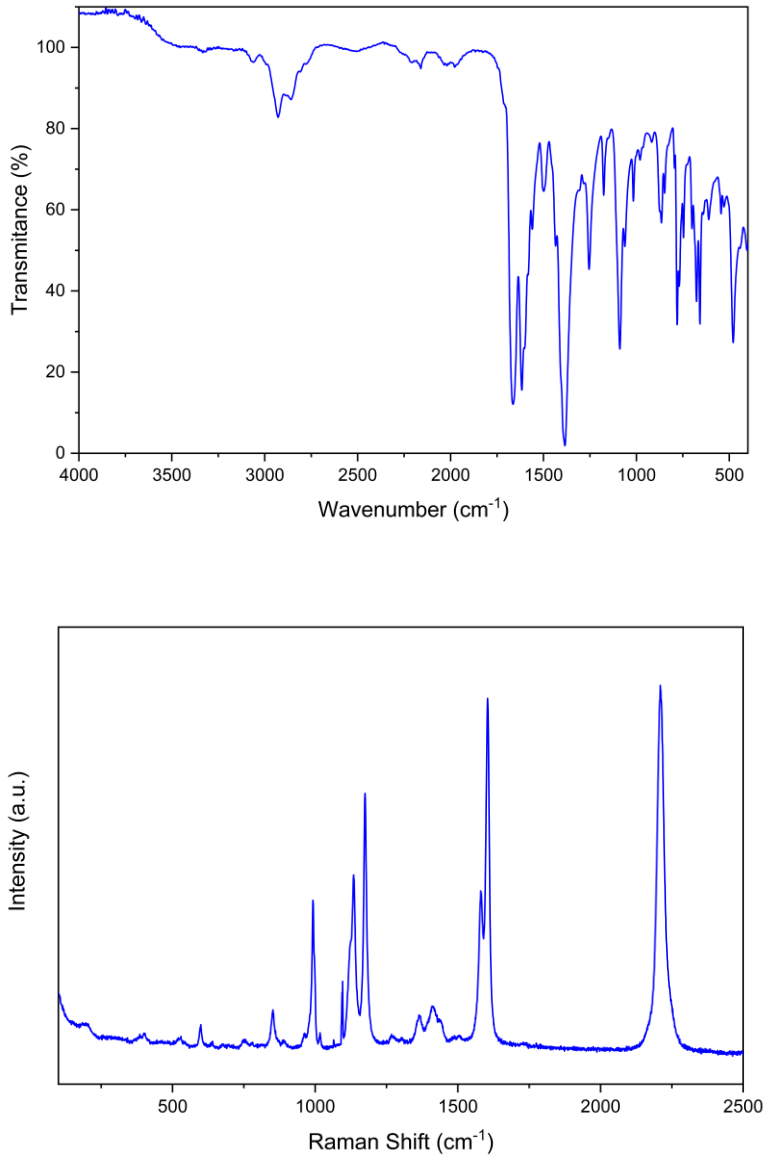

Figure 3.14: FT-IR and Raman spectra of 6.

3.4.1.4 Topology of **6**

Using the computational package ToposPro a topological analysis of **6** was carried.[257] The topological net was determined to be a 4-nodal (3, 3, 4, 4)-connected net. The structure contains two structurally distinct 3-connected nodes, which corresponds to the two conformations of the $BTEB_{ppm}^{3-}$ linker. These can be seen as pink and purple spheres for **i** and **ii** respectively in **Figure 3.15**. The topological representation also considers the two structurally distinct 4-connected nodes which correspond to the **β** (green spheres) and **γ** (orange spheres) arrangements for the $\{Cu_2\}$ SBUs. The overall point symbol for **6** was determined to be $\{8^2.10\}_2\{8^3.10^2.12\}\{8^3\}_2\{8^5.10\}_2$ representing a topology that has not previously been reported in the RCSR database.[61]

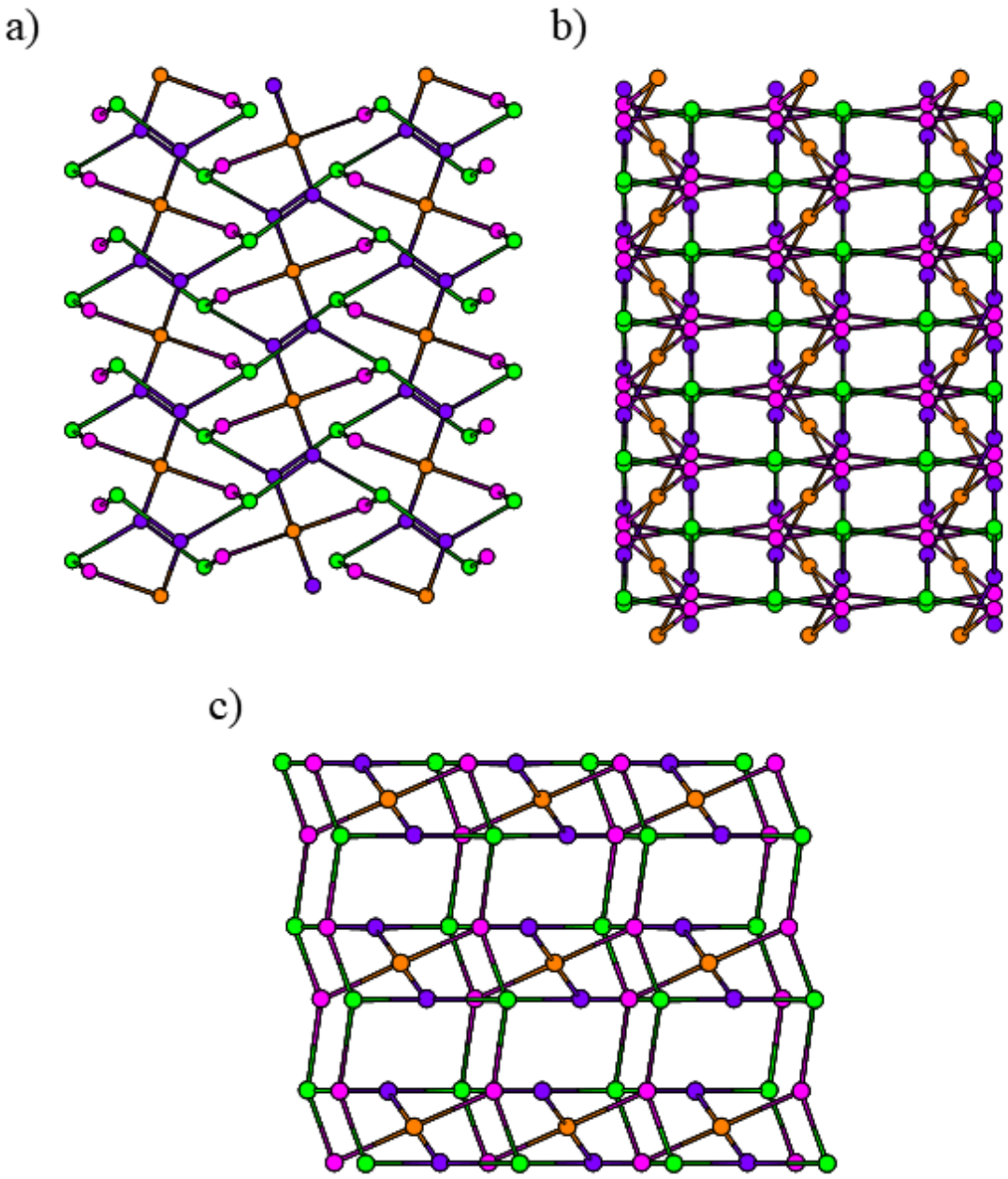

Figure 3.15: Graphical representation of the topological reduction for 6 viewed along the crystallographic a) *a*-axis, b) *b*-axis and c) *c*-axis (i – pink, ii – purple, {Cu_2} with β arrangement – green, {Cu_2} with γ arrangement – orange).

3.4.2 $[Cu_3(BTEB_{ppm})_2(DMF)(H_2O)_2]$ (**7**)

Through the simple alteration of the reaction conditions that were used to synthesise **6**, another MOF, $[Cu_3(BTEB_{ppm})_2(DMF)(H_2O)_2]$ (**7**), was synthesised using H_3BTEB_{ppm}. In this instance $Cu(NO_3)_2 \cdot 3H_2O$ and H_3BTEB_{ppm}, in a 2:1 mole ratio, were heated in 1 mL of a solution with 1 % (vol./vol.) HOAc in DMF at 85 ºC. Upon completion of the reaction, blue square, plate-like crystals were observed to have grown around the base of the reaction vial. The square plate-shaped crystals were collected and used for single-crystal X-ray analysis. In some instances, while synthesising the MOF, trace amounts of **6** were found to co-crystalise on the reaction vial near the surface of the reaction mixture. This minor side product was manually separated from the main product. The crystals of **7** were measured, and the structure was solved in the monoclinic space group *C*2/*c*. with unit cell dimensions for the structure determined to be a = 29.642(4) Å, b = 32.317(4) Å, c = 41.341(5) Å, α = 90°, β = 103.21(2)°, γ = 90°.

7 has the empirical formula $[Cu_3(BTEB_{ppm})_2(DMF)(H_2O)_2]$. The asymmetric unit contains three Cu^{2+} ions coordinated by two fully deprotonated $BTEB_{ppm}^{3-}$ linkers and solvent molecules. The three Cu^{2+} ions form the distinctive $\{Cu_2\}$ paddlewheel SBUs. One $\{Cu_2\}$ SBU is composed of Cu(1) and its symmetry equivalent Cu(1)' while the second $\{Cu_2\}$ SBU is composed of Cu(2) and Cu(3). Each Cu^{2+} ion is coordinated by four O-donor atoms from carboxylate groups of the $BTEB_{ppm}^{3-}$ linkers and one O-donor atom from a DMF or an H_2O solvent molecule. This places each Cu^{2+} ion in a square base pyramidal coordination environment with the O-donor atoms from the four carboxylate groups forming the square base of the pyramid and the O-donor atom of the solvent molecule located at the apical position. The carboxylate groups coordinate to the Cu^{2+} ions in a *syn,syn*-bidentate (μ_2-η^1:η^1) bridging mode forming the $\{Cu_2\}$ SBUs. The structural parameters of the $\{Cu_2\}$ SBUS are comparable to those of other literature known $\{Cu_2\}$ SBUs and in compounds previously discussed in **Chapter 2**. The origin of the O-donor atoms at the apical position differs across the three Cu^{2+} ions with Cu(1), its symmetry equivalent, and Cu(3) being coordinated by H_2O solvent molecules and Cu(2) being coordinated by a DMF solvent molecule.

The two $\{Cu_2\}$ SBUs are found to have different arrangements of the coordinating benzoate moieties. The $\{Cu_2\}$ SBU, which consists of Cu(1) and Cu(1)', is coordinated by *para*-benzoate moieties. This gives the $\{Cu_2\}$ SBU the structural arrangement of **α** considering the nomenclature described in **Section 3.3** (**Figure 3.16 a)**). The secondary $\{Cu_2\}$ SBU is comprised of Cu(2) and Cu(3) with each of the Cu^{2+} ions being coordinated by two *para*-benzoate and two *meta*-benzoate moieties in a *trans* configuration, denoted by the symbol **δ** (**Figure 3.16 b)**). The two different geometrical arrangements occur in a 1:2 ratio giving the notation $\boldsymbol{\alpha\delta_2}$, which agrees with the charge-balancing stoichiometry and allowable combinations as shown in **Figure 3.1**.

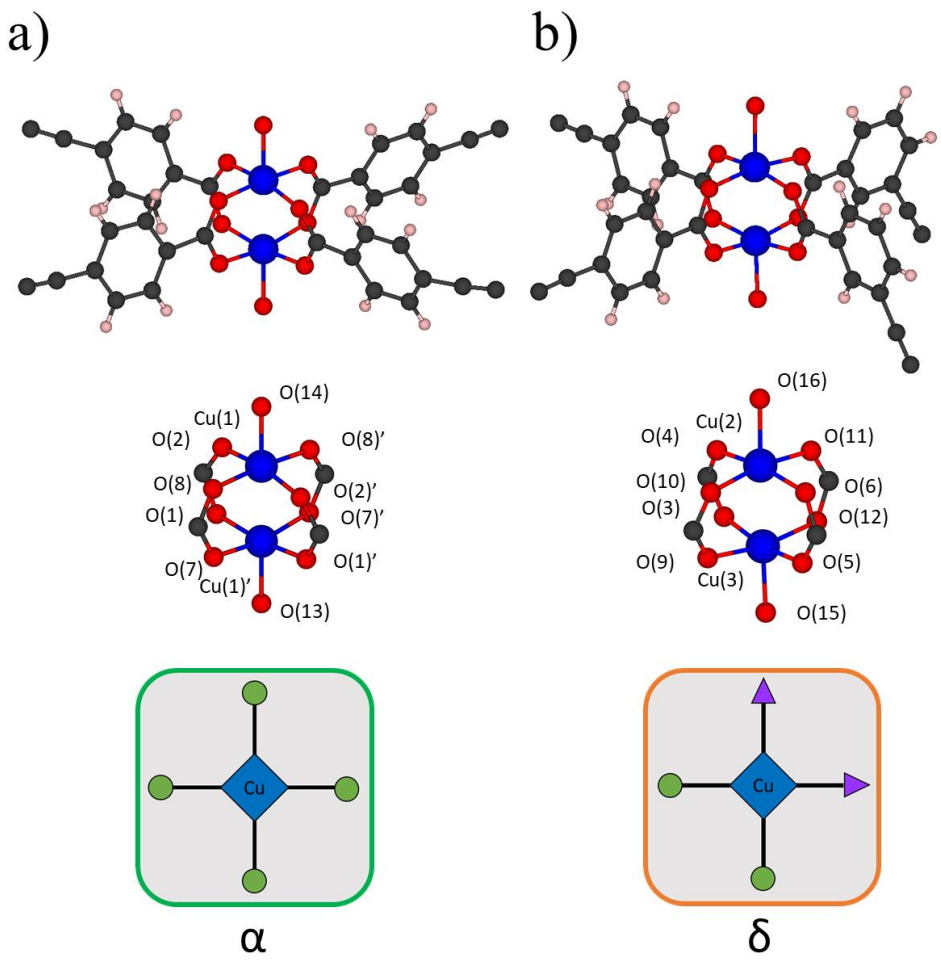

Figure 3.16: The two arrangements of the benzoate moieties around the two {Cu_2} SBUs found in 7. (C – black, O – red, H – pink, Cu - blue)

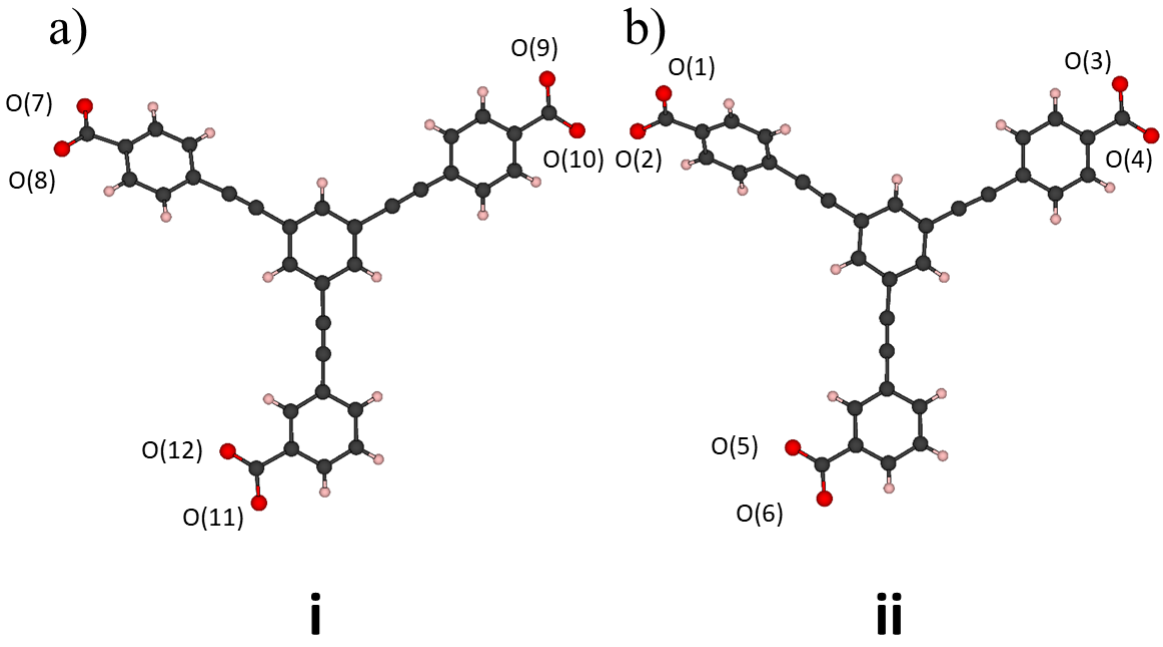

Figure 3.17: Two conformations, a) i and b) ii, of the $BTEB_{ppm}^{3-}$ linker found in 7(C – black, O – red, H – pink)

The $BTEB_{ppm}^{3-}$ linker adopts two conformations within the structure of **7** (**Figure 3.17**). The two conformations are similar in structure with the dihedral angles between the benzoate moieties and central phenyl ring having only slight variations, < 15º, between the two conformations (**Table 3.3**). In the two conformations, **i** and **ii (**see **Figure 3.17),** the *para*-benzoate moieties that have the largest dihedral angles, 29.4º and 48.2 coordinate to Cu(1) and Cu(1)' to form $\{Cu_2\}$ SBUs with the **α** arrangement. The *para*-benzoate moieties with the smaller dihedral angles, 14.8º and 0.5º, in combination with the *meta*-benzoate moieties coordinate to Cu(2) and Cu(3) to produce the $\{Cu_2\}$ SBUs with **δ** arrangement. While the two conformations of the $BTEB_{ppm}^{3-}$ linkers in **7** are similar to each other, they are distinctively unalike to two conformations found in **6**.

Table 3.3: Dihedral angles between the mean plane of the central phenyl ring and the mean plane of the benzoate moieties in 7.

Conformation	Dihedral angles involving *para*-benzoate moiety (º)	Dihedral angles involving *para*-benzoate moiety (º)	Dihedral angles involving *meta*-benzoate moiety (º)
i	29.4(4) º	14.8(3) º	1.5(3) º
ii	48.2(2) º	0.5(2) º	2.9(3) º

The extended structure is comprised of interpenetrated two-dimensional frameworks. Each framework forms a series of cuboid-shaped units as shown in (**Figure 3.18 a)**). The $\{Cu_2\}$ SBUs with **δ** arrangement act as the eight vertices of the cuboid represented as orange cubes in **Figure 3.18 a)**. The **δ** $\{Cu_2\}$ SBUs have a distance of *ca.* 21.9 Å along the short edge of the cuboid and *ca.* 27.3 Å along the longest edge. Each cuboid unit contains one $\{Cu_2\}$ SBU with an **α** arrangement which is shown as a green cube in **Figure 3.18 a)**. In **Figure 3.18 a)** and **b),** two additional $\{Cu_2\}$ SBUs with the **α** arrangement are shown to complete the connections between the top four $\{Cu_2\}$ SBUs and the bottom four $\{Cu_2\}$ SBUs in the unit. However, these additional $\{Cu_2\}$ SBUs are located within adjacent cuboid units. The cuboid units extend into the two-dimensional networks with the $\{Cu_2\}$ SUBs with the **δ** arrangement located on the outer external faces of the 2D assemblies while the$\{Cu_2\}$ SUBs with **α** arrangement are located at within the 2D layered structure (**Figure 3.18 c)**). The two-dimensional framework has a 4-connected framework topology while viewed along the crystallographic *c*-axis (**Figure 3.18 d)**). Large square windows located on the external faces of the sheet may allow access to the pores located within the framework.

In the complete structure of **7** the frameworks are doubly interpenetrated, with each framework being interlinked to two other sheets in a lamellar like fashion (**Figure 3.19 a)**). The sheets stack along the crystallographic *c*-axis. The interpenetration reduces the void space within each sheet layer, however, and a series of large channels are formed that extend into the structure along the [110], [111] and

[001] directions. The largest of these channels extend along the crystallographic *c*-axis (**Figure 3.19 c)**).

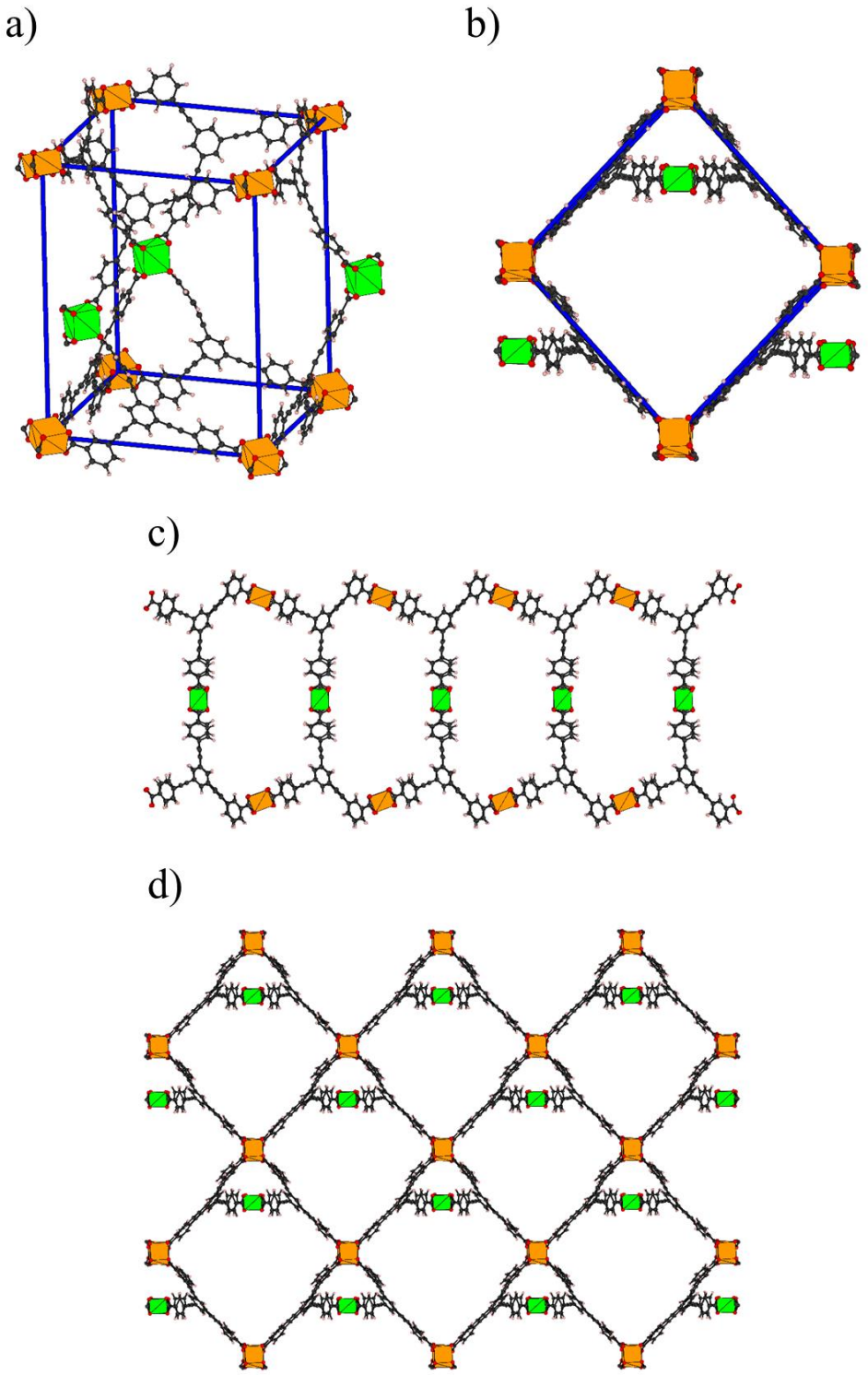

Figure 3.18: a) Cuboid-shaped unit with {Cu_2} SBUs with the δ arrangement located at each vertex. b) Cuboid-shaped unit viewed down the top square face. The sheet view along the c) crystallographic *a*-axis d) perpendicular to the sheet in the direction of the crystallographic *c*-axis. (Edges of the cuboid unit – blue lines, {Cu_2} SBU with δ arrangement - orange, {Cu_2} SBU with α arrangement – green, C – black, O – red, H- pink)

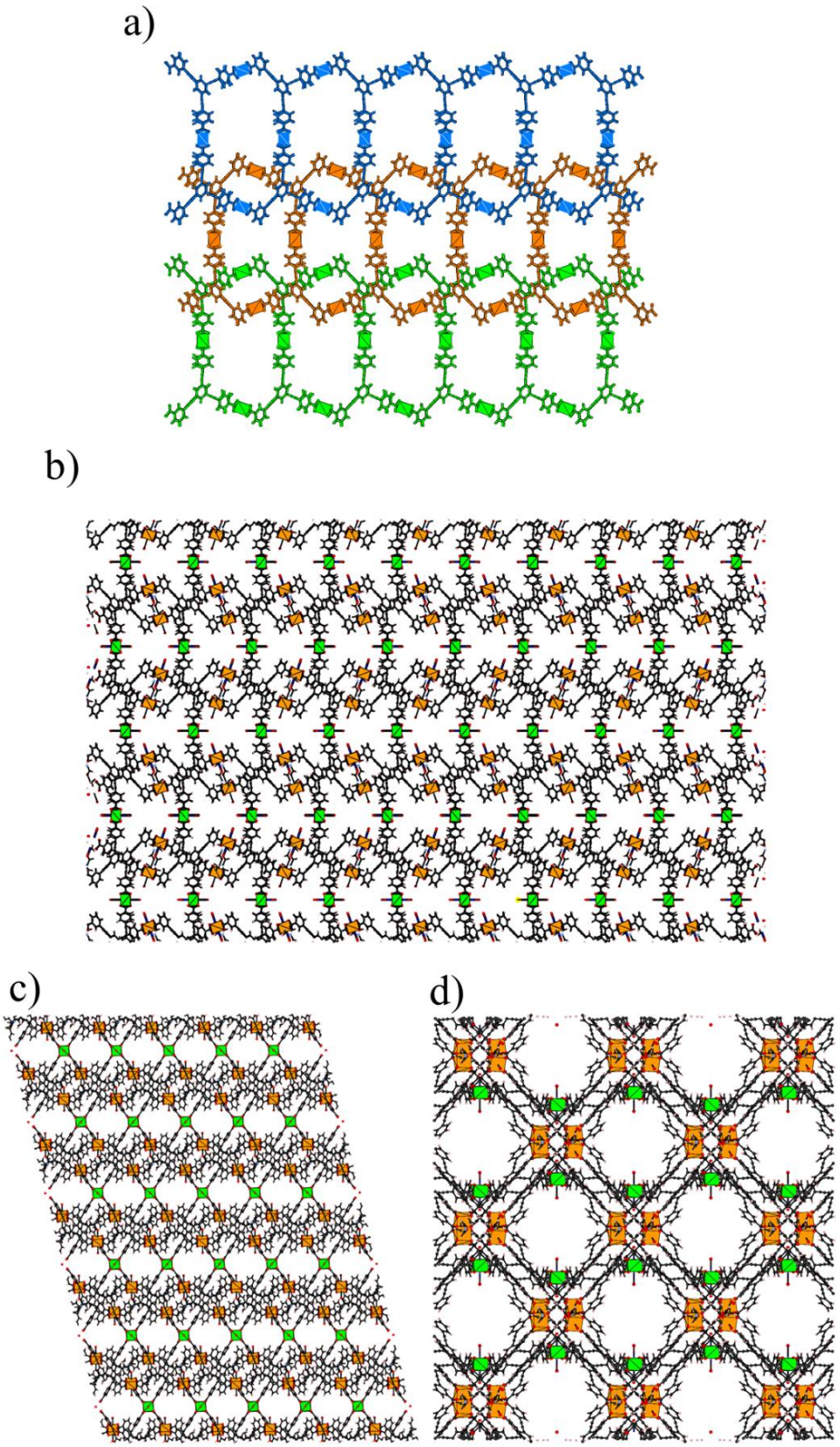

Figure 3.19: a) The interpenetration that occurs between the two-dimensional sheets found in 7. The central sheet (orange) is interpenetrated by two other sheets (blue and green). The packing diagram of 7 viewed along the crystallographic b) *a*-, c) *b*-, and d) *c*-axes, respectively.

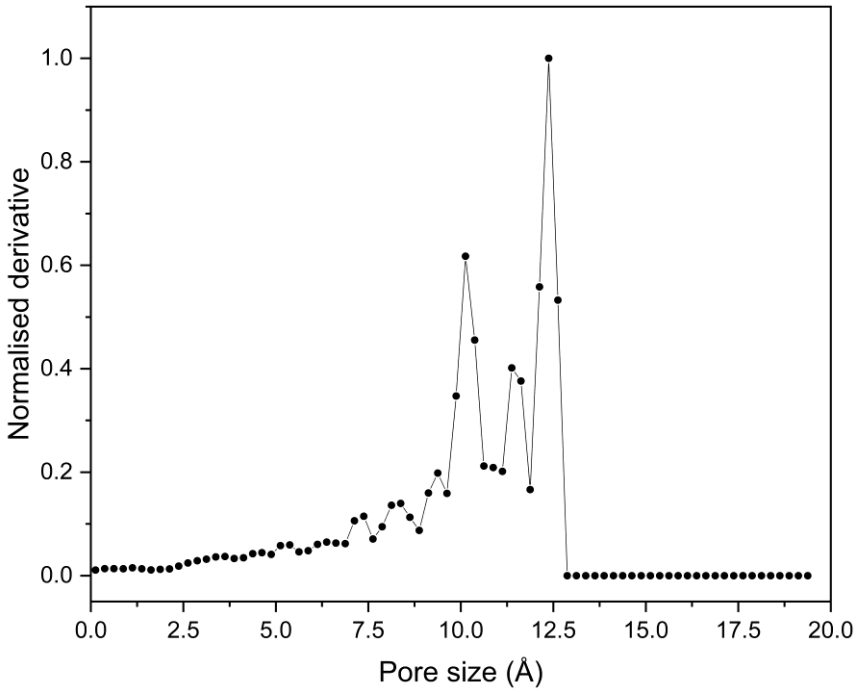

Figure 3.20: Simulated pore-size distribution of 7,

Computational methods were used to analyse the potential porosity of **7**. The Poreblazer software package was used to analyse the pore-size distribution and accessible surface area.[225] It was calculated that the desolvated structure has a He pore volume of *ca.* 1.599 cm^3/g and an accessible surface area found to be *ca.* 3946 m^2/g. The limiting channel diameter was determined to be *ca.* 9.5 Å and the maximum pore diameter was found to be *ca.* 12.6 Å. The calculated pore-size distribution shown in **Figure 3.20** indicates that the largest source of void volume observed within the structure was due to the channels that extend in the crystal structure along the crystallographic *c*-axis. The gradual increase of the normalised derivative of the pore volume with respect to its radius is indicative of square-shaped pores found within **7**.[225]

3.4.2.1 X-ray powder diffraction

The phase purity of **7** was verified using PXRD analysis. The sample was first prepared by grinding fresh crystals of **7** into a fine powder while keeping them within the mother liquor. The powdered crystals were then loaded into a quartz capillary. This was done to minimise any loss in crystallinity due to solvent loss and associated capillary forces. The sample was measured at 215 K, using a Bruker APEX II DUO X-ray diffractometer. Using the Expo2014 software package, the background signal and the fit of the experimental diffraction pattern to the theoretical diffraction pattern was calculated.[228,229]

Using the Rietveld method, the unweighted profile R-factor and the weighted profile R-factor were calculated for the diffraction pattern. The two factors were determined to be Rp = 2.518 and Rwp = 4.708, respectively. It was found that the experimental diffraction pattern matches well with the theoretical diffraction pattern that was obtained using single-crystal data (**Figure 3.21**).

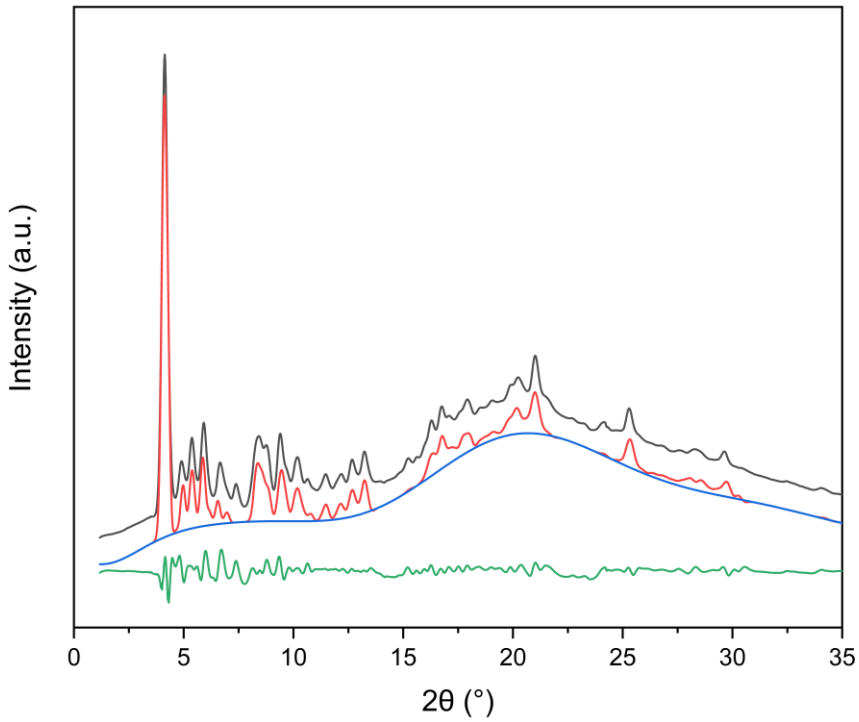

Figure 3.21: PXRD pattern for 7. (Measured diffraction pattern – black, calculated background signal – blue, predicted diffraction pattern – red, difference between measured and predicted – green.)

3.4.2.2 Thermogravimetric analysis

To examine the thermal stability of the **7,** thermogravimetric analysis was performed. The sample was prepared by removing fresh crystals from the mother liquor and drying the crystals between two sheets of filter paper to remove surface solvent residues. The analysis was carried out by heating the sample at 4 ºC per minute under a nitrogen atmosphere (**Figure 3.22**). An initial weight loss of *ca.* 44.3 % mass was found to occur between 20 ºC to 110 ºC. This is due to the loss of solvent molecules that are located in the voids within the framework. A secondary weight loss of *ca.* 11.42 %, between 110ºC to 273 ºC, ca be attributed to the loss of strongly bound solvent molecules that coordinate to the metal centres. A loss of *ca.* 6.87 % occurs between 273 ºC and 367 ºC owing to the decarboxylation of the $BTEB_{ppm}^{3-}$ linkers. A final weight loss of *ca.* 4.23 % results from the carbonisation and decomposition of the $BTEB_{ppm}^{3-}$ linkers.

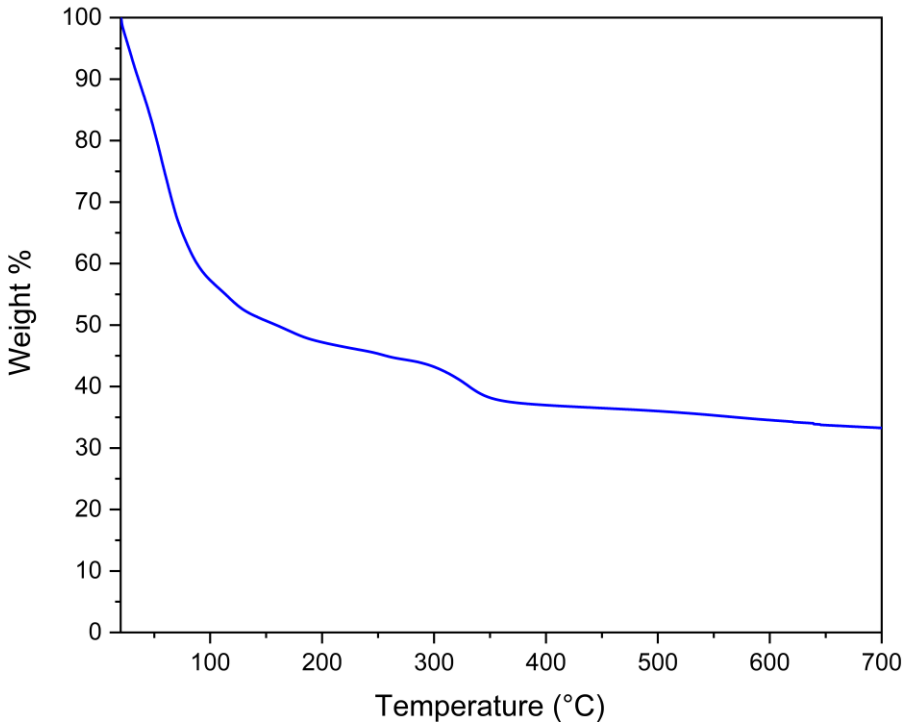

Figure 3.22: Thermogravimetric analysis of 7 heated at 4 ºC under a nitrogen atmosphere.

3.4.2.3 FT-IR and Raman spectroscopy

FT-IR and Raman spectroscopy were used in the characterisation of **7** (**Figure 3.23**). The two spectra are dominated by the signals from the $BTEB_{ppm}^{3-}$ linker. This confirms the presence of the $BTEB_{ppm}^{3-}$ linker within the structure of the MOF. In the FT-IR spectrum, a broad band is found at 3459 cm^{-1} which is due to the presence of H-bonded solvent molecules located within the pores of the MOF or coordinated to the apical positions on the Cu^{2+} ions in the SBUs. A pair of bands at 2933 cm^{-1} and 2856 cm^{-1} is attributed to the ν(C-H) vibrations from DMF molecules both, located within the pore structure and coordinated to Cu^{2+} ions within the framework of the MOF. Bands associated with aromatic overtones are found at 2211 cm^{-1}, 2161 cm^{-1}, 2018 cm^{-1} and 1977 cm^{-1}. A strong band due to the ν(O=C) stretching in the DMF molecules is found at 1664 cm^{-1}. The asymmetric carboxylate ν_{as}(COO) stretching vibration of the $BTEB_{ppm}^{3-}$ linker is found at 1616 cm^{-1}, and the corresponding symmetric ν_s(COO) vibrational band is found at 1435 cm^{-1}. A Deacon and Philips value Δ = 184 cm^{-}, corresponds to the observed bidentate bridging mode.[233]

The Raman spectrum of **6** is mainly composed of bands from the $BTEB_{mmp}^{3-}$ linkers. The spectrum was measured from 100 cm^{-1} to 2500 cm^{-1}. A strong band as 2209 cm^{-1} corresponds to the symmetric ν(C≡C) stretch. Two strong bands are found at 1603 cm^{-1} and 1582 cm^{-1} which correspond to aromatic ν(C=C) vibrations of the phenyl rings. Three bands corresponding to aromatic ν(C-C) bond vibrations are found at 1174 cm^{-1}, 1134 cm^{-1} and at 1124 cm^{-1}. The strong band found at 994 cm^{-1} can be attributed to C-H bending vibrations from the central 1,3,5-trisubstituted phenyl ring.[235]

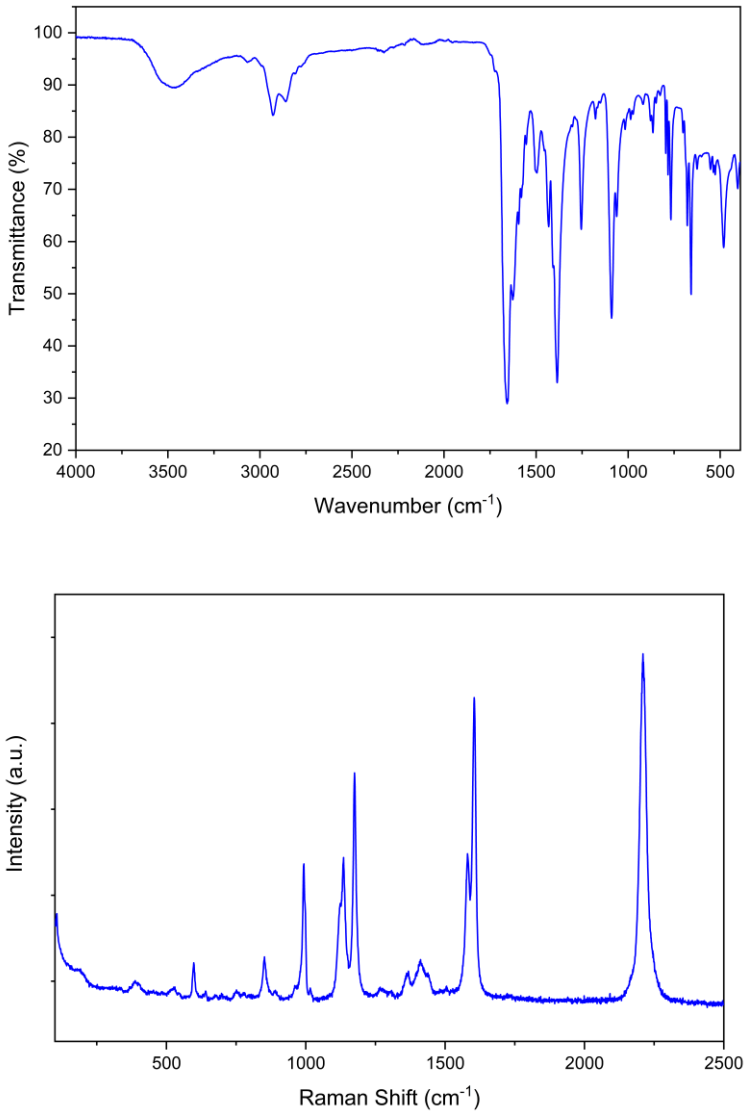

Figure 3.23: FT-IR and Raman spectra of 7.

3.4.2.4 Topology of **7**

Using the software package, ToposPro, a topological analysis of **7**was carried out.[257] The net topology for **7** was determined to be a 3-nodal, (3,4,4)-connected net. The overall point symbol was ascertained and found to be $\{4.8^2\}_4\{4.8^5\}_2\{4^2.8^4\}$. This is a newly discovered net that has not previously been reported in the RCSR database.[61] The 3-connected node corresponds to the two conformations of the $BTEB_{ppm}^{3-}$ linkers. While the $BTEB_{ppm}^{3-}$ linkers are found in two conformations within the framework, they were deemed to be topologically identical within the structure. The two remaining 4-connected nodes correspond to the two $\{Cu_2\}$ SBU types. The overall stoichiometry for **7** is reflected in the point symbol, $(3\text{-c})_4(4\text{-c})_2(4\text{-c})$. In **Figure 3.24**, the $\{Cu_2\}$ SBUs with **α** arrangement are highlighted in green while the $\{Cu_2\}$ SBUs with **δ** arrangement are highlighted in orange.

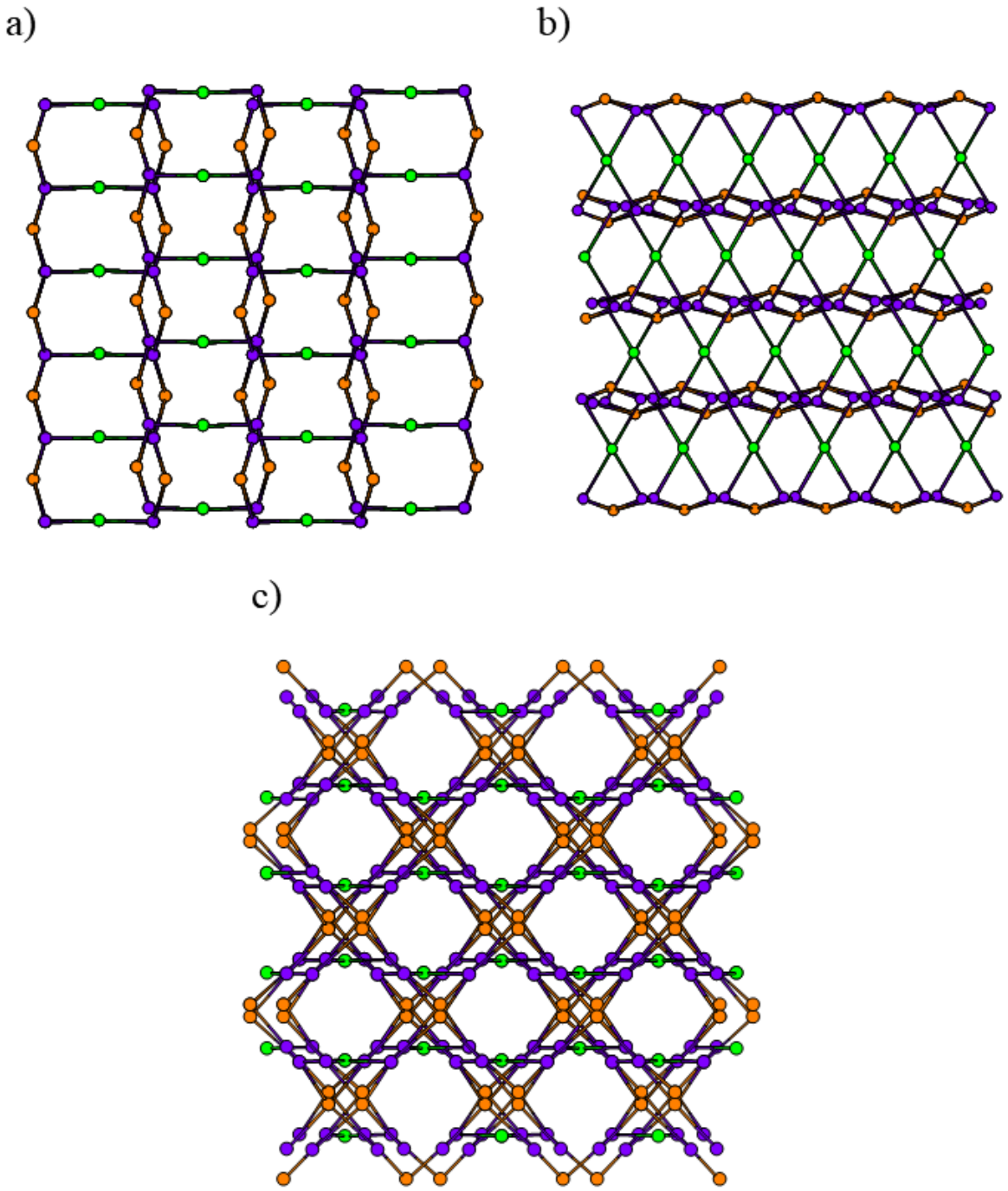

Figure 3.24: Topological representation of 7 viewed along the crystallographic a) *a*-axis, b) *b*-axis and c) c-axis. ({Cu_2} SBU with α arrangement – green, {Cu_2} SBU with δ arrangement – orange, $BTEB_{ppm}^{3-}$ linker – purple).

Table 3.4: Crystallographic details for 6 and 7

Identification code	6	7
Empirical formula	$C_{69}H_{41}Cu_3NO_{15}$	$C_{69}H_{41}Cu_3NO_{15}$
Formula weight	1314.65	1314.65
Temperature/K	215(2)	215(2)
Crystal system	Monoclinic	Monoclinic
Space group	*P21/c*	*C2/c*
***a* / Å**	21.759(7)	29.642(4)
***b* / Å**	20.042(7)	32.317(4)
***c* / Å**	40.745(13)	41.341(5)
***α* / º**	90	90
***β* / º**	94.52(2)	103.21(2)
***γ* / º**	90	90
Volume / Å^3	17715(10)	38618(9)
Z	4	8
gρ_{calc}/ g/cm^3	0.493	0.452
μ / mm^{-1}	0.618	0.567
F(000)	2376	5352
Crystal size / mm^3	0.280 × 0.190 × 0.190	0.160 × 0.110 × 0.050
Radiation	CuKα (λ = 1.54178 Å)	CuKα (λ = 1.54178 Å)
θ range for data collection / º	3.098 to 57.499	2.051 to 45.853
Index ranges	-23<=h<=23, -21<=k<=21, -44<=l<=33	-27<=h<=27, -29<=k<=30, -38<=l<=38
Reflections collected	83372	72251
Independent reflections	23782 [R(int) = 0.0755]	16150 [R(int) = 0.1001]
Data/restraints/parameters	23782 / 0 / 793	16150 / 4 / 699
Goodness-of-fit on F^2	0.958	1.078
Final R indexes [I>=2σ (I)]	R_1 = 0.0705, wR_2 = 0.2104	R_1 = 0.0855, wR_2 = 0.02668
Final R indexes [all data]	R_1 = 0.1024, wR_2 = 0.2104	R_1 = 0.1264, wR_2 = 0.2968
Largest diff. peak/hole / e.Å^{-3}	0.815 and -0.436	0.489 and -0.344

3.4.3 $[Cu_3(BTEB_{mmp})_2(H_2O)_3]$ (**8**)

$[Cu_3(BTEB_{mmp})_2(H_2O)(DMF)_2]$ (**8**) was synthesised by reacting $Cu(OAc)_2{\cdot}2H_2O$ and H_3BTEB_{mmp}, in a 1.5 : 1 mole ratio in a DMF solution, containing 1 vol% HOAc. The solution was heated to 85 ºC for 48 h. After the reaction, blue, square plate-like crystals were discovered to have grown on the walls of the reaction vial near the surface of the reaction solution. The crystals were collected, and it was found that the majority of the crystals were twined. By cutting a section off of a twined crystal, a single crystal was isolated. The crystal was analysed using single-crystal X-ray diffraction. The crystals structure was measured and solved in the orthorhombic space group $I2_12_12_1$. The unit cell parameters were determined to be a = 26.854(6) Å, b = 32.384(8) Å, c = 42.121(9) Å, $\alpha = \beta = \gamma$ = 90°.

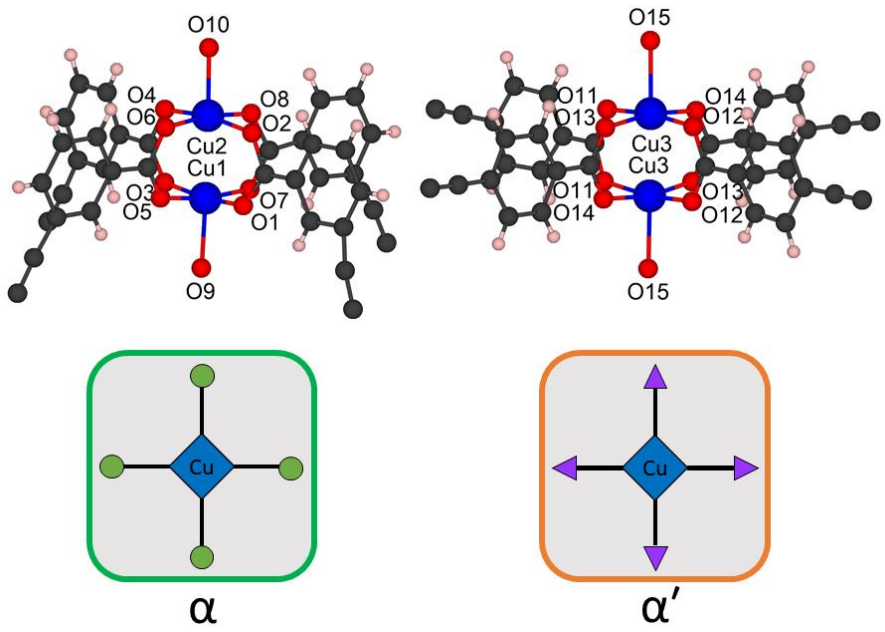

Figure 3.25: Labelled representation of the two $\{Cu_2\}$ SBUs found in the structure of 8. b) Graphical representation of the coordination of the benzoate moieties to the $\{Cu_2\}$ SBUs. Both SBUs have the α arrangement. (C – black, O – red, H – pink, Cu – dark blue)

The structure of **8** was found to be composed of interpenetrated two-dimensional sheets; the structure has the empirical formula $[Cu_3(BTEB_{mmp})_2(H_2O)(DMF)_2]$. The asymmetric unit of **8** contains three Cu^{2+} ions coordinated by one complete $BTEB_{mmp}^{3-}$ linker and two half completed $BTEB_{mmp}^{3-}$ linkers. The Cu^{2+} ions form the dimeric $\{Cu_2\}$ SBUs with one $\{Cu_2\}$ SBU being comprised of Cu(1) and Cu(2) while the second $\{Cu_2\}$ SBU is comprised of Cu(3) and its symmetry equivalent Cu(3)'. The Cu^{2+} ions are coordinated by four O-donor atoms from carboxylate groups creating the base of the square base pyramidal coordination environment. The carboxylate groups bridge two Cu^{2+} ions in a *syn*,*syn*-bidentate (μ_2-η^1:η^1) binding mode forming the $\{Cu_2\}$ paddlewheel SBUs. All bond lengths and angles found of the SBU are similar to literature known $\{Cu_2\}$ SBUs and the compounds

previously discussed.[223] O-donor atoms from H_2O solvent molecules coordinate to the Cu^{2+} ions at their apical positions, completing the square base pyramidal coordination environment.

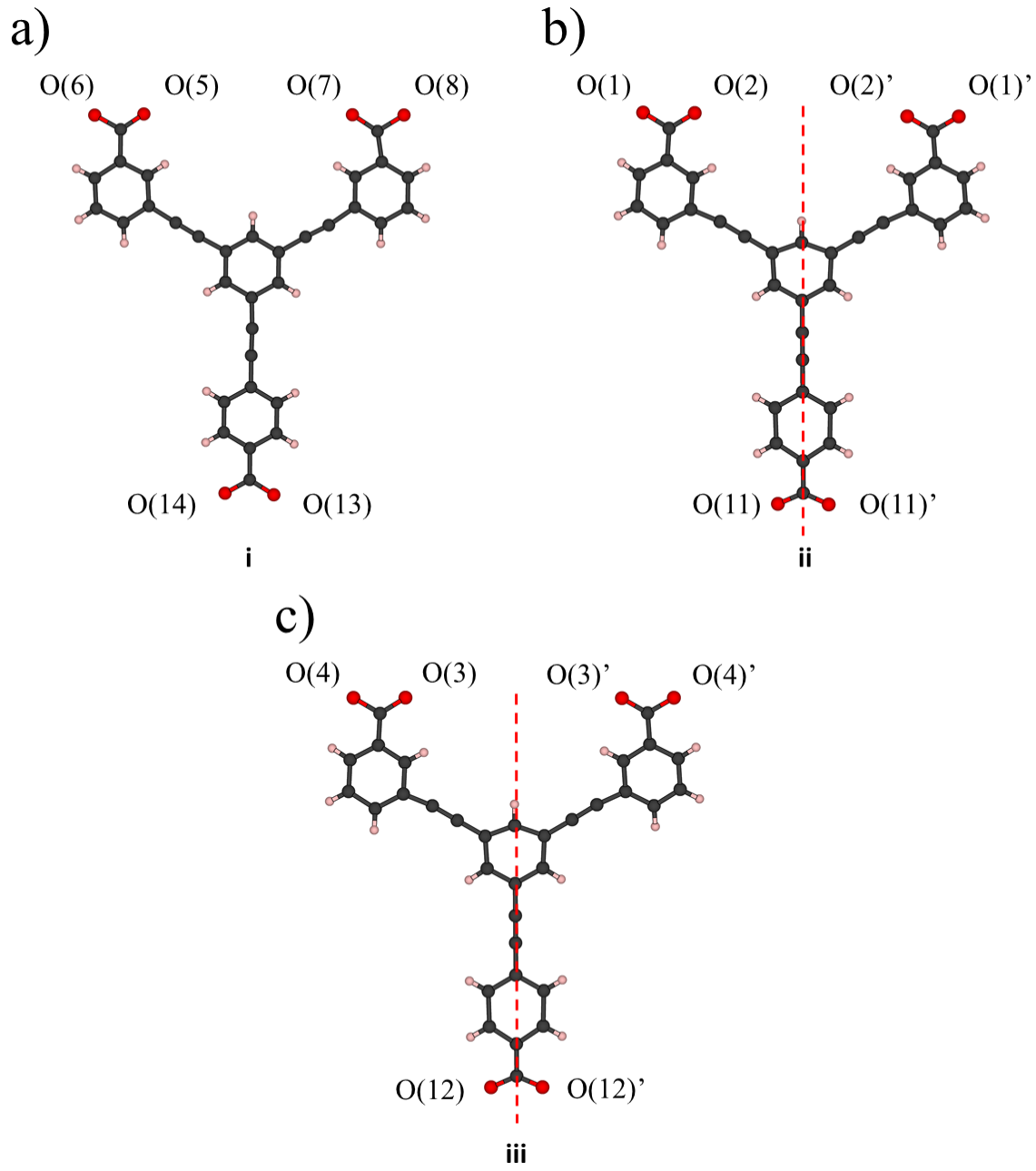

Figure 3.26: The three crystallographically distinct conformations of the $BTEB_{mmp}^{3-}$ linkers in 8. a) i, b) ii, c) iii. The plane of symmetry that divides the two conformations ii and iii is shown in red. (C – black, O – red, H – pink)

Two structurally distinct $\{Cu_2\}$ SBUs are present within the framework (**Figure 3.25**). Each $\{Cu_2\}$ SBU is coordinated by four tridentate $BTEB_{mmp}^{3-}$ linkers. One $\{Cu_2\}$ SBU, which is comprised of Cu(1) and Cu(2), is coordinated by four *meta*-benzoate moieties. This arrangement is denoted by the symbol **α** (**Figure 3.25 a)**). A second $\{Cu_2\}$ SBU, which is comprised of Cu(3) and Cu(3)', is coordinated by four *para*-benzoate moieties giving an **α'** arrangement (**Figure 3.25 b)**). The " ' " symbol indicates that while it is the same arrangement of moieties coordinating to the $\{Cu_2\}$ SBU,

in this instance, the majority of coordinating moieties are the secondary moieties on the $BTEB_{ppm}^{3-}$ linker. The two different geometrical arrangements are found in a ratio of 2:1, represented by the notation **$\alpha_2\alpha$'**. This combination of arrangements is in line with charge considerations and the possible combinations summarised in **Table 3.1**.

Table 3.5: Dihedral angles between the average plane of the central phenyl ring and the plane of the peripheral benzoate moieties in 8. (O – red, C – black, H – pink)

Conformation	Dihedral angles involving *meta*-benzoate moiety (º)	Dihedral angles involving *meta*-benzoate moiety (º)	Dihedral angles involving *para*-benzoate moiety (º)
i	0.9(4)	1.6(4)	4.6(4)
ii	1.8(5)	-1.8(5)	5.3(10)
iii	4.0(4)	-4.0(4)	0.7(8)

Three cryptographically distinct $BTEB_{ppm}^{3-}$ linkers are found within the framework of **8**. The asymmetric unit contains one complete $BTEB_{ppm}^{3-}$ linker, see **Figure 3.26 a)** and two half-completed $BTEB_{ppm}^{3-}$. The two half-completed $BTEB_{ppm}^{3-}$ linkers are divided by a plane of symmetry that lies along the axis of the *para*-benzoate moiety (**Figure 3.26 a) & b)**). While each of the $BTEB_{ppm}^{3-}$ linkers are crystallographically distinct, they are structurally and topologically identical. This can be seen in the minor variations of the dihedral angles, < 5º, that are found in the three conformations (**Table 3.5**).

Two $\{Cu_2\}$ SBUs, with the **α** arrangement, are bridged by four $BTEB_{mmp}^{3-}$ linkers to create a larger unit called a "super paddlewheel" which is abbreviated as $\{Cu_4\}$ unit in future discussions (**Figure 3.27**).[196,301,302] Like the super-paddlewheel units found in **1** and **5** it is structurally similar to the smaller $\{Cu_2\}$ SBU, with both units acting as a 4-connecting node with C_4 symmetry. The $\{Cu_4\}$ can be treated as a $\{Cu_2\}$ SBU unit that has been elongated along the Cu-Cu axis of the paddlewheel. This expansion leads to the creation of an internal pore within the $\{Cu_4\}$ unit. The pore can be defined by the distance between the two internal copper ions. This inter Cu-Cu distance is *ca.* 9.2 (4) Å. The distance between the central phenyl rings of the $BTEB_{mmp}^{3-}$ linkerss, are found to be *ca.* 17.5 (13) Å.

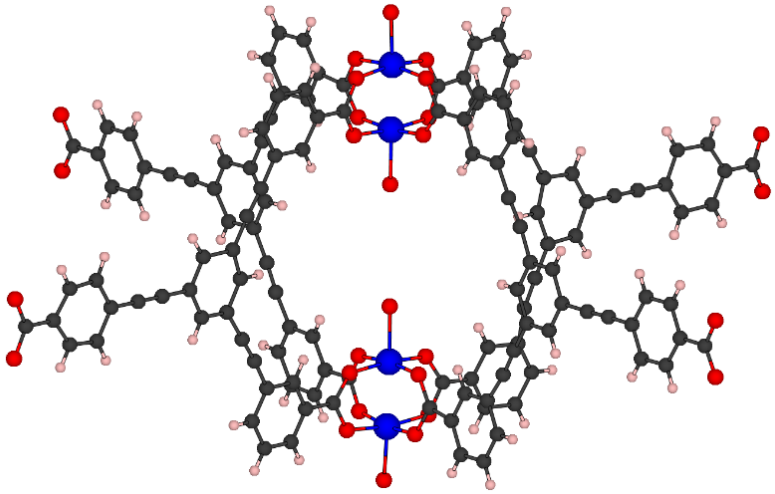

Figure 3.27: Four $BTEB_{mmp}^{3-}$ linkers bridging two $\{Cu_2\}$ SBUs to generate the $\{Cu_4\}$ super-paddlewheel unit. (C – black, O – red, H – pink, Cu – dark blue)

The $\{Cu_2\}$ SBU and $\{Cu_4\}$ unit assemble into a two-dimensional sheet with the two units alternating in a checkerboard-like pattern (**Figure 3.28 a) & b)**). This pattern creates a series of square pores within the sheet. The four vertices of the square pores are comprised of two $\{Cu_2\}$ SBUs and two $\{Cu_4\}$ units located at opposite corners, while the four sides of the pore are comprised of four $BTEB_{mmp}^{3-}$ linkers. The resulting pores have cross-sectional diameters of *ca.* 21.1 Å. The size difference of the $\{Cu_2\}$ and the $\{Cu_4\}$ units results in an unequal distance of the external Cu^{2+} ions to the central plane of the two-dimensional sheet (**Figure 3.28 c)**). The Cu^{2+} ions in the $\{Cu_2\}$ SBU are located *ca.* 1.28 Å to the central plane of the sheet, while the external Cu^{2+} ions in the $\{Cu_4\}$ unit are located *ca.* 7.2 Å to the mean plane of the sheet.

This difference in distance of Cu^{2+} ions to the central plane of the sheet causes the sheets to be shifted with respect to one another when packed. The sheets are packed such that the $\{Cu_2\}$ SBUs and $\{Cu_4\}$ units alternate their position in an *ABAB* pattern (**Figure 3.28 c)**). This pattern maximises the packing density between two adjacent sheets. The Cu-Cu axes of the $\{Cu_2\}$ SBUs and Cu-Cu axis of the $\{Cu_4\}$ unit are translationally shifted by approximately *ca.* 3.5 Å (**Figure 3.28 b)**).

The second set of sheets interpenetrates the first set through the large square-shaped pores. This secondary set of sheets is identical in structure to the first set of sheets. The two sets of sheets are interpenetrated in a *parallel, parallel* arrangement.[303] Due to the translation shift between stacked sheets, it causes the two sets of sheets to meet at an angle of *ca.* 79º (**Figure 3.28 d)**). The two sets of interpenetrated sheets generate a porous MOF with large channels that can be seen to extend in the directions of the crystallographic *a*- and *b*-axes (**Figure 3.29 a)& b)**).

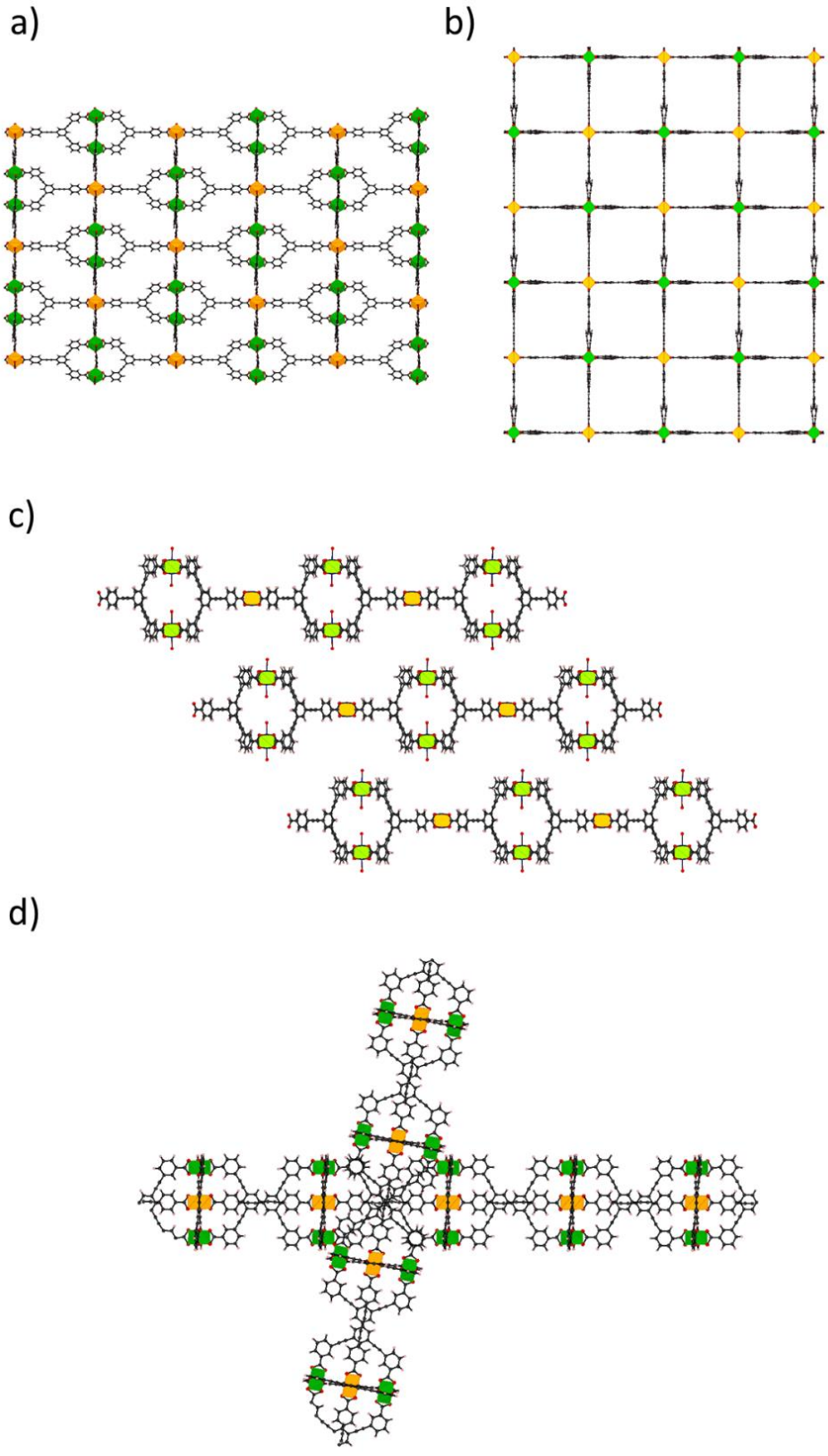

Figure 3.28: The {Cu_2} and {Cu_4} units alternating in a checkerboard pattern within the two-dimensional sheets viewed from a) an angle in [1,1,0] direction and b) the top face of the sheet. c) Stacking arrangement between the two-dimensional sheets. d) Two interpenetrated sheets which meet at an angle of 79º. ({Cu_2} SBUs with α arrangement – green cubes, {Cu_2} SBUs with α' arrangement – orange cubes, C – black, O – red, H – pink).

a)

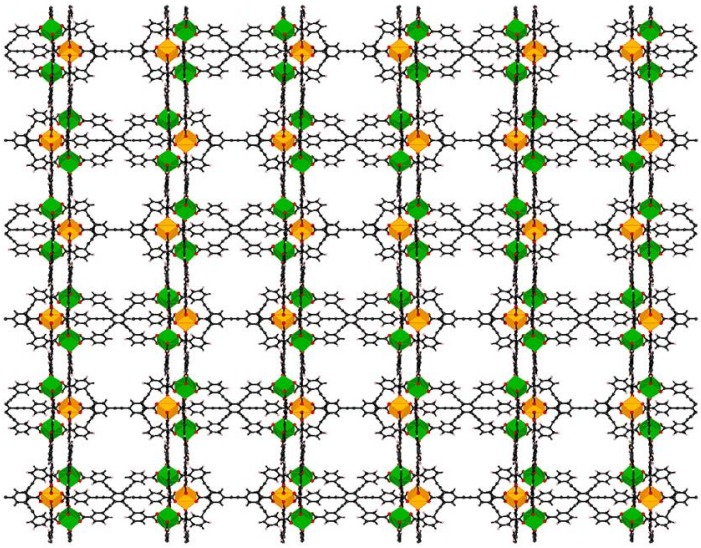

b)

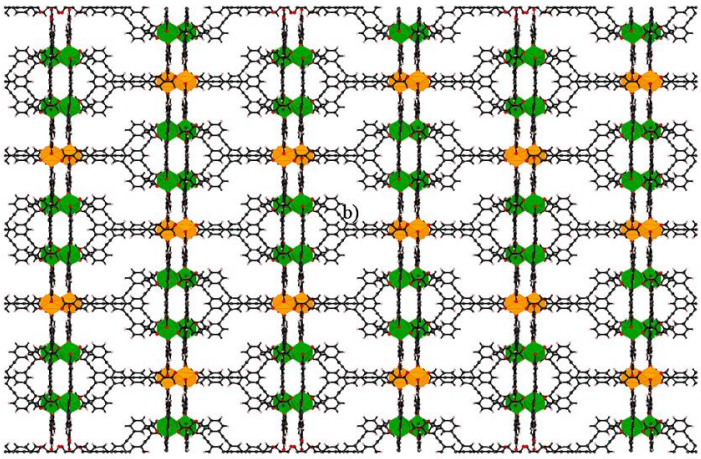

c)

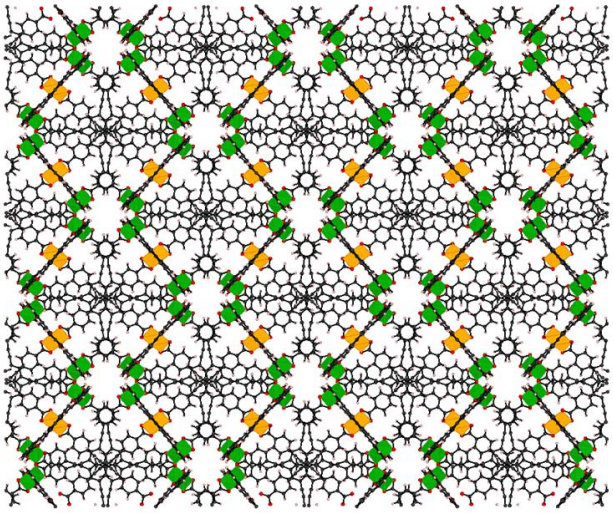

Figure 3.29: Packing diagram of 8 viewed along the crystallographic a) *a*-axis, b) *b*-axis and c) *c*-axis.(({Cu_2} SBUs with α arrangement – green cubes, {Cu_2} SBUs with α' arrangement – orange cubes, C – black, O – red, H – pink)

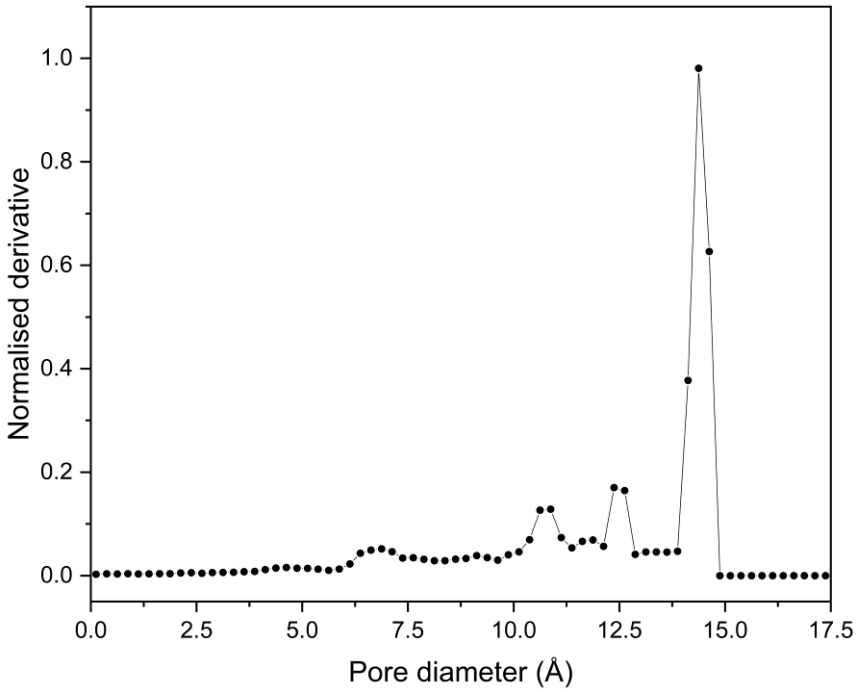

Figure 3.30: Simulated pore-size distribution of 8.

The Poreblazer software package was used to analyse the pore-size distribution and accessible surface area. [225] It was calculated that the desolvated structure has a He pore volume of *ca.* 1.770 cm^3/g and an accessible surface area of *ca.* 4194.51 m^2/g. The limiting channel diameter was found to be *ca.* 8.24 Å, and the maximum pore diameter was found to be *ca.* 14.6 Å. The calculated pore-size distribution can be seen in **Figure 3.30**. The largest pore diameter corresponds to the size of the square-shaped pores that form within each sheet, with the second set of the sheets forming the remaining sides on a pseudocubic pore.

3.4.3.1 Powder X-ray diffraction

To verify the bulk purity of **8**, X-ray powder diffraction experiments were carried out. The sample was first prepared by grinding pristine crystals of **8** while kept in the mother liquor. The powdered crystals were then loaded into a quartz capillary and measured at 215 K, on a Bruker APEX II DUO X-ray diffractometer. The Expo2014 software package was used for data analysis.[228,229]

Using the Rietveld method, the unweighted profile R-factor and the weighted profile R-factor were calculated to be Rp = 1.998 and Rwp = 3.372, respectively. It was found that the experimental diffraction pattern matches well with the theoretical diffraction pattern, which was obtained from the single-crystal diffraction data. (**Figure 3.31**).

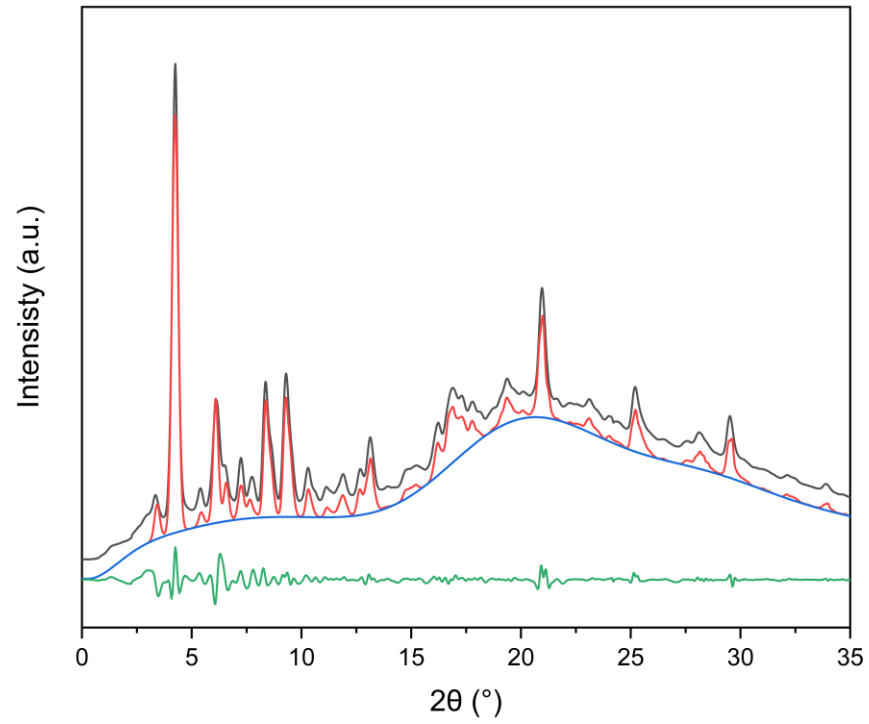

Figure 3.31: PXRD pattern for 8. (Measured diffraction pattern – black, calculated background signal – blue, predicted diffraction pattern – red, difference between measured and predicted – green.)

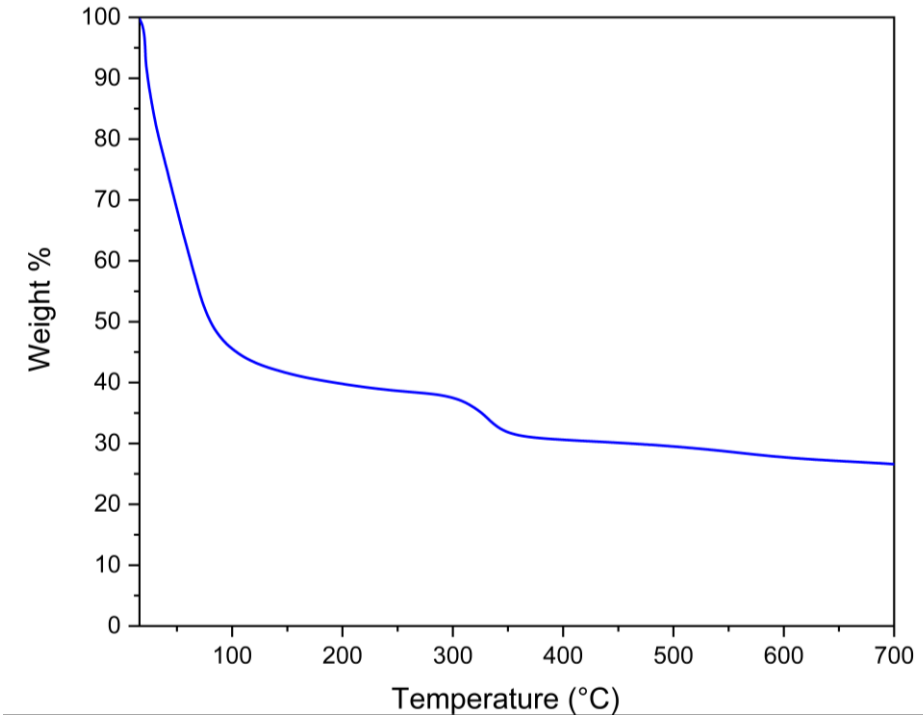

Figure 3.32: TGA of 8 heated at a rate of 4 ºC per minute under a nitrogen atmosphere.

3.4.3.2 Thermogravimetric analysis of **8**

A thermogravimetric analysis of **8** was performed to examine the thermal stability of the MOF. The compound was prepared by removing pristine crystals of **8** in a nitrogen atmosphere at a heating rate of 4 ºC per minute (**Figure 3.32**). An initial weight loss of *ca.* 55% occurred between 20 ºC and 100 ºC. This loss can be attributed to the loss of H_2O and DMF solvent molecules located within the voids of the structure. A further weight loss of *ca*. 5% occurs from 370 ºC to 700 ºC, which corresponds to the decomposition of the $BTEB_{mmp}^{3-}$ linker.

3.4.3.3 FT-IR and Raman spectroscopy

FT-IR and Raman spectroscopy was used the characterise **8**. In both spectra, $BTEB_{mmp}^{3-}$ -derived vibrations predominate the spectra. In the FR-IR spectrum, a broad band is found at 3465 cm^{-1} which is due to the H-bonding of solvent molecules located in the pores and coordinated to the Cu^{2+} ions. (**Figure 3.33 a)**) A pair of bands at 2932 cm^{-1} and 2846 cm^{-1} can be attributed to the ν(C-H) vibrations of DMF molecules. A strong band due to the asymmetric ν(O=C) stretching vibration of DMF molecules is found at 1654 cm^{-1}. The asymmetric carboxylate ν_{as}(COO) vibration gives rise to a band at 1625 cm^{-1}, and the corresponding symmetric vibrational mode causes a band at 1432 cm^{-1}. A Deacon and Philips Δ value of *ca.* 193 cm^{-1} corresponds to the observed bidentate bridging mode.[233]

The Raman spectrum of **8** is mainly composed of bands derived from the $BTEB_{mmp}^{3-}$ linkers. (**Figure 3.33 b)**) The spectrum was measured from 100 cm^{-1} to 2500 cm^{-1}. A strong band at 2209 cm^{-1} corresponds to the symmetric ν(C≡C) stretch. Two strong bands are found at 1604 cm^{-1} and 1580 cm^{-1} arising from the aromatic ν(C=C) vibrations of the phenyl rings. The symmetrical ν_s(C=O) bands are found at 1412 cm^{-1} and 1363 cm^{-1}. Three bands corresponding to aromatic C-C bonds are found at 1179 cm^{-1}, 1127 cm^{-1} and 1113cm^{-1}. The strong band found at 995 cm^{-1} can be attributed to C-H bending from the central 1,3,5-trisubstituted phenyl ring.[235]

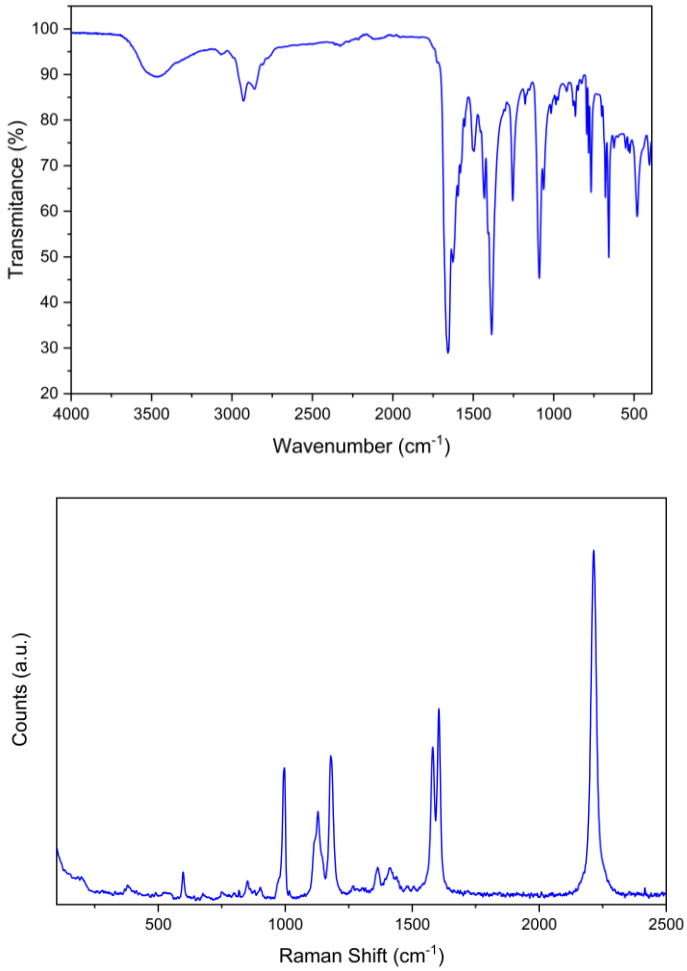

Figure 3.33: a) FT-IR and b) Raman spectra of 8.

3.4.3.4 Topological analysis

Topological analysis of **8** was carried out using the software package ToposPro. The topological net for **8** was determined to be a 3-nodal (3,4,4)-connected net. The overall point symbol was determined to be $\{4.8^2\}_4\{4^6\}_2\{8^4.12^2\}$. The 3-connected node corresponds to the $BTEB_{mmp}^{3-}$ linkers, while the two remaining 4-connected nodes correspond to the $\{Cu_2\}$ SBUs. In **Figure 3.34** the $\{Cu_2\}$ SBUs with the **α** arrangement are highlighted in green while the $\{Cu_2\}$ SBUs with the **α'** arrangement are highlighted in orange.

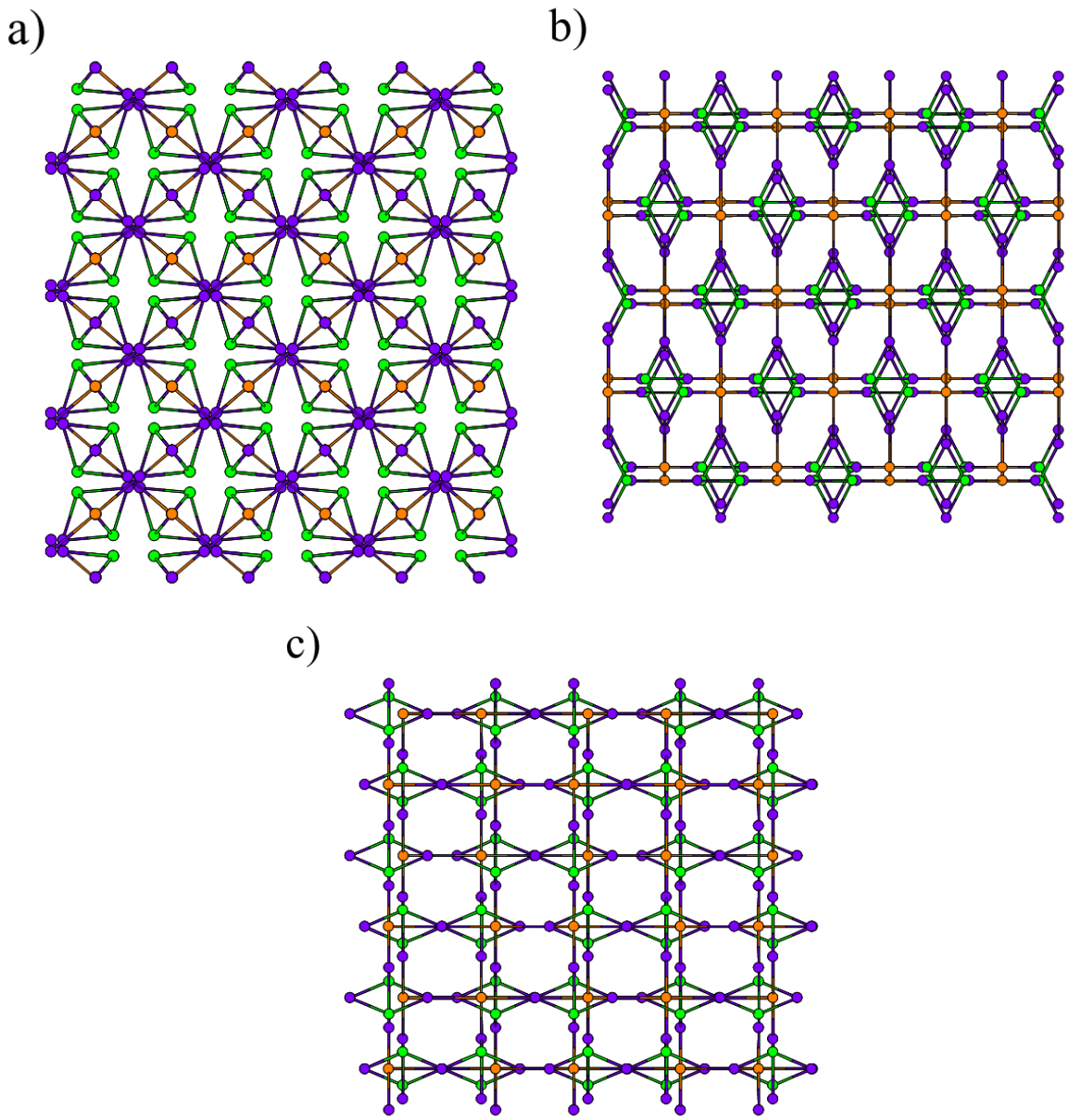

Figure 3.34: Topological representation of 8 viewed along the crystallographic a) *a*-axis, b) *b*-axis and c) *c*-axis. ({Cu_2} SBUs with α arrangement – green, {Cu_2} SBUs with α' arrangement - orange, $BTEB_{mmp}^{3-}$ linkers - purple)

Table 3.6: Crystallographic details for 8.

Identification code	8
Empirical formula	$C_{66}H_{36}Cu_3O_{15}$
Formula weight	1259.57
Temperature / K	215(2)
Crystal system	Orthorhombic
Space group	$I2_12_12_1$
***a* / Å**	26.854(6)
***b* / Å**	32.384(8)
***c* / Å**	42.121(9)
***α* / º**	90
***β* /º**	90
***γ* / º**	90
Volume / Å^3	36630(15)
Z	8
ρ_{calc}/ g/cm^3	0.457
μ / mm^{-1}	0.588
F(000)	5112
Crystal size / mm^3	? × ? × ?
Radiation	CuKα (λ = 1.54178 Å)
θ range for data collection / º	1.721 to 50.563°
Index ranges	-26<=h<=26, -32<=k<=32, -40<=l<=41
Reflections collected	120263
Independent reflections	19097 [R(int) = 0.2212]
Data/restraints/parameters	19097 / 94 / 281
Goodness-of-fit on F^2	1.134
Final R indexes [I>=2σ (I)]	R1 = 0.1137, wR2 = 0.2884
Final R indexes [all data]	R1 = 0.1994, wR2 = 0.3657
Largest diff. peak/hole / e.Å^{-3}	0.779 and -0.676

3.5 Use of tetracarboxylate linkers

3.5.1 $[Cu_{0.66}Zn_{1.33}(BTEB_{ppi})(H_2O)_2]$ (**9**) and $[Cu_2(BTEB_{ppi})(H_2O)_2]$ (**10**)

3.5.1.1 Synthesis of $[Cu_{0.66}Zn_{1.33}(BTEB_{ppi})(H_2O)_2]$ (**9**)

Initial attempts to synthesise MOFs containing the H_4BTEB_{ppi} linker focused on the use of Cu^{2+} salts as inorganic reagents. A large number of conditions were examined, including but not limited to variations of counterions, metal/ linker ratios, and modulators. All of these commonly used methods that have previously been used to synthesise the other MOFs within this chapter, **6 -8**, in this case only led to the formation of fine blue powder instead of single crystals. In order to synthesise crystals of sufficient size and quality, we utilised a competitive binding strategy involving the addition of Zn^{2+} salts in the synthesis. The addition of Zn^{2+} ions in the synthesis was the most effective method of synthesising larger single crystals that could be analysed by single-crystal X-ray diffraction. $[Cu_{0.33}Zn_{0.67}(BTEB_{ppi})(H_2O)_2]$ (**9**) was synthesised by heating a mixture $Cu(NO_3)_2{\cdot}3H_2O$ and $Zn(NO_3)_2{\cdot}6H_2O$ in a mole ratio of 1:2 with H_4BTEB_{ppi} in 1:1 mole ratio of ligand to metal. This ratio of Cu^{2+} to Zn^{2+} was found to have the optimal effect on the crystal size, quality, and purity of the bulk material. Increasing the levels of Cu^{2+} ions decreased the crystal size and the formation of the blue powder. Increasing the levels of Zn^{2+} ions in the reaction system reduced the quality of the crystals, with further additions producing by-products, most notably **12**.

The reaction mixture was heated in DMF at 85° for 48 h. Over the course of the reaction blue, cubic crystals grew upon the inner walls of the reaction vial. The crystals were collected and found to be of sufficient quality for single-crystal X-ray analysis. The crystals were measured and solved in the trigonal space group *R3m*. The unit cell dimensions were determined to be a = 30.486(7) Å, b = 30.486(7) Å, c = 39.713(9) Å, $\alpha = \beta = 90^o$, $\gamma = 120^o$. This synthesis was then reapplied later, but in this instance, only $Cu(NO_3)_2{\cdot}3H_2O$ was used instead of a combination of Cu^{2+} and Zn^{2+}. This lead to the formation of a blue microcrystalline powder with the formula $[Cu_2(BTEB_{ppi})(H_2O)_2]$ (**10**) which, as discussed in later sections, was found to be isostructural to **9**.

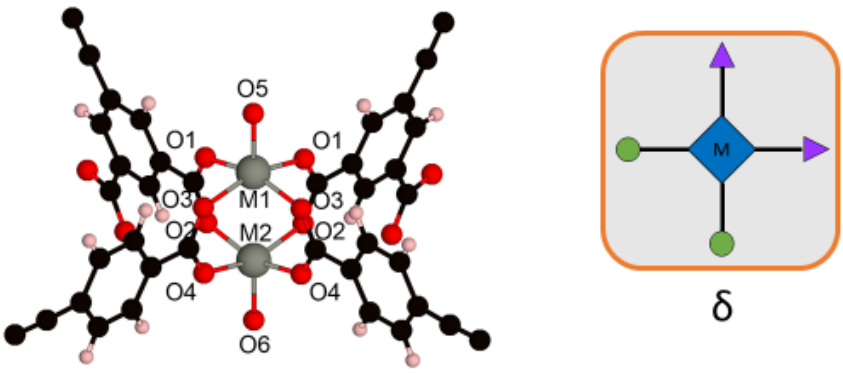

Figure 3.35: a) Labelled representation $\{M_2\}$ SBU in 9. b) Graphical representation of the arrangement of the *para*-benzoate and isophthalate moieties around the $\{M_2\}$ SBU.

9 was found to be a three-dimensional MOF comprised of $BTEB_{ppi}^{4-}$ linkers, linking $\{M_2\}$ paddlewheel SBUs. The asymmetric unit contains two M^{2+} ions coordinated by half of a fully deprotonated $BTEB_{ppi}^{4-}$ linker. Due to the combination of Cu^{2+} ions and Zn^{2+} ions used in the synthesis, both metal ions are contained within $\{M_2\}$ paddlewheel SBUs. Beyond the composition of the metal ions, the structure of the $\{M_2\}$ SBUs is similar to the $\{Cu_2\}$ SBUs.[223] O-donor atoms of coordinating carboxylate groups from the $BTEB_{ppi}^{4-}$ linkers coordinate to the two metal centres in a *syn,syn*-bidenate (μ_2-η^1:η^1) binding mode. The O-donor atoms act as the base of the square pyramidal coordination environment to each of the M^{2+} ion while the O-donor atoms, from H_2O solvent molecules, coordinate to the apical position. The resulting M-O bond distances are shorter than is typical for the Jahn-Teller distorted apical positions in the $\{Cu_2\}$ SBUs. Given that this elongation does not occur in the d^{10} Zn^{2+} ions, it indicates the presence of Zn^{2+} ions within the $\{M_2\}$ SBUs. The $\{M_2\}$ SBU is coordinated by four $BTEB_{ppi}^{4-}$ linkers *via* two *para*-benzoate moieties and two isophthalate moieties.

Element	Atomic %	Weight %
C	73.71	60.91
O	23.27	25.61
Cu	1.03	4.48
Zn	2.00	8.99

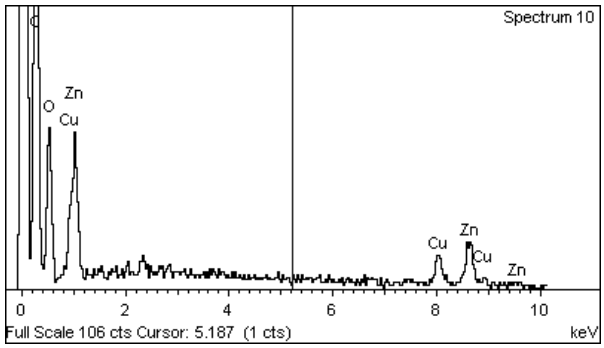

Figure 3.36: Table of results from EDZ measurments with atomic percentage and weight percentage along with the EDX spectrum of 9.

The moieties coordinated to the SBU in *cis* configuration as seen in **Figure 3.35** as denoted by the symbol **δ**. This overall symbol is in agreement with the combinations for tetra-carboxylate linkers summarised in **Table 3.1**. To confirm the identity of the M^{2+} ion, energy-dispersive X-ray spectroscopic analysis (EDX) was performed on crystals of **9**. It was found that **9** contains a 2:1 atomic ratio of Zn^{2+} to Cu^{2+} ions within its structure (

Element	Atomic %	Weight %
C	73.71	60.91
O	23.27	25.61
Cu	1.03	4.48
Zn	2.00	8.99

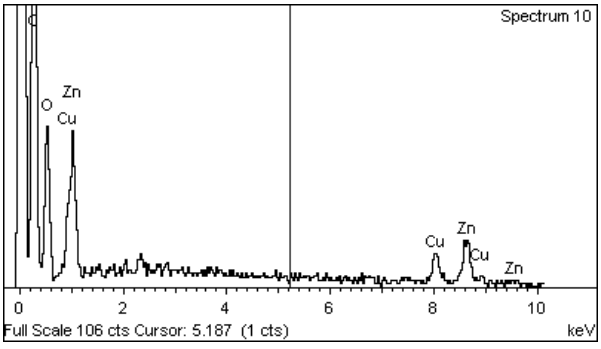

Figure 3.36). The significant quantity of Zn^{2+} ions explains the short M-O bonds involving the coordinated solvent molecules (**Table 3.7**).

Table 3.7: Selected bond lengths and bond angles in 9.

Atoms	Distance	Atoms	Angle
M1-O1	2.0468(19) Å	O1-M1-O1’	88.49(11) º
M1-O3	2.028(2) Å	O1-M1-O3	87.79(8) º
M1-O5	1.969(3) Å	O3-M1-O3’	88.29(13) º
M2-O2	2.0404(19) Å	O1-M1-O5	100.48(9) º
M2-O4	2.017(2) Å	O3-M1-O5	100.55(11) º
M2-O6	1.966(3) Å	O2-M2-O2’	86.18(11) º
		O2-M2-O4	88.40(8) º
		O4-M2-O4’	88.56(13) º
		O2-M2-O6	102.07(12) º
		O4-M2-O6	100.10(13) º

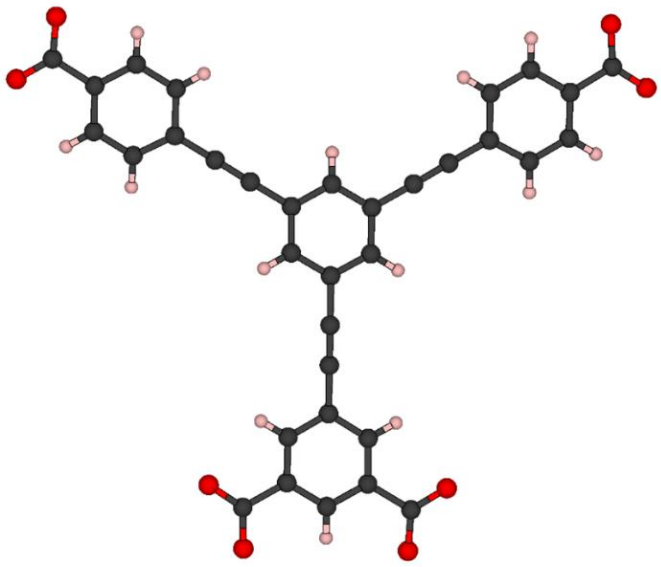

Figure 3.37 Conformation of the $BTEB_{ppi}^{4-}$ linker in 9 and 10.

Table 3.8: Dihedral angle between *para*-benzoate and isophthalate moieties to the central phenyl ring.

Conformation	Dihedral angel involving *para*-benzoate moiety 1 (º)	Dihedral angle involving *para*-benzoate moiety 2 (º)	Dihedral angle involving isophthalate moiety (º)
i	9.08(19)º	9.08(19)º	0.000(3)º

The $BTEB_{ppi}^{4-}$ linker is found in one conformation within the structure of **9**. The isophthalate moiety is co-planar to the central phenyl ring. The phenyl rings of the two *para*-benzoate moieties have a dihedral angle of *ca*. 9º with respect to the central phenyl ring. The approximate planarity of the conformation is similar to other literature-known linkers that have previously been used in the literature. [20,282,291, 304]

The $\{M_2\}$ SBUs and $BTEB_{ppi}^{4-}$ linkers combine to generate a porous three-dimensional framework. Two pore morphologies, which alternate along the crystallographic *c*-axis, occur within the framework. The larger of the two pores are encapsulated by twelve $\{M_2\}$ SBUs, which are linked to six $BTEB_{ppi}^{4-}$ linkers (**Figure 3.38**). The structure of the pore is that of a distorted cuboctahedron with the $\{M_2\}$ SBUs acting as the vertices and the $BTEB_{ppi}^{4-}$ linker acting as the distorted square faces. The distortion of the cuboctahedron is due to the large differences in the distance between the isophthalate moieties carboxylates being *ca.* 5 Å, and the distance between the *para*-benzoates moieties being *ca.* 23.4 Å on the $BTEB_{ppi}^{4-}$ linker.

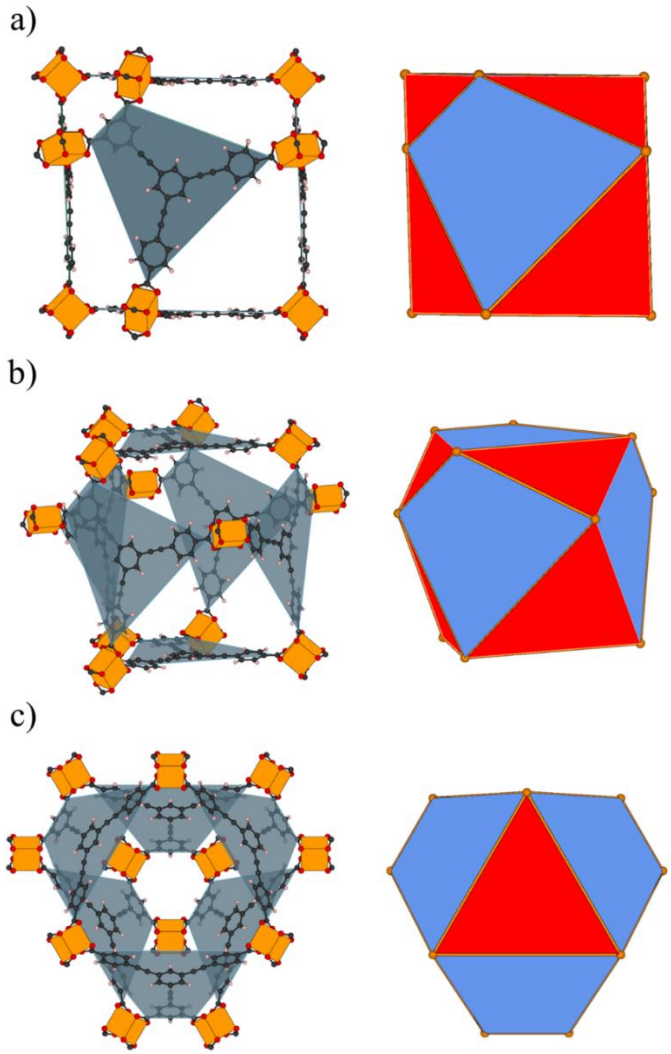

Figure 3.38: The cuboctahedral pore in 9 and a graphical representation of the cuboctahedron. The framework that encapsulates the pore is composed of $BTEB_{ppi}^{4-}$ linkers which act as the six distorted square faces and twelve $\{M_2\}$ SBUs located at the vertices. A

representative blue trapezoid is used to aid in highlighting the six distorted square faces of the cuboctahedron. a) Directly on one square face, b) with a slight rotation to the remaining faces of the cuboctahedron and c) along the crystallographic *c*-axis. ({M_2} SBU – orange cube, C - black, O - red, H – pink)

The central pore of the cuboctahedron is accessible through the eight triangular faces of the cuboctahedron. Due to the distortion of the cuboctahedron, the windows have four different diameters (**Figure 3.39**). The smallest window, of which there is one, has a diameter of *ca.* 5.3 Å. The next window in increasing size has a diameter of *ca.* 7.9 Å with three providing access to the central pore. The next largest window has a diameter of *ca.*15.1b Å, which like the previous, there are three which allow access to the pore. The largest window has a diameter of *ca.* 19.7 Å. The largest window is located transversely to the smallest window. The cuboctahedron is more distorted than that of other MOFs with similar linkers due to the reduced symmetry of the $BTEB_{ppi}^{4-}$ ligand as compared to other tetra-carboxylate linkers commonly found in MOFs with similar topology. [20,272,304,305]

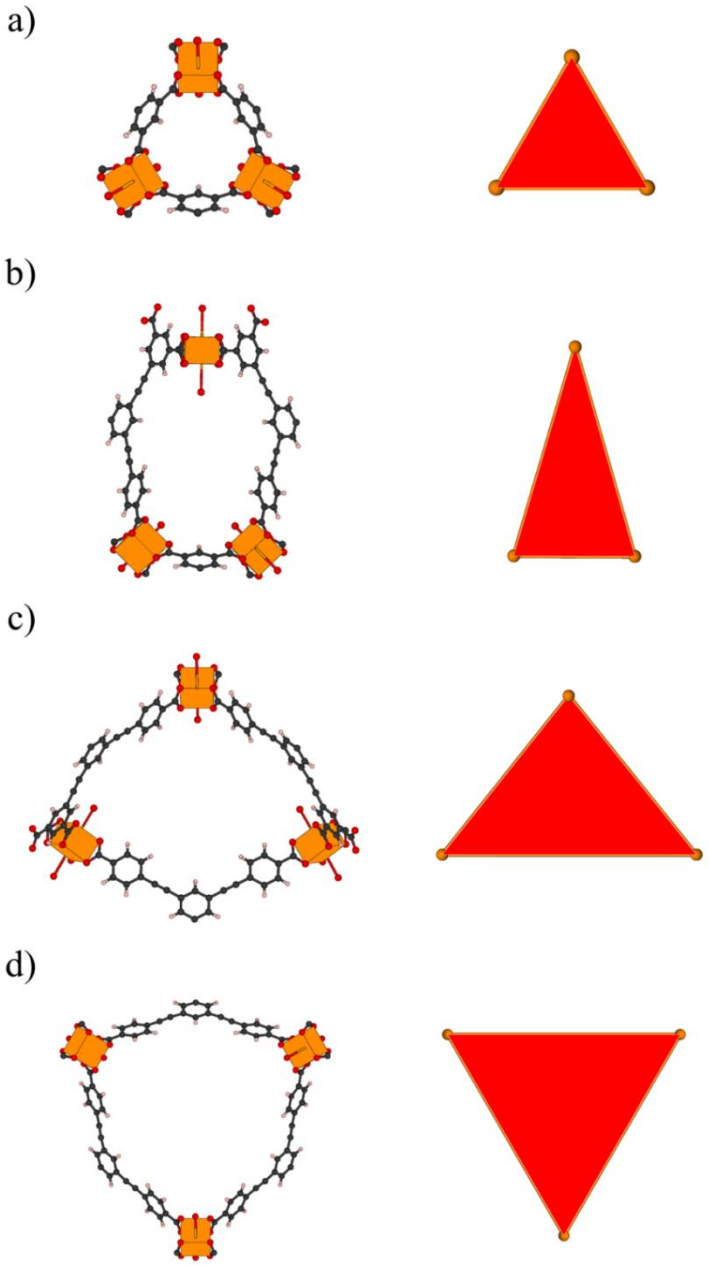

Figure 3.39: The four windows present in the structure of 9. In order of increasing size, a) the smallest window with a diameter of *ca.* 5.3 Å, b) the window with a diameter of *ca.* 7.9 Å, c) the window with a diameter of *ca.* 15.1 Å and d) the largest window with a diameter of *ca.* 19.7 Å. (C – black, O – red sphere, H – pink, {Cu_2} SBUs – orange cube / spheres, model of window shape – red triangle)

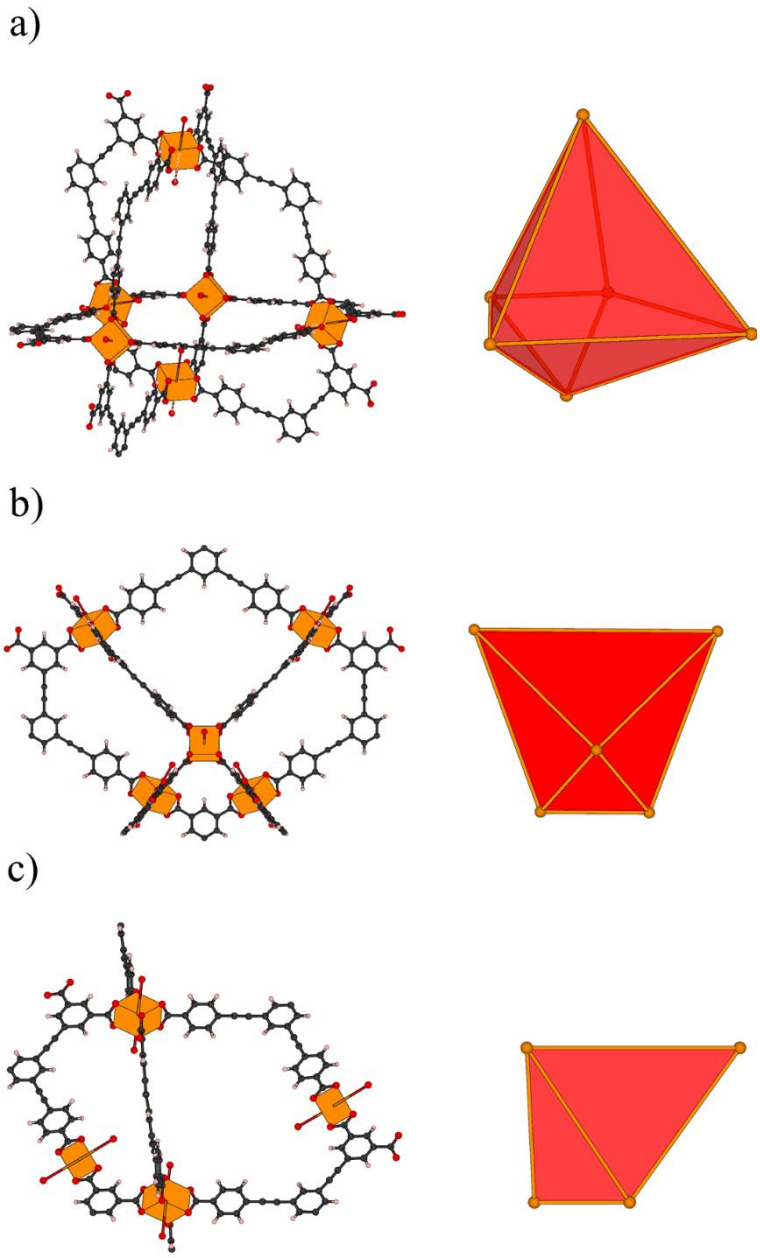

Figure 3.40: Secondary pore found in 9. It is encapsulated by six {M_2} SBUs and twelve $BTEB^{4-}$ linkers. ({M_2} SBU – orange cube, C – black, O – red, H – pink)

The second smaller pore is encapsulated by six {M_2} SBUs and twelve $BTEB_{ppi}^{4-}$ linkers (**Figure 3.38)**. The framework that encapsulates the pore as the structure of a tetrahedron which, like the pore previously discussed, is highly distorted. The six {M_2} SBUs are located at the vertices of the tetrahedron. In contrast to the previous pore, the $BTEB_{ppi}^{4-}$ linkers are located along the edges of the tetrahedron. Access to the pore is through eight large windows that are located along the faces of the tetrahedron.

The windows generate a series of channels that extend into the structure along the three-principle crystallographic axes (**Figure 3.39**). The structure is identical when viewing along the crystallographic *a* and *b*-axes with large channels extending into the structure along these directions.

A series of smaller channels, which have a diameter of *ca.* 5.3 Å, extend into the structure along the crystallographic *c*-axis. as shown in **Figure 3.41**

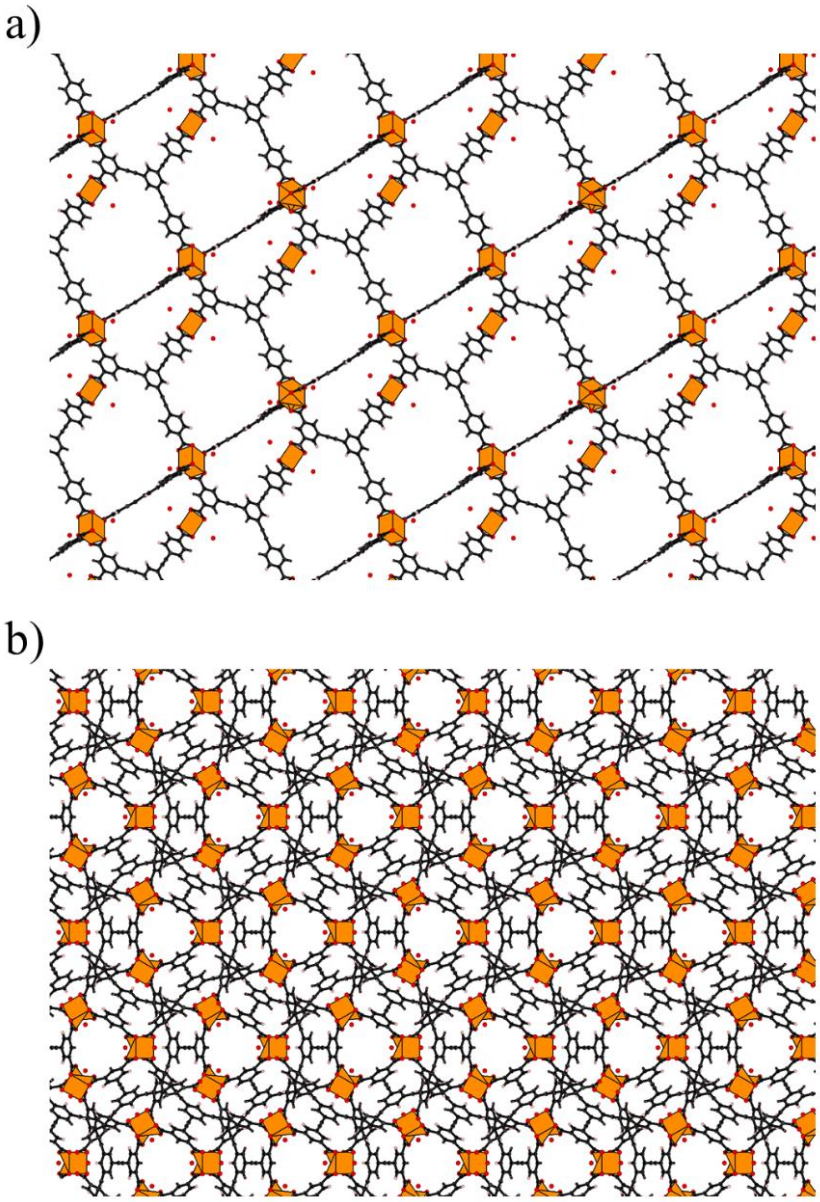

Figure 3.41: Structure of 9 viewed along the a) crystallographic *a*- and b-axis and b) crystallographic *c*-axis.

The Poreblazer software package was used to analyse the pore-size distribution and surface area.[225] The desolvated structure was found to have a He pore volume of *ca.* 2.559 cm^3/g and an accessible surface area of *ca.* 5563 m^2/g. The limiting pore diameter was found to be *ca.* 7.6 Å and the maximum pore diameter of *ca.* 18.5 Å. These pore diameters correspond well to the crystallographic data. The maximum pore diameter corresponds to the wall-to-wall diameter of the cuboctahedra pore. The calculated pore-size distribution can be seen in **Figure 3.42.**

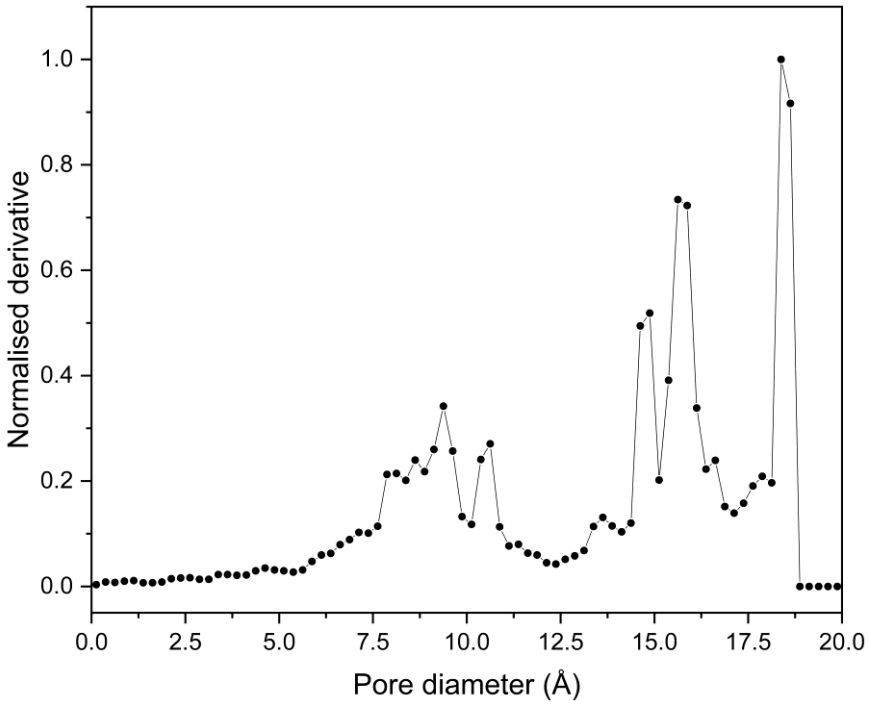

Figure 3.42: Simulated pore-size distribution of 9 and 10.

3.5.1.2 X-ray powder diffraction

PXRD analysis was carried out on **9** and **10** to determine the phase purity of the two compounds and to aid the identification of the structure of **10**. Like previous PXRD measurements, the two compounds were prepared using the standard procedure of first griding the crystalline product to a fine powder while kept in the mother liquor. The sample for **10** was prepared directly from the reaction vial because the micro-crystalline product was of sufficient size for analysis. The powdered crystals were then loaded into a quartz capillary. This is done to minimise any crystalline loss due to solvent loss and associated capillary forces. The sample was measured at 215 K, using a Bruker APEX II DUO X-ray diffractometer. The Expo2014 software package was used to calculated the background signal and fit the experimental diffraction to the theoretical diffraction pattern was calculated.[228,229]

Using the Rietveld method, the unweighted profile R-factor and the weighted profile R-factor were calculated for the diffraction pattern. The factors for **9** were determined to be Rp = 3.186 and Rwp = 4.876. This shows a strong agreement between the experimental powder pattern and the predicted powder pattern for the structure of **9** (**Figure 3.43 a)**).

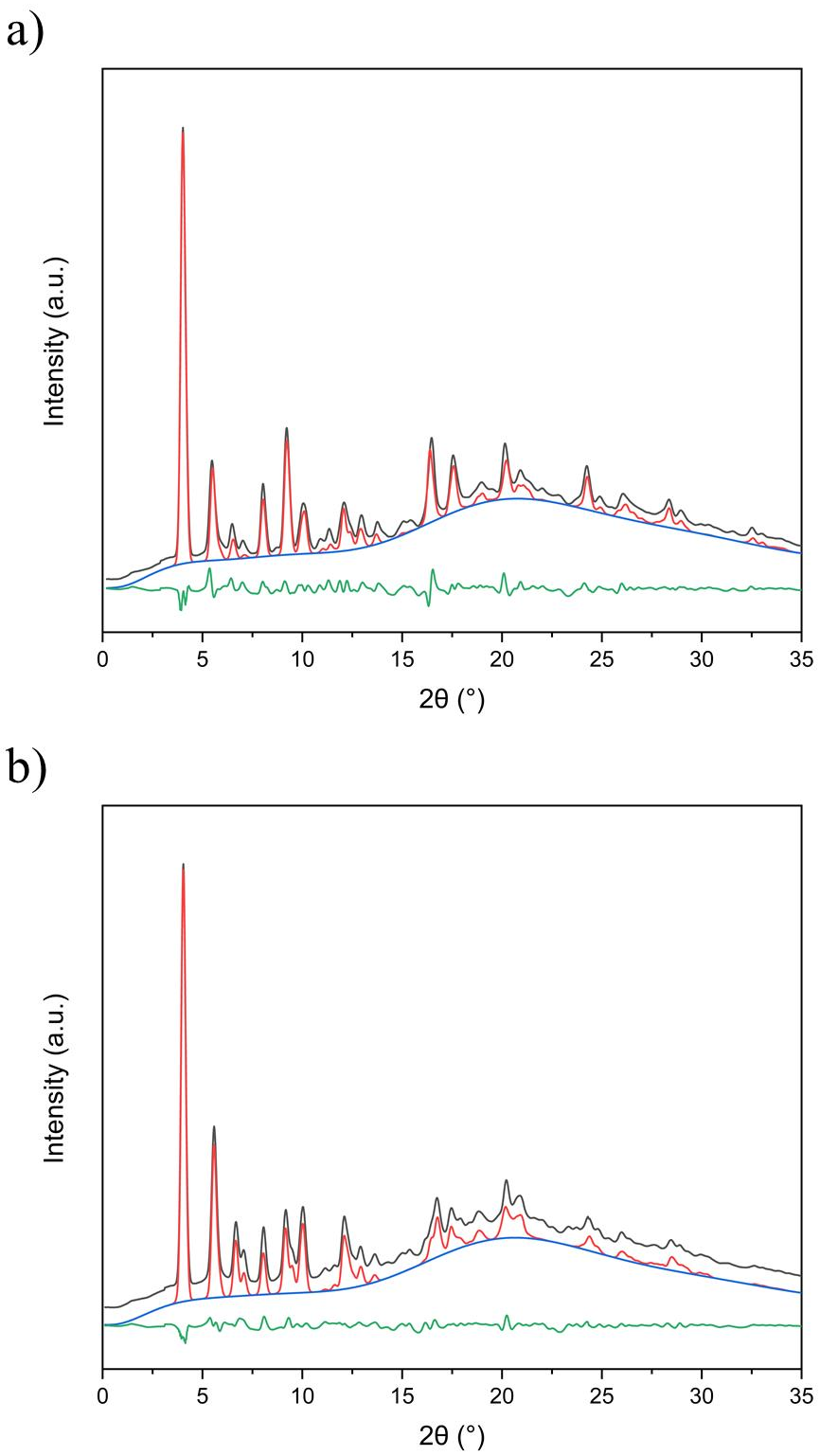

Figure 3.43: PXRD pattern for a) 9 and b) 10. (Measured diffraction pattern – black, calculated background signal – blue, predicted diffraction pattern – red, difference between measured and predicted – green.)

To determine if **10** is isostructural to **9**, the experimental powder pattern for **10** was fitted against the predicted patter for **9**. The R-factors were determined to be Rp = 2.498 and Rwp = 3.69. This confirms that the experimental diffraction patterns for **10** is a good fit to the theoretical diffraction

pattern of **9,** confirming that the two compounds are isostructural (**Figure 3.43 b)**). In the two spectra, the peak intensities differ as a result of differences in the preferred orientation of the crystalline samples, but the peak positions are located at the same position.

3.5.1.3 Thermogravimetric analysis

Thermogravimetric analysis of **9** was carried out to examine the material's thermal stability. The measurement was performed in air at a heating rate of 4 ºC per minute (**Figure 3.44**). An initial weight loss of *ca.* 65.2% occurred between 20 ºC and 121 ºC. This loss is attributed to the loss of solvent molecules located within the pores of the MOF. The loss of strongly bound solvent molecules which coordinated the M^{2+} ions, which leads to a weight loss of *ca* 5.3%, was found to occur between 121 ºC and 267 ºC. A final loss of *ca.* 23.1% weight occurs from 267 ºC to 471 ºC. This is due to the decomposition of the $BTEB_{ppi}^{4-}$ linkers. No further decomposition was found to occur at higher temperatures.

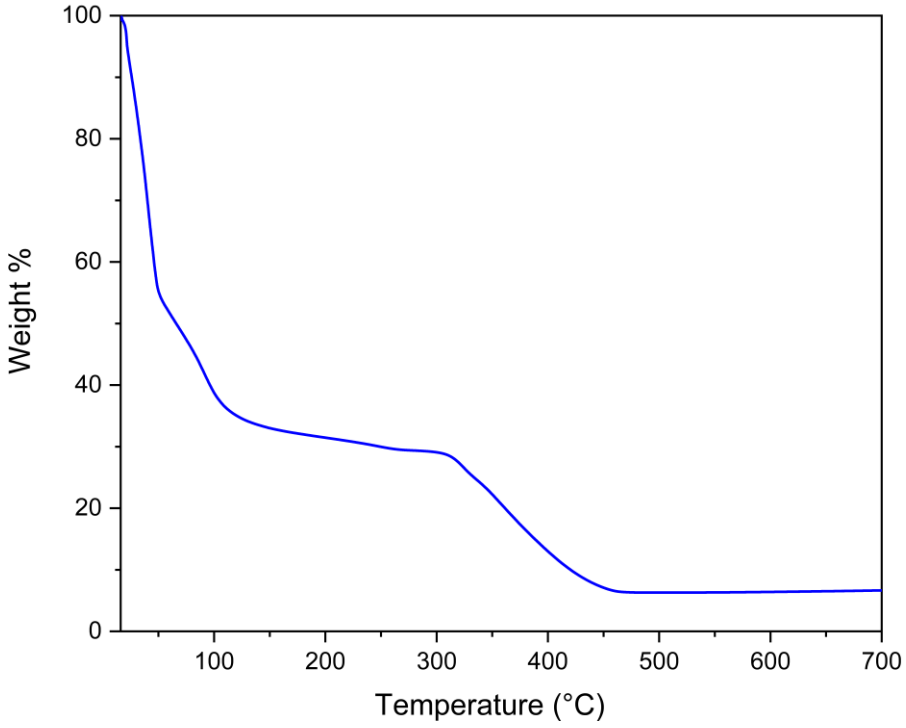

Figure 3.44: TGA of compound 9heated at a rate of 4 ºC per minute under air.

3.5.1.4 FT-IR and Raman spectroscopy

In the FR-IR spectrum of **9** a broad band is located at 3435 cm^{-1}. This is due to hydrogen bonded molecules which are found within the porous structure and coordinated to the M^{2+} ions (**Figure 3.45 a)**). A pair of bands at 2936 cm^{-1} and 2866 cm^{-1} is attributed to ν(C-H) stretches from DMF molecules both within the porous structure and coordinated to M^{2+}.[231] A strong band due to the ν(O=C) stretching in the DMF molecule is found at 1652 cm^{-1}. This stretch is found to overlap with the same associated peak in the carboxylate groups on the $BTEB_{ppi}^{4-}$ linkers. The asymmetric carboxylate

ν_{as}(COO) stretching mode is found at 1590 cm^{-1}, and the corresponding symmetric mode is found at 1385 cm^{-1}. Based upon the criterion outlined by Deacon and Philips the Δ value corresponding to the coordination mode, in this instance is found to be 195 cm^{-1}, corresponds to the observed bidentate bridging mode.[233,306]

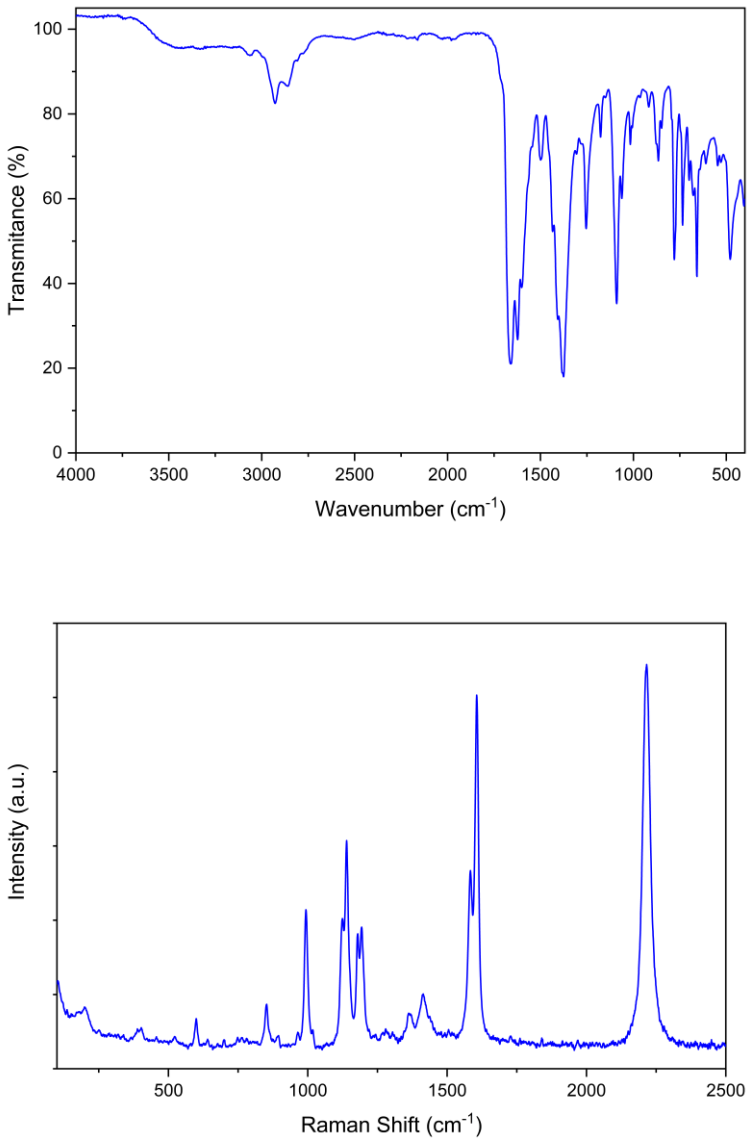

Figure 3.45: FT-IR and Raman spectra of 9.

The Raman spectrum of **9** is mainly composed of bands from the $BTEB_{mmp}^{3-}$ linkers. (**Figure 3.45 b)**) The spectrum was measured from 100 cm^{-1} to 2500 cm^{-1}. A strong band located at 2212 cm^{-1} corresponds to the symmetric ν(C≡C) of the acetylene groups. Two strong bands are found at 1600 cm^{-1} and 1579 cm^{-1} which correspond to ν(C=C) vibrations within the phenyl rings. Three bands corresponding to aromatic C=C bonds are found at 1179 cm^{-1}, 1127 cm^{-1} and 1113cm^{-1}. The strong band at 996 cm^{-1} is attributed to C-H bending within the central 1,3,5-trisubstituted phenyl ring.[235]

3.5.1.5 Topological analysis

Topological analysis of **9** and **10** was carried out using the software package ToposPro.[257] The $BTEB_{ppi}^{4-}$ linker is subdivided into two 3-connected nodes, with each being in the same environment, based upon best practices outlined by O'Keeffe *et al.*.[307] The topological net for **9** and **10** was determined to be a binodal (3,4)-c net. The overall point symbol for the network was determined to be $\{6.8^2\}_2\{6^2.8^2.10^2\}$ The topology of the system was found determined to be the common **fof-a** topology. This is a common topology that occurs between 4-c$\{Cu_2\}$ SBUs and tetra carboxylate linkers. It is commonly misattributed to a **nbo** topology..[305,308,282]

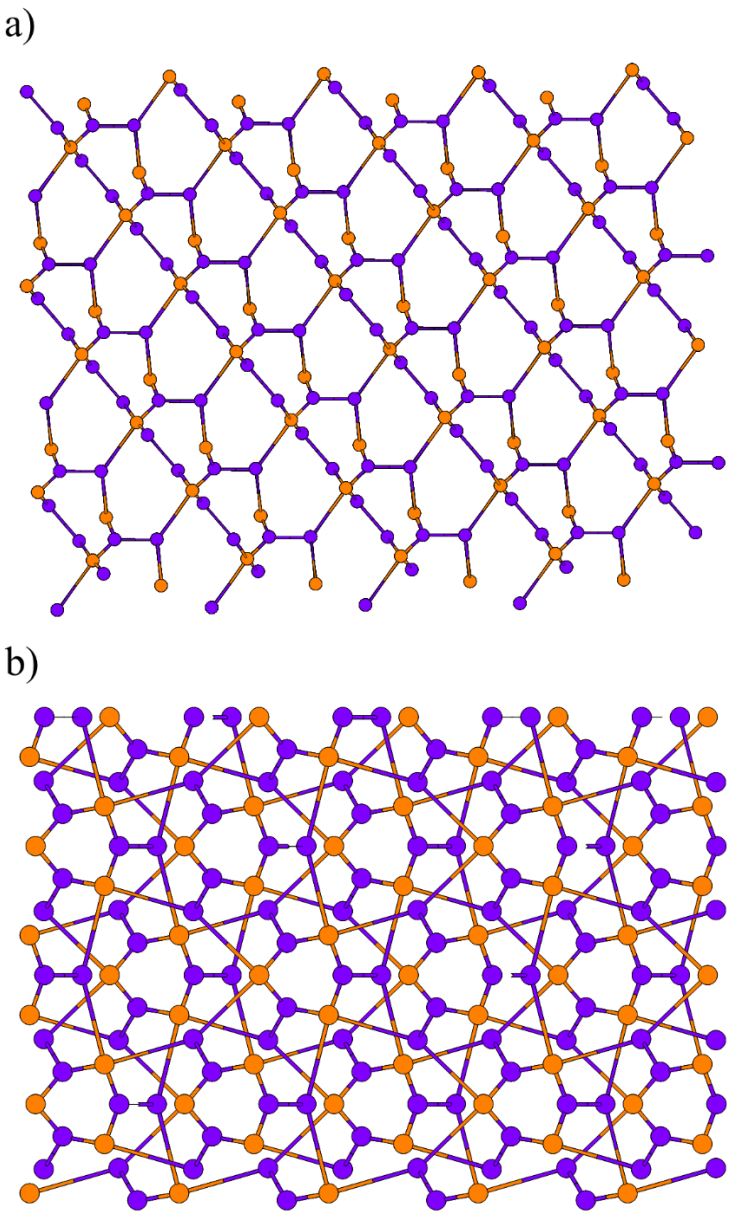

Figure 3.46: Topology of 9 and 10 viewed along the crystallographic a) a/b-axis and b) c-axis. (3-c node – purple, 4-c node – orange)

Table 3.9: Crystallographic information for 9.

Identification code	9
Empirical formula	$C_{34}H_{18}O_{10}Zn_2$
Formula weight	717.22
Temperature / K	215(2)
Crystal system	Trigonal
Space group	*R3m*
***a* / Å**	30.486(7)
***b* / Å**	30.486(7)
***c* / Å**	39.713(9)
***α* / º**	90
***β* /º**	90
***γ* / º**	120
Volume / Å^3	31964(16)
Z	9
ρ_{calc}/ g/cm^3	0.335
μ / mm^{-1}	0.526
F(000)	3258
Crystal size / mm^3	0.43×0.35×0.20
Radiation	CuKα (λ = 1.54178 Å)
θ range for data collection / º	2.009 to 52.521°
Index ranges	-31<=h<=30, -29<=k<=31, -38<=l<=40
Reflections collected	24334
Independent reflections	8102 [R(int) = 0.0325]
Data/restraints/parameters	8102 / 1 / 223
Goodness-of-fit on F^2	1.014
Final R indexes [I>=2σ (I)]	R1 = 0.0285, wR2 = 0.0655
Final R indexes [all data]	R1 = 0.0304, wR2 = 0.0664
Largest diff. peak/hole / e.Å^{-3}	0.156 and -0.382

3.5.2 $[Cu_2(BTEB_{mmi})(H_2O)_2]$ (**11**)

3.5.2.1 Synthesis of $[Cu_2(BTEB_{mmi})(H_2O)_2]$ (**11**)

$[Cu_2(BTEB_{mmi})(H_2O)_2]$ (**11**) was synthesised using H_4BTEB_{mmi} and $Cu(NO_3)_2{\cdot}3H_2O$, in a 1:2 mole ratio in a 0.5 % HOAc solution in DMF. The reaction mixture was then heated to 85 ºC for 48 h. Upon completion of the reaction, small, blue, multi-faceted prolate-spheroid like crystals were found observed to have grown along the bottom of the reaction vial alongside an amorphous, blue material as a secondary product. By gentle agitation of the reaction vial, the amorphous material became suspended in the solution while the crystals remained affixed to the surface of the reaction vial. This aided in the manual isolation of the crystals. Once isolated the crystals were discovered to be high-quality single crystals suitable for single-crystal X-ray analysis. The crystal structure of **11** was measured and solved in the hexagonal space group *P6₁22*. The unit cell dimensions were ascertained and calculated to be a = 21.5240(7) Å, b = 21.5240(9) Å, c = 21.0782(7) Å, $\alpha = \beta = 90^o$, $\gamma = 120^o$ (**Table 3.11**).

11 was found to be a three-dimensional framework comprised of $\{Cu_2\}$ SBUs linked by $BTEB_{mmi}^{4-}$ linkers. The asymmetric unit of **11** contains one Cu^{2+} ion and a half-completed $BTEB_{mmi}^{4-}$ linker. The carboxylate groups on the $BTEB_{mmi}^{4-}$ linker coordinate to the to Cu^{2+} ions, through the O-donor atoms of the carboxylate groups, in a *syn,syn*-bidentate (μ_2-η^1:η^1) bridging mode creating a $\{Cu_2\}$ paddlewheel SBU. The O-donor atoms form the base of the square base pyramidal coordination environment around the Cu^{2+} ions. An O-donor atom from a solvent molecule coordinates to the Cu^{2+} ion at the apical position. This solvent molecule could be an H_2O molecule or a disordered DMF molecule, from which only the O-donor atom is refined. The second Cu^{2+} ion in the $\{Cu_2\}$ SBU is symmetry related to the first. All bond lengths and bond angles found in $\{Cu_2\}$ SBUs are within typical values previously reported for $\{Cu_2\}$ SBUs.[223]

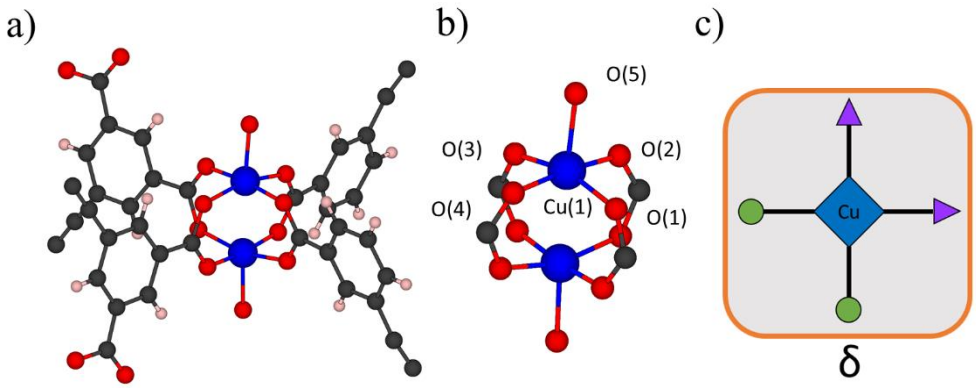

Figure 3.47: a) The arrangement of the *meta*-benzoate and isophthalate moieties coordinating to the $\{Cu_2\}$ SBU. b) Labelled atoms in the $\{Cu_2\}$ SBU. c) A graphical representation of the *meta*-benzoate and isophthalate moieties coordinating to the $\{Cu_2\}$ unit. The arrangement is denoted by the symbol δ. (C -black, O – red, H -pink, Cu – dark blue)

Each {Cu_2} SBU is coordinated by four of the tetradentate $BTEB_{mmi}^{4-}$ linkers with two *meta*-benzoate and two isophthalate moieties. The moieties coordinate to the {Cu_2} SBU with a *cis* like arrangement denoted by the symbol **δ** (**Figure 3.47**). This arrangement is the only arrangement present within the structure of **11**. The MOF is therefore denoted by the overall symbol **δ**. This is in agreement with the charge balancing requirements and the predicted allowable combination of arrangements for tetra-carboxylate linkers found in **Table 3.1**

The $BTEB_{mmi}^{4-}$ linker is present in one conformation within the structure of **11**. The *meta*-benzoate moieties each have a rotation of *ca.* 20º with respect to the plane of the central phenyl ring and are counter-rotated with respect to each other. The dihedral angle of the isophthalate moiety is approximately perpendicular to the central phenyl ring, with a rotation of *ca.* 86º (**Figure 3.48**). Due to the rotation of the moieties on the $BTEB_{mmi}^{4-}$ linker, the linker has a Δ screw-shaped geometry. This Δ screw-shaped geometry causes chirality in the overall framework. This chirality is reflected in the chiral *P6₁22* space group that the structure was solved in.

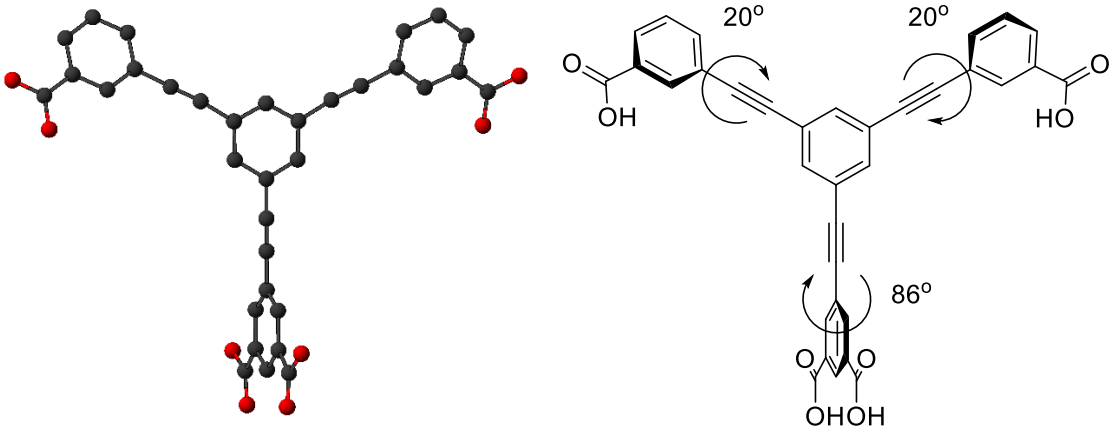

Figure 3.48: a) A graphical representation of the $BTEB_{mmi}^{4-}$ linker found in 11. b) A schematic representation of the $BTEB_{mmi}^{4-}$ linker with the rotation of the *meta*-benzoate and isophthalate moieties. (C- black, O – red)

Table 3.10: Dihedral angles between the *para*-benzoate and isophthalate moieties and the of the central phenyl ring in 11.

Conformation	Dihedral angle involving *meta*-benzoate moiety 1 (º)	Dihedral angle involving *meta*-benzoate moiety 2(º)	Dihedral angle involving isophthalate angle (º)
i	20º	-20º	86º

The overall structure of **11** is a three-dimensional framework with that contains two sets of channels that are found in a 3:1 ratio, extend into the structure along the crystallographic *c*-axis. The most numerous of these channels contains a series of {Cu_2} SBUs that line the walls of the channel (**Figure**

3.49 b)). The {Cu_2} SBUs are orientated in such a way that the solvent molecules, which coordinate to the apical position on the Cu^{2+} ions, are directed towards the centre of the channel. Due to the presence of the polar solvent molecules and the potential for vacant metal sites in an activated MOF, the channel has a polar character. The secondary channel arises from the central phenyl ring and the two *meta*-benzoate moieties. Due to the walls of the channel being comprised of phenyl rings, the channel has a non-polar character. The third set of channels is found to extend into the structure along the crystallographic *a*- and *b*-axis. This third set of channels interconnects the polar channels that extend along the crystallographic *c*-axis, while the hydrophobic channels remain isolated (**Figure 3.49**).

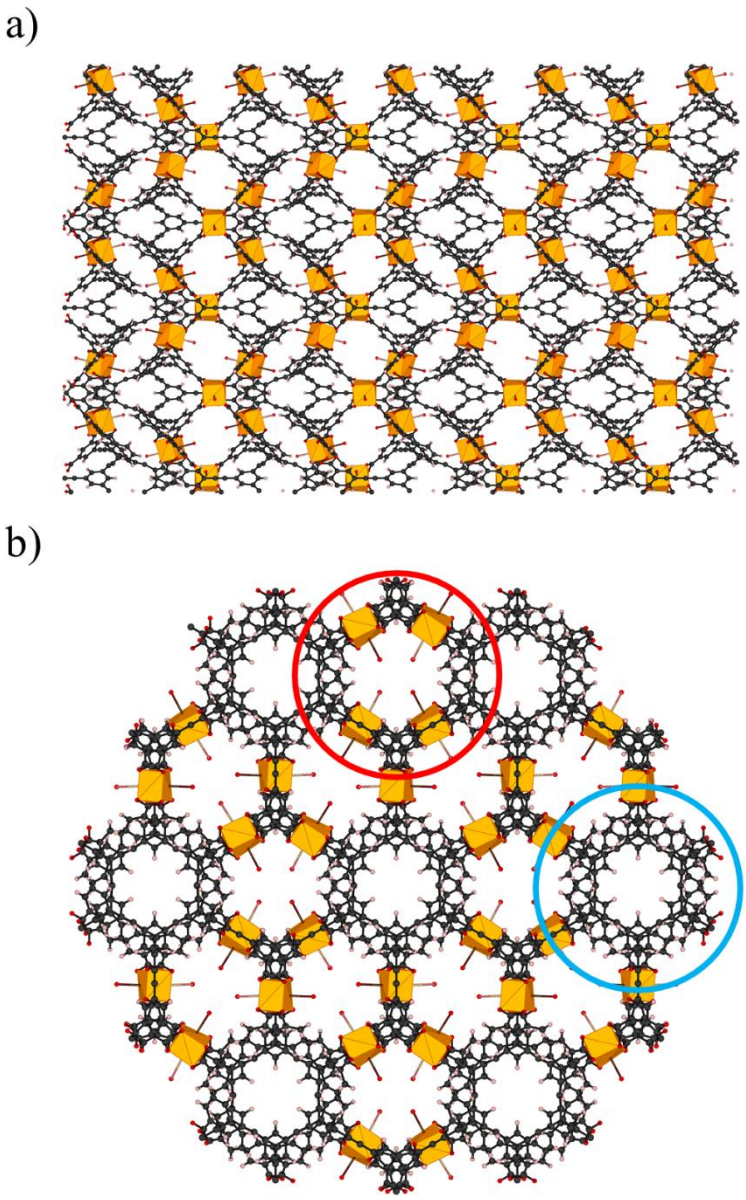

Figure 3.49: Packing representation of 11 viewed along the a) *a/b*- and, b) *c*-crystallographic axis. An example of the polar channels lined with {Cu_2} SBUs is highlighted by the red circle. An example of the non-polar channels is highlighted by the blue circle. ({Cu_2} SBUs – orange cubes, O - red, C - black, H – pink)

The chirality of the framework can be highlighted by sub-dividing the $BTEB_{mmi}^{4-}$ linkers into two pieces, the first piece being the isophthalate moiety, and the second piece comprised of the central phenyl ring and *meta*-benzoate moieties. By first focusing on the central phenyl ring and *meta*-benzoate moieties, a group of helical chains are generated that extend into the structure along the crystallographic *c*-axis (**Figure 3.50 a) & c)**). Each individual chain has a 3_1-screw axis that rotates around the central hydrophobic channel. Four chains combine to create the walls of the hydrophobic channel, with each chain highlighted in **Figure 3.50 a)** and **c)**. The isophthalate moieties combine with the $\{Cu_2\}$ SBUs to generate a second set of helical chains, which also have a 3_1 screw axis, that extend into the structure along the crystallographic *c*-axis (**Figure 3.50**).

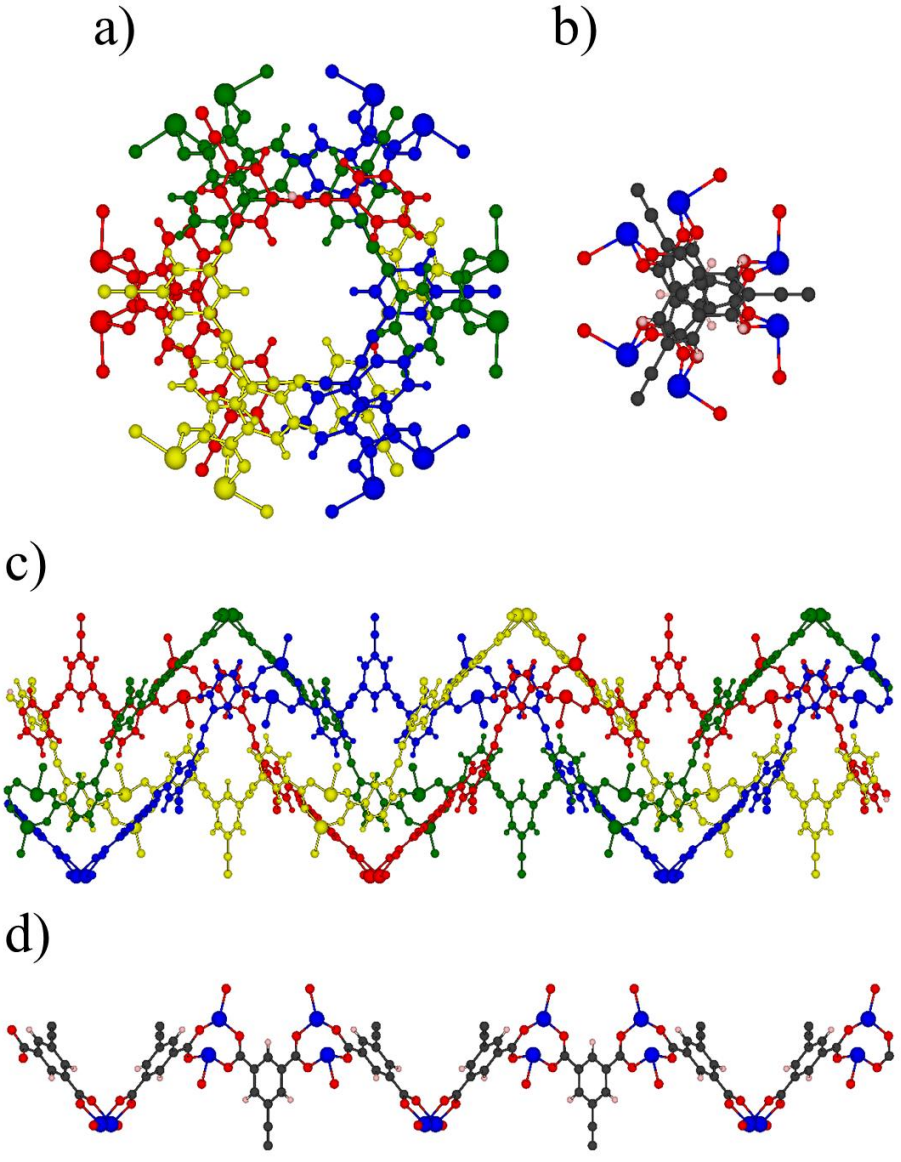

Figure 3.50: a) The chain of *meta*-benzoate moieties and central phenyl ring found in 11, with each of the four chains that rotate around the central channel highlighted (blue, green, yellow, red) and b) The chain of isophthalate moieties viewed along the *c*-crystallographic axis. c) The chain of *meta*-benzoate moieties and central phenyl ring chain and d) the isophthalate chain viewed along the crystallographic a-axis.

To examine the potential porosity of the MOF, the Poreblazer software package was used to analyse the pore-size distribution and accessible surface area.[225] It was calculated that the desolvated structure has a He pore volume of *ca.* 0.747 cm^3/g and an accessible surface area of *ca.* 1768.03 m^2/g. The channels in the structure were found to determined to have a limiting channel diameter of *ca.* 5.5 Å and a maximum pore diameter of *ca.* 8.3 Å. The calculated pore-size distribution can be seen in **Figure 3.51**.

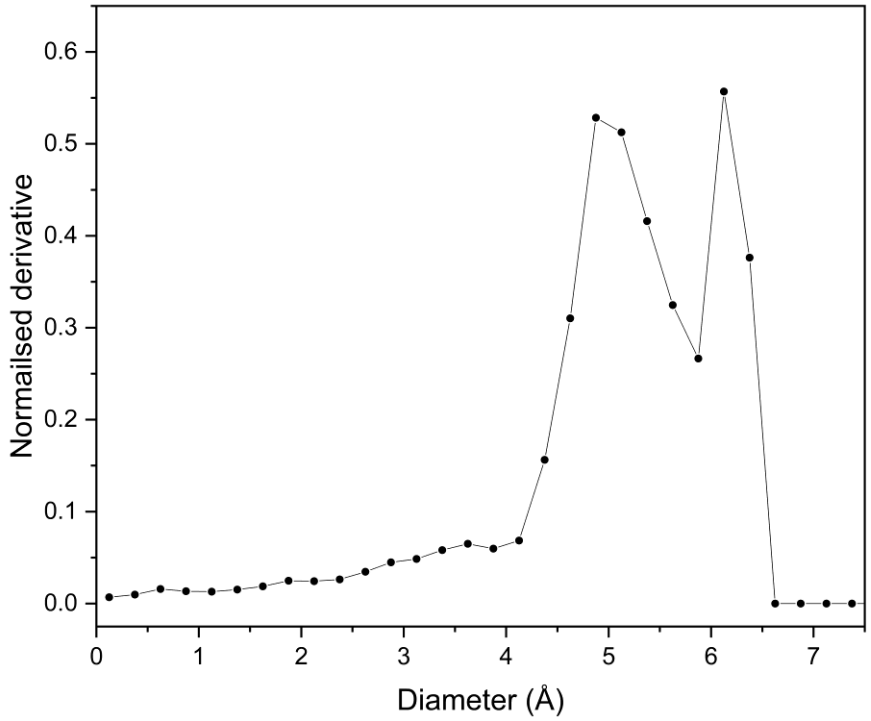

Figure 3.51: Simulated pore-size distribution for 11.

3.5.2.2 Powder X-ray diffraction

To determine the phase purity of the material, **11** was analysed by PXRD. The sample was prepared in a similar manner to previous samples and loaded into a quartz capillary. The sample was measured at 215 K, on a Bruker APEX II DUO X-ray diffractometer. Using the Expo2014 software package, the background signal and fit the experimental diffraction to the theoretical diffraction pattern was calculated (**Figure 3.52**).[228,229]

The unweighted profile R-factor and the weighted profile R-factor were calculated using the Rietveld method for the diffraction pattern.[230] The two factors were determined to be Rp = 1.212 and Rwp = 2.092, respectively. It was noted that the experimental diffraction pattern matched well with the theoretical diffraction pattern.

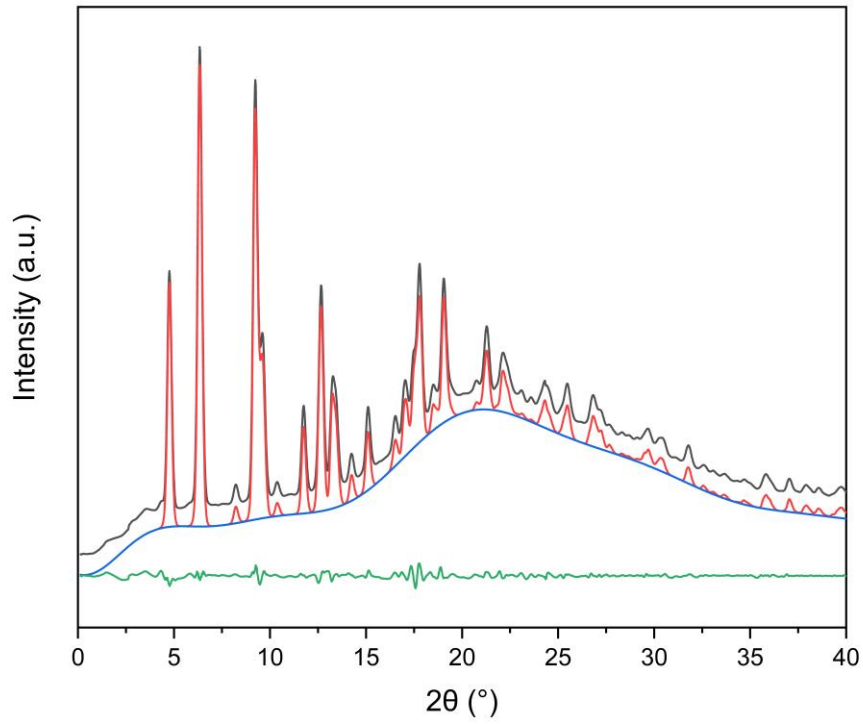

Figure 3.52: PXRD pattern for 11. (Measured diffraction pattern – black, calculated background signal – blue, predicted diffraction pattern – red, difference between measured and predicted – green.)

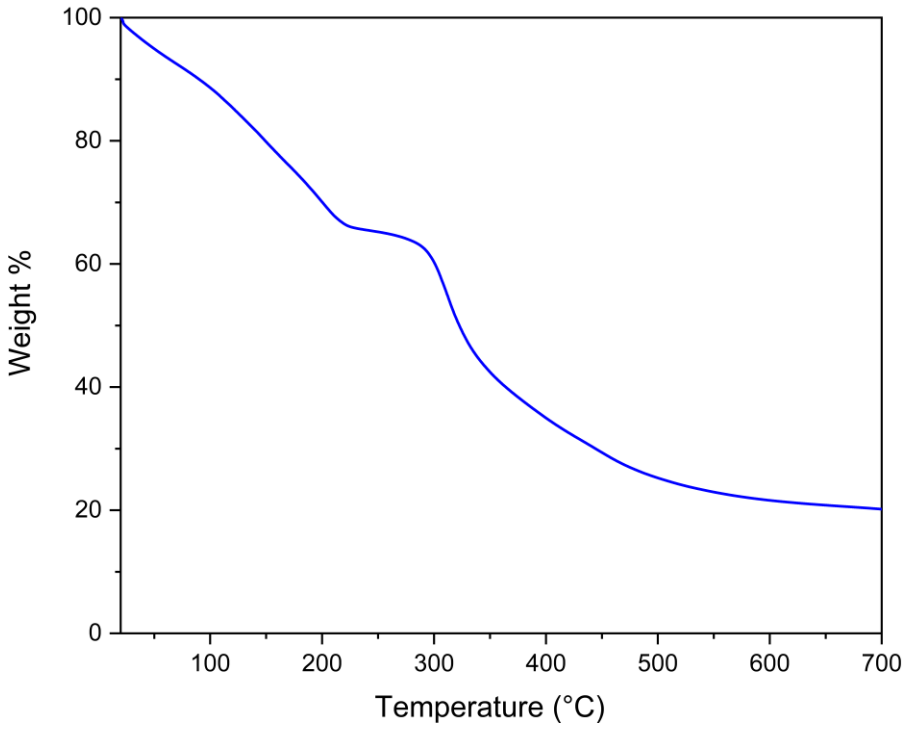

Figure 3.53: TGA of 11 heated at a rate of 4 ºC per minute under a nitrogen atmosphere.

3.5.2.3 Thermogravimetric analysis

The thermal stability of the compound was examined Thermogravimetric analysis of **11** was performed to examine the thermal stability of the compound. The measurement was carried out under air with a heating rate of 4 ºC per minute (**Figure 3.53**). An initial weight loss of *ca.* 35% occurred between 20 ºC and 230 ºC. This loss is calculated to be a loss of four DMF and four H_2O solvent molecules per unit cell of the crystal structure. The slow rate of loss of solvent mass can be attributed to the small channel diameter, which causes a slow rate of diffusion of solvents through the structure. A secondary loss of mass was found to occur between 268 ºC and 700 ºC. This loss is attributed to the decomposition of the $BTEB_{mmi}^{4-}$ linkers.

3.5.2.4 FT-IR and Raman spectroscopy

In the FR-IR spectrum of **11** a broad band is located at 3435 $cm^{-1,}$ which is due to the presence of hydrogen-bonded solvent molecules that are within the pores of the structure and coordinated to the Cu^{2+} ions within the $\{Cu_2\}$ SBUs (**Figure 3.54 a)**). A pair of bands at 2936 cm^{-1} and 2866 cm^{-1} is attributed to the ν(C-H) stretch from DMF molecules both within the porous structure and coordinated to the $\{Cu_2\}$ SBUs. A strong band due to the ν(O=C) stretching in the DMF molecule is found at 1652 cm^{-1}. This band overlaps the ν(C=O) stretch that is associated with the carboxylate groups of the $BTEB_{mmi}^{4-}$. The asymmetric carboxylate ν_{as}(COO) stretching mode of the $BTEB_{mmi}^{4-}$ linker is found at 1590 cm^{-1}, and the corresponding symmetric mode is located at 1385 cm^{-1}. The Deacon and Philips Δ value for the corresponding carboxylates are found to be *ca.* 195 cm^{-1}. This is in agreement with the to the observed bidentate bridging mode of the carboxylate groups.[233,306]

The Raman spectrum of **11** is mainly composed of bands from the $BTEB_{mmi}^{4-}$ linkers (**Figure 3.54 b)**). The spectrum was measured from 100 cm^{-1} to 2500 cm^{-1}. A strong band as 2212 cm^{-1} corresponds to the symmetric ν(C≡C) stretch of the acetylene groups. Two strong bands are found at 1600 cm^{-1} and 1579 $cm^{-1,}$ corresponding to ν(C=C) vibrational stretches within the phenyl rings. Three peaks corresponding to aromatic C=C bonds are found at 1179 cm^{-1}, 1127 cm^{-1} and 1113$cm^{-1.}$ The strong band at 996 cm^{-1} is attributed to C-H bending within the central phenyl ring.[235]

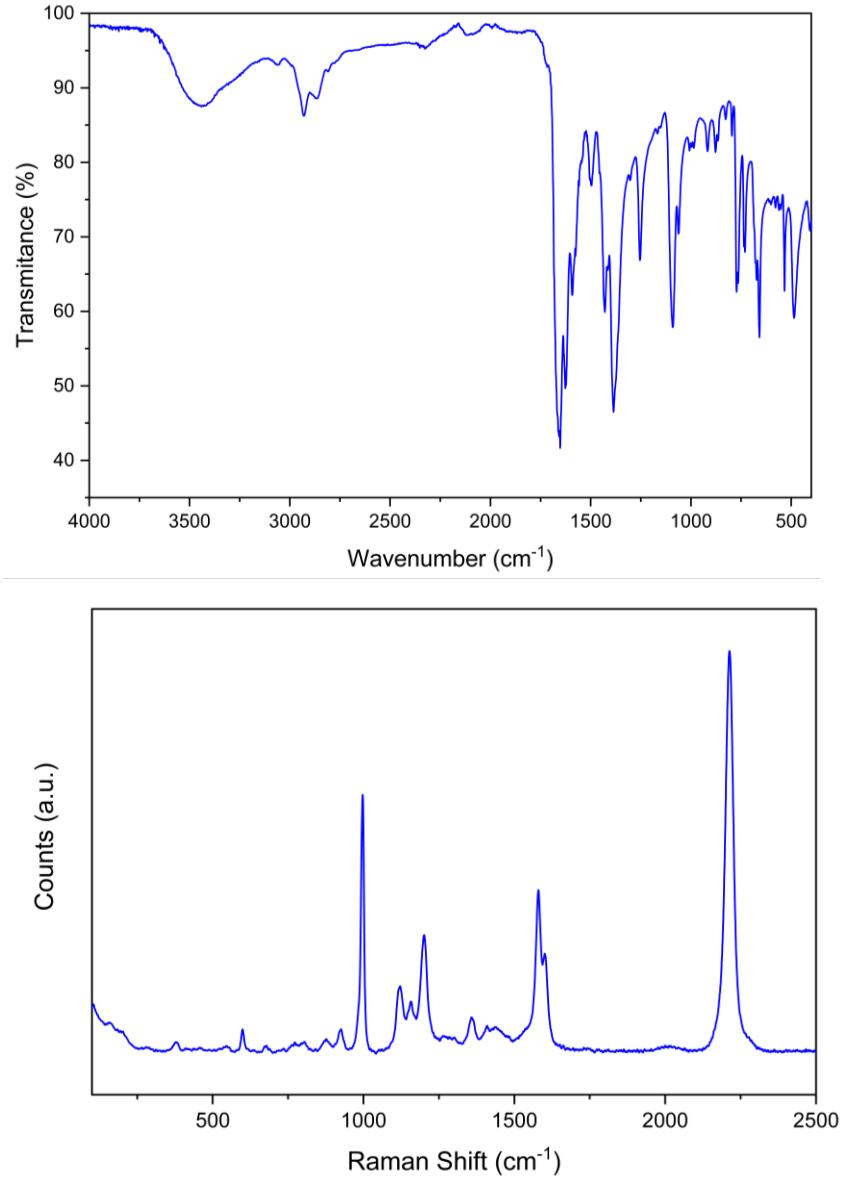

Figure 3.54: FT-IR and Raman spectra of 11.

3.5.2.5 Topology of **11**

Topological analysis of **11** was carried out using the software package ToposPro.[257] The $BTEB_{mmi}^{4-}$ linkers were subdivided into two 3-c nodes for the topological determination based upon the best practices outlined by O'Keeffe et. *al*.[307] The topological net for **11** was determined to be a trinodal (3,3,4)-connected net. The overall point symbol was determined to be $\{8^2.12\}\{8^3.10^2.12\}\{8^3\}$. The two 3-c nodes of the $BTEB_{mmi}^{4-}$ linker are non-equivalent in the structure due to the rotation of the benzoate moieties. As can be seen in **Figure 3.55** the node which corresponds to the isophthalate moiety is represented by the purple spheres while the node corresponding to the two *para*-benzoate moieties and central phenyl ring is coloured pink.

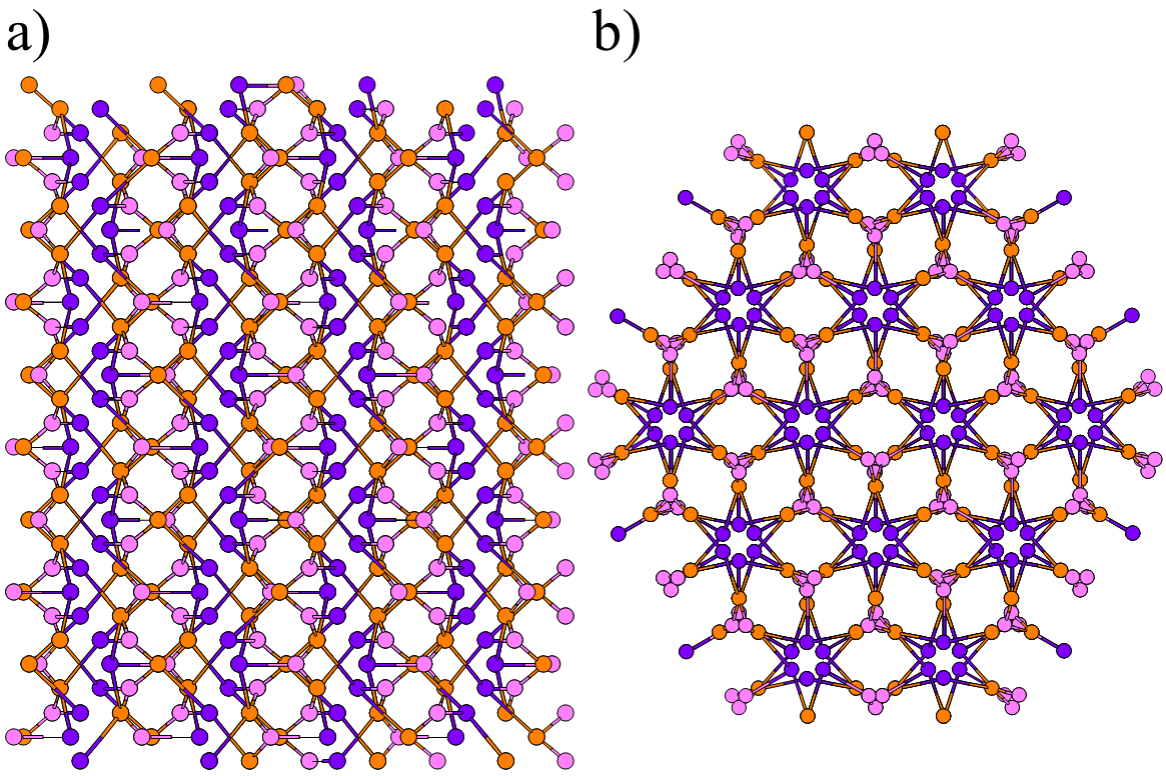

Figure 3.55: Topological representation of 11 viewed along crystallographic a) a/b-axis and b) c-axis. ({Cu_2} SBU - orange, isophthalate moiety - purple, *para*-benzoates and central phenyl ring – pink)

Table 3.11: Crystallographic details for 11.

Identification code	11
Empirical formula	$C_{40}H_{20}Cu_2O_{10}$
Formula weight	627.64
Temperature / K	215(2)
Crystal system	Hexagonal
Space group	*P6₁22*
***a* / Å**	21.5240(7)
***b* / Å**	21.5240(9)
***c* / Å**	21.0782(7)
***α* / º**	90
***β* /º**	90
***γ* / º**	120
Volume / Å^3	8456.9(7)
Z	4
ρ_{calc}/ g/cm^3	0.493
μ / mm^{-1}	0.688
F(000)	1272
Crystal size / mm^3	0.18×0.09×0.08
Radiation	
θ range for data collection / º	2.370 to 52.433
Index ranges	-15<=h<=20, -21<=k<=22, -21<=l<=21
Reflections collected	26968
Independent reflections	3214 [R(int) = 0.0752]
Data/restraints/parameters	3214 / 135 / 200
Goodness-of-fit on F^2	0.941
Final R indexes [I>=2σ (I)]	R_1 = 0.0650, wR_2 = 0.1727
Final R indexes [all data]	R_1 = 0. 0922, wR_2 = 0.1865
Largest diff. peak/hole / e.Å^{-3}	0.296 and -0.205

3.6 Use of pentacarboxylate linkers

Numerous attempts were carried out to synthesize a MOF which contained the two newly synthesized pentacarboxylate, H_5BTEB linkers. The synthetic conditions that were previously used in this chapter, for the other newly synthesised linkers, were found to be ineffective. From testing the broad range of conditions, the sole product that was produced was a blue amorphous powder. When examined by PXRD the powder was found to have extremely weak diffraction with few signals in the pattern. This result indicates that the product is amorphous and not the crystalline structure of a MOF. This result is not an unexpected outcome, however, for the use of pentacarboxylate linkers. There has only been a handful of literature examples that have been synthesised previously due to their synthesis difficulty. [278,309,310,304,311]

3.7 Conclusion and future work

In this chapter, we have successfully developed a new synthetic procedure for synthesising BTEB based linkers with a reduced symmetry compared to BTEB based linkers used in the literature. The synthesis utilises the different reactivity of chloride and iodide leaving groups in the Sonogashira reaction. Through careful control of the reaction conditions, it is possible to selectively add moieties to the 3,5-Dicholoriodobenzene starting material.The various combinations of the chosen moieties, *para*-benzoate, *meta*-benzoate and isophthalate, give rise to the linkers reduced symmetry. Six new BTEB based linkers are synthesised from the combinations. The number of carboxylate groups on the linkers varies between three to five, and the linkers have a range of different geometries.

The new BTEB based linkers with reduced symmetry and Cu^{2+} ions were then combined to synthesise a series of MOFs. The MOFs vary broadly in their frameworks and topologies. The new MOFs highlighted the linkers symmetry's impact on the framework's structure. **6** and **7** were synthesised using the $BTEB_{ppm}^{3-}$ linker with the difference in the structures arose from the dihedral angles between the moieties and the central phenyl ring. This difference in structures demonstrates the ability of alkyne space units to allow the linkers to access a more diverse range of conformations than would be possible with other spacer units. By using the $BTEB_{mmp}^{3-}$ linker, the impact of the simple exchange of a *para*-benzoate moiety to a *meta*-benzoate moiety has on a structure is highlighted. The structure of **8** is comprised of a series of two-dimensional, interpenetrated sheets. Each sheet contains super paddlewheel building units. These super paddlewheel building units occur when a BTEB linker contains two *meta*-benzoate moieties.

The $BTEB_{ppi}^{4-}$ linker requires a competitive binding strategy for its use in the synthesis of **9**. Using just Cu^{2+} salts in the synthesis led to the formation of a blue powder product. A 2:1 mole rai of Zn^{2+} to Cu^{2+} allowed for the growth of large enough crystals to be analysed. The blue powder product was

later identified using PXRD analysis and was confirmed to be isostructural to **9**, but only Cu^{2+} ions were present within the SBUs, giving the product **10**.

Attempts to use the new petacarboxyltae linkers to synthesise MOFs were found to be unsuccessful. However, this was not an unexpected outcome; it was previously known that peptacarboxylate groups often lead to complex synthesis. While the attempts in this work were unsuccessful, it does not rule out the possibility of MOFs containing these linkers. Work continues in this area to synthesise MOFs containing these linkers.

To aid in comparisons between the MOFs a new structural descriptor was developed. The descriptor is based upon the geometrical arrangement of the different moieties of the BTEB based linkers that coordinated to the $\{Cu_2\}$ SBUs. As previously mentioned, only certain combinations of arrangements can form together to satisfy the MOFs' charge balance and coordination requirements. The MOFs synthesised in this chapter were all found to fulfil these requirements. As shown in **Table 3.12** all MOFs were found to be in line with the allowable combinations.

Table 3.12:Possible combinations of arrangements for the moieties to coordinate to the $\{Cu_2\}$ SBUs with the combinations found in this body of work highlighted.

Primary moiety	Secondary moiety	The ratio of carboxylates on the primary and secondary moieties	The possible combination of arrangements
para-benzoate	*meta*-benzoate	2:1	**$\alpha_2\alpha'$**, $\alpha\gamma_2$, **$\alpha\delta_2$**, $\alpha\gamma\delta$, **$\beta_2\gamma$**, $\beta_2\delta$, $\alpha\beta\beta'$, $\beta_5\beta'$, $\alpha_5\beta'_4$, $\alpha_3\beta'_2\gamma$, $\alpha_3\beta'_2\delta$, …
meta-benzoate	*para*-benzoate	2:1	
para-benzoate	isophthalate	1:1	$\alpha\alpha'$, **γ**, **δ**, $\gamma\delta$, $\beta\beta'$, …
meta-benzoate	isophthalate	1:1	
isophthalate	*para*-benzoate	4:1	$\alpha_4\alpha'$, $\alpha_3\delta_2$, $\alpha_3\gamma_2$, $\alpha_3\delta\gamma$, $\alpha_2\beta_2\gamma$, $\alpha_2\beta_2\delta$, …
isophthalate	*meta*-benzoate	4:1	

The flexibility of the new synthetic strategy for BTEB based linkers allows for utilising more various moieties. Thus, expanding the family of linkers even further. Some examples of these possible moieties include pyridyl rings, salicylates, nicotinates, etc. The use of these mixtures of moieties could dramatically impact the structure and properties of synthesised MOFs. Another exciting area that requires further study is using two or more linkers in combination to synthesise a MOF. The

possible linker combinations can be as diverse as the linkers themselves. An example of an intriguing linker combination includes linkers with opposite moieties, i.e., H_3BTEB_{ppm} and H_3BTEB_{mmp} in combination, where the two linkers can be as isometrically opposite to each other. Using the linkers in combination allows for a greater variety of allowable arrangement combinations.

Chapter 4

Effects of BTEB based ligands with reduced symmetry on the structure and properties of inorganic SBUs

4 Effects of BTEB based ligands with reduced symmetry on the structure and properties of inorganic SBUs

4.1 Introduction

In this chapter, we wish to examine the effects of BTEB based linkers with reduced symmetry on the structure of the inorganic SBUs in MOFs. In the previous chapter, we focused on using Cu^{2+} ions to synthesise the inorganic SBUs due to their strong tendency to form dimeric paddlewheel SBUs. Using these predictable building units, it was possible to isolate the influence of the linkers symmetry on the structure of the MOF. In order to examine the influence of the linkers on the structure of the inorganic SBUs, metal ions that are capable of forming a broader range of SBUs are required. In this work, we chose to focus on the use of Zn^{2+} and Co^{2+} ions.

In comparison to Cu^{2+} ions, these metal ions have contrasting preferred coordination geometries. Zn^{2+} are hard ions owing to their filled d^{10} orbitals. Steric interactions between the coordinating ligands are the dominant influence on the coordination geometry around the Zn^{2+} ion. Due to this, they are capable of having a broad range of coordination geometries. In contrast, Co^{2+} ions tend to adopt octahedral or tetrahedral coordination geometries. This is dependent on the ligand field strength of the coordinating ligands.

Using the newly synthesised linkers from **Chapter 3** we will attempt to synthesise MOFs containing Zn^{2+} and Co^{2+} ions to develop new SBUs. The properties of the newly synthesised MOFs will then be examined. After several attempts using the newly synthesised linkers, only H_4BTEB_{ppi} and H_5BTEB_{iip} were successfully used to synthesise MOFs. H_4BTEB_{ppi} was used to synthesise $[NH_2(CH_3)_2]_6[Zn_9(BTEB_{ppi})_6]$ (**12**) and $[Co_2(BTEB_{ppi})(DMF)_3]$ (**13**). $[NH_2(CH_3)_2]_6[Zn_9(BTEB_{ppi})_6]$ (**12**) was determined to be an anionic framework that contains two uncommon inorganic SBUs. One SBU is a rare 5-connected SBU that has only been previously reported once in the literature as an SBU present within a MOF.[312]

A secondary $[Co_2(BTEB_{ppi})(DMF)_3]$(**13**) MOF was successfully synthesised using the H_4BTEB_{ppi} linker. In the $\{Co_2\}$ SBUs, which are used in the construction of the MOF, one of the Co^{2+} ions in the SBU was discovered to have three coordinated DMF solvent molecules. The presence of these solvent molecules is an indication that the MOF could be utilised as a water oxidation catalyst. The predicted catalytic properties of the MOF are based upon literature reports of Co^{2+} containing MOFs being used in this application.[313,314,315,316,204]

In attempts to utilise pentacarobxylate linkers, only a MOF containing Zn^{2+} ions and the H_5BTEB_{iip} could be synthesised. Unexpectedly the linker was found to only coordinate to the metal ions using the isophthalate moieties. The *para*-benzoate moiety was found to play a non-structural role in the framework of the MOF and is directed towards large cubic pores in the MOF. The large number of

free carboxylates are an attractive feature in MOFs owing to their use in a broad range of applications, including catalysis, dye absorption and drug absorption.[317,318,319]

4.2 Use of tetracarboxylate linkers

4.1.1 $[NH_2(CH_3)_2]_6[Zn_9(BTEB_{ppi})_6]$ (**12**)

4.1.1.1 Synthesis of $[NH_2(CH_3)_2]_6[Zn_9(BTEB_{ppi})_6]$ (**12**)

$[NH_2(CH_3)_2]_6[Zn_9(BTEB_{ppi})_6]$ (**12**) was synthesised by reacting $Zn(OAc)\cdot 2H_2O$ and H_4BTEB_{ppi}, in an equimolar ratio, in DMF, with 1% HOAc added as a modulator. After heating the solution at 85 ºC for 72 h a white precipitate initially occurred, which over 30 minutes redissolved. After the reaction had completed, clear, colourless, square plate-like crystals were found on the inner walls of the reaction vial. The crystals were isolated and washed with fresh DMF and were of sufficient quality and size for single-crystal X-ray analysis. The crystals were measured and solved in the orthorhombic space group *C222*, with the unit cell parameters determined to be a = 28.222(2) Å, b = 30.267(2) Å, c = 48.186(3) Å, $\alpha = \beta = \gamma = 90^{o}$.

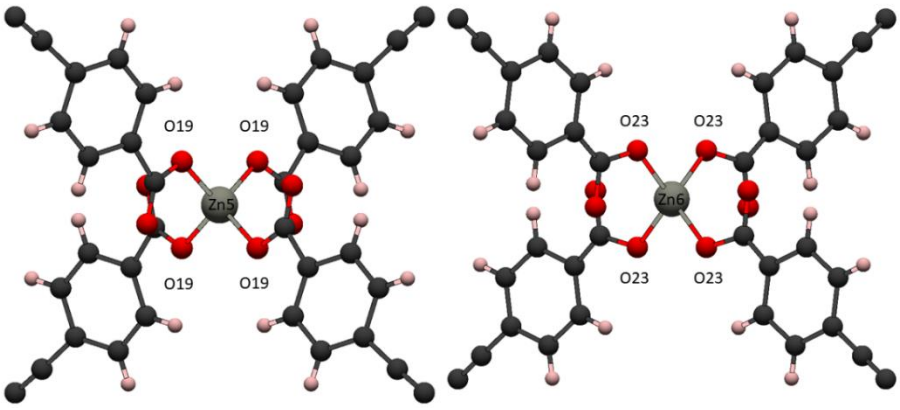

Figure 4.1: The two non-symmetry equivalent Zn^{2+} ions coordinated by O-donor atoms from four *para*-benzoate moieties in a distorted tetrahedral coordination environment. (O – red, C – black, H – pink, Zn – grey)

12 has the structure of a three-dimensional framework containing two structurally distinct inorganic SBUs and the $BTEB_{ppi}^{4-}$ linkers found in four crystallographically distinct conformations. One inorganic SBU contains a mononuclear Zn^{2+} ion coordinated by four O-donor atoms in a distorted tetrahedral coordination environment. Four O-donor atoms, originating from *para*-benzoate moieties, coordinate to the Zn^{2+} ion with a (η_1) coordination mode. Two crystallographically distinct mononuclear Zn^{2+} SBUs are present in the asymmetric unit. The four O-donor atoms that coordinated to the Zn^{2+} are all symmetry-related with a Zn(5)-O(19) bond length of *ca.* 1.943(15) Å and a Zn(6)-O(23) bond length of *ca.* 2.002(10) Å. The bond angles between the O-donor atoms that coordinate to Zn(5) range from *ca.* 105.7(12)º to *ca.* 116.8(16)º, while for the Zn(6) atom, the angles between

the coordinating O-donor atoms range from *ca.* 94.5(8)º to *ca.* 121.9(9)º (**Table 4.1**). This range of bond angles between the O-donor atoms leaves the two Zn^{2+} ions in a distorted tetrahedral geometry (**Figure 4.1**).

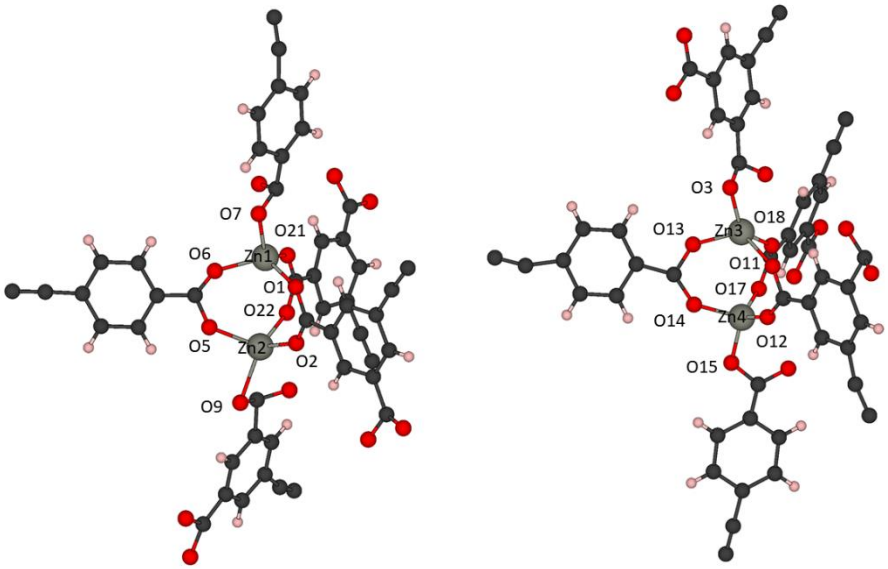

Figure 4.2: Two non-symmetrically equivalent Zn_2 SBUs found within the framework of 12. Note the difference in orientation of the isophthalate moieties, which coordinate to the equatorial positions on the {Zn_2} SBU. (O – red, C – black, H – pink, Zn – grey)

The second inorganic SBU consists of a {Zn_2} dimer coordinated by five carboxylate groups (**Figure 4.2**). In the dimeric SBU, four O-donor atoms coordinate to each Zn^{2+} ion. Three carboxylate groups bridge the two Zn^{2+} ions in a (μ_2-η^1:η^1) mode, at the equatorial positions of the {Zn_2} SBU. Two of the three equatorial carboxylates originate from isophthalate moieties, while the remaining carboxylate originates from a *para*-benzoate moiety. An O-donor atom coordinates to the axial sites on the Zn2+ ions from two monodentate carboxylates, completing the tetrahedral coordination environment around each Zn^{2+} ion. The origin of the coordinating carboxylate differs across the two Zn^{2+} ions in the SBU. Zn(1) and Zn(4) are coordinated by *para*-benzoate moieties at this axial position, while an isophthalate moiety coordinates Zn(2) and Zn(3).

Two crystallographically unique {Zn_2} SBUs are present within the framework of the MOF, with each being distinguished by the orientation of the isophthalate moieties, which coordinate to the equatorial positions on the SBU. Due to the orientations of the isophthalate moieties, each {Zn_2} SUB has a chiral character. Due to the {Zn_2} SBUs being present in a 1:1 ratio, the chiralities counteract with each other causing the framework can be seen as a racemic structure (**Figure 4.2).**

Table 4.1: Selected bond lengths and bond angles found in 12.

Atoms	Distance	Atoms	Angle
Zn1-O1	1.937(8)	O1-Zn1-O6	116.4(4)
Zn1-O6	1.928(6)	O1-Zn1-O21	108.8(3)
Zn1-O7	2.164(16)	O6-Zn1-O21	111.5(3)
Zn1-O21	2.010(7)	O1-Zn1-O7	95.2(5)
Zn2-O2	1.941(8)	O6-Zn1-O7	96.4(5)
Zn2-O5	2.020(11)	O7-Zn1-O21	128.1(6)
Zn2-O9	2.185(17)	O2-Zn2-O5	122.5(5)
Zn2-O10	2.431(16)	O2-Zn2-O22	93.4(5)
Zn2-O22	2.025(8)	O5-Zn2-O22	107.5(6)
Zn3-O3	2.021(11)	O2-Zn2-O9	109.8(6)
Zn3-O4	2.356(12)	O5-Zn2-O9	91.9(6)
Zn3-O11	2.215(10)	O22-Zn2-O9	135.2(7)
Zn3-O13	1.980(14)	O2-Zn2-O10	100.2(6)
Zn3-O17	1.898(10)	O5-Zn2-O10	135.6(6)
Zn4-O12	2.007(11)	O9-Zn2-O10	79.1(5)
Zn4-O14	1.885(11)	O22-Zn2-O10	59.8(5)
Zn4-O15	1.870(9)	O3-Zn3-O13	101.0(5)
Zn4-O18	1.960(10)	O3-Zn3-O17	138.6(5)
Zn5-O19	1.943(15)	O13-Zn3-O17	103.3(5)
		O3-Zn3-O11	103.2(5)
		O11-Zn3-O13	123.8(6)
		O11-Zn3-O17	90.3(5)
		O3-Zn3-O4	55.9(5)
		O4-Zn3-O11	116.0(6)
		O4-Zn3-O13	119.6(7)
		O4-Zn3-O17	82.9(5)
		O12-Zn4-O14	105.0(5)
		O12-Zn4-O18	121.4(5)
		O14-Zn4-O18	109.8(7)
		O14-Zn4-O15	96.7(6)

		O15-Zn4-O18	105.2(6)
		O19-Zn4-O19	106.8(16)
		O19-Zn4-O19	105.7(12)
		O19-Zn4-O19	116.2(14)

The $BTEB_{ppi}^{4-}$ linker is found in four crystallographically distinct conformations. However, the linkers can be divided into two structurally distinct building units within the structure of the MOF. The rotation of the *para*-benzoate and isophthalate moieties with respect to the central phenyl ring differentiate the four conformations. In **Table 4.2** the differences in the four different conformations can be seen. While the conformations have varying sizes in the dihedral angles, the four conformations can be divided into two groups, **i / ii** and **iii / iv.** Within the structure of the MOF, the conformations create two sets of sandwich-like stacked units, in which each set contains three linkers (**Figure 4.3**). The two external $BTEB_{ppi}^{4-}$ linkers of the stacked unit adopt either conformation **i** or **ii** while the linkers located at the centre has conformation **iii** or **iv**. In the two stacked units, the $BTEB_{ppi}^{4-}$ linkers stack in the order **i** – **iii** − **i** or **ii** – **iv** − **ii.** Both units are stabilised by a π-π interaction between the central phenyl rings on each $BTEB_{ppi}^{4-}$ linkers. The central phenyl rings are in a parallel displaced arrangement with a centre to centre distance of *ca.* 4.041(7) - 4.127(9) Å. The phenyl rings have a normal distance of *ca.* 3.3(15) Å and a horizontal displacement of *ca.*2.29(13) – 2.48(2) Å (

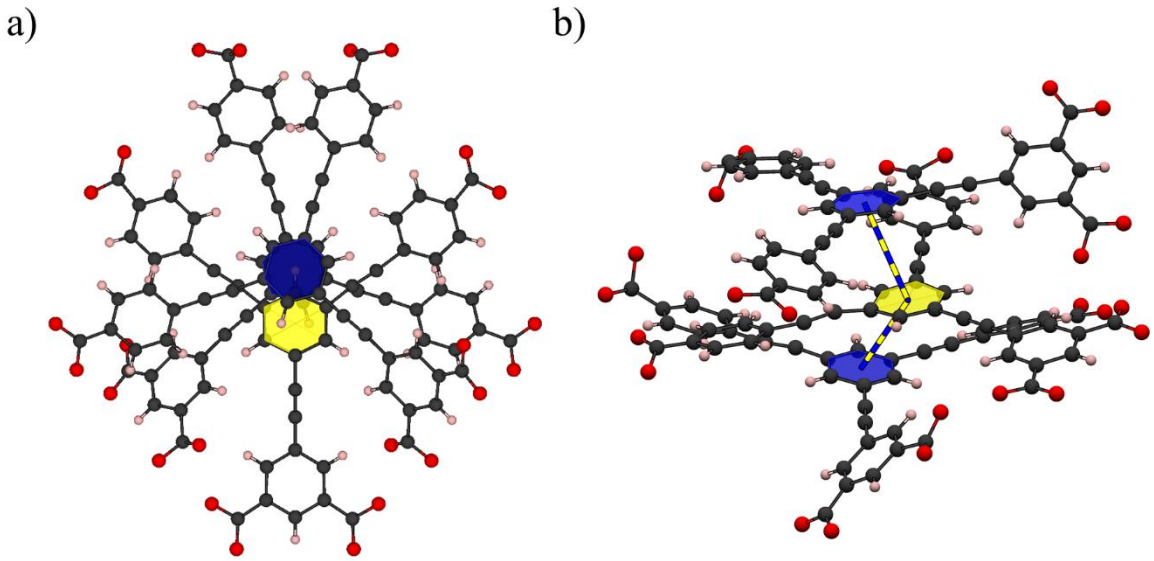

Figure 4.3: π-π interaction within the i-iii-i sandwich arrangement. a) viewed down the stacking axis and b) viewed from the side. (mean plane on central phenyl for conformation i – blue hexagon, mean plane of central phenyl for conformation iii – yellow hexagon, π-π interaction between phenyl rings - blue and yellow line.)

Table 4.3). The angle between the plane of the two interacting phenyl rings is *ca.* 7.4(4) – 7.9(5) º. These geometrical parameters are in line with those of literature reported π-π interactions between phenyl rings.[320,245]

The four conformations of the $BTEB_{ppi}^{4-}$ linkers are distinguishable by the location on the inorganic SBUs that they coordinate to. Conformations **i** and **ii** coordinate solely to the 5-connected $\{Zn_2\}$ SBUs. The *para*-benzoate moiety that has a rotation of *ca.* 27.9 and *ca*. 46.8 º with respect to the central phenyl ring on conformations **i** and **ii**, coordinate to the $\{Zn_2\}$ SBUs at the axial position of the SBU. The second *para*-benzoate moiety, with a rotation of *ca.* 0.6 and *ca.* 8.4 º, coordinate to the $\{Zn_2\}$ SBU at the equatorial position. These carboxylate groups bridge the two Zn^{2+} ions in a bidentate *syn,syn*-bridging mode. The two carboxylate groups on the isophthalate moiety coordinate to two different sites on the $\{Zn_2\}$ SBU. One carboxylate coordinates to a Zn^{2+} ion at the axial position of the $\{Zn_2\}$ SBU, while the second carboxylate group bridges the two Zn^{2+} ions in *syn,syn*-bridging mode (**Figure 4.2**).

The conformations **iii** and **iv** serve as the link between the mononuclear Zn SBUs and the $\{Zn_2\}$ SBUs. The isophthalate moiety on conformations **iii** and **iv** coordinates to two $\{Zn_2\}$ SBUs at the equatorial sites in a *syn,syn*-bridging mode. The *para*-benzoate moieties on the two conformations coordinate to two different mononuclear Zn SBUs as shown in **Figure 4.1**; the *para*-benzoate moieties occupy all coordination sites around the Zn^{2+} ion due to symmetry.

Table 4.2:Dihedral angles between the average plane of the central phenyl ring and the plane of the peripheral benzoate moieties in 12

Conformation	The dihedral angle between *para*-benzoate (1) and central phenyl ring	The dihedral angle between *para*-benzoate (2) and central phenyl ring	The dihedral angle between isophthalate and central phenyl ring
i	27.9(4) º	8.4(5) º	40.4(4) º
ii	46.8(5) º	0.6(5) º	40.7(5) º
iii	10.6(7) º	10.6(7) º	5.5(8) º
iv	7.5(6) º	7.5(6) º	16.1(9) º

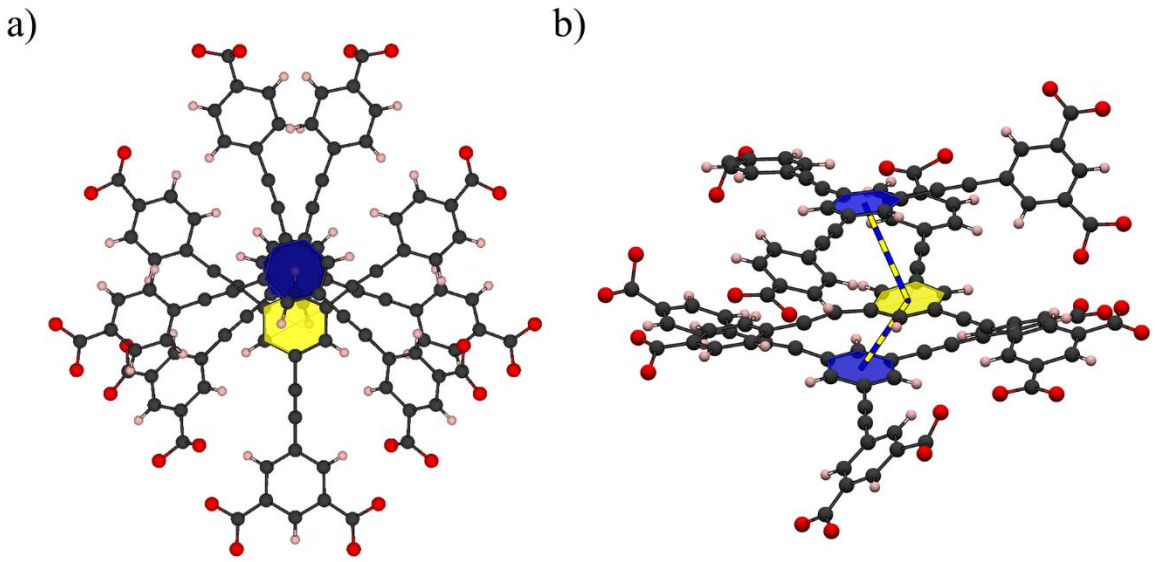

Figure 4.3: π-π interaction within the i-iii-i sandwich arrangement. a) viewed down the stacking axis and b) viewed from the side. (mean plane on central phenyl for conformation i – blue hexagon, mean plane of central phenyl for conformation iii – yellow hexagon, π-π interaction between phenyl rings - blue and yellow line.)

Table 4.3:Geometrical parameters for the π-π interaction between the $BTEB_{ppi}^{4-}$ central phenyl rings in 12.

Conformations	Centre to centre distance (d)	Normal distance (R)	Horizontal displacement distance (*r*)	Tilt angle between two interacting central phenyl rings
i-iii	4.137(9) Å	3.310(15) Å	2.48(2) Å	7.9(5) Å
ii-iv	4.041(7) Å	3.328(6) Å	2.292(13) Å	7.4(4) Å

The framework of the MOF has an overall anionic charge due to the ratio of $BTEB_{ppi}^{4-}$ linkers to Zn^{2+} ions. The anionic charge attributed to the framework from each SBU depends on the number of coordinating carboxylates. The mononuclear Zn SBU has an overall charge of 2- with the Zn^{2+} ion is coordinated by four 1- carboxylate groups. At the same time, the $\{Zn_2\}$ SBU would have an overall charge of 1- from the two Zn^{2+} ions being coordinated by five 1- charged carboxylate groups. This anionic charge is balanced in the crystal by the presence of cations within the pores of the MOF. A

common decomposition side product of DMF is the base dimethylamine. This amine would then become protonated in the presence of an acid, like the carboxylic acid on the linker and the HOAc reaction modulator, thus forming the cation dimethylammonium.[321] However, due to the disorder of the cation within the pore, it is unresolvable crystallographically.

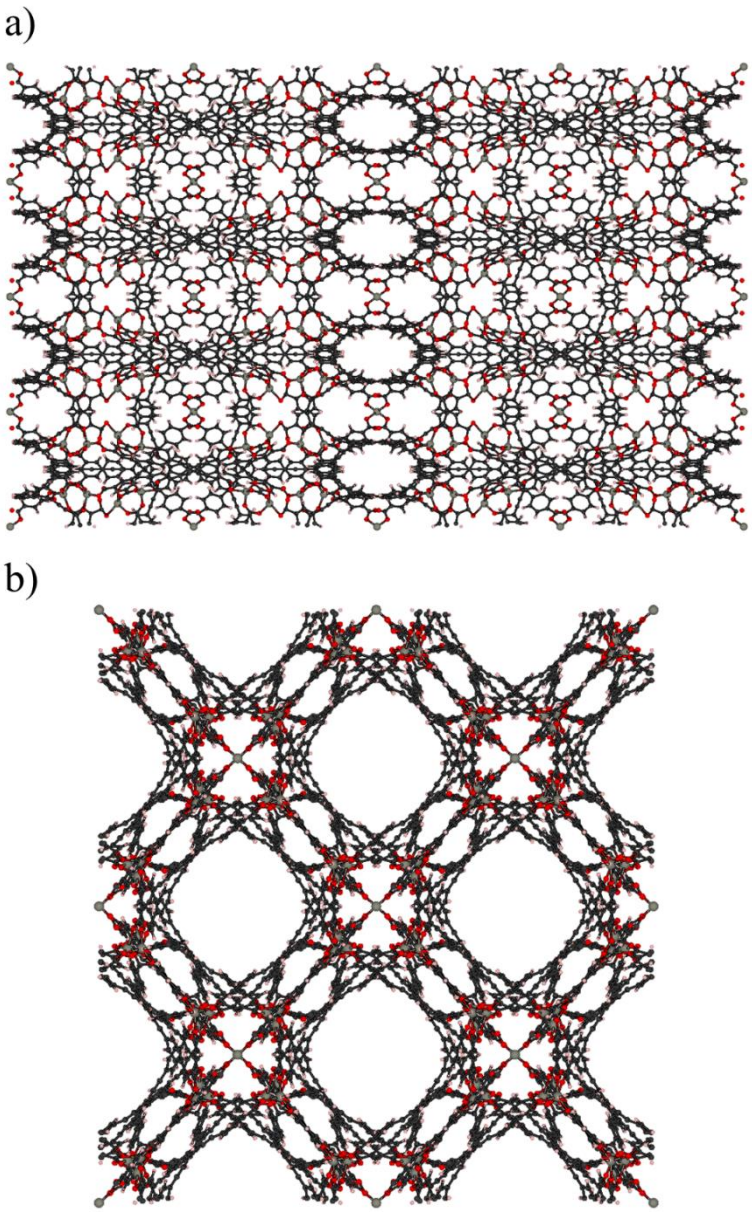

Figure 4.4: Packing arrangement of 12 viewed along the crystallographic a) *a* and *b*-axis and b) *c*-axis. Large channels extend into the structure along the crystallographic *c*-axis with smaller secondary channels along the crystallographic *a/b* that interconnect the larger channels. (C – black, O – red, H – pink, Zn – grey)

The overall structure of **12** is a three-dimensional framework with large channels that extend into the MOF along the crystallographic *c*-axis. A series of smaller secondary channels extend into the structure along the crystallographic *a* and *b*-axis, interconnecting the previously mentioned channels (**Figure 4.4**). In **Figure 4.4 b),** the inorganic SBUs are shown to be located within the walls of the

MOF. However, the mononuclear Zn SBU remain accessible through the channels that extend along the crystallographic *a*- and *b*-axis. This accessibility by solvents and gas molecules to the Zn SBU may attribute to the overall instability of the MOF. The $BTEB_{ppi}^{4-}$ linker can be seen to line the channels that extend along the crystallographic *c*-axis. Due to the lack of polar functional groups on the linkers, they impart a hydrophobic character to the channels of the MOF.

The potential surface area and pore-size distribution of the MOF were calculated using the Problazer software package.[225] A He pore volume of *ca.* 1.165 cm^3/g and an accessible surface area of *ca.* 2432 m^2/g was calculated for the desolvated MOF. The limiting pore diameter was determined to be *ca.* 9.90 Å, with the maximum pore diameter of *ca.* 13.7 Å. These pore diameters correspond well to the crystallographic estimations, with the maximum pore diameter corresponding to the channels that extend into the structure along the crystallographic *c*-axis. In **Figure 4.5** the pore-size distribution can be seen.

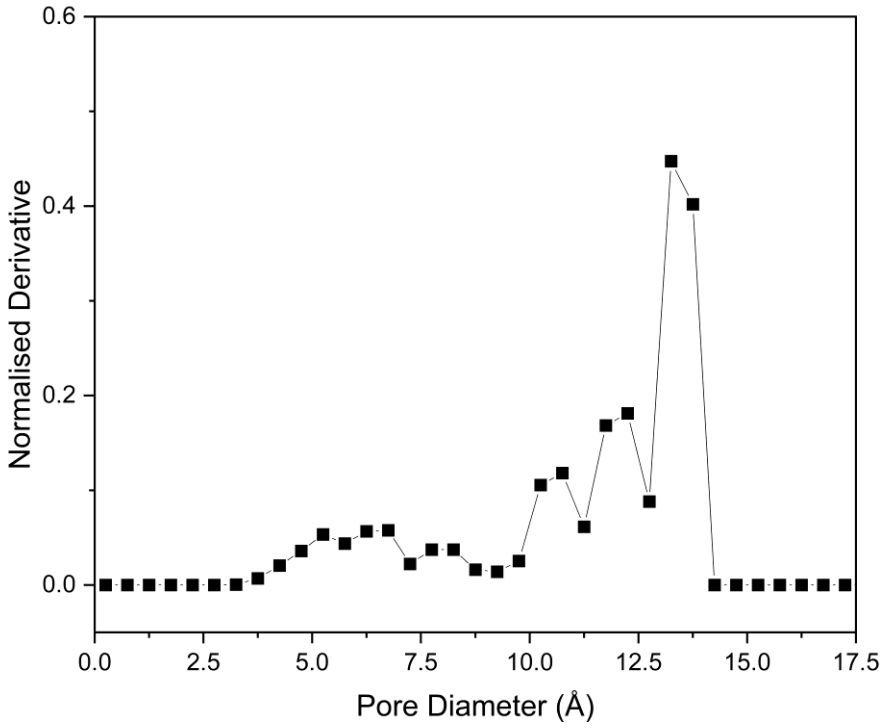

Figure 4.5: Simulated pore-size distribution of 12.

4.1.1.2 Topology of **12**

Using the ToposPro software package, a topological analysis of the MOF was carried out.[257] For topological determination, the $BTEB_{ppi}^{4-}$ linkers were first subdivided into two 3-c nodes within the structure. This is in line with the best practices outlined by O'Keffee *et al*.[307] The topological net for **12** was determined to be a hexa-nodal (3,3,3,3,4,5)-connected net. The overall point symbol was determined to be $\{6.7.8\}_4\{6.7^2\}_4\{6.7^3.8^3.9.10^2\}_4\{7.10^2\}_2\{8.10^2\}_2\{8^4.10^2\}$. The overall stoichiometry for the net, as reflected in the point symbol, is $(3\text{-c})_4(3\text{-c})_4(3\text{-c})_2(3\text{-c})_2(4\text{-c})(5\text{-c})_4$. [61] In **Figure 4.6**, the two 3-c nodes, corresponding to the $BTEB_{ppi}^{4-}$ linker found in conformation **i** and **ii,** are shown in

light green for the isophthalate moiety and dark green for the *para*-benzoate moieties. The two 3-c nodes corresponding to the $BTEB_{ppi}^{4-}$ linker found in conformation **iii** and **iv** are pink for the isophthalate moiety and purple for the *para*-benzoate moieties. The remaining 4-connected node corresponds to the Zn tetrahedron SBUs and the $\{Zn_2\}$ SBUs corresponding to the 5-connected node, are coloured blue and red in **Figure 4.6**, respectively.

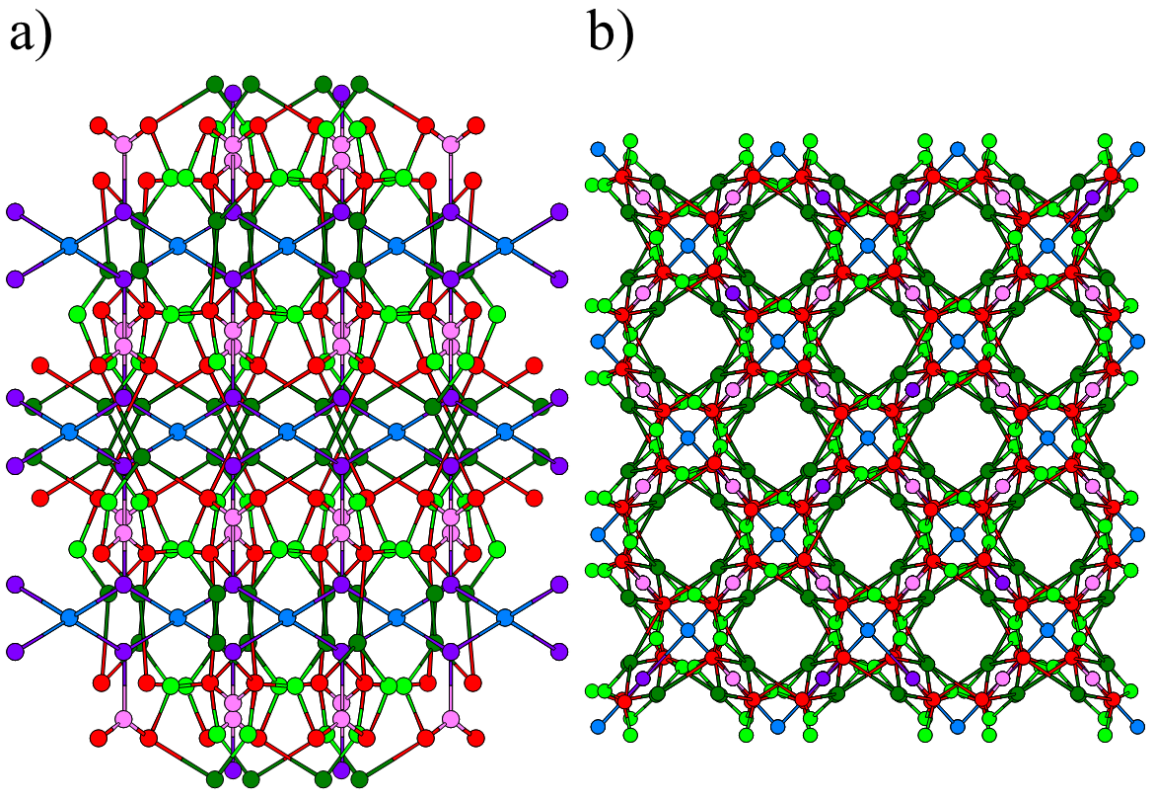

Figure 4.6:Topological reduction of 12 viewed along the a) crystallographic *a/b* axis and b) crystallographic *c* axis. (Zn tetrahedron SBU – blue, $\{Zn_2\}$ SBU – red, $BTEB_{ppi}^{4-}$ with conformations i and ii – light and dark green, $BTEB_{ppi}^{4-}$ with conformations iii and iv – pink and purple)

4.1.1.3 X-ray powder diffraction

PXRD analysis was used to verify the phase purity of **12**. Preparing the sample for measurement was done using the previously described technique of grinding crystals of the MOF to a powder within the mother liquor before loading the sample into a quartz capillary. The sample was measured at 215 K on a Bruker APEX II DUO X-ray diffractometer. The background signal and the fit of the experimental diffraction to the theoretical diffraction pattern were calculated using the Expo 2014 software package.[228,229] Using the Reitvield[230] method, the unweighted R-factor and the weighted R-factor were determined to be Rp = 2.329 and Rwp = 3.605, respectively. The experimental diffraction pattern matched well with the theoretical diffraction pattern confirming the phase-purity of the material (**Figure 4.7**).

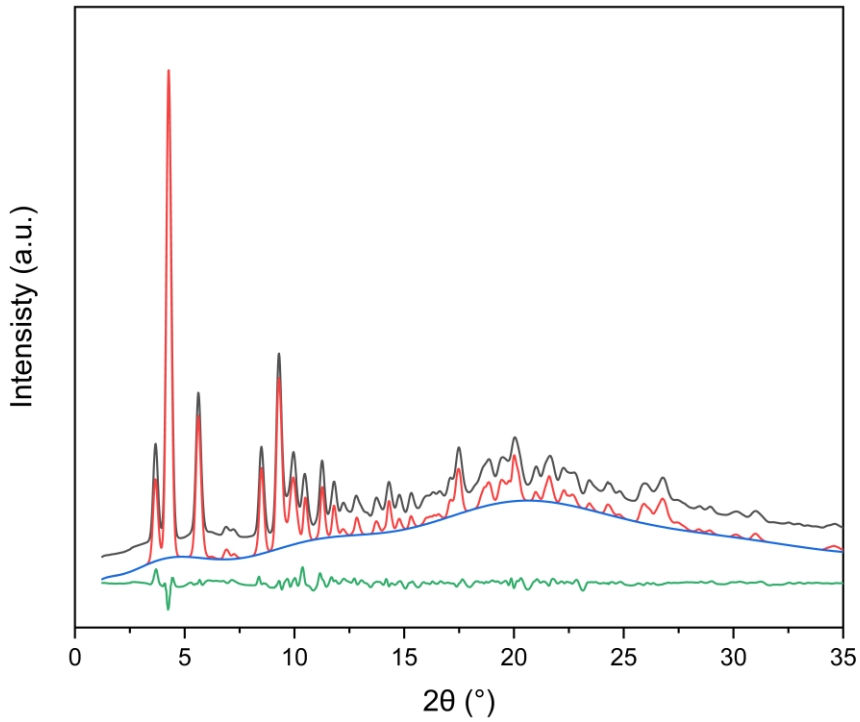

Figure 4.7: PXRD pattern of 12. (measured PXRD pattern – black, calculated background correction - blue, fitted theoretical PXRD pattern – red, the difference between measured and theoretical PXRD pattern – green.)

4.1.1.4 Thermogravimetric analysis

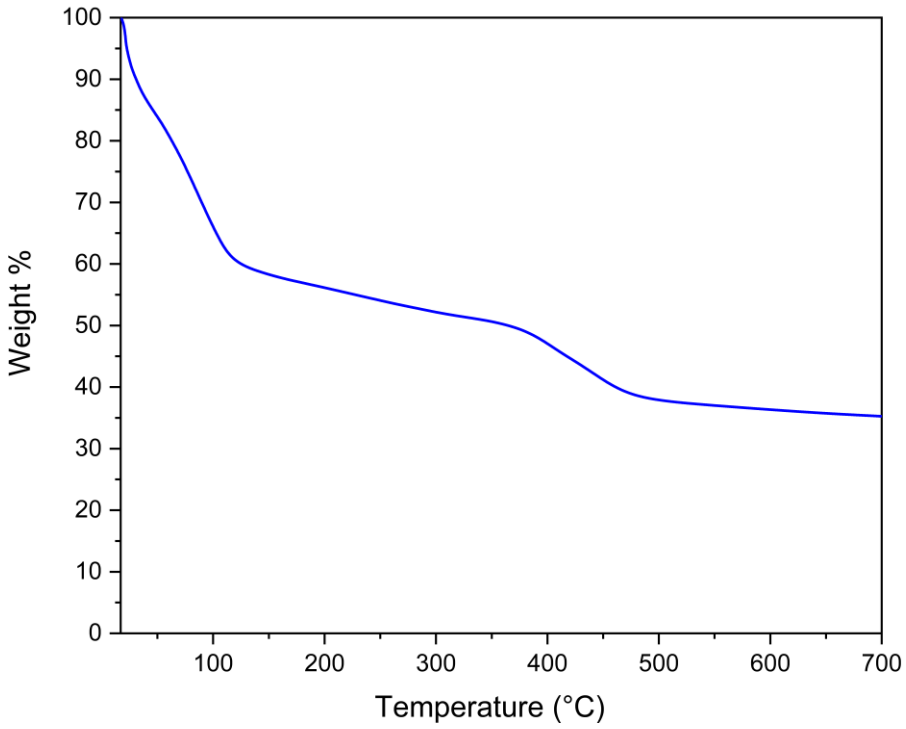

Figure 4.8: TGA analysis of 12 heated under a nitrogen atmosphere at 4 ºC per minute.

Thermogravimetric analysis was performed to examine the thermal stability of **12** (**Figure 4.8**). The compound was first prepared by drying crystals of **12** between two sheets of filter to remove any surface solvents from the crystals. The sample was heated under a nitrogen atmosphere with a rate of 4 ºC per minute. An initial weight loss of *ca.* 42.5 % occurred between 20 ºC and 125 ºC. This initial loss of mass can be attributed to the loss of solvent molecules located within the pores of the MOF. A further loss in mass occurs between 125 ºC and 375 ºC, which is due to the loss of slower diffusing solvent molecules within the porous structure. The subsequent significant loss in mass was found to occur between 337 ºC and 498 ºC, with a weight loss of *ca.* 11.5 % attributed to the decarboxylation of the $BTEB_{ppi}^{4-}$ linkers. A further loss of 2.6 % mass occurs between 498 ºC and 700 ºC with the further decomposition of the $BTEB_{ppi}^{4-}$ linkers.

4.1.1.5 FT-IR and Raman spectroscopy

In the FT-IR spectrum, the broad band at 3464 cm^{-1} may arise from two sources. One source is due to $NH_2Me_2^+$ counter ions that form from the decomposition of the DMF solvent (**Figure 4.9 a**). A pair of bands at 2928 cm^{-1} and 2861 cm^{-1} is attributed to the ν(C-H) stretching from DMF molecules within the porous structure. At 1654 $cm^{-1,}$ the ν(O=C) stretching in the DMF molecule can be seen. Due to a large number of coordination modes of the carboxylate groups to the Zn^{2+} ions, a significant overlap of peaks occurs for the asymmetric stretch. The asymmetric carboxylate ν_{as}(COO) stretching modes were found at 1633 cm^{-1}, 1605 cm^{-1}, and 1588 cm^{-1} respectively. The corresponding symmetric mode ν_s(COO) are found at 1456 cm^{-1}, 1435 cm^{-1} 1408 cm^{-1}.The corresponding symmetrical stretch to each asymmetrical stretch is not identifiable, making it difficult to determine the Deconc Philipgs Δ for the various carboxylates. The calculated Δ across all combinations of pairings range from 132 cm^{-1} to 225cm^{-1}. This range covers all expected bonding modes for carboxylates to metal centres.

The Raman spectrum of **12** is mainly composed of bands from the $BTEB_{ppi}^{4-}$ linkers (**Figure 4.9 b**). The spectrum was measured from 100 cm^{-1} to 2500 cm^{-1}. A strong band at 2219 cm^{-1} corresponds to the symmetric ν_s(C≡C) stretch. Two strong bands corresponding to the phenyl ring aromatic ν(C=C) stretch are located at 1605 cm^{-1} and 1582 $cm^{-1,}$ respectively. Bands at 1412 cm^{-1} and 1363 cm^{-1} are attributed to ν_s(C=O) bands of the carboxylate groups. In-plane δ(C-H) bending modes due to the *para*-benzoate moieties can be seen, while slightly lower wavenumbers of 1134 cm^{-1} and 1121 cm^{-1} correspond to the δ(C-H) bending modes in the isophthalate moiety. A large band attributed to the central phenyl in-plane δ(C-H) bending occurs at 992 cm^{-1}. Two bands at 889 cm^{-1} and 848 cm^{-1} correspond to the out of plane ω(C-H) waging modes for the isophthalate moiety and the central phenyl, respectively. The isophthalate gives rise to weaker bands due to the polarisation induced by the carboxylate groups. The out of plane ω(C-H) wagging for the *para*-benzoate moiety occurs at 642 cm^{-1}.

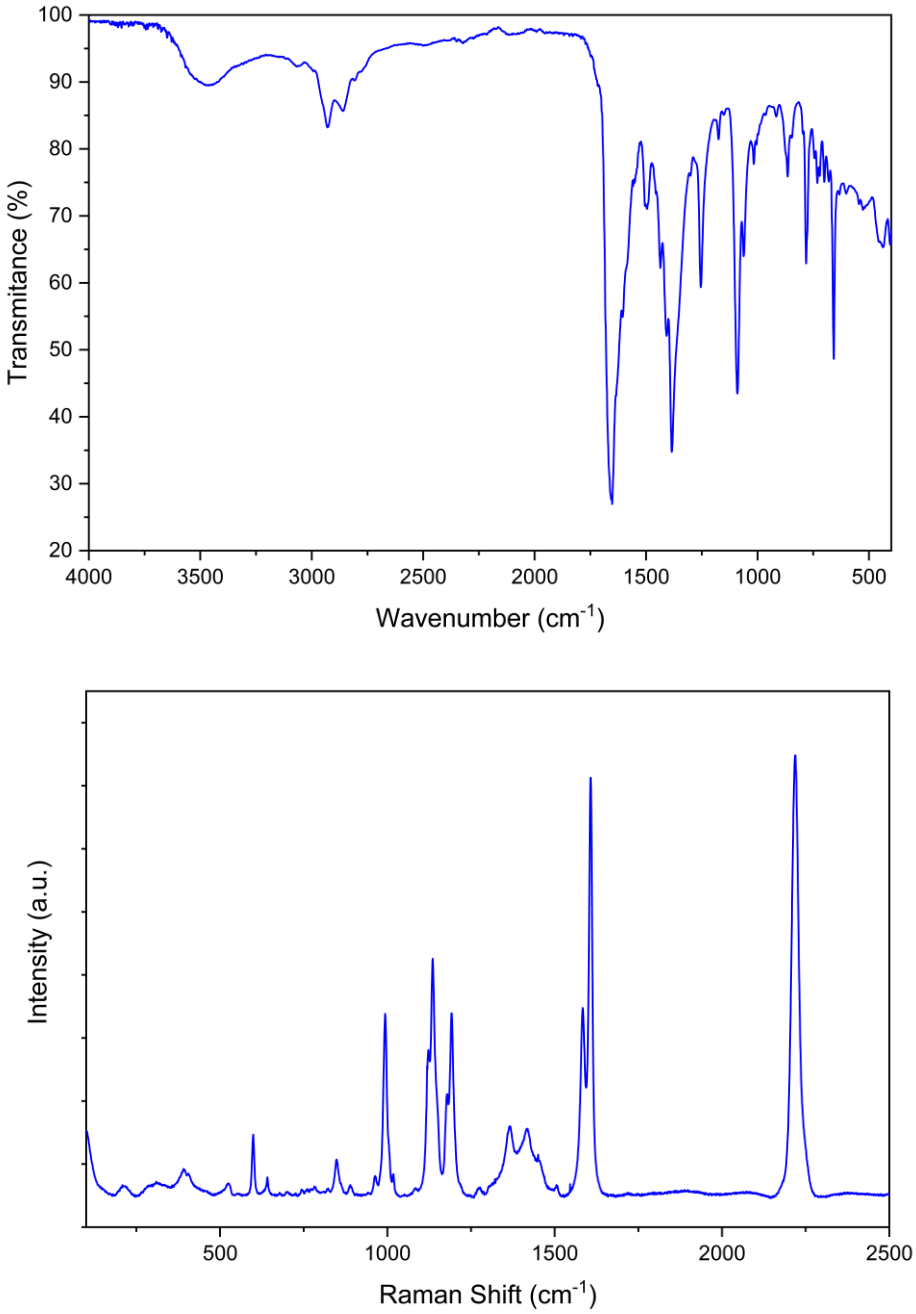

Figure 4.9: a) FT-IR and b) Raman spectra of 12.

Table 4.4: Crystallographic details for 12.

Identification code	12
Empirical formula	$Zn_9O_{48}C_{191}H_{78}$
Formula weight	3728.86
Temperature / K	215(2)
Crystal system	Orthorhombic
Space group	*C222*
***a* / Å**	28.222(2)
***b* / Å**	30.267(2)
***c* / Å**	48.186(3)
***α* / º**	90
***β* /º**	90
***γ* / º**	90
Volume / Å^3	41161(5)
Z	8
ρ_{calc}/ g/cm^3	0.602
μ / mm^{-1}	0.859
F(000)	7512
Crystal size / mm^3	0.500 × 0.450 × 0.400
Radiation	1.54178 Å
θ range for data collection / º	1.834 to 52.748
Index ranges	-28<=h<=28, -15<=k<=30, -49<=l<=38
Reflections collected	61887
Independent reflections	23151 [R(int) = 0.0896]
Data/restraints/parameters	23151 / 976 / 1062
Goodness-of-fit on F^2	0.928
Final R indexes [I>=2σ (I)]	R_1 = 0.0738, wR_2 = 0.1954
Final R indexes [all data]	R_1 = 0.1376, wR_2 = 0.2408
Largest diff. peak/hole / e.Å^{-3}	0.251 and -0.356

4.1.2 $[Co_2(BTEB_{ppi})(DMF)_3]$ (**13**)

4.1.2.1 Synthesis of $[Co_2(BTEB_{ppi})(DMF)_3]$ (**13**)

$[Co_2(BTEB_{ppi})(DMF)_3]$ (**13**) was synthesised by heating a solution of $Co(NO_3)_2 \cdot 6H_2O$ and H_3BTEB_{ppi}, in a 2:1 mole ratio, in DMF with a 1% addition of HOAc. After heating the solution for 96 h at 85 ºC, it yielded large violet, prismatic crystals that grew on the base of the reaction vial. A pink amorphous side product was also produced, which, through gentle agitation of the reaction vial, was separated from the crystals. Fresh DMF was used to clean the isolated crystals further. The synthesised crystals were of sufficient size and quality for single-crystal X-ray analysis. The structure was measured and solved in the orthorhombic space group *Fdd2* with the crystallographic parameters a = 50.464(9) Å, b = 57.890(9) Å, c = 13.204(2) Å, $\alpha = \beta = \gamma = 90^o$.

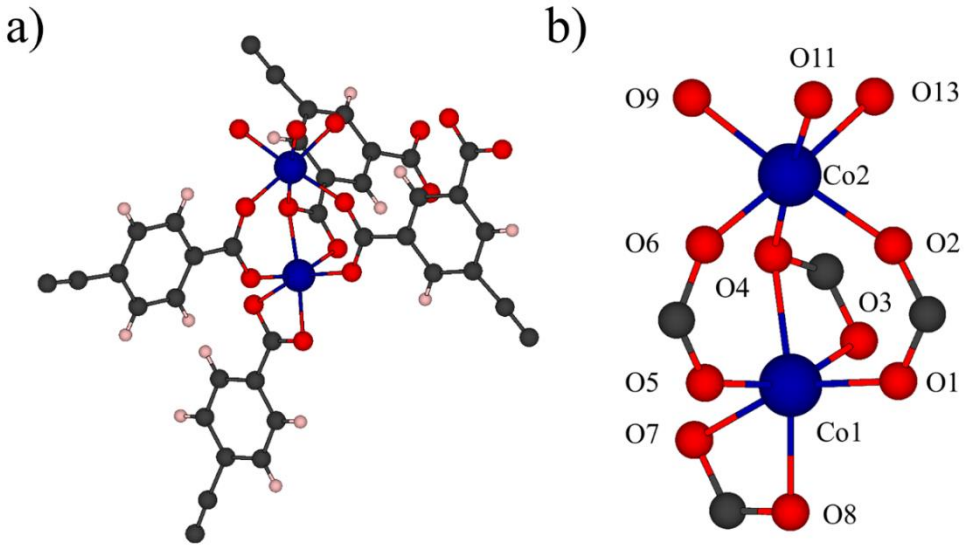

Figure 4.10: The coordination environment around the {Co_2} SBU found in 13 with a) solvent removed for charity and b) phenyl rings removed for charity. (C - black, O - red, H - pink, Co - blue)

13 is a three-dimensional framework with the chemical formula $[Co_2(BTEB_{ppi})(DMF)_3]$. The MOF's framework contains an inorganic SBU connected by $BTEB_{ppi}^{4-}$ linkers. The inorganic SBU is a dimeric structure with the two Co^{2+} ions bridged by carboxylate groups. O-donor atoms coordinate to the Co^{2+} ions creating a distorted octahedral coordination geometry (**Figure 4.10**). Four carboxylate groups coordinate to Co(1) with various coordination modes. One carboxylate group coordinates to the Co^{2+} ion in a chelating (η^2) coordination mode. The remaining three carboxylate groups bridge the two Co^{2+} ions. Two carboxylate groups bridge the two Co^{2+} ions in a *syn*, *syn* bidentate (μ_2-η^1:η^1) coordination mode, similar to that of the carboxylate groups coordinating in the {Cu_2} paddlewheel SBUs discussed in previous chapters. The final remaining carboxylate group, containing O(3) and O(4), bridges the two ions while chelating to Co(1) in a (μ_2-η^2:η^1) mode. The remaining coordination sites on the Co(2) ion are occupied by O-donor atoms, O(9), O(11) and

O(13), from three DMF solvent molecules. Selected bond lengths and angles are shown in **Table 4.5** to highlight the distorted octahedral coordination geometry around each Co^{2+} ion. Based on literature reports of similar compounds, the presence of these coordinated solvent molecules is an indication that the MOF could be utilised as a water oxidation catalyst.

Table 4.5: Selected bond lengths and angles in 13.

Atoms	Distance	Atoms	Angle
Co1-O1	2.026(5) Å	O1-Co1-O3	91.0(2) º
Co1-O3	2.183(5) Å	O1-Co1-O4	104.51(19) º
Co1-O4	2.201(5) Å	O1-Co1-O5	99.5(2) º
Co1-O5	1.984(6) Å	O3-Co1-O4	59.6(3) º
Co1-O7	2.202(7) Å	O8-Co1-O7	59.8(3) º
Co1-O8	2.040(7) Å		
		Co1-O4-Co2	106.9(2) º
Co2-O2	2.066(6) Å		
Co2-O4	2.087(5) Å	O2-Co2-O4	90.2(2) º
Co2-O6	2.059(6) Å	O2-Co2-O6	93.8(2) º
Co2-O9	2.041(7) Å	O2-Co2-O9	176.1(2) º
Co2-O11	2.103(7) Å	O2-Co2-O11	88.8(6) º
Co2-O13	2.095(5) Å	O2-Co2-O13	87.7(2) º

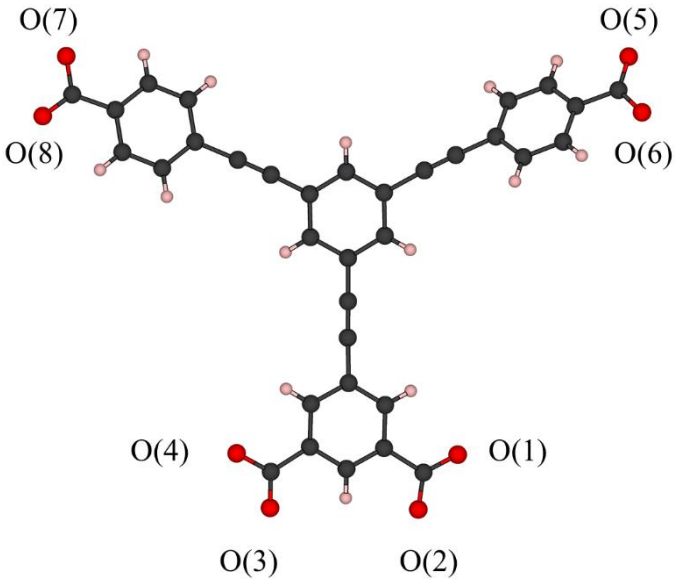

Figure 4.11: The conformation of the $BTEB_{ppi}^{4-}$ linker found in 13.

The $BTEB_{ppi}^{4-}$ linker is found in one conformation within the structure of the MOF (**Figure 4.11**). The *para*-benzoate and isophthalate moieties are rotated with respect to the central phenyl ring (**Table 4.6**). The *para*-benzoate moieties have dihedral angles of *ca.* 39.0 º and *ca.* 14.1º, while the

isophthalate moiety has a dihedral angle of *ca.* 9.5 º. The *para*-benzoate moiety with an angle of 39.0º corresponds to the bridging carboxylate group containing O(5) and O(6). While the *para*-benzoate moiety with a rotation of 14.1 º corresponds to the (η^2) chelating carboxylate group, coordinates to Co(1). The remaining two carboxylate groups originate from the isophthalate moiety.

Table 4.6: Dihedral angle of the *para*-benzoate and isophthalate moieties with respect to the central phenyl ring.

Conformation	The dihedral angle between *para*-benzoate (1) moiety and the central phenyl ring	The dihedral angle between *para*-benzoate (2) moiety and the central phenyl ring	The dihedral angle between isophthalate moiety and the central phenyl ring
i	39.0(3)	14.1(3)	9.5(2)

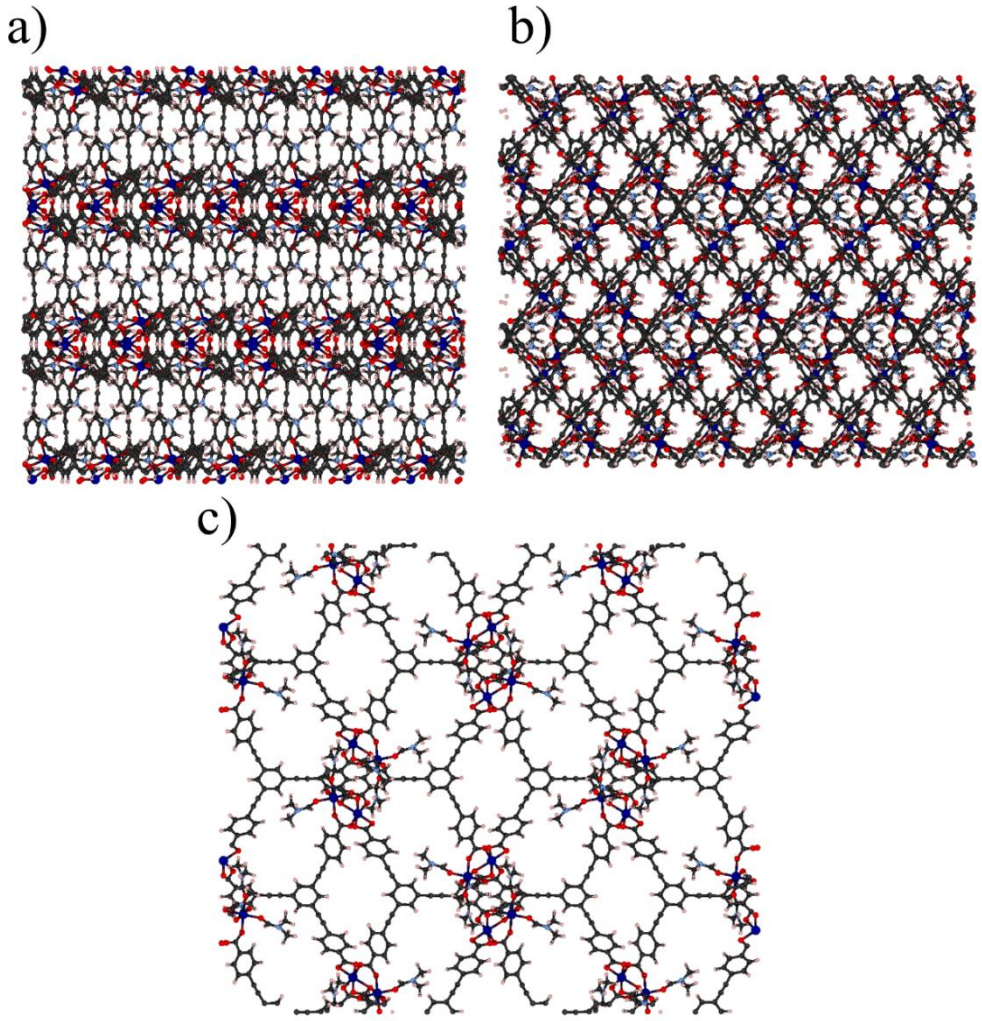

Figure 4.12: Packing representation of 13 viewed along the crystallographic a) *a*-axis, b) *b*-axis, and c) *c*-axis. (C- black, O – red, H – pink, Co – blue)

The extended structure of **13** is a porous three-dimensional framework with channels that extend into the structure along the crystallographic *c*-axis (**Figure 4.12 c)**). Comparatively, when viewed along the crystallographic *a*- and *b*-axis, the structure is densely packed (**Figure 4.12 b) & c)**). The $\{Co_2\}$ SBUs are interconnected by the $BTEB_{ppi}^{4-}$ linkers to generate a series of chain-like units that extend into the structure along the crystallographic *c*-axis (**Figure 4.13**). The *para*-benzoate moieties interlink the chains of $\{Co_2\}$ SBUs that run parallel to the pores within the structure. The DMF solvent molecules coordinated to Co(2) are directed towards the channels in the structure (**Figure 4.12 c) & Figure 4.13**). This orientation is of great interest as it allows for rapid access of H_2O solvent molecules to the Co^{2+} ions. An essential factor for catalytically active MOFs for the water oxidation reaction to have high turnover frequencies.

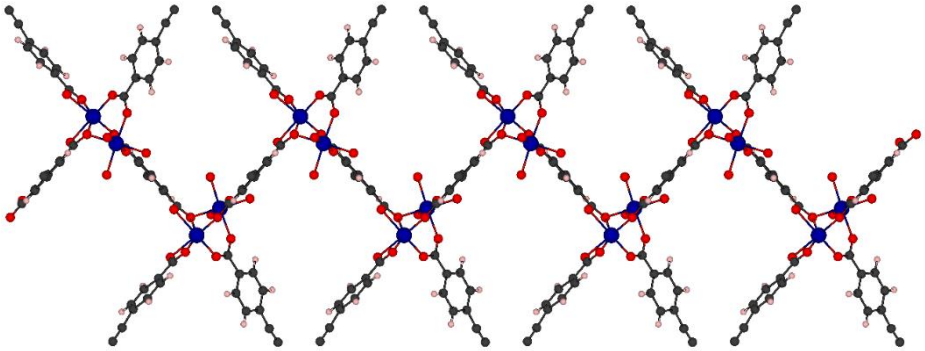

Figure 4.13: A section of the $\{Co_2\}$ SBU chains that extend into the structure along the crystallographic *c*-axis with the DMF molecules removed for clarity. Isophethelate moieties interconnect the SBUs along the chain while the *para*-benzoate moieties interconnect the chains with one another. (C- black, O – red, H – pink, Co – blue)

In order to examine the potential pore-size distribution and surface area, the Poreblazer software package was utilised.[225] The calculations revealed that the desolvated structure had a He pore volume of *ca.* 1.146 cm^3/g and an accessible surface area of *ca.* 3069 m^2/g. The limiting pore diameter and maximum pore diameter were calculated to be *ca.* 6.5 Å and *ca.* 8.8 Å, respectively. These calculated pore diameters are in agreement with the crystal graphic estimations from the structure. The limited pore diameter corresponds to the channels that extend into the structure along the crystallographic *c*-axis. The pore-size distribution indicates the presence of two pores within the MOF. The smaller pore centred at 7.6 Å arises from the uniform channels which connect large spherical pores centred at 8.6 Å(**Figure 4.14**).[225]

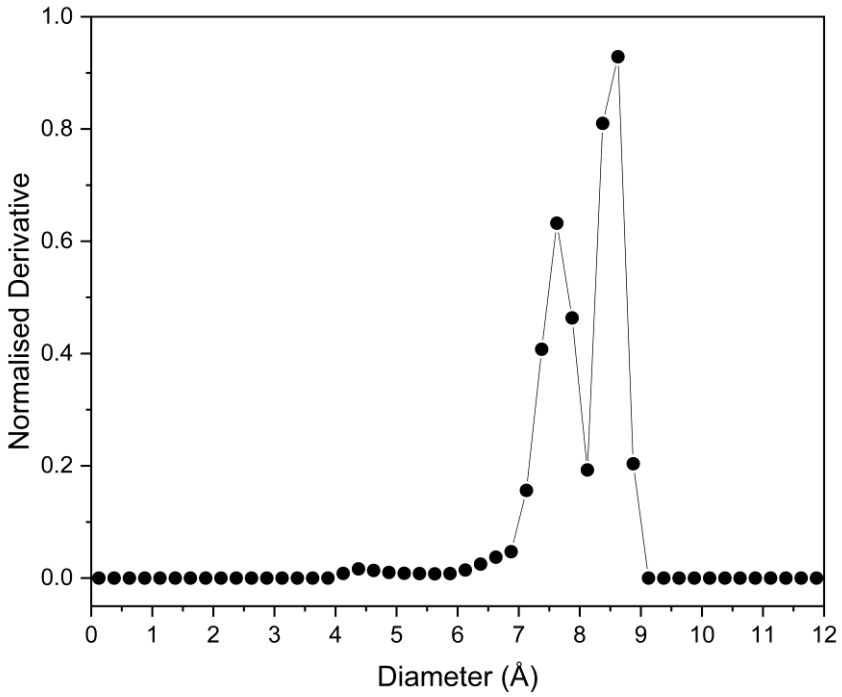

Figure 4.14: Simulated pore-size distribution of 13.

4.1.2.2 Topology of **13**

The topology of the structure was determined using the topological computational package Topos Pro.[257] The $HBTEB_{iip}^{4-}$ linkers are treated as two 3-connected nodes in the topological reduction of the MOF. The topological net for **13** was determined to be a binodal (3,4)-connected net. The overall point symbol that was ascertained was $\{6^2.10^4\}\{6^2.10\}_2$ with an overall stoichiometry of (3-c) (3-c) (4-c) (**Figure 4.15**).

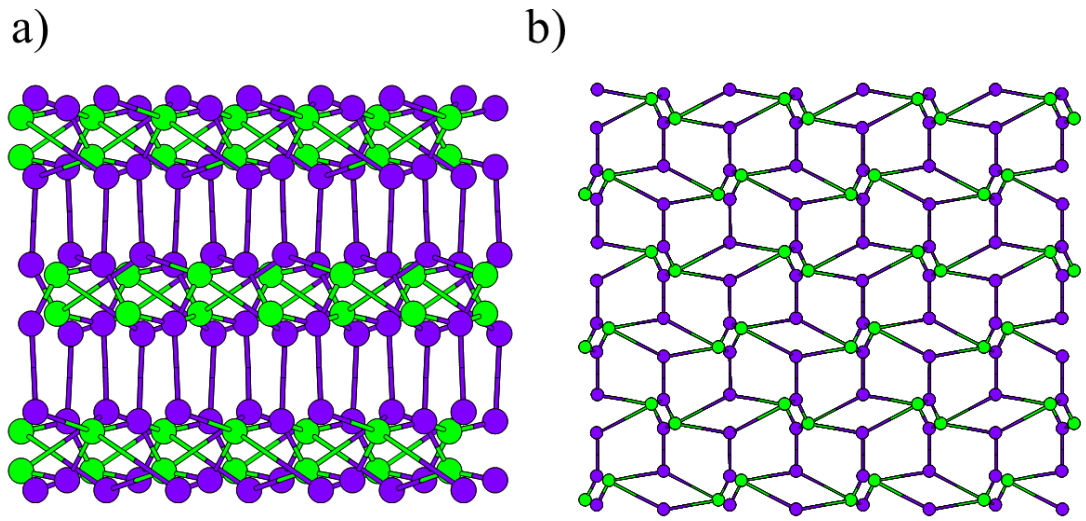

Figure 4.15: Topological reduction of 13 viewed along the a) crystallographic *a* and *b*-axis and b) crystallographic *c*-axis. ($\{Co_2\}$ SBU – green, $BTEB_{ppi}^{4-}$ linker nodes – purple)

4.1.2.3 Powder X-ray diffraction

To confirm the phase purity of **13**, the MOF was analysed using PXRD. The sample was prepared in the usual manner of griding fresh crystals of the MOF within the mother liquor and loading the subsequent powder into a quartz capillary. The sample was then measured at 215 K, on a Bruker APEX II DUO X-ray diffractometer. The software package Expo 2014 was then used to calculate the background signal and the experimental diffraction fit to the theoretical diffraction pattern.[228,229] Using the Rietveld method, the unweighted R-factor and the weighted R-factor were determined to be Rp = 0.960 and Rwp = 1.583, respectively. The experimental diffraction pattern matched well with the theoretical diffraction pattern confirming the phase purity of the sample (**Figure 4.16**).

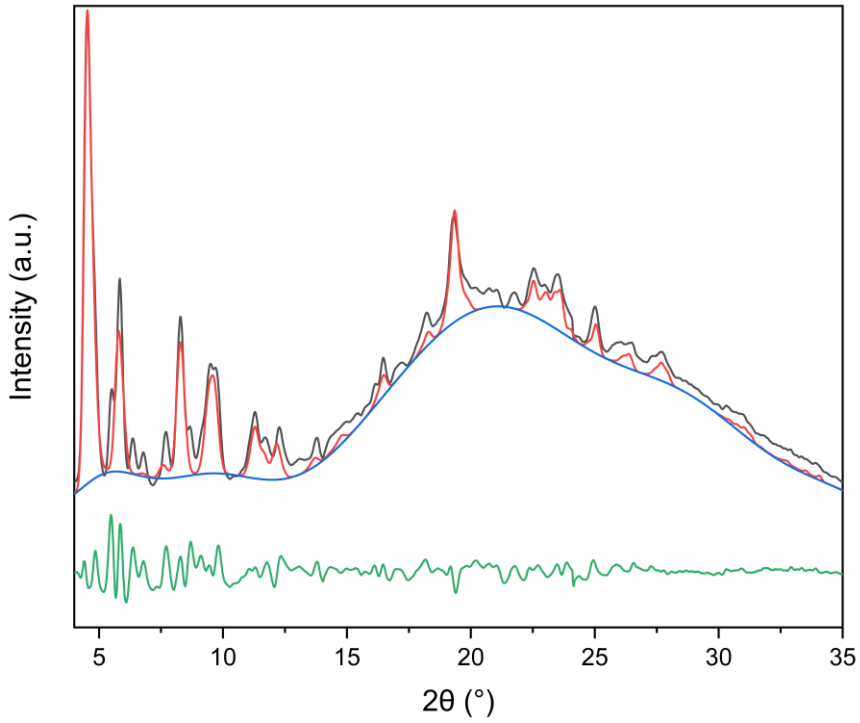

Figure 4.16: PXRD pattern of 13. (measured PXRD pattern – black, calculated background correction - blue, fitted theoretical PXRD pattern – red, the difference between measured and theoretical PXRD pattern – green.)

4.1.2.4 Thermogravimetric analysis

To examine the thermal stability of **13** thermogravimetric analysis was performed (**Figure 4.17**). The compound was heated under a nitrogen atmosphere with a heating rate of 4 ºC per minute. An initial weight loss of *ca*. 46.3 % occurred between 20 ºC and 175 ºC. This loss is attributed to the loss of solvent molecules within the pores of the structure and the loss of strongly bond solvent molecules coordinated to the Co^{2+} ions. This is followed by a further weight loss of *ca*. 15.7 % from 346 ºC to 506 ºC. This is attributed to the thermal decarboxylation reaction of the $BTEB_{ppi}^{4-}$ linkers. A final

loss of mass occurred between 506 ºC and 700 ºC, with a loss of 24.3 % due to the thermal decomposition of the organic linkers.

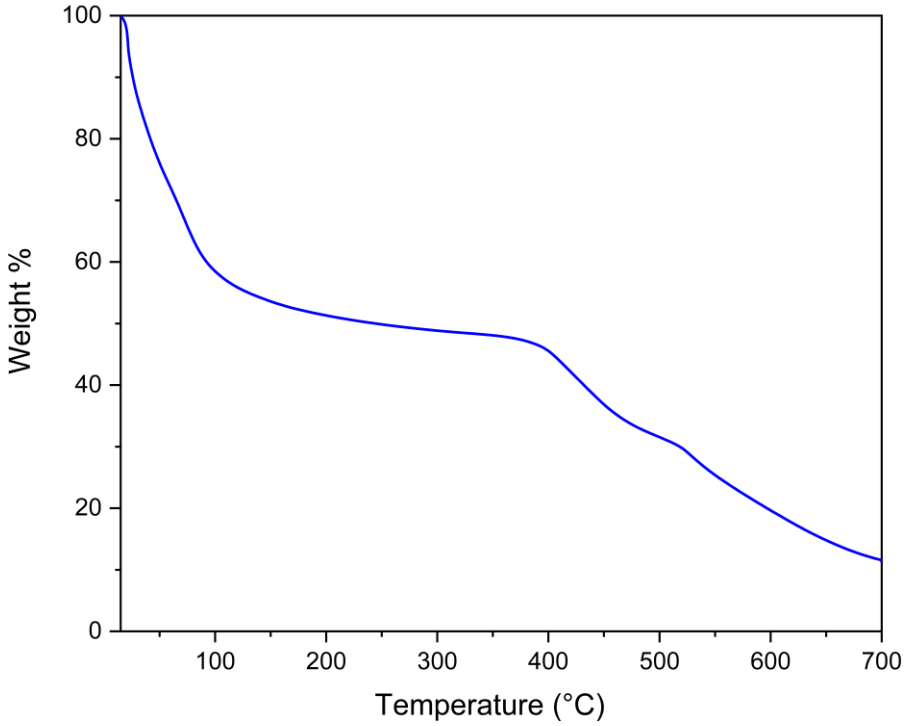

Figure 4.17: TGA of 13 heated under a nitrogen atmosphere at 4 ºC per minute

4.1.2.5 FT-IR and Raman spectroscopy

In the FT-IR spectrum, the broad band at 3454 cm^{-1} may arise due to hydrogen bonding solvent molecules located within the pores of the MOF. These hydrogen bonding solvent molecules likely originate from the metal salt starting material and the wet DEF solution used in the synthesis. At 2933 cm^{-1} and 2878 cm^{-1}, a pair of bands are attributed to the ν(C-H) stretching from DMF molecules within the porous structure.[231] At 1654 $cm^{-1,}$ the ν(O=C) stretching of DMF solvents can be seen. Due to the multiple bonding modes of the carboxylates to the Co^{2+} ions, it is not possible to distinguish which symmetrical and asymmetrical stretches are associated with each carboxylate. The observable asymmetric carboxylate ν_{as}(COO) stretching modes were found on the shoulder of the DMF ν(C=O) band are and located at 1631 $cm^{-1}$and 1602 cm^{-1}. The corresponding observable symmetric mode ν_s(COO) occur at 1465 $cm^{-1}$and 1435 cm^{-1}. The calculated Deacon Philips Δ values across all combinations of pairings range from 1 cm^{-1} to 137 cm^{-1}. This range of values covers all possible coordination modes of carboxylates to metal ions.[233]

The Raman spectrum of **14** is mainly composed of bands from the $HBTEB_{iip}^{4-}$ linkers. A strong band at 2224 cm^{-1} corresponds to the symmetric ν_s(C≡C) stretch. Two strong bands corresponding to the phenyl rings' aromatic ν(C=C) stretch are located 1608 cm^{-1} and 1581 cm^{-1}. Bands at 1412 cm^{-1} and 1363 cm^{-1} are attributed to ν_s(C=O) stretching bands of the carboxylate groups. In-plane C-H bending modes due to the *para*-benzoate moieties can be seen while slightly lower wavenumbers of 1207 cm^{-}

[1] and 1121 cm^{-1} correspond to the δ(C-H) bending modes in the isophthalate moiety. A large band attributed to the central phenyl in-plane δ(C-H) bending occurs at 992 cm^{-1}. Two bands at 889 cm^{-1} and 848 cm^{-1} correspond to the out of plane ω(C-H) waging modes for the isophthalate moiety and the central phenyl, respectively. The isophthalate gives rise to weaker bands due to the polarisation induced by the carboxylate groups. The out of plane ω(C-H) wagging for the *para*-benzoate moiety occurs at 642 cm^{-1}.

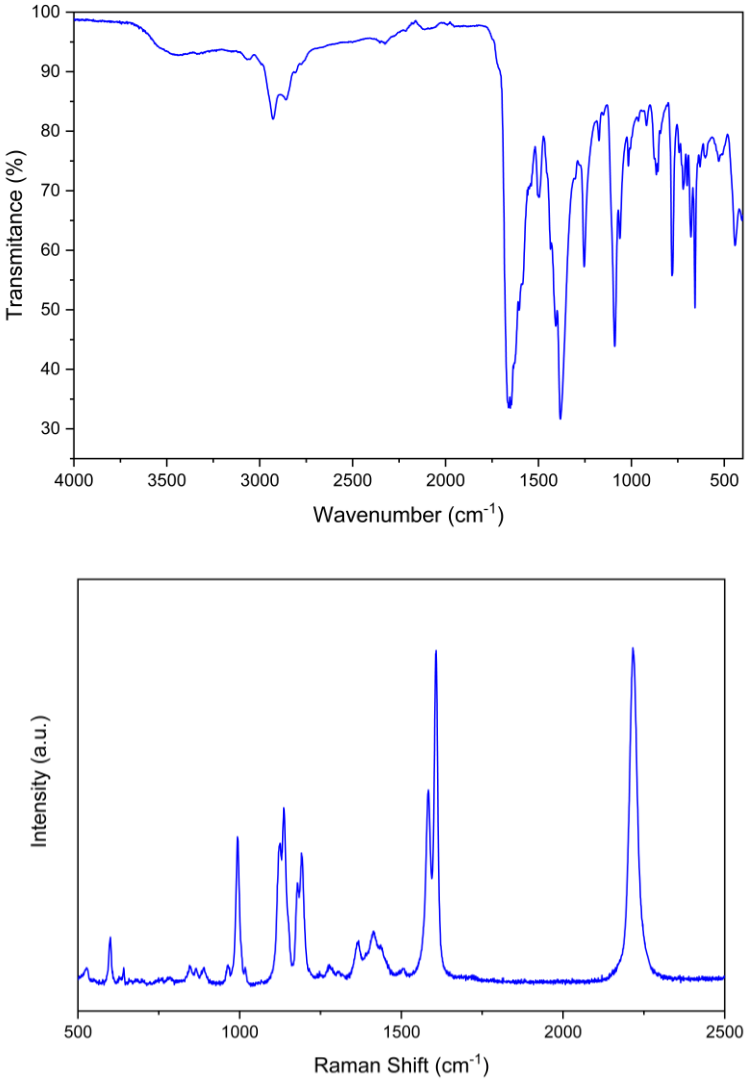

Figure 4.18: FT-IR and Raman spectra of 13.

4.1.2.6 Cyclic voltammetry of **13** in Cp.

Crystals of **13** were first prepared for analysis by heating the crystalline sample at 40 ºC under vacuum for 24 h. The freshly prepared sample was then blended with commercial carbon paste (Cp, a blend of carbon black and an organic binder). The combined material was then ground in a mortar and pestle to grind the crystals to a fine powder and incorporate them into the Cp material. The electrochemical experiments were then carried out using a solution of KNO_3 (1 M) and KPi buffer (50 mM, pH 7.2) in H_2O at 20 ºC

Cyclic voltammetry experiments were then carried out on the sample using a 20 wt% loading of **13** in CP (**Figure 4.19**). The sample was used to prepare an electrode with a surface area of 0.02 cm^2. The experimental setup used a Pt-mesh counter-electrode and an Ag/AgCl (3M) reference electrode in combination with the newly prepared sample electrode to complete the standard three-electrode configuration. The measurement was carried out at a scan rate of 100 mV/s. An initial increase in current density was found to occur from 1.15 V (vs. NHE). This increase in current is due to the oxidation of Co^{2+} ions to Co^{3+} ions. This increase in current was found to continue until 1.4 V (vs. NHE). A further increase in the applied voltage leads to a significant increase in current density. This increase is due to the oxidation of coordinated H_2O solvent molecules.

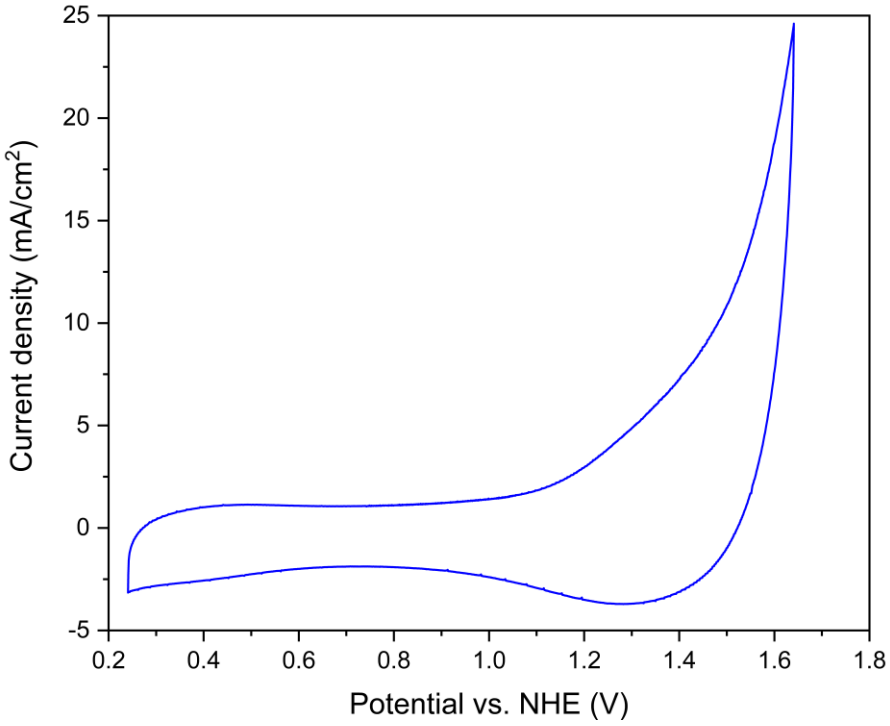

Figure 4.19: Cyclic voltammogram of a 20 wt% loading of 13 in CP measured at a rate of 100 mV/s.

4.1.2.7 Linear sweep voltammetry of **13** in CP

Crystals of **13** were first activated by heating the crystals to 40 ºC under vacuum for 24 h. The activated crystals were then added to a commercial carbon paste. The mixture was ground using a mortar and pestle to grind the crystals to a fine powder and to incorporate the powder into the CP. A solution of HNO_3 (1 M) and KPi buffer (50 mM, pH 7.2) in H_2O was used as the electrolyte medium in which the experiment was carried out.

Linear sweep voltammetry experiments were then carried out on the sample using a 20% loading and 10% of **13** in CP (**Figure 4.20**). The sample was used to prepare an electrode with a surface area of 0.02 cm^2. The experimental setup used a Pt-mesh counter-electrode and an Ag/AgCl (3M) reference electrode in combination with the newly prepared sample electrode to complete the standard three-

electrode configuration. The measurement was carried out at a scan rate of 1 mV/s. It was found that when the potential applied to the electrode went beyond 1.05 V (vs. NHE) a significant degree of noise was detected in the measured current. This noise in the signal is attributed to the formation of bubbles on the surface of the **13** in Cp electrode. This formation of bubbles on the surface of the electrode was found to increase rapidly when the potential went beyond 1.45 V (vs. NHE). The twenty-period adjacent average was taken to smooth the noise generated by the bubble formation to aid in the analysis of the results. It was found that the high loading of **13** caused the prepared electrode to become brittle. Standard procedures to minimise the effects of bubble formation during the experiment include using a rotating disc electrode. However, a larger sample of **13** than that could be synthesised would be required. Attempts to synthesise a large sample of material proved challenging; further work to synthesise sufficient material is needed.

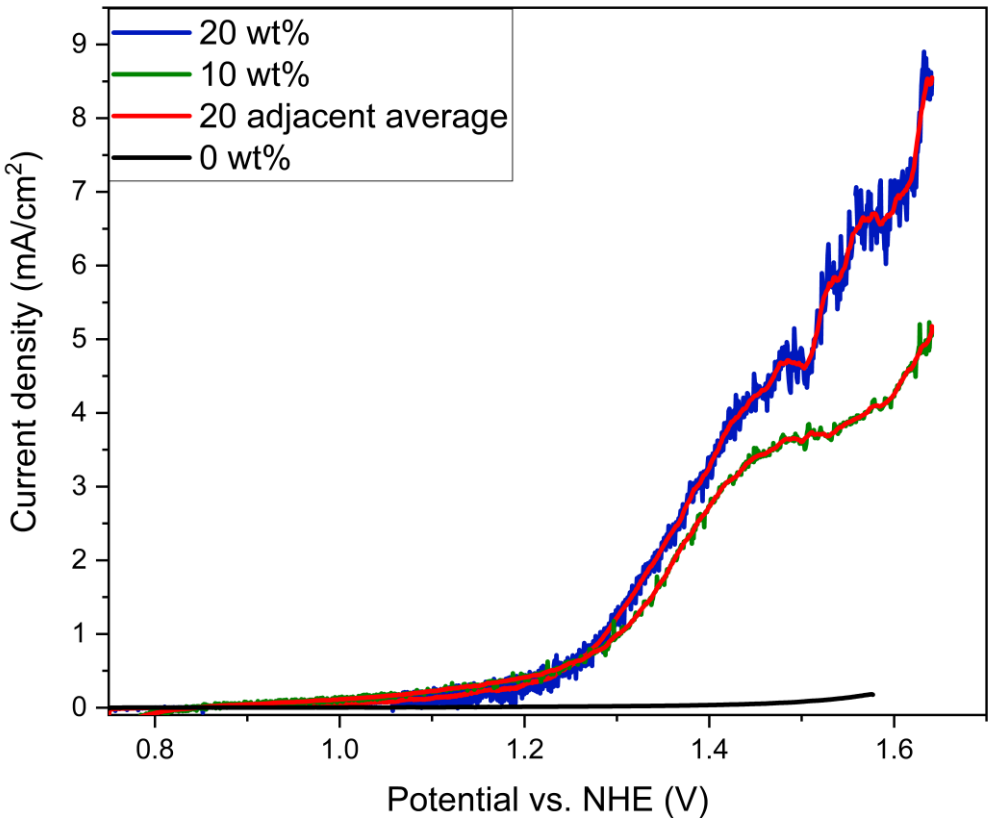

Figure 4.20: Linear sweep voltammogram for 13 in CP measured from 0.75 V (vs. NHE) at a rate of 1 mV/s.

Compared to the minimal increase of current density when only CP is used for the electrode, the **13** in CP shows a significant increase in current density. This increase in current density indicates that a catalytic oxidation reaction of H_2O is occurring during the experiment. An initial increase in current density occurs from *ca.* 0.25 V of overpotential for the two loadings of **13** in Cp. This initial increase in current density is due to the oxidation of the Co^{2+} ions in the SBU to Co^{3+} ions.[205] From *ca.*0.4 V overpotential, a significant increase in current density occurs. The increase in current is due to the oxidation of H_2O solvent molecules, which coordinate to the Co^{2+} ions in the SBU. [205] For the sample

with 10 wt% loading of **13** in CP a decrease in current density was found to occur at 0.7 V overpotential. This is likely due to a mass transfer limitation occurring. However, for the sample with 20 wt% loading of **13** in CP a significant increase in noise in the signal occurred at 0.7 V (vs. NHE), which causes it to become challenging to determine if a mass transfer limitation is occurring.

Using the twenty-period adjacent average for the two loadings of **13** in CP the onset potentials were estimated. The estimates were determined from the intersection of the tangent lines of the Faradic (current density > 0.2 mA/cm^2) and non-Faradic (current density < 0.1 mA/cm^2) currents (**Figure 4.21**). It was found that the two loadings of 20 wt%. and 10 wt%. had an estimated overpotential of 435 mV and 474 mV, respectively. In comparison to pure CP, acting as a control experiment, a significant increase in current is found to occur. This shows that the CP material has a minor contribution to the current density of the material.

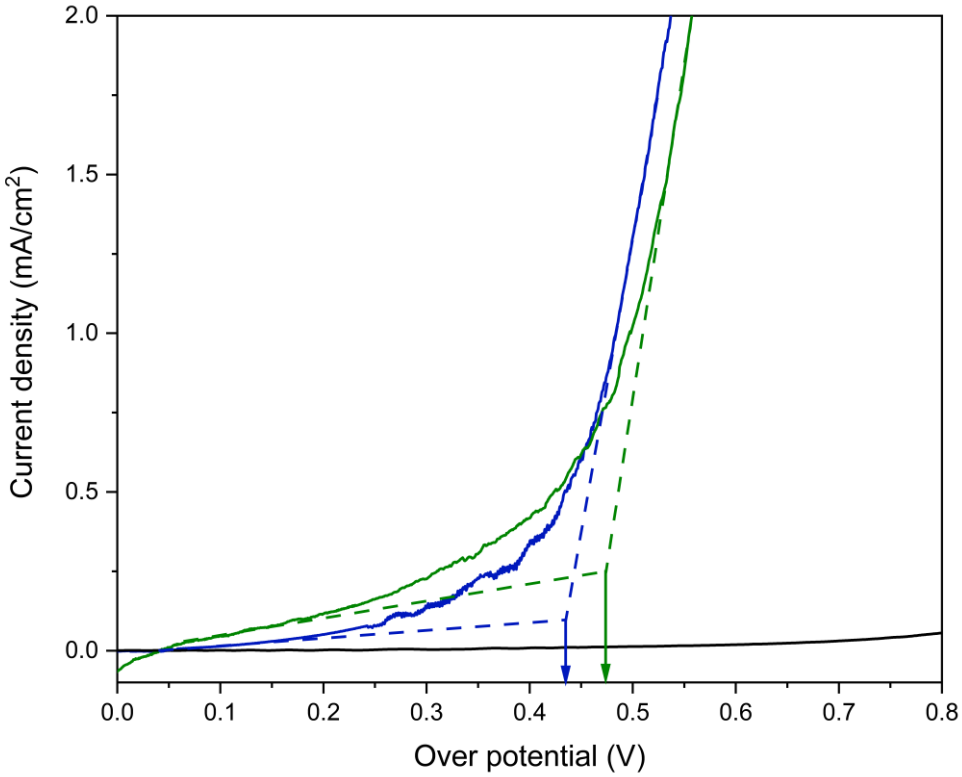

Figure 4.21: Comparison of the electrochemical behaviour between the two loadings of 13 in CP measured at a scan rate of 1 mV/s. (Blue – 20 wt% loading, green – 10 wt% loading, black – CP)

4.1.2.8 Tafel slope

Tafel plots were plotted for the two different blends of **13** in CP from the results obtained in the LSV experiments. The plots were examined using the overpotential values in the range of 0.5-0.6 V (vs. NHE) range where H_2O oxidation occurs and the slope of the LSV is approximately linear. From the plots, the Tafel slopes were obtained for each weight loadings (**Figure 4.22**). The Tafel slope

depends on the rate-determining step of the electrochemical process and a lower slope corresponds to a more significant rate increase in the current density following the onset of the water oxidation reaction. From the graph, the slopes were found to be 0.240 mV/dec and 0.241 mV/dec for 20 wt% and 10 wt%, respectively.

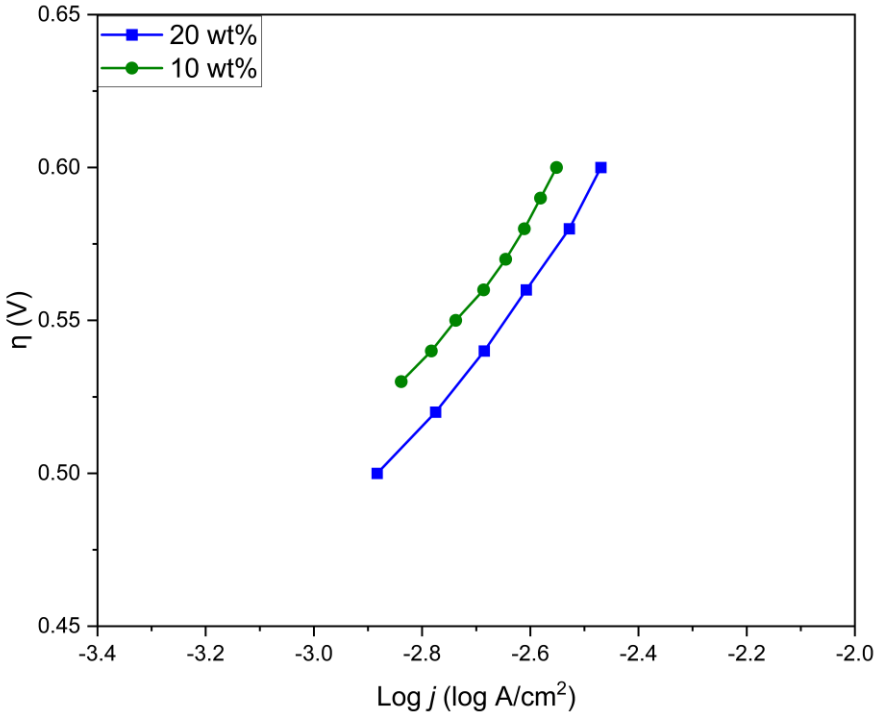

Figure 4.22: Tafel plot for 20 wt% and 10 wt% of 13 in Cp.

4.1.2.9 Bulk H_2O electrolysis of **13** in CP.

Chronoamperometry was used to evaluate the stability of the electrode (**Figure 4.24**). The experiment was carried out for 5 h. using a 20 wt% loading of **13** in CP as the working electrode, a Pt mesh counter electrode and Ag/AgCl reference electrode at a set voltage of 1.2 V (vs. Ag/AgCl). A solution of KNO_3 (1 M) and KPi buffer (50 mM, pH 7.2) in H_2O, at 20 ºC was used as the electrolyte medium. The results from the experiment show that the active material remained active over the course of 4 h. Due to the low mechanical stability of the CP electrode, a jump in current density occurred at four points during the course of the experiment. In two instances, a piece of the electrode material had broken off from the bulk of the electrode, highlighted by the red arrows in **Figure 4.24**. This breakdown of the polished electrode surface causes the underlying material to be revealed. Due to an increase in active sites, this new increase in surface area causes an increase in the current density.

Throughout the experiment, a significant number of bubbles formed upon the electrode surface. At two points during the experiment, the measurement was paused, and the bubbles were manually removed by gentle agitation of the working electrodes. Two green arrows in **Figure 4.24** highlight these events. After the removal of the bubbles, the experiment was allowed to continue. It was found

that a jump in current density occurred after the first removal of the bubbles. This increase in current is likely due to the loss of surface electrode material, similar to the losses previously mentioned during the linear sweep voltammetry experiments. The secondary removal appears to have suffered no loss.

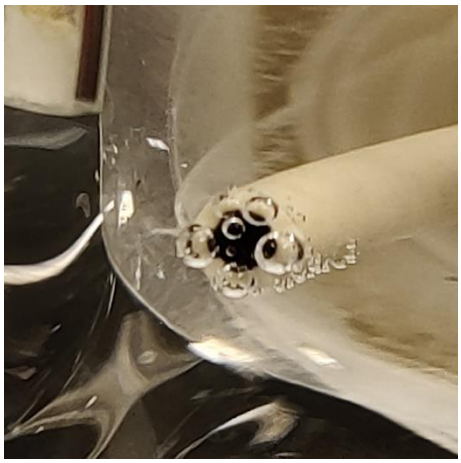

Figure 4.23: Bubble formation on electrode surface.

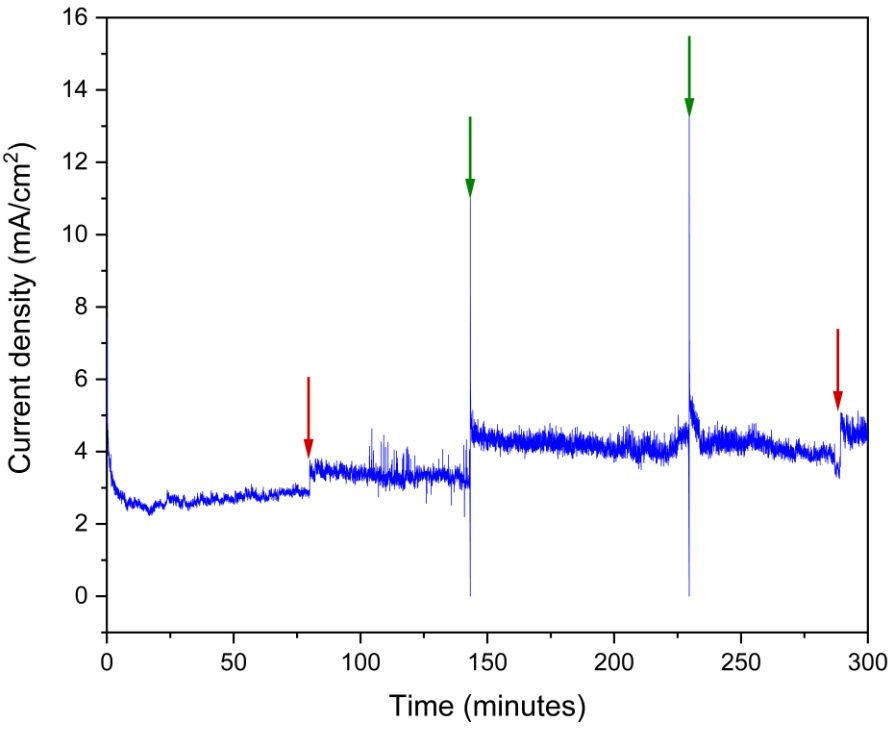

Figure 4.24: Bulk electrolysis of a 20 wt% of 13 in CP measured at a constant voltage of 1.2 V (vs. Ag/AgCl).

Table 4.7: Crystallographic information for 13.

Identification code	13
Empirical formula	$C_{86}H_{70}Co_4N_6O_{22}$
Formula weight	1775.20
Temperature / K	215(2)
Crystal system	Orthorhombic
Space group	*Fdd2*
***a* / Å**	50.464(9)
***b* / Å**	57.890(9)
***c* / Å**	13.204(2) Å
***α* / º**	90
***β* /º**	90
***γ* / º**	90
Volume / Å^3	38574(11)
Z	8
ρ_{calc}/ g/cm^3	0.611
μ / mm^{-1}	2.926
F(000)	7296
Crystal size / mm^3	0.600 × 0.400 × 0.400
Radiation	1.54178 Å
θ range for data collection / º	2.323 to 52.780
Index ranges	-51<=h<=51, -59<=k<=52, -13<=l<=13
Reflections collected	29837
Independent reflections	10122 [R(int) = 0.0514]
Data/restraints/parameters	10122 / 13 / 485
Goodness-of-fit on F^2	1.047
Final R indexes [I>=2σ (I)]	R_1 = 0.0567, wR_2 = 0.1538
Final R indexes [all data]	R_1 = 0. 0759, wR_2 = 0.1692
Largest diff. peak/hole / e.Å^{-3}	0.326 and -0.368

4.3 Use of pentacarboxylate linkers

4.3.1 $[Zn_7(HBTEB_{iip}^{4-})_3(DEF)_7](NO_3)_2$ (**14**)

14 was synthesised by heating a solution of H_5BTEB_{iip} and $Zn(OAc)_2{\cdot}H_2O$, in a 1:8 mole ratio, in dimethylformamide (DEF) at 85 ºC for 48 h. An initial colour change to a yellow solution was observed, which after further elapsed time, cubic crystals grew from the solution. Alongside the crystals, a white amorphous coordination polymer was produced as a side product. Separation of the crystals from the amorphous side product was possible through gentle agitation of the vial. While the side product became suspended in the solution, the solvent was replaced with fresh DEF. The crystals were found to be of sufficient size and quality to be analysed by single-crystal X-ray crystallography. The crystal was measured and solved in the cubic space group $Pm\bar{3}m$ with the following crystallographic parameters: $a = b = c = 32.4290\ (17)$, $\alpha = \beta = \gamma = 90^{o}$.

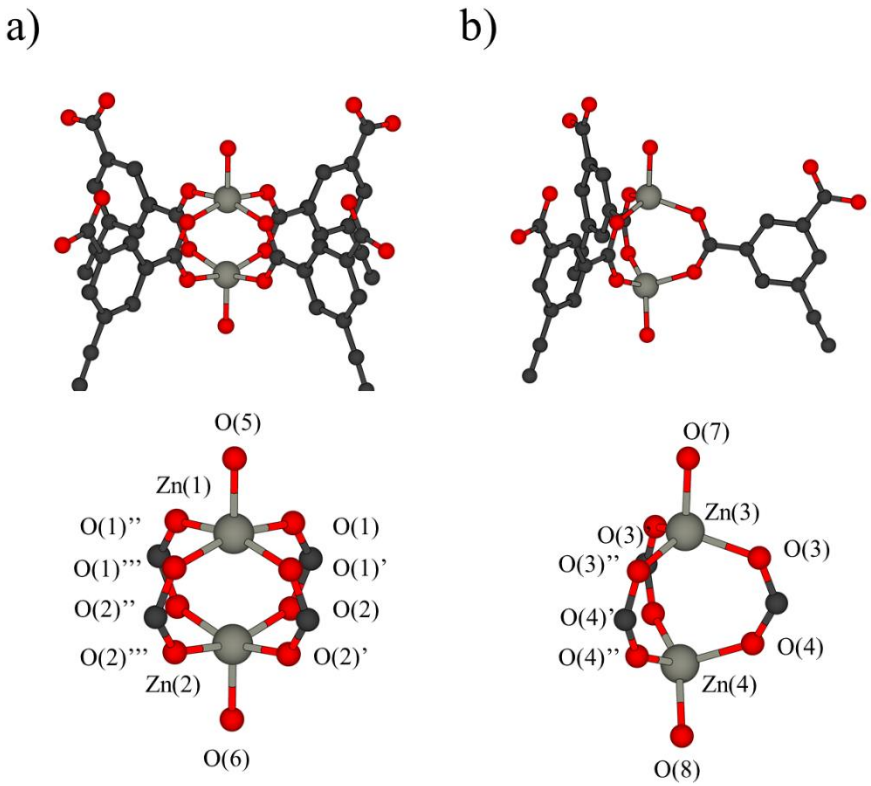

Figure 4.25: The a) 4-connected and b) 3-connected $\{Zn_2\}$ paddlewheel SBUS found in 14 with important atoms labelled. (Zn – grey, O – red, C – black)

14 was determined to be a porous three-dimensional polymer containing a series of dimer Zn^{2+} SBUs interconnected with $HBTEB_{iip}^{4-}$ linkers. The Zn^{2+} ions were used to construct two structurally distinct $\{Zn_2\}$ paddlewheel SBUs (**Figure 4.25**). One SBU is similar in structure to the $\{Cu_2\}$ SBUs discussed previously in **Chapter 2** and **Chapter 3**. Four carboxylate groups bridge two Zn^{2+} ions in a *syn,syn*-bidentate, (μ_2-η^1:η^1) bridging mode. Four O-donor atoms of the coordinated carboxylate groups create the base of a square base pyramidal coordination geometry around the Zn^{2+} ion. An O-

donor atom from a DEF solvent molecule coordinates to the apical position on the Zn^{2+} ion. The remainder of the DEF solvent molecule remains unresolved due to the disorder of the molecule.

In the second SBU, the Zn^{2+} ions are coordinated by three carboxylate groups by means of their O-donor atoms. The fourth coordination site on the Zn^{2+} ion is occupied by the O-donor atom from a solvent molecule. Like the solvent molecule coordinated to Zn^{2+} ion in the previously discussed SBU, the O-donor atom is believed to originate from a DEF solvent molecule. Due to the disorder of the molecule, the remainder of the ligand is unresolved. The four O-donor atoms coordinate to the Zn^{2+} ions in a tetrahedral coordination geometry. The two SBUs act as 4- and 3-connected nodes based upon the number of coordinating carboxylates to the Zn^{2+} ions in the SBU. This difference in connectivity will be used to aid in distinguishing the two $\{Zn_2\}$ SBUs in future discussions.

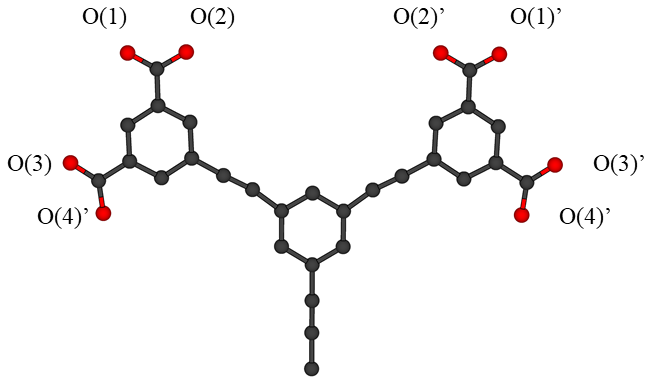

Figure 4.26: The conformation of the $HBTEB_{iip}^{4-}$ linker as found in 14. The *para*-benzoate moiety is unresolved in the structure due to the free rotation of the moiety around the alkyne spacer unit. (C – black, O – red)

Table 4.8: Dihedral angles between isophthalate moieties and *para*-benzoate moiety to the central phenyl ring.

Conformation	The dihedral angle involving isophthalate moiety 1 (º)	The dihedral angle involving isophthalate moiety 2 (º)	The dihedral angle involving *para*-benzoate moiety (º)
i	89.9º	89.9	n.a.

The linker is found in one conformation within the structure of the MOF, as seen in **Figure 4.26**. The carboxylate groups on the isophthalate moieties coordinate to each of the inorganic $\{Zn_2\}$ SBUs. The isophthalate moieties lie co-planar to the mean plane of the central phenyl ring on the linker. The *para*-benzoate moiety is non-coordinating to the structural $\{Zn_2\}$ SBUs and therefore plays no role in the formation of the framework of the MOF. Due to the near-zero barrier of ration around the acetylenic spacer units and the *para*-benzoate moiety does not coordinate to an SBU, it can freely

rotate in the structure. This free rotation causes the *para*-benzoate moiety to be highly disordered, leading to the moiety being unresolved in the structure.

The {Zn_2} SBUs are interconnected by the isophthalate moieties generating a MOP-like unit (**Figure 4.27**). Six 4-connected {Zn_2} SBUs and eight 3-connected {Zn_2} SBUs combine to create the unit which has the structure of a rhombic dodecahedron. The {Zn_2} SBUs act as the vertices of the rhombic dodecahedron, while the isophthalate moieties act as the edges. Twelve rhombic faces of the rhombic dodecahedron allow access to the central pore encapsulated by the MOP like unit. The central pore has a diameter of *ca.* 13 Å. The MOP units are interconnected by the $HBTEB_{iip}^{4-}$ linkers, with four linkers connecting two adjacent MOP units. The four linkers form a secondary smaller cage MOP unit which has the structure of a super paddlewheel. The MOP contains two 4-connected {Zn_2} SBUs linked by the four $HBTEB_{iip}^{4-}$ linkers. Like the previous super-paddlewheel units reported in **Chapter 2** and **Chapter 3**, a pore is formed between the four $HBTEB_{iip}^{4-}$ linkers with a diameter of *ca.* 6 Å.

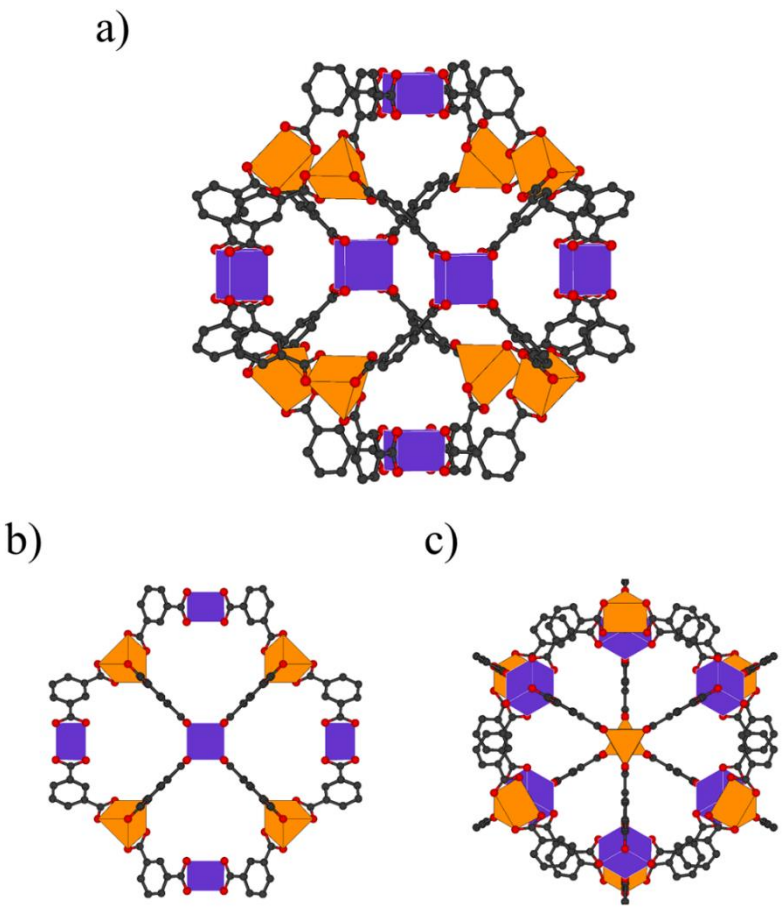

Figure 4.27: a) The rhombic dodecahedral MOP unit found in14 comprised of six 4-c {Zn_2} SBUs and eight 3-c {Zn_2} SBUs linked by 24 isophthalate moieties. The cage can be viewed along the crystallographic b) *a*-axis and c) the [1,1,1] vector. (C -black, O -red, 4-c {Zn_2} SBUs – purple, 3-c {Zn_2} SBUs orange)

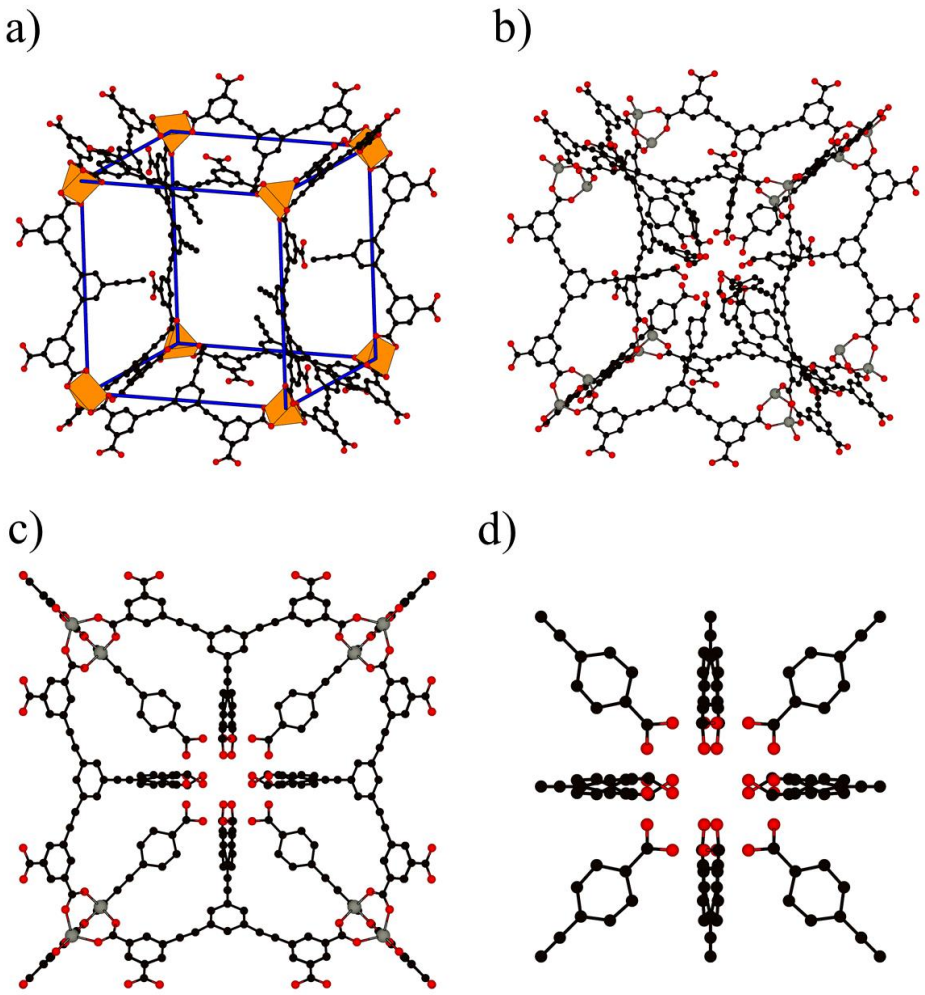

Figure 4.28: a) The cubic unit found in 14. The eight 3-c {Zn_2} SBUs are linked by blue bonds to highlight the cubic shape of the unit. The twelve $HBTEB_{iip}^{4-}$ linkers act as the cube's edges with the *para*-benzoate moieties directed towards the centre of the unit. b) The cubic unit with the unresolved *para*-benzoate moieties modelled to show their occupancy in the true structure of the MOF. c) the cubic unit with the modelled moieties viewed along the crystallographic *a*-axis. d) The *para*-benzoate moieties modelled in the structure. (C – black, O – red, {Zn_2} SBU – orange prism, Zn - grey)

The MOP units connect in a pseudocubic packing arrangement. This arrangement generates a large cubic pore between eight rhombic dodecahedral MOP-like units (**Figure 4.28 a**). The eight MOP units are located at the vertices of the cubic pore, while the super paddlewheel units act as the edges. Eight 3-connected {Zn_2} SBUs are directed towards the centre of the pore alongside twelve *para*-benzoate moieties from the $HBTEB_{iip}^{4-}$ linkers. These *para*-benzoate moieties occupy a significant fraction of the void space that would be present within the pore. The *para*-benzoate moieties were modelled to demonstrate occupancy of the moieties within the would-be pore and can be seen in (**Figure 4.28 b & c)**. Due to twelve carboxylate groups being located close to each other, significant hydrogen bonding between the linkers is expected. The modelled *para*-benzoate moieties are shown in (**Figure 4.28 d)** and emphasise the proximity of the moieties with respect to each other.

Interestingly the arrangement and distance between the moieties are ideal positions for the {Zr_6} 12-connected SBU, which is commonly reported in the literature, to occupy the site between the moieties.[322,267,] This is an exciting and unexpected outcome for the structure and offers a potential avenue for future research into mixed metal MOFs. [323, 84, 324, 325]

The extended structure of the MOF comprises a series of these cubic pores **Figure 4.29**. The windows located on the eight faces of the cubic pore allow for solvent and gas molecules to move between the pores.

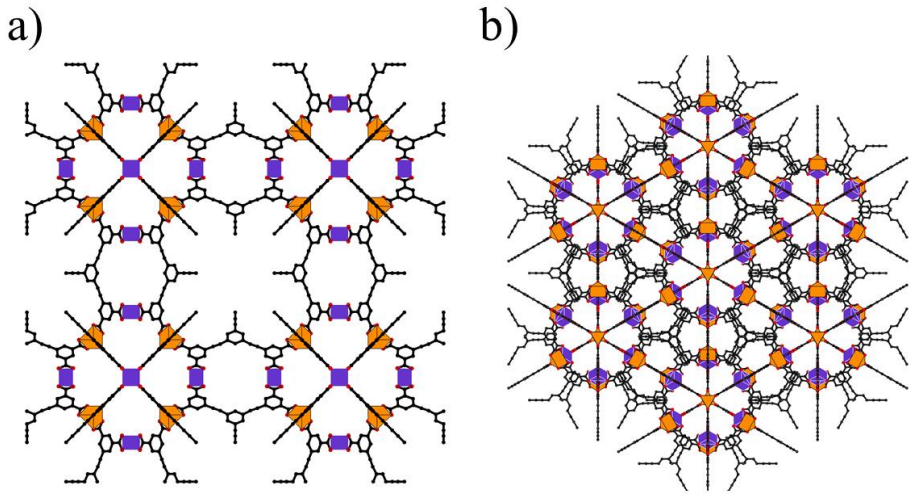

Figure 4.29: Extended structure of 14 viewed along the crystalograic a) a-, b-, and c-axis and b) [1,1,1]. (C – black, O – red, 3-c {Zn_2} SBU – orange prism, 4-c {Zn_2} SBU – purple cube)

The MOF has an overall cationic charge due to the 3-connected SBUs present in the MOF having a monocationic charge per SBU. The 4-connected SBUs, however, have a neutral charge similar to that of paddlewheel SBUs discussed in previous chapters. To balance the cationic charge of the framework eight anionically charged units are required per rhombic MOP unit. These anionic charges may arise from two possible sources. The most likely source of counterions is the presence of NO_3^- anions from the salt starting material remaining within the pores of the MOF. Due to the disorder of the anions within the pores, it is impossible to resolve them crystallographically. A secondary source is the deprotonation of the non-coordination *para*-benzoate moiety.

a)

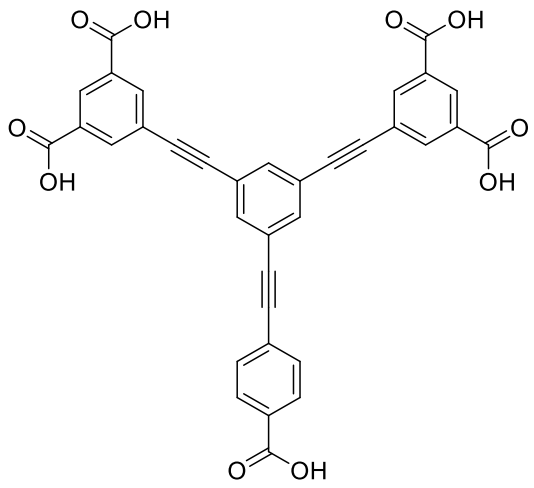

b)

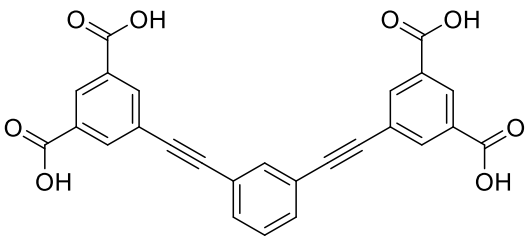

Figure 4.30: a) the H_5BTEB_{iip} linker used to synthesise 14 and b) the 5,5'-(1,3-phenylenebis(ethyne-2,1-diyl))diisophthalic acid linker used to synthesises the literature compound.

The newly synthesised MOF was discovered to be isostructural to a MOF previously described in the literature.[326] The likeness of the two structures can be seen to arise from the similarity of the organic linkers used in the construction of the MOFs (**Figure 4.30**). The MOF previously described in the literature is a tetracarboxylate linker that contains two isophthalate moieties attached to a central phenyl ring. This linker, however, does not contain tertiary *para*-benzoate moiety. This absence of the *para*-benzoate moiety causes a large pore to form at the centre of the cubic unit. The presence of the large pore allows for the formation of large channels that extend into the structure that are otherwise absent in **14**.

To examine the potential pore-size distribution and surface area of the MOF, the structure was analysed using the Poreblazer software package. [225] The calculations revealed that the desolvated structure had a He pore volume of *ca*. 1.852 cm^3/g and an accessible surface area of *ca*. 4273 m^2/g. The limiting pore diameter and maximum pore diameter were calculated to be *ca*. 7.9 Å and *ca*. 17.03 Å, respectively. These calculated pore diameters are in agreement with the crystal graphic estimations of the structure. The limited pore diameter corresponds to the pore located within the MOP like unit. The larger pore diameter is a pore that is formed between two adjacent cubic units

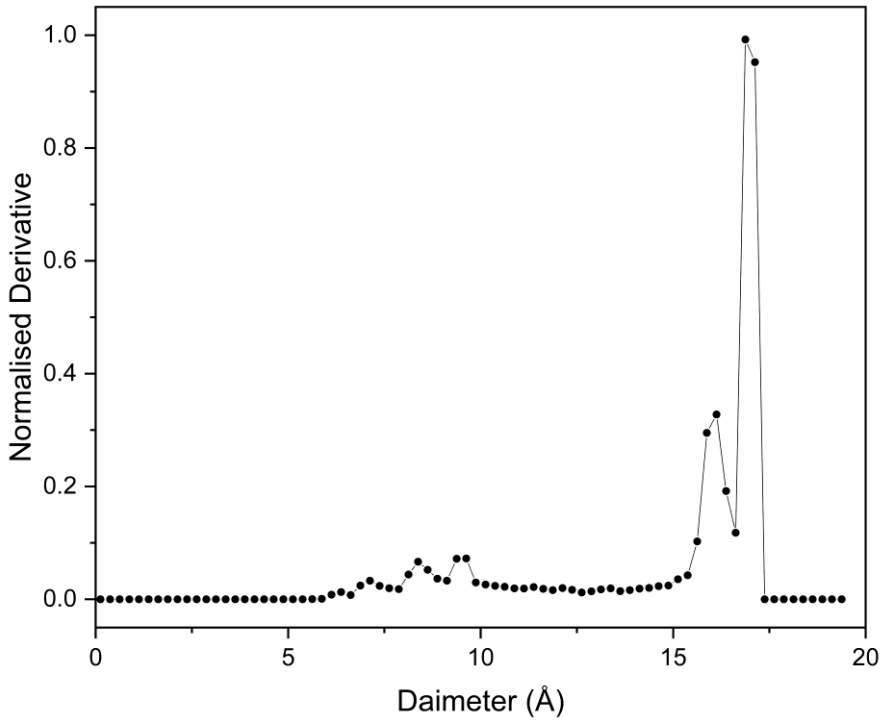

Figure 4.31: Simulated pore-size distribution of 14.

4.3.1.1 Powder X-ray diffraction

The bulk purity of the compound was confirmed using PXRD. Freshly prepared crystals were ground to a powder in the mother liquor and loaded into a quartz capillary. This was performed in order to stabilise the compound throughout the experiment. The sample was measured at 215 K, on a Bruker APEX II DUO X-ray diffractometer. Using the Expo2014 software package, the background signal and the fit of the experimental diffraction to the theoretical diffraction pattern was calculated.[228,229] Using the Reitveild method, the unweighted R-factor and the weighted R-factor were calculated for the diffraction pattern. The two factors were determined to be Rp = 1.390 and Rwp = 2.944, respectively.[230] The experimental diffraction pattern matched well with the theoretical diffraction pattern as seen in **Figure 4.32 a**.

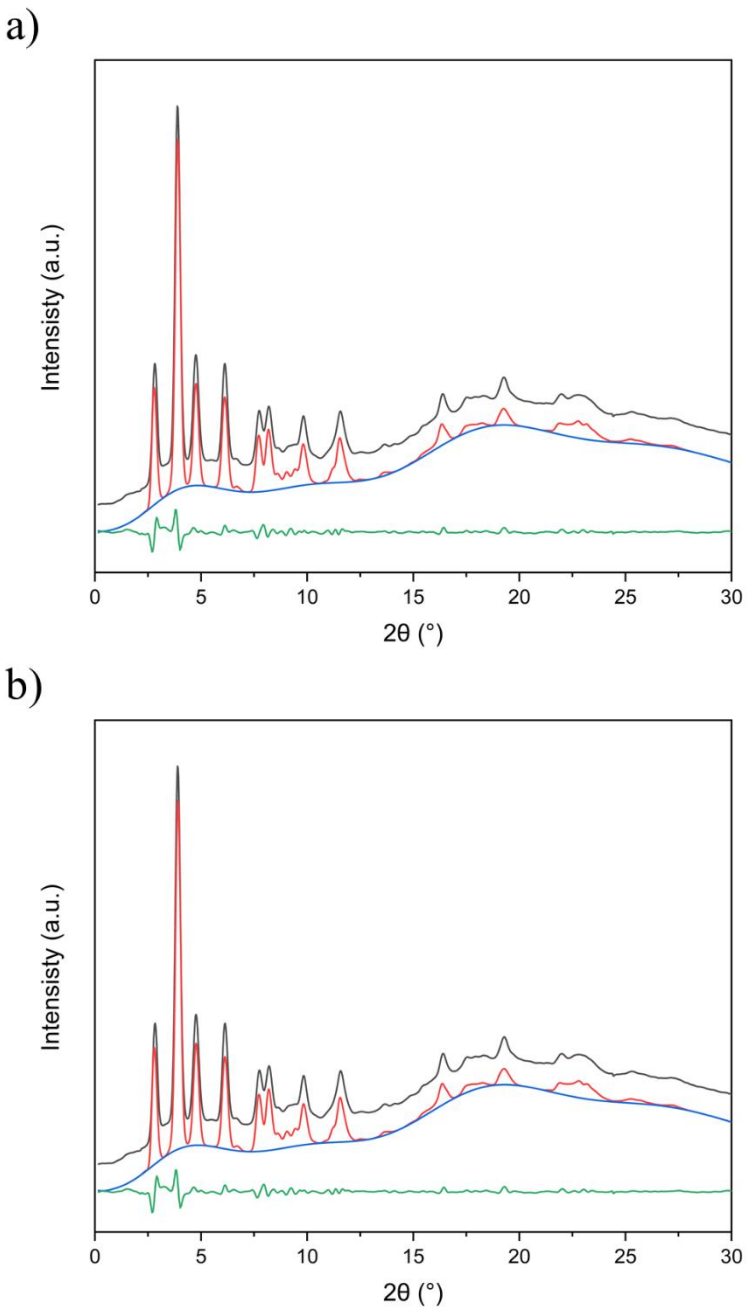

Figure 4.32: a) PXRD spectra of 14. b) Predicted powder pattern for the literature known compound fitted to the measured powder pattern for 14. (Measured PXRD pattern – black, calculated background correction - blue, fitted theoretical PXRD pattern – red, difference between measured and theoretical PXRD pattern – green.)

To confirm that the newly synthesised MOF is isostructural to the literature known compound, the theoretical powder pattern of the literature know compound was fitted to the measured pattern of the newly synthesised compound (**Figure 4.32 b**). Using the Rietveld method, the unweighted R-factor and the weighted R-factor were calculated as Rp = 1.411 and Rwp = 2.980. The excellent fit of the two patterns verifies that structures are indeed isostructural.

4.3.1.2 Topology

Topological analysis of **14** was carried out using the computational package ToposPro.[257] In the topological reduction of the MOF the $HBTEB_{iip}^{4-}$ linkers are treated as two 3-connected nodes.[307] Given that these two 3-c nodes are in the same environment, the topological net for **12** was determined to be a 3-nodal (3,3,4)-connected net. The overall point symbol was determined to be $\{6.8.10\}_{12}\{6^6\}_3\{8^3\}_4$. This net is designated by the RCRS symbol **zjz**.

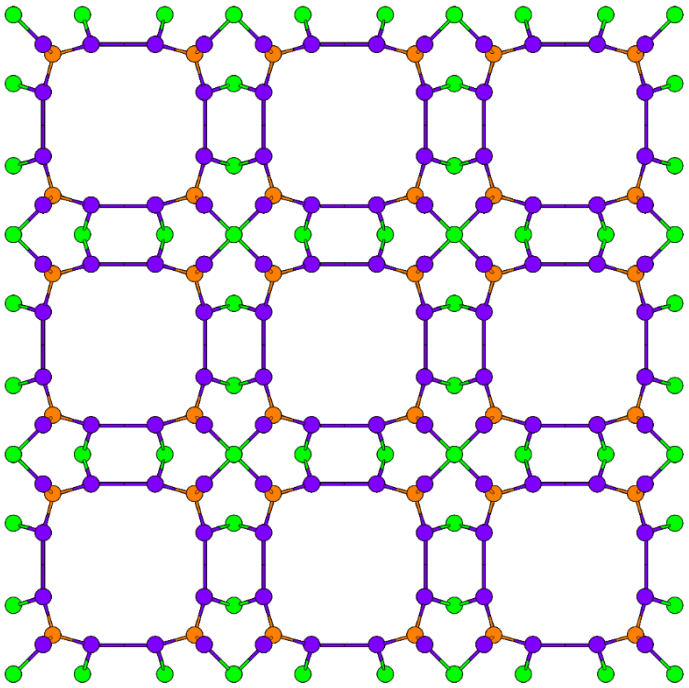

Figure 4.33: Topological reduction of 14 viewed along the crystallographic *a*-axis. (4-c $\{Zn_2\}$ SBUs - green, 3-c $\{Zn_2\}$ SBUs - orange, 3-c $HBTEB_{iip}^{4-}$ linkers - purple)

4.3.1.3 Thermogravimetric analysis

To thermal stability of **14** was studied using thermogravimetric analysis (**Figure 4.34**). The compound was heated under a nitrogen atmosphere with a heating rate of 4 ºC per minute. An initial weight loss of *ca*. 47.2 % was found to occur between 20 ºC and 129ºC. This loss in mass is due to the loss of solvent molecules located within the porous structure. A further loss of 7.8 % occurs between 129 ºC and 347 ºC. This gradual loss in mass over the wide temperature range is due to the loss of stronger found solvent molecues and slow diffusion through the porous structure. This is then followed by a weight loss of *ca*. 9.8 % from 392 ºC to 512 ºC attributed to the decarboxylation of the $BTEB_{iip}^{5-}$ linkers. The remaining weight loss of *ca*. 5.1 % is due to further thermal decomposition of the $BTEB_{iip}^{5-}$ linkers.

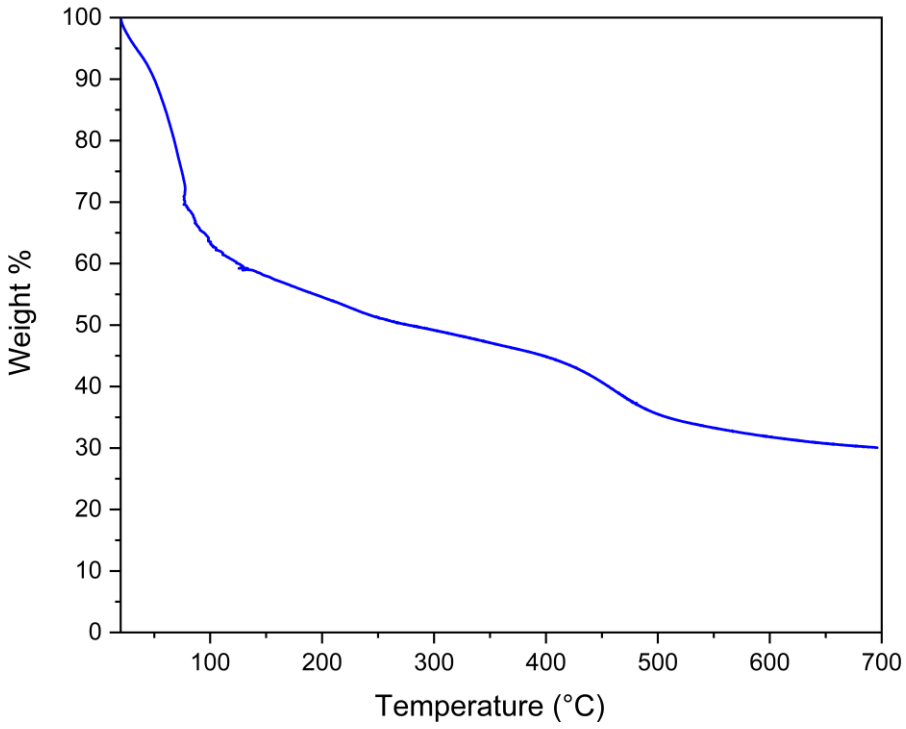

Figure 4.34: TGA of 14 measured from 20 ºC to 700 ºC at a rate of 4 ºC per minute under a nitrogen atmosphere

4.3.1.4 FT-IR and Raman spectroscopy

In the FT-IR spectrum, the broad band at 3456 cm^{-1} may arise due to H_2O solvents located within the pores of the MOF. These H_2O solvent molecules likely originate from the metal salt starting material and the wet DEF solution used in the synthesis. At 2933 cm^{-1} and 2878 cm^{-1}, a pair of bands are attributed to the ν(C-H) stretching from DMF molecules within the porous structure. The 1654 $cm^{-1,}$ the ν(O=C) stretching in the DMF molecule can be seen. Due to the presence of two different $\{Zn_2\}$ SBUs within the MOF, the carboxylates on the two different $\{Zn_2\}$ SBUs give rise to different bands. It is not possible, however, to distinguish with bands are attributed to which SBU. The asymmetric carboxylate ν_{as}(COO) stretching modes were found at 1631 cm^{-1}, 1602 cm^{-1}. The corresponding symmetric mode ν_s(COO) occur at 1455 $cm^{-1}$and 1431 cm^{-1}. The calculated Deacon Philips Δ values across all combinations of pairings range from 171 cm^{-1} to 176 cm^{-1}. These values correspond to a bidentate bridging mode of the carboxylate group.

The Raman spectrum of **14** is mainly composed of bands from the $HBTEB_{iip}^{4-}$ linkers. A strong band at 2224 cm^{-1} corresponds to the symmetric ν_s(C≡C) stretch. Two strong bands corresponding to the phenyl rings' aromatic ν(C=C) stretch are located 1608 cm^{-1} and 1581 cm^{-1}. Bands at 1412 cm^{-1} and 1363 cm^{-1} are attributed to ν_s(C=O) stretching bands of the carboxylate groups. In-plane C-H bending modes due to the *para*-benzoate moieties can be seen while slightly lower wavenumbers of 1207 cm^{-1} and 1121 cm^{-1} correspond to the δ(C-H) bending modes in the isophthalate moiety. A large band attributed to the central phenyl in-plane δ(C-H) bending occurs at 992 cm^{-1}. Two bands at 889 cm^{-1} and 848 cm^{-1} correspond to the out of plane ω(C-H) waging modes for the isophthalate moiety and

the central phenyl, respectively. The isophthalate gives rise to weaker bands due to the polarisation induced by the carboxylate groups. The out of plane ω(C-H) wagging for the *para*-benzoate moiety occurs at 642 cm^{-1}.

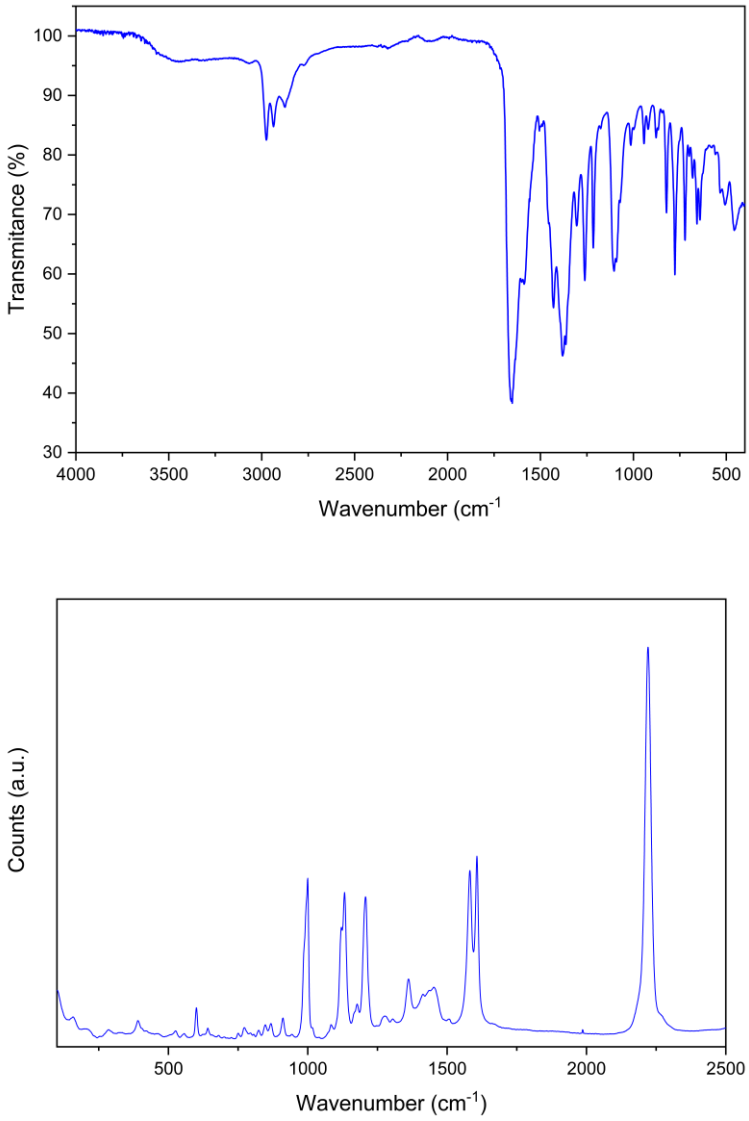

Figure 4.35: a) FT-IR and b) Raman spectrum of 14.

Table 4.9: Crystallographic parameters for 14.

Identification code	14
Empirical formula	$Zn_7C_{140}H_{119}O_{43}N_9$
Formula weight	3073.20
Temperature / K	215(2)
Crystal system	Cubic
Space group	*Pm-3m*
***a* / Å**	32.4290(17) Å
***b* / Å**	32.4290(17) Å
***c* / Å**	32.4290(17) Å
***α* / º**	90
***β* /º**	90
***γ* / º**	90
Volume / Å^3	34104(5)
Z	1
ρ_{calc}/ g/cm^3	0.482
μ / mm^{-1}	0.591
F(000)	4857.0
Crystal size / mm^3	? × ? × ?
Radiation	0.71073 Å
θ range for data collection / º	1.256 to 34.856
Index ranges	-27<=h<=27, -27<=k<=27, -27<=l<=26
Reflections collected	153673
Independent reflections	2143 [R(int) = 0.8409]
Data/restraints/parameters	2143 / 0 / 166
Goodness-of-fit on F^2	2.254
Final R indexes [I>=2σ (I)]	R_1 = 0.3203, wR_2 = 0.6403
Final R indexes [all data]	R_1 = 0.3937, wR_2 = 0.6644
Largest diff. peak/hole / e.Å^{-3}	2.42 and -0.93

4.4 Conclusion and future work

In conclusion, we have successfully synthesised a series of MOFs containing Zn^{2+} and Co^{2+} ions. Using the H_4BTEB_{ppi} linker, two new MOFs, $[NH_2(CH_3)_2]_6[Zn_9(BTEB_{ppi})_6]$ (**12**) and $[Co_2(BTEB_{ppi})(DMF)_3]$ (**13**), were synthesised and found to contain attractive structural units. **12** is an anionic MOF that contains two inorganic SBUS that are uncommon in the literature. The SBUs had the structure of a monomeric Zn^{2+} ion coordinated by four carboxylate groups and a dimeric Zn^{2+} SBU coordinated by five carboxylates. The five connected SBUs is of particular interest as, to the best of our knowledge, it has been reported as the inorganic SBU within a MOF in the literature only once before. [312]

The secondary MOF synthesised with the H_4BTEB_{ppi} linker was the cobalt-based MOF, **13**. The inorganic SBUs of the MOF was of a dimeric Co^{2+} SBU coordinated by four carboxylate groups. In the structure of the SBU, three DMF molecules coordinate to on the Co^{2+} ions. This feature is of great interest due to cobalt-based MOFs previously being reported to catalyse the water oxidation reaction. A preliminary investigation of the material's ability to catalyse the reaction was carried out. The MOF was determined to be an active catalyst for the water oxidation reaction. The MOF was found to have an overpotential of 435 mV at a 20 wt% loading of the MOF in carbon paste. Longterm stability studies of the material determined that the electrode was unstabled over extended periods of time. The formation of bubbles on the electrode's surface leads to the electrode's degradation throughout the experiment. Further work is required to examine the catalytic properties of the material thoroughly.

The final MOF in this chapter $[Zn_{28}(HBTEB_{iip}^{4-})_{12}(DEF)_{28}](NO_3)_8$ (**14)** was synthesised using the newly synthesised linkers from **Chapter 3** and utilised the pentacarboxylate H_5BTEB_{iip} in combination with Zn^{2+} ions. The MOF was found to be a cationic framework comprised of MOP like units interlinked by the $HBTEB_{iip}^{4-}$. The *para*-benzoate moiety on the linker was found to have a non-structural role in the framework and remains as a free carboxylate within the structure. The presence of free carboxylate groups present in a MOF is an attractive feature, which rarely occurs MOFs due to the tendency of the carboxylate groups to coordinate with the inorganic SBUs. The presence of the free carboxylate demonstrates the intense driving for the linkers and SBUs to form regular and straightforward frameworks. Future work is required to study the material's potential catalytic properties in reactions catalysed by weak acids like benzoic acid and acetic acid. In this role, the MOF could be utilised as a hetrogenised version of a weak acid catalyst.

MOFs utilising the remaining linkers from **Chapter 3** could not be synthesised. However, this is not an entirely unexpected result as the linkers that remain have the lowest symmetry of the newly synthesised linkers. This lack of structures does not eliminate the possibility that MOFs could be synthesised with these linkers and Zn^{2+} or Co^{2+} ions; merely the broad scope of examined reactions are not capable of synthesising a MOF. It is also possible that MOFs containing these linkers could

be synthesised with a broader selection of transition metals. This leaves an extensive and exciting area of MOFs to be examined.

Chapter 5

Experimental

5 Experimental

5.1 Methods

Solvothermal synthesis was carried out using 1.5 mL reaction/mass spectrometry vials from VWR seal using a PET lid with PTFE liner. The vials were heated using a custom heating block a hotplate.

Single crystal X-ray diffraction analysis: Single-crystal X-Ray analysis and refinement were performed by Dr. Nianyong Zhu using a Bruker APEX2 Duo diffractometer. X-Ray intensity data were measured at 100 K using a MiTeGen micromount, or 215 K – 230 K, mounted in a glass capillary containing a small amount of solvent, using an Oxford Cryosystem Cobra low-temperature device. Frames were integrated with the Bruker SAINT software package, and the data was corrected for absorption effects using the multi-scan method (SADABS).[327] Structures were solved by intrinsic phasing using XT[328] or by direct methods (SHELXS) and refined with the programs Olex2[329] and XL[330] least-squares refinement. Some structures contain large solvent-accessible void volumes in which solvent molecules could not be located reliably. To account for this, the Platon-SQUEEZE[331] routine was used to calculate the void volume and re-generate the reflection file by excluding the diffraction contributions of these unlocated solvent molecules. The final results are based on the new reflection data.

Powder X-ray diffraction: Analysis was carried out using an APEX II DUO X-ray diffractometer by Dr. Nianyong Zhu or Dr. Brendan Twamley. Samples were ground under solvent and sealed inside 0.3 - 1.0 mm diameter borosilicate glass or "special glass" capillaries from WJM Glas Müller GmbH. The capillaries were mounted and centred on a goniometer head. The data were collected upon 360◦ ϕ rotation frames at two values of 10◦ and 20◦, with exposure times of 15 minutes per frame at a detection distance of 120 mm. Overlapping sections of data were then combined and the data was processed using the Bruker APEX2 routine XRD2-Eval subprogram. Analysis and background corrections were carried out using Expo2014.[228, 229]

NMR spectroscopy: ^{1}H and $^{13}C\{^{1}H\}$ NMR, spectra were recorded on a Bruker DPX 400 instrument operating at 400.13 MHz by Dr. John O'Brien and Dr. Manuel Rüther. Samples were prepared in deuterated solvents as mentioned. Standard abbreviations for spectra are used: s (singlet); d (doublet); t (triplet); qt (quartet); q (quaternary); m (multiplet); br (broad); J (coupling constant).

Thermogravimetric analysis: Thermogravimetric analysis (TGA) was carried out using a Perkin Elmer Pyris-1 Thermogravimetric analyser under a nitrogen stream at a flow rate of 20 mL min^{-1} . Measurements were carried out between 20°C and 700°C at a heating rate of 4°C per minute.

Fourier-transform infrared spectroscopy (FT-IR): Infrared spectroscopy was recorded on a PerkinElmer Spectrum One FTIR spectrometer using a universal ATR sampling accessory. Data was

collected and processed using Spectrum v5.0.1 (2002 PerkinElmer Instrument LC) software. The scan rate was 16 scans per minute with a resolution of 40 scans in the range 4000-400 cm^{-1}.

Mass Spectrometry:Mass spectrometry was carried out on a Micromass LCT Electrospray mass spectrometer by Dr. Martin Feeney and Dr. Gary Hessman. Samples were prepared by dissolving the compound in HPLC grade solvents. Additions of NH_4OH or $HCl_{(aq)}$ were added as needed to aid in dissolving the compound.

Elemental Analysis: Elemental C, H, N, quantitative analysis was performed on samples requiring additional conformation of phase purity by Rónán Crowley using an Exeter Analytical CE 440 at the Analytical Laboratory, UCD Belfield, Dublin.

Energy-dispersive X-ray spectroscopy (EDX): The samples was measured on a Ziess ULTRA scanning electron microscope using a 20 mm^2 Oxford Inca EDX detector and a 20 kV acceleration voltage.

Electrochemistry: The experiments were carried out using a Bio-logic Science Instrument VSP Potentiostat. A three-electrode set-up was used in all experiments, with further information detailed in the results sections for each experiment. A water bath was used to keep all reaction mixtures at 25°C during the experiments.

5.2 Ligand synthesis

All chemicals and some solvents were purchased from Sigma-Aldrich Chem. Co. Ltd., Fluorochem Ltd. or VWR chemicals. Common solvents were obtained from local solvent suppliers at the hazardous materials facility in Trinity College Dublin and used as received unless otherwise stated. Water was deionised in-house using a Millipore Synergy 185 water purification system.

The linkers and their corresponding intermediates were synthesised as per the following modified literature methods.

2,4,6-tris((trimethylsilyl)ethynyl)aniline

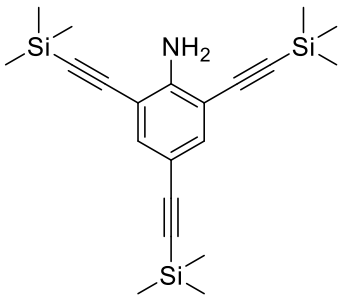

2,4,6-tribromoaniline (5 g, 15.15 mmol), $PdCl_2(PPh_3)_2$ (531 mg, 0.75 mmol, 5 mol%) and CuI (144 mg, 0.75 mmol, 5 mol%) were first dissolved in dry triethylamine (100 mL). Trimethlysilane acetylene (8.5 mL, 60 mmol) was added to the solution. After the solution was heated to 80 ºC for 72hrs it was cooled and the solvent was removed under reduced pressure. The dark solid that remained was taken up in CH_2Cl_2 (150 mL) and washed with a saturated solution of NH_4Cl (3 x 150 mL). The organic layer was then dried with $MgSO_4$ and the resulting crude was purified by flash chromatograph on silica gel (petroleum ether/ CH_2Cl_2 100:30) Yield 5.4 g, 14.18 mmol, 93 %. ^1H NMR ($CDCl_3$, 400 MHz) δ_H (ppm): 7.37 (1H, s, CH), 4.97 (2H, s, NH_2), 0.24 (27H, s, CH_3), 0.20 (9H, s, CH_3) ppm.

2,4,6-triethynylaniline

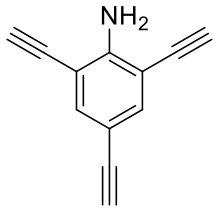

2,4,6-tris((trimethylsilyl)ethynyl)aniline (5.4 g, 14.18 mmol) and K_2CO_3 (5 g) were first dissolved 100 mL of a 1:1 mixture CH_2Cl_2/MeOH. The suspension was allowed to stir for 3 hrs. After the reaction was completed, 300 mL of deionised water was added with a further 100 mL of CH_2Cl_2. The organic layer was washed, separated and dried with $MgSO_4$. The product was used without further purification. Yield: 2.17 g, 13.17 mmol, 92 %. ^{1}H NMR ($CDCl_3$, 400 MHz) δ_H (ppm): 7.44 (2H,s,CH), 5.02 (2H, s, NH), 3.40 (2H, s, C≡CH) 2.92 (1H, s, C≡CH).

trimethyl 3,3',3''-((2-aminobenzene-1,3,5-triyl)tris(ethyne-2,1-diyl))tribenzoate

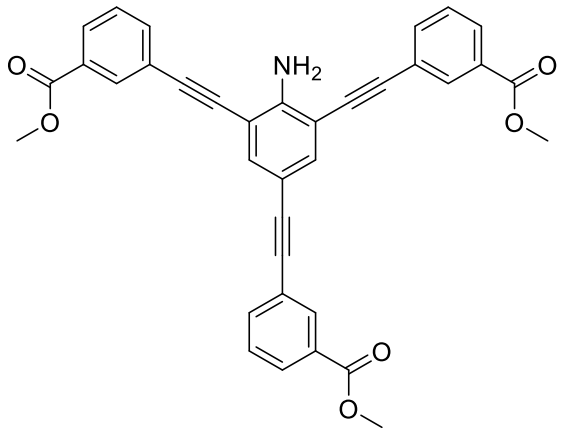

2,4,6-triethynylaniline (2.17 g, 13.15 mmol), 4-iodo-methylbenzoate (11 g, 42 mmol), $PdCl_2(PPh_3)_2$ (276 mg, 0.4 mmol, 3 mol%) and CuI (75 mg, 0.4 mmol, 3 mol%) were first dissolved in dry triethylamine. The solution was heated at 85 ºC under and inert atmosphere for 24 hours. After the reaction had completed the solvent was removed under reduced pressure and the crude product was taken up in CH_2Cl_2 (150 mL). The solution was washed with saturated NH_4Cl solution (2 x 150 mL). The organic phase was isolated, dried with $MgSO_4$ and removed under reduced pressure. The crude was purified by flash chromatograph on silica gel (EtOAc/ hexane 1:4) Yield: 3.88 g, 6.83 mmol, 52 %. ^{1}H NMR ($CDCl_3$, 400 MHz) δ_H (ppm): 8.21(2H, t, J = 1.5, CH), 8.17 (1H, t, J = 1.49, CH), 8.03 (2H, dt, J_1 = 7.8 J_2 = 1.46, CH) 7.98 (1H, dt, J_1 = 8.06 J_2 = 1.22, CH), 7.72 (2H, dt, J_1 = 7.5 J_2 = 1.22, CH), 7.66 (1H, dt, J_1 = 7.82 J_2 = 1.22, CH), 7.58 (2H, s, CH), 7.47 (2H, t, J = 7.8, CH), 7.42 (1H, t, J = 7.82, CH), 3.95 (6H, s, CH_3), 3.94 (3H, s, CH_3).

Synthesis of *3,3',3''-((2-aminobenzene-1,3,5-triyl)tris(ethyne-2,1-diyl))tribenzoic acid* (**4**)

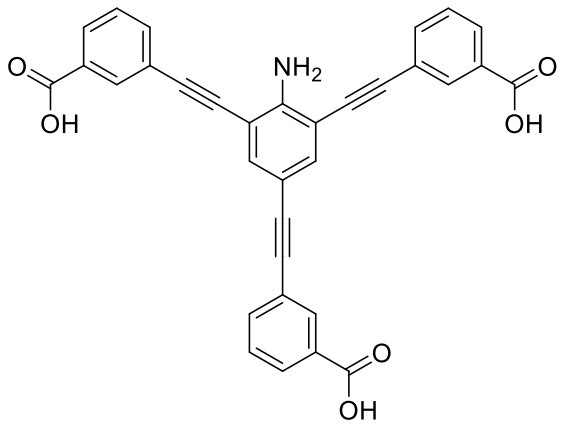

3 (3.8g, 6.8 mmol) and LiOH (4 g) was dissolved in a 100 mL mixture of water/THF 1:1. The solution was left to stir at room temperature for 7 hrs. After the reaction had completed the solution was acidified with 6M HCl. The resultant precipitate was filtered off and redissolved in EtOAc (150 mL). The solution was then washed with deionised water. The organic layer was then isolated and dried with $MgSO_4$. The crude product was purified by flash chromatography on silica gel (THF) Yield: 2.03 g, 3.8 mmol, 59 %. %. ^{1}H

NMR (DMSO-D_6, 400 MHz) δ_H (ppm): 8.16 (2H, t, J=1.54 Hz, CH) 7.95 (2H, t, J=1.52, CH) 7.87 (2H, dt, J_1 = 8.0 Hz J_2 = 1.14 Hz, CH), 7.83 (1H, dt, J_1 = 7.84 Hz, J_2 = 1.36 Hz, CH), 7.80 (2H, dt, J_1 = 7.9 Hz J_2 = 1.07 Hz, CH), 7.64 (1H, dt, J_1 = 7.96 Hz J_2 = 1.32 Hz, CH), 7.52 (2H, s, CH), 7.48 (2H, t, J_1 = 7.82 Hz), 7.45 (1H, t, J_1 = 7.74), 6.29 (2H, s, NH_2).

Representative procedure A: preparation of methyl 3-((trimethylsilyl)ethynyl)benzoate

Methyl 3-bromobenzoate (5 g, 23.25 mmol), $PdCl_2(PPh_3)_2$ (489 mg, 0.7 mmol, 0.03 mole eq.) and CuI (132 mg, 0.7 mmol, 0.03 mole eq.) were first dissolved in a mixture of THF/TEA (100 ml, 1:1, v/v) and stirred under an inert atmosphere. Trimethlysilane acetylene (3.6 mL, 25.6 mmol, 1.1 mole eq.) was added to the solution. The solution was heated to 65 ºC for 24 hrs. Upon completion, the solution was cooled, and the solvent was removed under reduced pressure. The crude dark solid product that remained was dissolved in DCM (150 mL) and washed with a saturated solution of NH_4Cl (100 mL x 3) and finally with brine. The organic layer was then isolated and dried using $MgSO_4$. The resulting crude was purified by flash column chromatograph (silica gel with $CHCl_2$:Hexane, 1:4 v/v). A similar procedure was performed to prepare the remaining TMS protected compounds starting from the appropriate bromoarenes.

methyl 3-((trimethylsilyl)ethynyl)benzoate

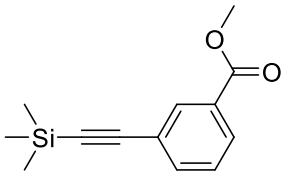

Yield: 4.92 g, 21.09 mmol, 90 %. ^{1}H NMR ($CDCl_3$, 400 MHz) δ_H (ppm): 8.16 (1H, t, J = 1.5 Hz), 7.98 (1H, dt, J = 7.8, 1.2 Hz), 7.65 (1H, dt, J = 7.7, 1.2 Hz), 7.39 (1H, t, J = 7.8 Hz), 3.93 (3H, s), 0.28 (9H, s). ^{13}C{^{1}H}-NMR ($CDCl_3$, 100 MHz) δ_c (ppm): 166.3, 136.0, 133.1, 130.3, 129.4, 128.4, 123.6, 103.9, 95.3, 52.21, 0.1. FT-IR (diffuse reflectance): ν max (cm^{-1}) = 2954 w, 2895 w, 2159 w, 1714 m,1600 m, 1449 m, 1276 s, 1244 m, 1108 m, 836 s, 758 s, 697 m.

methyl 4-((trimethylsilyl)ethynyl)benzoate

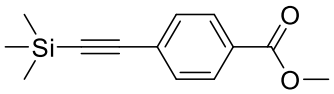

Yield: 4.6 g, 19.8 mmol, 85 %.^{1}H NMR ($CDCl_3$, 400 MHz) δ_H (ppm): 7.97 (2H, d, J = 9.0 Hz), 7.52 (2H, d, J = 9.0 Hz), 3.91 (3H, s), 0.26 (9H, s). ^{13}C{^{1}H}-NMR ($CDCl_3$, 100 MHz) δ_c (ppm): 166.6, 132.0, 129.8, 129.5, 127.9, 104.2, 97.8, 52.4, 0.1. FT-IR (diffuse reflectance): ν max (cm^{-1}) = 2952 w, 2899 w, 2159 w, 1716 m, 1602 m, 1442 m, 1405 w, 1274 s, 1244 m, 1108 m, 835 s, 758 s, 695 m, 666 m.

dimethyl 5-((trimethylsilyl)ethynyl)isophthalate

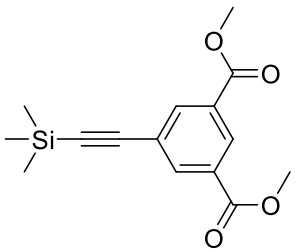

Yield: 4.72 g, 16.5 mmol, 88 %.^{1}H NMR ($CDCl_3$, 400 MHz) δ_H (ppm): 8.60 (1H, t, J = 1.6 Hz), 8.29 (2H, d, J = 1.6 Hz), 3.94 (6H, s), 0.26 (9H, s). ^{13}C{^{1}H}-NMR ($CDCl_3$, 100 MHz) δ_c (ppm): 165.7, 137.0, 131.0, 130.5, 124.4, 102.9, 96.9, 52.7, 0.0. FT-IR (diffuse reflectance): νmax (cm^{-1}) = 2963 w, 2895 w, 2159 w, 1602 m, 1445 m, 1401 w, 1277 s, 835 s, 758 s, 690 m.

Representative procedure B: preparation of methyl 3-ethynylbenzoate

Methyl 3-((trimethylsilyl)ethynyl) benzoate (4.92 g, 21.7 mmol) was first dissolved in DCM (150 mL). In a separate solution, K_2CO_3 (2.53g) was dissolved in MeOH (150 mL), and the solution was added to the original solution of methyl 3-((trimethylsilyl)ethynyl)benzoate in DCM. The mixture was stirred at RT. for 4 hours. The solvent was removed under reduced pressure, and the crude product was purified using flash column chromatography (silica gel with CH_2Cl_2: hexane, 1:4, v/v as mobile phase). Similar procedures were carried out to synthesise the remaining terminal alkyne compounds.

methyl 3-ethynylbenzoate

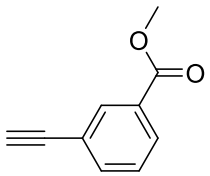

Yield: 2.91 g, 18.17 mmol, 85 %.. ^{1}H NMR ($CDCl_3$, 400 MHz) δ_H (ppm): 8.09 (1H, s), 7.94 (1H, d, J = 7.9 Hz), 7.59 (1H, d, J = 7.7 Hz), 7.34 (1H, t, J = 7.8 Hz), 3.85 (3H, s), 3.05 (1H, s). ^{13}C{^{1}H}-NMR ($CDCl_3$, 100 MHz) δ_c (ppm): 165.2, 135.2, 132.2, 129.4, 128.8, 127.5, 121.5, 81.5, 77.1, 51.3.

methyl 4-ethynylbenzoate

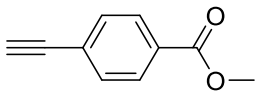

Yield: 2.63 g, 16.42 mmol, 83 %. ^{1}H NMR ($CDCl_3$, 400 MHz) δ_H (ppm): 7.99 (2H, d, J = 9.0 Hz), 7.54 (2H, d, J = 9.0 Hz), 3.91 (3H, s), 3.23 (1H, s). ^{13}C{^{1}H}-NMR ($CDCl_3$, 100 MHz) δ_c (ppm): 166.5, 132.2, 130.2, 129.6, 126.9, 82.91, 80.2, 52.4. FT-IR (diffuse reflectance): νmax (cm^{-1}) = 3241 m, 2951 w, 2103 w, 1699 s, 1606 m, 1433 m, 1349 m, 1277 s, 1192 m, 1174 m, 1108 s, 1016 m, 957 m, 859 m, 770 s, 719 s, 676 s, 528 m, 460 w.

dimethyl 5-ethynylisophthalate

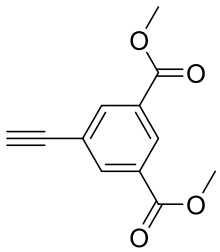

Yield: 2.86 g, 13.11 mmol, 80 %.^{1}H NMR ($CDCl_3$, 400 MHz) δ_H (ppm): 8.62 (1H, t, J = 1.6 Hz), 8.30 (2H, d, J = 1.6 Hz), 3.94 (6H, s), 3.17 (1H, s); ^{13}C{^{1}H}-NMR ($CDCl_3$, 100 MHz) δ_c (ppm): 165.54, 137.15, 131.06, 130.77, 123.29, 81.65, 79.31, 52.69; FT-IR (diffuse reflectance): νmax (cm^{-1}): 3270 m, 3067 m , 2957 w, 2104 w, 1593 s, 1488 m, 1381 m, 781 s.

Representative procedure **C:** preparation of methyl 4-((3,5-dichlorophenyl)ethynyl)benzoate

Methyl 3-ethynylbenzoate (1.5 g, 9.36 mmol, 1 mole eq.), 3,5-dichloro iodobenzene (2.81 g, 10.3 mmol, 1.1 mole eq.), $PdCl_2(PPh_3)_2$ (328 mg, 0.468 mmol, 0.05 mole eq.) and CuI (89 mg, 0.468 mmol, 0.05 mole eq.) were first dissolved in a solution of trimethylamine:THF (1:1, v/v, 150 ml). The solution was then stirred under N_2 at 50 ºC for 24 hours. Upon completion, the mixture was allowed to cool, and the solvent was removed under reduced pressure. The crude product was then dissolved in CH_2Cl_2 (150 ml) and washed with a saturated aqueous solution of NH_4Cl (100 ml x 3) and finally by brine (100ml). The organic layer was then separated, dried over anhydrous $MgSO_4$,

filtered and concentrated under reduced pressure to give the crude product. The crude product was purified by flash column chromatography (silica gel with CH_2Cl_2: Hexane, 2:3, v/v, as mobile phase). Similar procedures were performed to prepare the other (3,5-dichlorophenyl)ethynyl arene derivatives.

methyl 3-((3,5-dichlorophenyl)ethynyl)benzoate

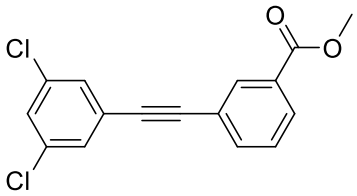

Yield: 2.45 g, 8.03 mmol, 86 %.^{1}H NMR ($CDCl_3$, 400 MHz) δ_H (ppm): 8.03 (2H, d, J = 8.4 Hz), 7.57 (2H, d, J = 8.4 Hz), 7.41 (2H, d, J = 1.9 Hz), 7.35 (1H, t, J = 1.9 Hz), 3.93 (3H, s). $^{13}C\{^1H\}$-NMR ($CDCl_3$, 100 MHz) δ_C (ppm): 166.5, 135.2, 131.8, 130.3, 130.0, 129.7, 127.0, 125.7, 90.9, 89.5, 52.5. HR-MS (ESI): m/z Calculated for $C_{16}H_{10}Cl_2O_2$ $[M+H]^+$ 304.0048; Found 304.0051

methyl 4-((3,5-dichlorophenyl)ethynyl)benzoate

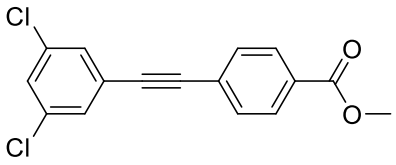

Yield: 2.36 g, 7.73 mmol, 82 %.^{1}H NMR ($CDCl_3$, 400 MHz) δ_H (ppm): 8.19 (1H, t, J=1.4 Hz), 8.03 (1H, dd, J_1=7.8 Hz, J_2=2.7 Hz, CH), 7.68 (1H, dd, J_1=7.8 Hz, J_2=2.7 Hz, CH), 7.44 (1H, t, J=7.8Hz,CH), 7.40 (1H, d, J=1.9 Hz, CH), 7.33 (1H, t, J=1.9 Hz, CH), 3.93 (3H, s, CH_3). $^{13}C\{^1H\}$-NMR ($CDCl_3$, 100 MHz) δ_C (ppm): 166.2, 135.7, 135.0, 132.9, 130.6, 129.9, 129.8, 128.8, 128.6, 125.7, 122.7, 90.6, 87.5, 52.4. HR-MS (ESI): m/z Calculated for $C_{16}H_{10}Cl_2O_2$ $[M+H]^+$ 304.0052; Found 304.0053

dimethyl 5-((3,5-dichlorophenyl)ethynyl)isophthalate

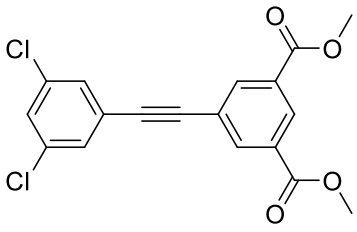

Yield: 1.72 g, 4.74 mmol, 68 %.^{1}H NMR ($CDCl_3$, 400 MHz) δ_H (ppm): 8.64 (1H, t, J=1.6 Hz), 8.33 (2H, d, J =1.6 Hz), 7.41 (2H, d, J =1.9 Hz), 7.35 (1H, t, J=1.9 Hz), 3.96 (6H, s) ppm. $^{13}C\{^1H\}$-NMR ($CDCl_3$, 100 MHz) δ_C (ppm): 165.43, 136.60, 135.06, 131.11, 130.69, 129.87, 129.15, 125.27, 123.36, 89.50, 88.35, 52.64. HR-MS (ESI): m/z Calculated for $C_{18}H_{12}Cl_2O_4$ $[M+H]^+$ 363.0191; Found 363.0189

Representative procedure **D**: preparation of dimethyl 4,4'-((5-((3-(methoxycarbonyl)phenyl) ethynyl)-1,3-phenylene)bis(ethyne-2,1-diyl))dibenzoate

methyl 4-((3,5-dichlorophenyl)ethynyl)benzoate (2 g, 6.55 mmol, 1 mole eq.), $PdCl_2(CH_3CN)_2$ (34 mg, 0.131 mmol, 0.02 mole eq.), X-Phos (187 mg, 0.393 mmol, 0.06 eq.) an Cs_2CO_3 (8.45 g, 26.22 mmol, 4 mole eq.) were first dissolved in 1,4-Dioxane (50ml) and stirred under an inert atmosphere at 50 ºC for 30 minutes. Over this period, the solution changed colour from yellow to red/orange. After the colour change, the temperature of the solution was then increased to 90 ºC. In a separate round bottomed flask, methyl 3-ethynylbenzoate was dissolved in 1,4-Dioxane (50ml). This solution was added dropwise into the reaction solution over 3 hours. After the final addition of the alkyne

solution, the temperature was raised to 100 ºC and stirred for an additional 3 hours. Upon completion of the reaction, the reaction was cooled, and the solvent was removed under reduced pressure. The yellow-brown crude product was then dissolved DCM (100ml) and washed with deionised water (100 ml x 3) followed by brine (100ml). The organic layer was isolated, dried using anhydrous $MgSO_4$, and the solvent was removed under reduced pressure. The crude product was then purified using flash column chromatography (silica gel with DCM: EtOAc, 40:1, v/v, as mobile phase). Similar procedures were then carried out with various combinations of the 3,5-dichlorophenyl)ethynyl arene derivatives and terminal alkyne compounds to synthesise the remaining ester protected ligands.

dimethyl 3,3'-((5-((4-(methoxycarbonyl)phenyl)ethynyl)-1,3-phenylene)bis(ethyne-2,1-diyl))dibenzoate

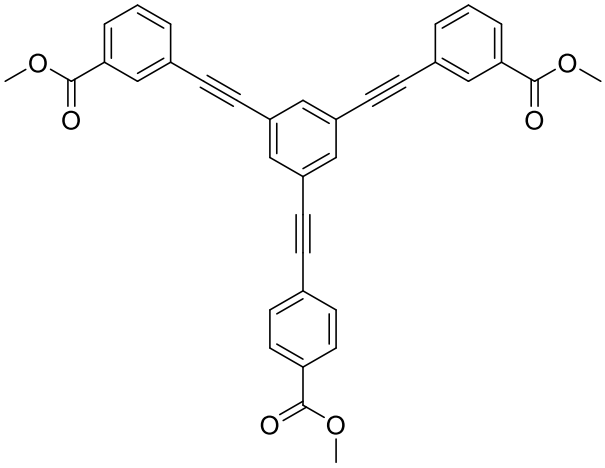

Yield: 2.6 g, 4.71 mmol, 71 %^{1}H NMR ($CDCl_3$, 400 MHz) δ_H (ppm): 8.21 (2H, t, J=1.5 Hz), 8.04 (2H, d, J=8.4 Hz) 8.03, (2H, dt, J_1=7.7 Hz, J_2=1.4, Hz), 7.71 (2H, dt, J_1=7.7, Hz, J_2=1.4 Hz), 7.68 (3H, s), 7.6 (2H, d, J=2.8 Hz), 7.45 (2H, t, J=7.7 Hz, CH), 3.95 (6H, s), 3.93 (3H, s). $^{13}C\{^1H\}$-NMR ($CDCl_3$, 100 MHz) δ_C (ppm): 166.4, 166.3, 135.7, 134.5, 134.4, 132.9, 131.6, 130.6, 129.9, 129.6, 129.5, 128.6, 127.3, 123.9, 126.7, 123.1, 90.4, 89.9, 89.7, 88.4, 52.3, 52.2. HR-MS (ESI): m/z Calculated for $C_{36}H_{24}O_6$ $[M]^-$ 552.1573; Found 552.1573.

dimethyl 5-((3,5-bis((3-(methoxycarbonyl)phenyl)ethynyl)phenyl)ethynyl)isophthalate

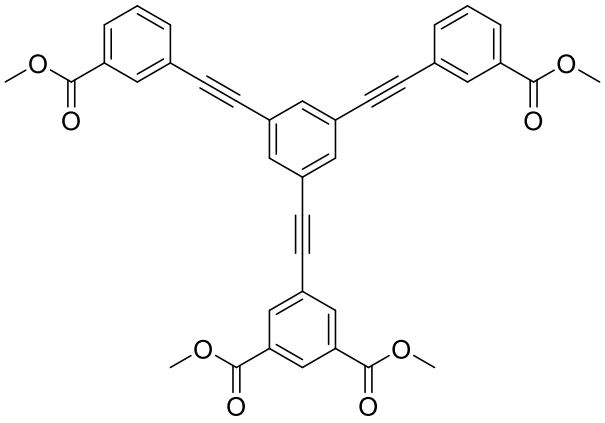

Yield: 2.13 g, 3.49 mmol, 63 %^{1}H NMR ($CDCl_3$, 400 MHz) δ_H (ppm): 8.67 (1H, t, j=1.3 Hz, CH), 8.40 (2H, d, J=1.2 Hz, CH), 8.24 (2H, t, J=1.5 Hz, CH), 8.06 (2H, dt, J_1=7.8 Hz, J_2=1.3 Hz, CH), 7.74 5H, m, CH), 7.48 (2H, t, 7.8 Hz, CH), 4.00 (3H, s, CH_3), 3.97 (3H, s, CH_3). $^{13}C\{^1H\}$-NMR ($CDCl_3$, 100 MHz) δ_C (ppm): 166.3, 165.5, 136.6, 135.8, 134.7, 134.4, 132.9, 131.1, 130.6, 130.5, 129.7, 128.6, 123.9, 123.8, 123.5, 123.2, 89.8, 89.4, 88.6, 88.4, 52.6, 52.4. HR-MS (ESI): m/z Calculated for $C_{38}H_{26}O_6$ $[M]^-$ 610.1628; Found 610.1632

dimethyl 4,4'-((5-((3-(methoxycarbonyl)phenyl)ethynyl)-1,3-phenylene)bis(ethyne-2,1-diyl))dibenzoate

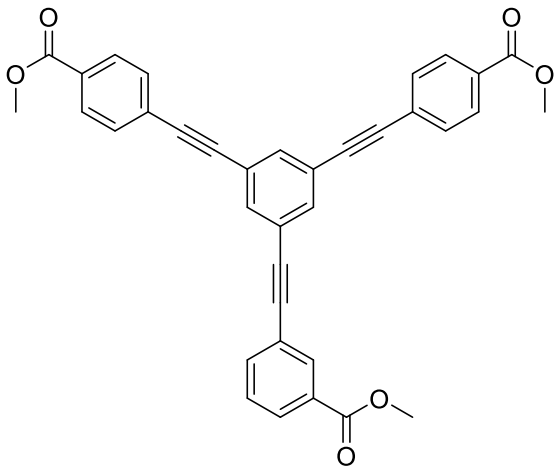

Yield: 2.9 g, 5.25 mmol, 80 %^{1}H NMR ($CDCl_3$, 400 MHz) δ_H (ppm): 8.21 (1H, t, J=1.3 Hz, CH), 8.03 (5H, m,, CH),7.7 (4H, m, CH), 7.59 (4H, d, J=8.4,CH), 7.45 (1H, t, J=7.8 Hz, CH), 3.94 (3H, s, CH), 3.93 (6H, s, CH). $^{13}C\{^{1}H\}$-NMR ($CDCl_3$, 100 MHz) δ_C (ppm): 166.5, 166.3, 135.7, 134.4, 132.9, 130.6, 129.9, 129.7, 129.6, 128.6, 127.3, 123.9, 123.7, 123.1, 90.4, 89.8, 88.4, 52.4, 52.3. HR-MS (ESI): m/z Calculated for $C_{36}H_{24}O_6$ $[M]^-$ 552.1573; Found 552.1572.

dimethyl 5-((3,5-bis((4-(methoxycarbonyl)phenyl)ethynyl)phenyl)ethynyl)isophthalate

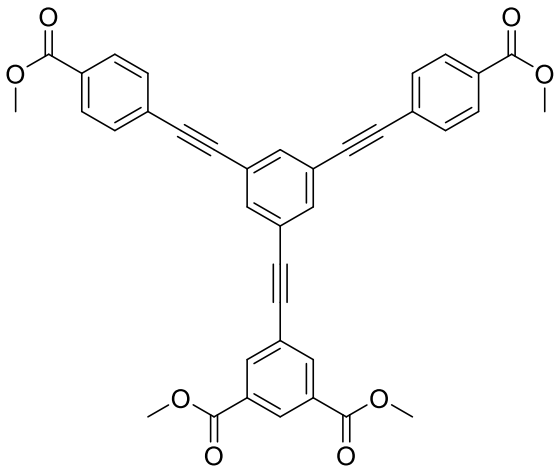

Yield: 2.45 g, 4.01 mmol, 73 %^{1}H NMR ($CDCl_3$, 400 MHz) δ_H (ppm): 8.67 (1H, t, J=1.6 Hz, CH), 8.38 (2H, d, J=1.6 Hz, CH), 8.06 (4H, d, J=8.5 Hz, CH), 7.72 (3H, s, CH), 7.61 (4H, d, J= 8.4, CH), 3.40 (6H, s, CH_3), 3.39 (6H, s, CH_3). $^{13}C\{^{1}H\}$-NMR ($CDCl_3$, 100 MHz) δ_C (ppm): 166.5, 165.5, 136.6, 134.7, 134.6, 131.6, 131.1, 130.5, 130.0, 129.6, 127.3, 123.8, 123.7, 123.5, 90.3, 90.1, 89.3, 88.7, 52.6, 52.30. HR-MS (ESI): m/z Calculated for $C_{38}H_{26}O_8$ $[M]^-$ 610.1628; Found 610.1627

tetramethyl 5,5'-((5-((3-(methoxycarbonyl)phenyl)ethynyl)-1,3-phenylene)bis(ethyne-2,1-diyl))diisophthalate

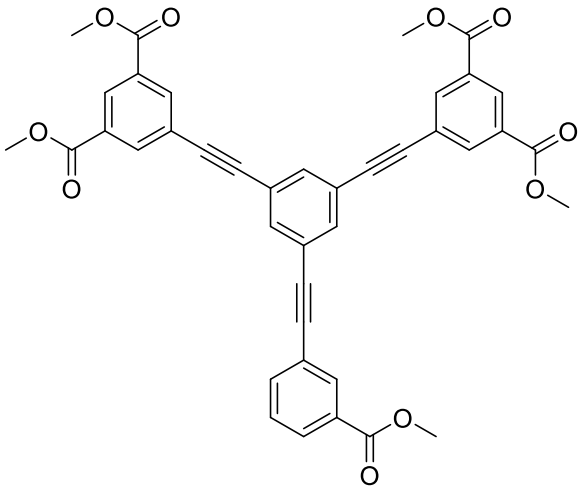

Yield: 3.2 g, 4.79 mmol, 73 %^{1}H NMR ($CDCl_3$, 400 MHz) δ_H (ppm): 8.68 (2H, t, J=1.6 Hz, CH), 8.40 (4H, d, J=1.6 Hz, CH), 8.25 (1H, t, J = 1.5 Hz), 8.06 (1H, dt, J_1 = 7.9 Hz, J_2 = 2.8 Hz), 7.75 (1H, dt, J_1 = 7.9 Hz, J_2 = 2.8 Hz), 7.73 (3H, s), 7.49 (1H, t, J=7.8 Hz), 4.00 (12H, s), 3.97 (3H, s). $^{13}C\{^{1}H\}$-NMR ($CDCl_3$, 100 MHz) δ_C (ppm): 166.3, 165.5, 136.6, 135.8, 134.7, 134.4, 132.9, 131.0, 130.6, 130.5, 129.7, 128.6, 124.0, 123.7, 123.5, 123.1, 89.9, 89.3, 88.7, 88.3, 52.6, 52.4. HR-MS (ESI): m/z Calculated for $C_{40}H_{28}O_{10}$ $[M]^-$ 668.1682; Found 668.1683

tetramethyl 5,5'-((5-((4-(methoxycarbonyl)phenyl)ethynyl)-1,3-phenylene)bis(ethyne-2,1-diyl))diisophthalate

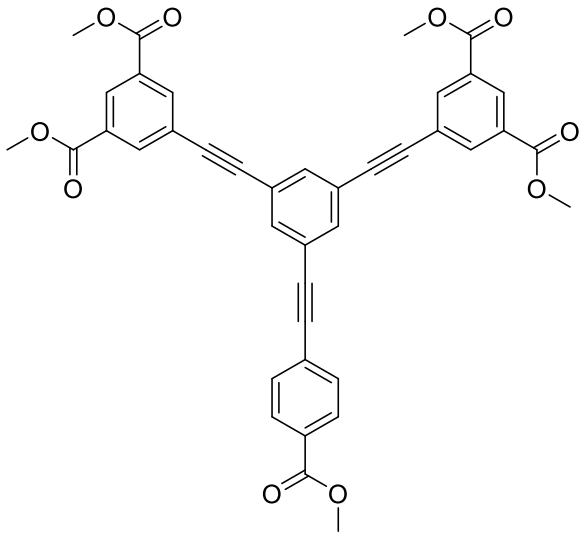

Yield: 2.54 g, 3.8 mmol, 57 %. ^{1}H NMR ($CDCl_3$, 400 MHz) δ_H (ppm): 8.68 (2H, t, J = 1.6 Hz), 8.40 (4H, t, J = 1.6 Hz), 8.07 (2H, d, J = 8.4 Hz), 7.73 (3H, s), 7.63 (2H, d, J=8.4 Hz), 4.00 (12H, s), 3.96 (3H, s). $^{13}C\{^{1}H\}$-NMR ($CDCl_3$, 100 MHz) δ_C (ppm): 166.5, 165.5, 136.6, 134.7, 134.6, 131.6, 131.1, 130.5, 130.0, 129.6, 127.3, 123.8, 123.7, 123.5, 90.3, 90.1, 89.3, 88.7, 52.6, 52.30. HR-MS (APCI): m/z Calculated for $C_{40}H_{28}O_{10}$ $[M]^-$ 668.1682; Found 668.1682

Representative procedure **D**: deprotection of 3,3'-((5-((4-carboxyphenyl)ethynyl)-1,3-phenylene)bis(ethyne-2,1-diyl))dibenzoic acid

dimethyl 3,3'-((5-((4-(methoxycarbonyl) phenyl)ethynyl)-1,3-phenylene) bis (ethyne-2,1-diyl)) dibenzoate (2.6 g, 4.71 mmol, 1 mole eq.) and LiOH (563 mg, 23.5 mmol, 5 mole eq.) was dissolved in a mixture of H_2O/THF (100ml, 1:1, v/v). The solution was then stirred at room temperature for 7 hours. Upon completion, the organic phase was then removed under reduced pressure. The remaining aqueous solution was then acidifed with 6M HCl aq. to a pH of 2, where upon reaching the required pH, the product precipitated from the solution. The resultant precipitate was then filtered off and purified with flash column chromatography (silica gel with THF as mobile phase). Similar procedures were carried out for the remaining ester protected compounds.

3,3'-((5-((4-carboxyphenyl)ethynyl)-1,3-phenylene)bis(ethyne-2,1-diyl))dibenzoic acid (H_3BTEB_{mmp})

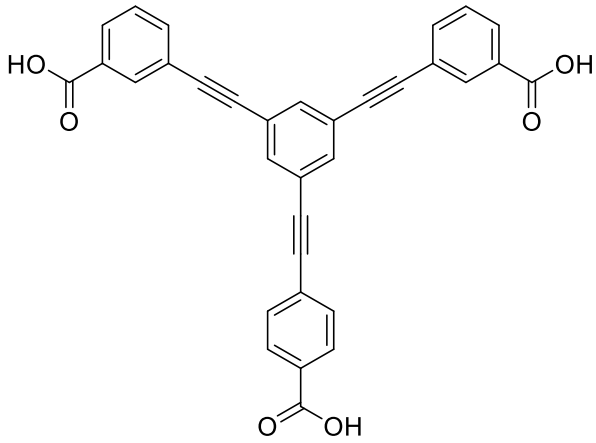

Yield: 1.85 g, 3.62 mmol, 77 %. ^{1}H NMR ($CDCl_3$, 400 MHz) δ_H (ppm): 8.13 (1H, s), 8.00 (4H, d, J = 8.2 Hz), 7.87 (2H, s), 7.84 1H, s), 7.83 (1H, d, J = 8.0 Hz), 7.71 (4H, d, J = 7.84 Hz), 7.60 (2H, t, J = 7.7 Hz). $^{13}C\{^{1}H\}$-NMR ($CDCl_3$, 100 MHz) δ_C (ppm): 166.9, 166.4, 135.7, 134.5, 134.4, 132.8, 131.6, 130.6, 129.9, 129.5, 129.3, 128.6, 127.3, 123.9, 126.4, 123.1, 90.4, 89.8, 89.7, 88.3. HR-MS (ESI): m/z Calculated for $C_{33}H_{17}O_6$ $[M]^-$ 509.1039; Found 509.1030.

5-((3,5-bis((3-carboxyphenyl)ethynyl)phenyl)ethynyl)isophthalic acid (H_4BTEB_{mmi})

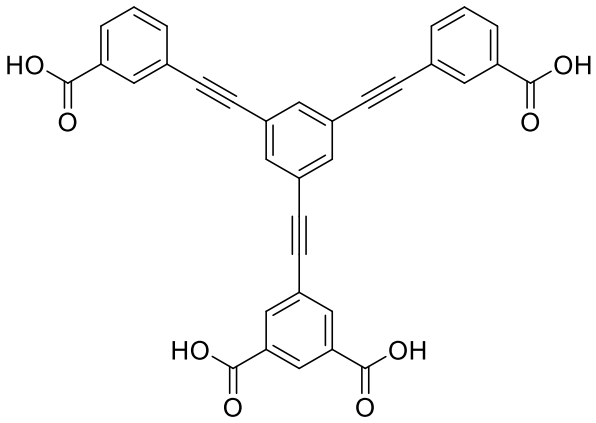

Yield: 1.23 g, 2.22 mmol, 63 %. ^{1}H NMR ($CDCl_3$, 400 MHz) δ_H (ppm): 13.41 (4H, br), 8.47 (1H, s), 8.30 (2H, s), 8.12 (2H, s), 7.99 (2H, d, J = 7.6 Hz), 7.91 (2H, s), 7.87 (1H, s), 7.82 (2H, d, J = 7.4 Hz), 7.59 (2H, t, J = 7.6 Hz). $^{13}C\{^1H\}$-NMR ($CDCl_3$, 100 MHz) δ_C (ppm): 166.9, 166.3, 136.2, 135.9, 134.9, 132.7, 132.6, 131.9, 130.7, 130.6, 130.3, 129.8, 123.9, 123.7, 123.3, 122.6, 90.4, 89.5, 89.3, 88.6. HR-MS (ESI): m/z Calculated for $C_{34}H_{17}O_8$ $[M]^-$ 554.1002; Found 554.099

4,4'-((5-((3-carboxyphenyl)ethynyl)-1,3-phenylene)bis(ethyne-2,1-diyl))dibenzoic acid (H_3BTEB_{ppm})

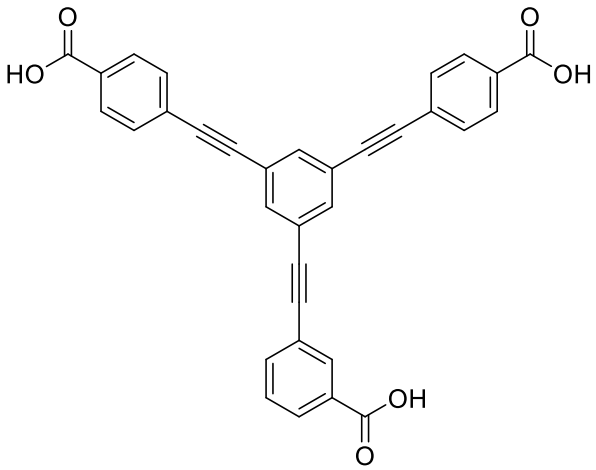

Yield: 1.98 g, 3.62 mmol, 77 %. ^{1}H NMR ($CDCl_3$, 400 MHz) δ_H (ppm): 13.23 (3H, br), 8.13 (2H, s), 8.00 (2H, d, J = 7.8 Hz), 7.89 (1H, s), 7.86 (2H, s), 7.83 (2H, d, J = 7.7 Hz), 7.71 (2H, d, J = 7.7 Hz), 7.60 (2H, t, J = 7.7 Hz). $^{13}C\{^1H\}$-NMR ($CDCl_3$, 100 MHz) δ_C (ppm):166.9, 166.4, 135.7, 134.5, 134.4, 132.8, 131.6, 130.6, 129.9, 129.5, 129.3, 128.6, 127.3, 123.9, 126.4, 123.1, 90.4, 89.8, 89.7, 88.3. HR-MS (ESI): m/z Calculated for $C_{33}H_{17}O_6$ $[M]^-$ 509.1039; Found 509.1043

5-((3,5-bis((4-carboxyphenyl)ethynyl)phenyl)ethynyl)isophthalic acid (H_4BTEB_{ppi})

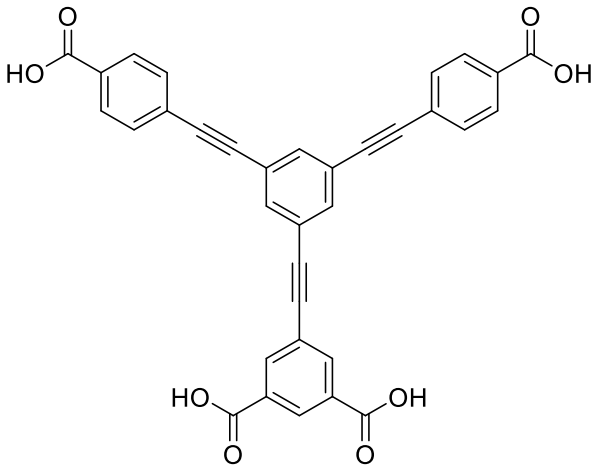

Yield: 1.31 g, 2.36 mmol, 58 %.^{1}H NMR ($CDCl_3$, 400 MHz) δ_H (ppm): 13.35 (4H, br), 8.46 (1H, s), 8.30 (2H, s), 7.99 (4H, d, J = 8.2 Hz), 7.89 (2H, s), 7.84 (1H, s), 7.70(4H, d, J = 8.2 Hz). $^{13}C\{^1H\}$-NMR ($CDCl_3$, 100 MHz) δ_C (ppm): 167.1, 166.2, 136.3, 135.0, 134.9, 132.8, 132.5, 132.2, 131.4, 130.6, 130.1, 126.4, 123.8, 123.3, 90.6, 90.3, 89.6, 89.3. HR-MS (ESI): m/z Calculated for $C_{34}H_{17}O_8$ $[M]^-$ 553.0923; Found 553.0928.

5,5'-((5-((3-carboxyphenyl)ethynyl)-1,3-phenylene)bis(ethyne-2,1-diyl))diisophthalic acid (H_5BTEB_{iim})

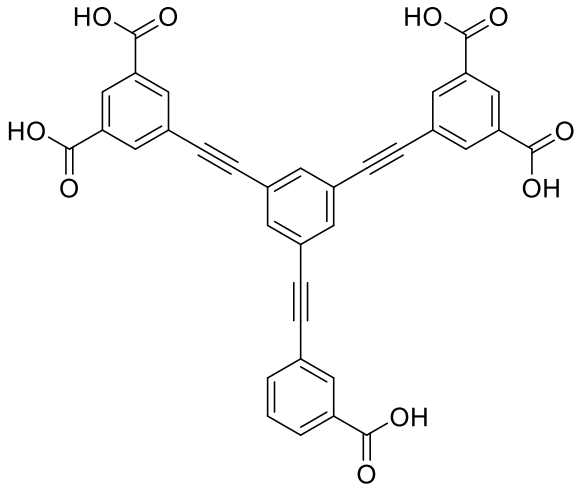

Yield: 1.65 g, 2.76 mmol, 57 %. ^{1}H NMR ($CDCl_3$, 400 MHz) δ_H (ppm): 13.49 (5H, br), 8.42 (2H, s), 8.23 (4H, s), 8.07 (1H, s), 7.95 (1H, d, J = 7.7Hz), 7.86 (1H, s), 7.82(2H, s), 7.76 (1H, d, J = 7.7 Hz), 7.53 (1H, t, J = 7.7 Hz). $^{13}C\{^1H\}$-NMR ($CDCl_3$, 100 MHz) δ_C (ppm): 166.9, 166.2, 136.2, 135.8, 134.9, 132.7, 132.5, 131.9, 130.5, 130.2, 129.6, 123.8, 123.6, 123.2, 122.6, 90.4, 89.5, 89.3, 88.5. HR-MS (ESI): m/z Calculated for $C_{35}H_{17}O_{10}$ $[M]^-$ 597.0827; Found 597.0827

5,5'-((5-((4-carboxyphenyl)ethynyl)-1,3-phenylene)bis(ethyne-2,1-diyl))diisophthalic acid (H_5BTEB_{iip})

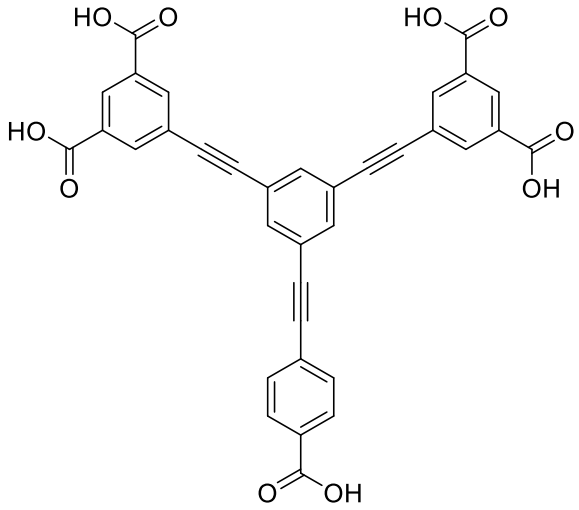

Yield: 1.17 g, 1.95 mmol, 51 %.^{1}H NMR ($CDCl_3$, 400 MHz) δ_H (ppm): 13.40 (5H, br), 8.49 (2H, s), 8.30 (4H, s), 8.00 (2H, d, J = 8.3 Hz), 7.97 (1H, s), 7.92 (2H, s), 7.71 (2H, d, J = 8.3 Hz). $^{13}C\{^1H\}$-NMR ($CDCl_3$, 100 MHz) δ_C (ppm): 167.2, 166.6, 136.1, 135.2, 135.0, 133.1, 132.2, 131.7, 130.7, 130.1, 126.4, 123.8, 123.1, 90.6, 90.3, 89.7, 89.2. HR-MS (ESI): m/z Calculated for $C_{35}H_{17}O_{10}$ $[M]^-$ 597.0827; Found 597.0820

5.3 Coordination compound synthesis

Stock solutions of all ligands (0.1 M in DMF) and metal salts (0.2 M in DMF) were made prior to synthesis to aid the preparation of multiple reaction vials with the same synthetic procedures.

$[Cu_{36}(BTEB_{mmm}NH_2)_{24}(H_2O)_{28}(DMF)_8]$ (**1**)

$H_3BTEB_{mmm}NH_2$ (50 µL, 2.63 mg, 5 µmol) and $Cu(NO_3)_2{\cdot}3H_2O$ (37.5 µL, 1.81 mg, 7.5 µmol) was added to a 1.5 mL reaction vial with DMF (1.2 mL). The vial was then agitated to ensure complete dissolution of the reaction and a uniform mixture. The mixture was heated at 85°C for 48 hours. Green crystals were obtained. The crystals were separated manually and washed with DMF. Yield: 0.2 mg, 2 % yield with respect to $H_3BTEB_{mmm}NH_2$.

$[Cu_{12}(BTEB_{mmm}NH_2)_8(H_2O)_{12}]$ (**2)**

$H_3BTEB_{mmm}NH_2$ (50 µL, 2.63 mg, 5 µmol) and $Cu(NO_3)_2{\cdot}3H_2O$ (37.5 µL, 1.81 mg, 7.5 µmol) was added to a 1.5 mL reaction vial with a DMF:EtOH (4:1 v/v, 1.2 mL). The vial was then agitated to ensure complete dissolution of the reaction and a uniform mixture. The mixture was heated at 85°C for 48 hours. Blue octahedral crystals were obtained. The crystals were separated manually and washed with DMF. Yield: 0.3 mg, 14 % yield with respect to $H_3BTEB_{mmm}NH_2$. CHN analysis of dried material with two water molecules and four DMF molecules per constitutional formula ($C_{276}H_{160}N_{12}O_{54}Cu_{12}$) calcd. C 62.89 % H 3.06 % N 3.19 %; found C 61.47 % H 2.97 % N 2.17 %

$[Cu_{36}(BTEB_{mmm}NH_2)_{24}(azpy)(DMF)_{34}]$ (**3**)

$H_3BTEB_{mmm}NH_2$ (50 µL, 2.63 mg, 5 µmol), $Cu(NO_3)_2{\cdot}3H_2O$ (37.5 µL, 1.81 mg, 7.5 µmol) and Azpy from a 0.1 M DMF stock solution (50 µL, 0.9 mg, 5 µmol) was added to a 1.5 mL reaction vial containing DMF(1.2 mL). The vial was then agitated to ensure the complete dissolution of the reagents and a uniform mixture. The mixture was heated at 85°C for 48 hours. Green crystals were obtained. The crystals were separated manually and washed with DMF. Yield: 0.15 mg, 2 % yield with respect to $H_3BTEB_{mmm}NH_2$.

$[Cu_{36}(BTEB_{mmm}NH_2)_{24}(Azpy)_6(DMF)_{30}]$ (**4**)

$H_3BTEB_{mmm}NH_2$ (50 µL, 2.63 mg, 5 µmol), $Cu(NO_3)_2{\cdot}3H_2O$ (37.5 µL, 1.81 mg, 7.5 µmol) and Azpy from a 0.1 M DMF stock solution (300 µL, 5.53 mg, 30 µmol) was added to a 1.5 mL reaction vial containing DMF(1 mL). The vial was then agitated to ensure the complete dissolution of the reagents and a uniform mixture. The mixture was heated at 85°C for 48 hours. Green cubic crystals were obtained. The crystals were separated manually and washed with DMF. Yield: 0.2 mg. 1 % yield with respect to $H_3BTEB_{mmm}NH_2$.

$[Cu_6(BTEB_{mmm}NH_2)_4(PPP)_2(Azpy)(H_2O)_2]$ (**5**)

Crystals of **2** (2 mg), and Azpy from a 0.1 M DMF stock solution (300 µL, 5.53 mg, 30 µmol) and PPP (20 µL) were added to a 1.5 mL reaction vial containing 1.2 mL of DMF. The solution was then agitated to ensure the complete dissolution of the reagents and a uniform mixture. The solution was then heated at 85 ºC for 72 hours. Green plate crystals were obtained. The crystals were separated manually and washed with DMF. Yield 0.1 mg

$[Cu_3(BTEB_{ppm})_2(DMF)(H_2O)_2]$ (**6**)

H_3BTEB_{ppm} (50 µL, 2.55 mg, 5 µmol) and $Cu(NO_3)_2{\cdot}3H_2O$ (37.5 µL, 1.81 mg, 7.5 µmol) was added to a 1.5 mL reaction vial with DMF (1.2 mL). The vial was then agitated to ensure complete dissolution of the reaction and a uniform mixture. The mixture was heated at 85°C for 48 hours. Blue square plate crystals were obtained. The crystals were separated manually and washed with DMF. Yield: 0.2 mg, , 9 % yield with respect to H_3BTEB_{ppm}.

$[Cu_3(BTEB_{ppm})_2(DMF)(H_2O)_2]$ (**7**)

H_3BTEB_{ppm} (50 µL, 2.55 mg, 5 µmol) and $Cu(NO_3)_2{\cdot}3H_2O$ (50 µL, 2.42 mg, 10 µmol) was added to a 1.5 mL reaction vial with DMF (1.2 mL). The vial was then agitated to ensure complete dissolution of the reaction and a uniform mixture. The mixture was heated at 85°C for 48 hours. Blue rhombohedral crystals were obtained. The crystals were separated manually and washed with DMF. Yield: 0.3 mg. 8 % yield with respect to H_3BTEB_{ppm}.

$[Cu_3(BTEB_{mmp})_2(H_2O)_3]$ (**8**)

H_3BTEB_{ppm} (50 µL, 2.55 mg, 5 µmol) and $Cu(NO_3)_2{\cdot}3H_2O$ (37.5 µL, 1.81 mg, 7.5 µmol) was added to a 1.5 mL reaction vial with 1 vol % HOAc in DMF (1.2 mL). The vial was then agitated to ensure complete dissolution of the reaction and a uniform mixture. The mixture was heated at 85°C for 48 hours. Blue square plate crystals were obtained. The crystals were separated manually and washed with DMF. Yield: 0.25 mg 12 % yield with respect to H_3BTEB_{mmp}. CHN analysis of dried material with one water molecule and one DMF molecule per constitutional formula ($C_{69}H_{45}O_{17}NCu_3$) calcd: C 61.36 % H 3.36 % N 1.04 %; found C 61.53 % H 3.11 % N 1.78 %

$[Cu_{0.66}Zn_{1.33}(BTEB_{ppi})(H_2O)_2]$ (**9**)

H_4BTEB_{ppi} (50 µL, 2.77 mg, 5 µmol), $Cu(NO_3)_2{\cdot}3H_2O$ (16.5 µL, 0.8 mg, 3.33 µmol) and $Zn(NO_3)_2{\cdot}6H_2O$ (33.5 µL, 1.99 mg, 6.66 µmol) was added to a 1.5 mL reaction vial with DMF (1.2 mL). The vial was then agitated to ensure complete dissolution of the reaction and a uniform mixture. The mixture was heated at 85°C for 48 hours. Pale blue crystals were obtained. The crystals were separated manually and washed with DMF. Yield: 0.35 mg, 10 % yield with respect to H_3BTEB_{ppi}.

$[Cu_2(BTEB_{ppi})(H_2O)_2]$ (**10**)

H_4BTEB_{ppi} (50 µL, 2.77 mg, 5 µmol) and $Cu(NO_3)_2{\cdot}3H_2O$ (50 µL, 2.42 mg, 10 µmol) was added to a 1.5 mL reaction vial with DMF (1.2 mL). The vial was then agitated to ensure complete dissolution of the reaction and a uniform mixture. The mixture was heated at 85°C for 48 hours. Blue microcrystals were obtained as a powder. The powder was separated, isolated and washed with DMF. Yield: 0.3 mg, 9 % yield with respect to H_3BTEB_{ppi}.

$[Cu_2(BTEB_{mmi})(H_2O)_2]$ (**11**)

H_4BTEB_{mmi}(50 µL, 2.77 mg, 5 µmol) and $Cu(NO_3)_2{\cdot}3H_2O$ (50 µL, 2.42 mg, 10 µmol) was added to a 1.5 mL reaction vial with 0.5 % HOAc in DMF (1.2 mL). The vial was then agitated to ensure complete dissolution of the reaction and a uniform mixture. The mixture was heated at 85°C for 48 hours. Blue multifaceted crystals were obtained. The crystals were separated manually and washed with DMF. Yield: 0.1 mg, 4 % yield with respect to H_3BTEB_{ppi}

$[NH_2(CH_3)_2]_6[Zn_9(BTEB_{ppi})_6]$ (**12**)

H_4BTEB_{ppi} (50 µL, 2.77 mg, 5 µmol) and $Zn(NO_3)_2 \cdot 6H_2O$ (25 µL, 1.49 mg, 5 µmol) was added to a 1.5 mL reaction vial with DMF (1.2 mL). The vial was then agitated to ensure complete dissolution of the reaction and a uniform mixture. The mixture was heated at 85°C for 72 hours. Colourless crystals were obtained. The crystals were separated manually and washed with DMF. Yield: 0.2 mg, 6 % yield with respect to H_3BTEB_{ppi}. CHN analysis of dried material with one DMF molecule and six dimethylammonium cations per constitutional formula ($C_{219}H_{145}O_{52}N_7Zn_9$) calcd. C 61.24 % H 3.40 % N 2.28 %; found C 59.92 % H 3.59 % N 2.26 %

$[Co_2(BTEB_{ppi})(DMF)_3]$ (**13**)

H_4BTEB_{ppi} (50 µL, 2.77 mg, 5 µmol) and $Co(NO_3)_2 \cdot 6H_2O$ (50 µL, 2.91 mg, 10 µmol) was added to a 1.5 mL reaction vial with DMF (1.2 mL). The vial was then agitated to ensure complete dissolution of the reaction and a uniform mixture. The mixture was heated at 85°C for 72 hours. Violet crystals were obtained. The crystals were separated manually and washed with DMF. Yield: 0.3 mg, 12 % y ield with respect to H_3BTEB_{ppi}. CHN analysis of dried material with two water molecules and one DMF molecule per constitutional formula ($C_{37}H_{23}O_{11}NCo_{12}$) calcd. C 57.31 % H 2.99 % N 1.81 %; found C 58.32 % H 3.08 % N 2.02 %

$[Zn_7(HBTEB_{iip}^{4-})_3(DEF)_7](NO_3)_2$ (**14**)

H_5BTEB_{iip} (50 µL, 2.99 mg, 5 µmol) and $Zn(OAc)_2 \cdot H_2O$ (200 µL, 8.06 mg, 40 µmol) was added to a 1.5 mL reaction vial with DEF (1.2 mL). The vial was then agitated to ensure complete dissolution of the reaction and a uniform mixture. The mixture was heated at 85°C for 48 hours. Yellow cubic crystals were obtained. The crystals were separated manually and washed with DMF. Yield: 0.15 mg, 5 % yield with respect to H_3BTEB_{iip}.

Chapter 6

Conclusion and future work

6 Conclusion and future work

In summary, synthetic procedures and single-crystal X-ray structures for several newly synthesised MOFs and MOPs are reported in this study. The compounds incorporate a number of BTEB organic linker derivatives with a diverse set of transition metal ions.

The initial focus was on the synthesis of an amino functionalised derivate of BTEB with the synthesis of 3,3',3''-((2-aminobenzene-1,3,5-triyl)tris(ethyne-2,1-diyl))tribenzoic acid. Reacting this new linker in combination with $Cu(NO_3)_2{\cdot}3H_2O$ in DMF led to the formation of the MOP $[Cu_{36}(BTEB_{mmm}NH_2)_{24}(H_2O)_{28}(DMF)_8]$ (**1**). Single crystal X-ray analysis showed that the MOP is comprised of 18 $\{Cu_2\}$ SBUs linked by $BTEB_{mmm}NH_2^{3-}$ linkers to form a cuboctahedral structure. An interesting aspect of the MOPs structure is that six $\{Cu_2\}$ SBUs form an inner octahedral structure which is then surrounded by the outer cuboctahedral shell. Through the simple modification of synthesis, with the addition of EtOH to the solution, a drastically different MOP was synthesised. The new MOP, $[Cu_{12}(BTEB_{mmm}NH_2)_8(H_2O)_{12}]$ (**2**), has the structure of an octahedron with its six $\{Cu_2\}$ SBUs linked by eight $BTEB_{mmm}NH_2^{3-}$ linkers. The structural diversity in the two MOPs arises from the rotational flexibility allowed by the acetylene spacer units on the $BTEB_{mmm}NH_2^{3-}$ linker. In the structure of **1**, the $BTEB_{mmm}NH_2^{3-}$ is found in two different conformations. In one conformation, the linker is planar, while in the second conformation, one of the benzoate moieties has a dihedral angle of 90º with respect to the central phenyl ring. In the second MOP, **2**, this perpendicular dihedral angle is applied to all *meta*-benzoate moieties. This diversity in conformations demonstrates how the conformation of the organic linkers can dramatically influence the structure and, therefore, the properties of the MOP.

Using the technique known as pillaring the newly synthesised MOPs units were then utilised as structural units in the formation of MOFs. A selection of bipyridyl ligands, with varying distances between the N-donor atoms on the pyridyl rings, were examined as pillaring ligands. Of the bipyridyl ligands examined, only the Azpy ligand was capable of pillaring the MOP units into frameworks by coordinating to the apical position on the $\{Cu_2\}$ SBUs, which make up the MOPs. By modifying the ratio of Azpy to $H_3BTEB_{mmm}NH_2$ in the reaction, the degree of pillaring could be controlled. Using an approximate 1:1 ratio of the two organic ligands the MOP **1** was pillared into the one-dimensional coordination polymer, $[Cu_{36}(BTEB_{mmm}NH_2)_{24}(azpy)(DMF)_{34}]$ (**3**). In the construction of the polymer, the Azpy ligand was found to coordinate to two $\{Cu_2\}$ SBUs located transversely to each other on the outer cuboctahedral framework. When the ratio of Azpy to $H_3BTEB_{mmm}NH_2$ was increased, the extent of the pillaring was also increased. The use of excess Azpy in the synthesis leads to the pillaring of **1** into a three-dimensional framework. In the MOFs structure, the Azpy ligand coordinates to all of the $\{Cu_2\}$ SBUs of the MOP units forming a **fcu** framework the MOPs acting as 24-connected nodes. The full structure of the MOF contained two of these frameworks in a dual-interpenetrated fashion.

We then attempted to pillar the smaller MOP, **2**, into a pillared structure using the same method as that of the previous structures. A new strategy was required for this to occur as it was quickly discovered that the EtOH required for the synthesis of **2** detrimentally impacted the pillaring reaction. The new strategy required synthesising the MOP prior to the pillaring reaction. The pillaring reaction was then done by placing crystals of the MOP at the base of the reaction vial containing the Azpy ligand in a DMF solution. To aid in bringing the MOP into solution, the ligand PPP was added to the reaction mixture. Rather than the expected pillaring of the MOP an entirely new structure was synthesised. The new structure, $[Cu_6(BTEB_{mmm}NH_2)_4(PPP)_2(Azpy)(H_2O)_2]$ (**5**), contained two-dimensional sheets of "super paddlewheel" units, which were then pillared by the Azpy ligand.

Following this work, we then moved to examine the influence of the linkers geometry on the structure of a MOF. The linkers were based upon the BTEB ligand but with various combinations of *meta*-benzoate, *para*-benzoate and isophthalate moieties. The new family of the ligands were reacted with Cu^{2+} ions due to their strong tendency to form $\{Cu_2\}$ SBUs. Keeping the structure of the inorganic SBUs consistent across the range of MOFs allows for the separation of the influence of the linkers geometry from other factors.

The first two MOFs discussed contained the H_3BTEB_{ppm} organic linker, $[Cu_3(BTEB_{ppm})_2(DMF)(H_2O)_2]$ **6** and $[Cu_3(BTEB_{ppm})_2(DMF)(H_2O)_2]$ **7**. With the two MOFs comprised of the same linker and inorganic SBU, the only origin of the structural variation is due to the linkers various conformations. **6** has the appearance of pillared two-dimensional sheets with a layered-like structure with the "pillaring" linkers originating from the *para*-benzoate moieties on one conformation rather than a second ligand like that used in **Chapter 2**. **7** has a vastly different structure with its interpenetrated two-dimensional sheets. The sheets interpenetrate and stack perpendicular to the plane of the sheets.

The linker H_3BTEB_{mmp} was found to produce a vastly different structure than that of the H_3BTEB_{ppm} with the synthesis of $[Cu_3(BTEB_{mmp})_2(H_2O)_3]$ **8**. The structure was found to be a vast array of interpenetrated two-dimensional sheets. The sheets contained the structural unit known as a "super paddlewheel, " commonly found with BTEB linkers containing two *meta*-benzoate moieties. The contrast in the structure of this MOF demonstrated how the simple change in the position of a carboxylate group from a *para* to a *meta* position leads to a dramatic alteration to the framework's structure.

With the use of H_4BTEB_{ppi} two isostructural MOFs were synthesised $[Cu_{0.66}Zn_{1.33}(BTEB_{ppi})(H_2O)_2]$ **9** and $[Cu_2(BTEB_{ppi})(H_2O)_2]$ **10**. When just Cu^{2+} ions were used to synthesise the MOF, a fine blue microcrystalline powder was produced. This material made it impossible to determine the crystal structure, so a new method was required to produce sufficient size and quality crystals for single-crystal X-ray analysis. It was found that these parameters could be controlled through the addition of Zn^{2+} ions in the reaction solution. It is believed that this control comes from a competitive binding

mechanism between the copper-carboxylate bond and zinc-carboxylate bonds, which slowed the rate of crystallisation, allowing for the gradual growth of larger crystals. The structure of **10** was then verified using powder X-ray diffraction, confirming that the two compounds are isostructural.

Again with the simple exchange of one of the moieties, the *para*-benzoates to *meta*-benzoates produce the linker H_4BTEB_{mmi}. Which, when in combination with the $\{Cu_2\}$ SBUs lead to the chiral MOF $[Cu_2(BTEB_{mmi})(H_2O)_2]$ **11**. Rather than an open porous structure like that of **9** and **10** the structure of **11** was found to be dense with small channels extending along one axis of the crystal structure. This dense structure arises from the pseudo tetrahedral geometry of the H_4BTEB_{mmi} linker. The dihedral angle between the moieties and the central phenyl imparts a chirality to the linker conformation, which imparts chirality into the framework of the MOF.

Following this work, we then studied the influence of the organic linkers symmetry on the structure and properties of the inorganic SBUs. We did this by using the newly synthesised BTEB based linkers with reduced symmetry in combination with metal ions capable of forming a wider range of structures for the inorganic SBUs. The first MOF to be discussed was $[NH_2(CH_3)_2]_6[Zn_9(BTEB_{ppi})_6]$ **12**, which was a highly complex MOF with the organic linker found in four different conformations with link two structurally different inorganic SBUs. The fascinating aspect of the MOFs structure was the two inorganic SBUs. One SBU was a mononuclear Zn^{2+} ion coordinated by four carboxylate groups in a tetrahedral coordination environment. The second SBU was a dinuclear $\{Zn_2\}$ SBU coordinated by five carboxylate groups. These two inorganic SBUs are uncommon in the literature, with the dinuclear $\{Zn_2\}$ SBU being reported only once before. To find these two uncommon SBUs within the same structure shows how the reduction of the linkers symmetry can allow access to potentially new inorganic SBUs.

Using the same organic linker in combination with Co^{2+} ions led to the formation of an entirely new framework, $[Co_2(BTEB_{ppi})(DMF)_3]$ **13**. The inorganic SBUs of the MOF were found to be dinuclear $\{Co_2\}$ SBUs coordinated by four carboxylate groups. One of the Co^{2+} ions was found to have three coordinated solvent molecules. Given that these coordinated solvent molecules, and their potential UMCs, are attractive features in MOFs used for the electrochemical water splitting reaction, a preliminary investigation of the MOFs catalytic properties.

The final MOF to be synthesised was $[Zn_7(HBTEB_{iip}^{4-})_3(DEF)_7](NO_3)_2$ (**14**). The only MOF in this body of work utilising one of the newly synthesised penta-carboxylate organic linkers, H_5BTEB_{iip}. The linker, however, was incorporated into the MOF in an unexpected manner. The linker acts as a four-connected linker with the *para*-benzoate moiety remaining uncoordinated and directed towards the pore of the MOF. This is an unusual and highly sought-after feature to have in a MOF that typically requires deprotection methods not to disrupt the synthesis of the underlying framework.

The works in this thesis A number of avenues for further research are available, building upon the work discussed in this thesis. Examples of these directions include:

- The utilisation of different functional groups used to functionalize the BTEB derivative. These different functional groups offer a large area of chemistry where the properties of the MOPs and pillared MOFs could be altered.
- With regards to the pillaring of the **1** leading to the structures of **3** and **4** only a small selection of bipyridyl based linkers have been examined so far. The range of pillaring ligand was limited to only linkers bipyridyl linkers. This could be expanded to include tri- and tetra-pyridyl based ligands. These should allow the formation of structures that would not be achievable with linear linkers.
- The new synthetic procedure for the synthesis of BTEB based linkers with reduced symmetry offers the broadest scope for further study. With the flexibility of the synthesis, a large number of moieties may be utilised in synthesising new linkers. In this work, we limited the number of moieties to three due to time constraints, with just these three moieties leading to six new linkers. The list of moieties used the synthesise the linkers could easily be expanded to accommodate other moieties, with each additional moiety used leading to a significant increase in the number of possible linkers. For a given set of moieties, the range of possible organic linkers now grows on the order of n^2 rather than n, allowing access to a far larger area of chemical space than was previously possible.
- Further work is required on the implementation of the penta-carboxylate-based linkers H_5BTEB_{iip} and H_5BTEB in combination with $\{Cu_2\}$ paddlewheel SBUs. While there have been previous reports of MOFs containing penta-carboxylate linkers with $\{Cu_2\}$ SBUs , they have also been reported as being challenging to synthesise. The lack of structures in this body of work with the new linkers may arise from the difficulty of their synthesis rather than an incompatibility between the linker and the SBU. A broader trail of reaction conditions needs to be carried out to determine which of these two possible causes is responsible for the lack of structures.
- Further developments can also be carried out by combining the new organic linkers and other transition metal ions. Like the choice of moiety for the linkers, the choice of metal ions was limited due to time constraints. A large number of metal ions remain unexamined for the synthesis of new MOFs with these BTEB based linkers with reduced symmetry with the potential for a vast array of new SBUs from which MOFs can be constructed.

In conclusion, we provide many examples of the effects of linker functionalisation and symmetry reduction in metal-organic frameworks and metal-organic polyhedra. The compounds were asses for their topology, porosity, and other physical properties using a combination of physical and computational techniques. Both methods of modifying the organic linkers were found to dramatically affect the structure and properties of the newly synthesised materials.

7 References

1 M. Lok, in *Synthesis of Solid Catalysts*, Wiley-VCH Verlag GmbH & Co. KGaA, Weinheim, Germany, 2009, pp. 135–151.

2 G. B. Kauffman and E. Ditor, *Choice Rev. Online*, 1995, **33**, 33-0324-33–0324.

3 R. Xu, W. Pang and Q. Huo, *Modern Inorganic Synthtic Chemistry*, Elsiver, 2017.

4 A. F. Cronstedt, *Kongl Vetenskaps Acad. Handl. Stock.*, 1776, 120.

5 C. Colella and A. F. Gualtieri, *Microporous Mesoporous Mater.*, 2007, **105**, 213–221.

6 R. L. Virta, Mineral resource of the month: natural and synthetic zeolites, http://www.geotimes.org/june08/article.html?id=nn_zeolites.html.

7 M. Pérez-Page, J. Makel, K. Guan, S. Zhang, J. Tringe, R. H. R. Castro and P. Stroeve, *Ceram. Int.*, 2016, **42**, 15423–15431.

8 A. V. Chadwick and J. N. Sherwood, in *Point Defects in Solids*, Springer US, Boston, MA, 1975, vol. 85, pp. 441–475.

9 N. L. Rosi, J. Eckert, M. Eddaoudi, D. T. Vodak, J. Kim, M. O'Keeffe and O. M. Yaghi, *Science (80-.).*, 2003, **300**, 1127–1129.

10 I. Huskić, I. V. Pekov, S. V. Krivovichev and T. Friščić, *Sci. Adv.*, 2016, **2**, 1–8.

11 B. F. Hoskins and R. Robson, *J. Am. Chem. Soc.*, 1989, **111**, 5962–5964.

12 S. J. Maginn, *J. Appl. Crystallogr.*, 1991, **24**, 265–265.

13 F. Containing and L. Rectangular, 1995, 10401–10402.

14 L. R. MacGillivray, S. Subramanian and M. J. Zaworotko, *J. Chem. Soc. Chem. Commun.*, 1994, 1325–1326.

15 G. M. J. Schmidt, *Pure Appl. Chem.*, 1971, **27**, 647–678.

16 A. I. Kitaigorodsky, *Chem. Soc. Rev.*, 1978, **7**, 133.

17 O. M. Yaghi, M. O'Keeffe, N. W. Ockwig, H. K. Chae, M. Eddaoudi and J. Kim, *Nature*, 2003, **423**, 705–714.

18 A. Schoedel, M. Li, D. Li, M. O'Keeffe and O. M. Yaghi, *Chem. Rev.*, 2016, **116**, 12466–12535.

19 L. K. Macreadie, E. J. Mensforth, R. Babarao, K. Konstas, S. G. Telfer, C. M. Doherty, J. Tsanaktsidis, S. R. Batten and M. R. Hill, *J. Am. Chem. Soc.*, 2019, **141**, 3828–3832.

20 B. Chen, N. W. Ockwig, F. R. Fronczek, D. S. Contreras and O. M. Yaghi, *Inorg. Chem.*, 2005, **44**, 181–183.

21 L. Zhai, Z.-X. Yang, W.-W. Zhang, J.-L. Zuo and X.-M. Ren, *Inorg. Chem.*, 2018, **57**, 4171–4180.

22 Y. Wang, L. Feng, W. Fan, K.-Y. Y. Wang, X. Wang, X. Wang, K. Zhang, X. Zhang, F. Dai, D. Sun and H.-C. C. Zhou, *J. Am. Chem. Soc.*, 2019, **141**, 6967–6975.

23 W. Zhou, Y.-P. Wu, Z.-H. Zhou, Z.-S. Qin, X. Ye, F.-Y. Tian and D.-S. Li, *Inorganica Chim. Acta*, 2016, **453**, 757–763.

24 J. Andreo, E. Priola, G. Alberto, P. Benzi, D. Marabello, D. M. Proserpio, C. Lamberti and E. Diana, *J. Am. Chem. Soc.*, 2018, **140**, 14144–14149.

25 E. A. Dolgopolova, A. M. Rice and N. B. Shustova, *Chem. Commun.*, 2018, **54**, 6472–6483.

26 M. Servati Gargari, V. Stilinovic, A. Bauzá, A. Frontera, P. McArdle, D. Van Derveer, S. W. Ng and G. Mahmoudi, *Chem. - A Eur. J.*, 2015, **21**, 17951–17958.

27 F. Li, G. H. Gu, C. Choi, P. Kolla, S. Hong, T. S. Wu, Y. L. Soo, J. Masa, S. Mukerjee, Y. Jung, J. Qiu and Z. Sun, *Appl. Catal. B Environ.*, 2020, **277**, 119241.

28 M. Whitehead, S. Turega, A. Stephenson, C. A. Hunter and M. D. Ward, *Chem. Sci.*, 2013, **4**, 2744–2751.

29 L. Pesce, C. Perego, A. B. Grommet, R. Klajn and G. M. Pavan, *J. Am. Chem. Soc.*, 2020, **142**, 9792–9802.

30 M. Yoshizawa and M. Fujita, *Pure Appl. Chem.*, 2005, **77**, 1107–1112.

31 W. Liu and J. F. Stoddart, *Chem*, 2021, **7**, 919–947.

32 S. Zarra, D. M. Wood, D. A. Roberts and J. R. Nitschke, *Chem. Soc. Rev.*, 2015, **44**, 419–432.

33 J. H. Jordan and B. C. Gibb, *Chem. Soc. Rev.*, 2015, **44**, 547–585.

34 I. A. Bhat, D. Samanta and P. S. Mukherjee, *J. Am. Chem. Soc.*, 2015, **137**, 9497–9502.

35 K. Mohomed, H. Abourahma, M. J. Zaworotko and J. P. Harmon, *Chem. Commun.*, 2005, **2**, 3277–3279.

36 J. J. Perry, J. A. Perman and M. J. Zaworotko, *Chem. Soc. Rev.*, 2009, **38**, 1400–1417.

37 C. A. Rowland, G. R. Lorzing, E. J. Gosselin, B. A. Trump, G. P. A. Yap, C. M. Brown and E. D. Bloch, *J. Am. Chem. Soc.*, 2018, **140**, 11153–11157.

38 G. A. Taggart, A. M. Antonio, G. R. Lorzing, G. R. Lorzing, G. P. A. Yap, E. D. Bloch and E. D. Bloch, *ACS Appl. Mater. Interfaces*, 2020, **12**, 24913–24919.

39 K. Byrne, M. Zubair, N. Zhu, X. P. Zhou, D. S. Fox, H. Zhang, B. Twamley, M. J. Lennox, T. Düren and W. Schmitt, *Nat. Commun.*, 2017, **8**, 1–9.

40 X. Yan, T. R. Cook, P. Wang, F. Huang and P. J. Stang, *Nat. Chem.*, 2015, **7**, 342–348.

41 Q. Q. Wang, S. Gonell, S. H. A. M. Leenders, M. Dürr, I. Ivanovic-Burmazovic and J. N. H. Reek, *Nat. Chem.*, 2016, **8**, 225–230.

42 W. Cullen, M. C. Misuraca, C. A. Hunter, N. H. Williams and M. D. Ward, *Nat. Chem.*, 2016, **8**, 231–236.

43 D. J. Tranchemontagne, Z. Ni, M. O'Keeffe and O. M. Yaghi, *Angew. Chemie - Int. Ed.*, 2008, **47**, 5136–5147.

44 K. M. Fromm, *Coord. Chem. Rev.*, 2008, **252**, 856–885.

45 I. M. Hauptvogel, V. Bon, R. Grünker, I. A. Baburin, I. Senkovska, U. Mueller and S. Kaskel, *Dalt. Trans.*, 2012, **41**, 4172–4179.

46 S. Takaishi, M. Hosoda, T. Kajiwara, H. Miyasaka, M. Yamashita, Y. Nakanishi, Y. Kitagawa, K. Yamaguchi, A. Kobayashi and H. Kitagawa, *Inorg. Chem.*, 2009, **48**, 9048–9050.

47 S. Seth and A. J. Matzger, *Cryst. Growth Des.*, 2017, **17**, 4043–4048.

48 T. Kitao, Y. Tokunaga, D. Umeyama, C. R. Kim, T. Uemura and S. Kitagawa, *Inorganica Chim. Acta*, 2015, **424**, 221–225.

49 M. Zhang, Y. P. Chen and H. C. Zhou, *CrystEngComm*, 2013, **15**, 9544–9552.

50 J. Martí-Rujas, N. Islam, D. Hashizume, F. Izumi, M. Fujita and M. Kawano, *J. Am. Chem. Soc.*, 2011, **133**, 5853–5860.

51 K. Ohara, M. Kawano, Y. Inokuma and M. Fujita, *J. Am. Chem. Soc.*, 2010, **132**, 30–31.

52 J. K. Schnobrich, K. Koh, K. N. Sura and A. J. Matzger, *Langmuir*, 2010, **26**, 5808–5814.

53 S. R. Caskey and A. J. Matzger, *Inorg. Chem.*, 2008, **47**, 7942–7944.

54 D. Kühne, F. Klappenberger, R. Decker, U. Schlickum, H. Brune, S. Klyatskaya, M. Ruben and J. V. Barth, *J. Am. Chem. Soc.*, 2009, **131**, 3881–3883.

55 T. Lin, G. Kuang, X. S. Shang, P. N. Liu and N. Lin, *Chem. Commun.*, 2014, **50**, 15327–15329.

56 S. Laokroekkiat, M. Hara, S. Nagano and Y. Nagao, *Langmuir*, 2016, **32**, 6648–6655.

57 A. F. Wells, *Three-dimensional nets and polyhedra*, New York, 1977.

58 A. F. Wells, *Three Dimensional Nets and Polyhedra*, Wiley, 1977.

59 G. Férey, *J. Solid State Chem.*, 2000, **152**, 37–48.

60 M. O'Keeffe, M. Eddaoudi, H. Li, T. Reineke and O. M. Yaghi, *J. Solid State Chem.*, 2000, **152**, 3–20.

61 M. O. Keeffe, M. a Peskov, S. J. Ramsden and O. M. Yaghi, *Acc. Chem. Res.*, 2008, **41**, 1782–1789.

62 M. Li, D. Li, M. O'Keeffe and O. M. Yaghi, *Chem. Rev.*, 2014, **114**, 1343–1370.

63 M. J. Kalmutzki, N. Hanikel and O. M. Yaghi, *Sci. Adv.*, 2018, **4**, 1–16.

64 Q.-F. Sun, J. Iwasa, D. Ogawa, Y. Ishido, S. Sato, T. Ozeki, Y. Sei, K. Yamaguchi and M. Fujita, *Science (80-.).*, 2010, **328**, 1144–1147.

65 N. Kamiya, M. Tominaga, S. Sato and M. Fujita, *J. Am. Chem. Soc.*, 2007, **129**, 3816–3817.

66 S. Lee, H. Jeong, D. Nam, M. S. Lah and W. Choe, *Chem. Soc. Rev.*, 2021, **50**, 528–555.

67 O. M. Yaghi, M. O'Keeffe, N. W. Ockwig, H. K. Chae, M. Eddaoudi and J. Kim, *Nature*, 2003, **423**, 705–714.

68 H. H. Wenk and W. Sander, *Eur. J. Org. Chem*, 2002, 3927–3935.

69 M. Eddaoudi, J. Kim, N. Rosi, D. Vodak, J. Wachter, M. O'Keeffe and O. M. Yaghi, *Science (80-.).*, 2002, **295**, 469–472.

70 H. Furukawa, M. A. Miller and O. M. Yaghi, *J. Mater. Chem.*, 2007, **17**, 3197–3204.

71 H. Furukawa, N. Ko, Y. B. Go, N. Aratani, S. B. Choi, E. Choi, A. Ö. Yazaydin, R. Q. Snurr, M. O'Keeffe, J. Kim and O. M. Yaghi, *Science (80-.).*, 2010, **329**, 424–428.

72 N. J. Young and B. P. Hay, *Chem. Commun.*, 2013, **49**, 1354–1379.

73 M. Zhang, M. Bosch, T. Gentle and H. C. Zhou, *CrystEngComm*, 2014, **16**, 4069–4083.

74 H. Deng, C. J. Doonan, H. Furukawa, R. B. Ferreira, J. Towne, C. B. Knobler, B. Wang and O. M. Yaghi, *Science (80-.).*, 2010, **327**, 846–850.

75 S. Marx, W. Kleist, J. Huang, M. Maciejewski and A. Baiker, *Dalt. Trans.*, 2010, **39**, 3795.

76 J. F. Eubank, F. Nouar, R. Luebke, A. J. Cairns, L. Wojtas, M. Alkordi, T. Bousquet, M. R. Hight, J. Eckert, J. P. Embs, P. A. Georgiev and M. Eddaoudi, *Angew. Chemie*, 2012, **124**, 10246–10250.

77 Y. Goto, H. Sato, S. Shinkai and K. Sada, *J. Am. Chem. Soc.*, 2008, **130**, 14354–14355.

78 E. D. Bloch, D. Britt, C. Lee, C. J. Doonan, F. J. Uribe-Romo, H. Furukawa, J. R. Long and O. M. Yaghi, *J. Am. Chem. Soc.*, 2010, **132**, 14382–14384.

79 T. Yamada and H. Kitagawa, *J. Am. Chem. Soc.*, 2009, **131**, 6312–6313.

80 K. M. L. Taylor-Pashow, J. Della Rocca, Z. Xie, S. Tran and W. Lin, *J. Am. Chem. Soc.*, 2009, **131**, 14261–14263.

81 S. Yuan, Y. P. Chen, J. S. Qin, W. Lu, L. Zou, Q. Zhang, X. Wang, X. Sun and H. C. Zhou, *J. Am. Chem. Soc.*, 2016, **138**, 8912–8919.

82 Y. Han, J. R. Li, Y. Xie and G. Guo, *Chem. Soc. Rev.*, 2014, **43**, 5952–5981.

83 K. P. Rao, M. Higuchi, J. Suryachandram and S. Kitagawa, *J. Am. Chem. Soc.*, 2018, **140**, 13786–13792.

84 D. Sun, W. Liu, M. Qiu, Y. Zhang and Z. Li, *Chem. Commun.*, 2015, **51**, 2056–2059.

85 M. Lalonde, W. Bury, O. Karagiaridi, Z. Brown, J. T. Hupp and O. K. Farha, *J. Mater. Chem. A*, 2013, **1**, 5453–5468.

86 Y. Noori and K. Akhbari, *RSC Adv.*, 2017, **7**, 1782–1808.

87 C. K. Brozek and M. Dincă, *Chem. Soc. Rev.*, 2014, **43**, 5456–5467.

88 B. Tu, Q. Pang, D. Wu, Y. Song, L. Weng and Q. Li, *J. Am. Chem. Soc.*, 2014, **136**, 14465–14471.

89 K. Harris, D. Fujita and M. Fujita, *Chem. Commun.*, 2013, **49**, 6703.

90 M. Tominaga, K. Suzuki, T. Murase and M. Fujita, *J. Am. Chem. Soc.*, 2005, **127**, 11950–11951.

91 N. Kamiya, M. Tominaga, S. Sato and M. Fujita, 2007, 3816–3817.

92 M. Ikemi, T. Kikuchi, S. Matsumura, K. Shiba, S. Sato and M. Fujita, *Chem. Sci.*, 2010, **1**, 68.

93 T. Kikuchi, S. Sato and M. Fujita, *J. Am. Chem. Soc.*, 2010, **132**, 15930–15932.

94 M. Tominaga, K. Suzuki, T. Murase and M. Fujita, *J. Am. Chem. Soc.*, 2005, **127**, 11950–11951.

95 Z. Ni and R. I. Masel, *J. Am. Chem. Soc.*, 2006, **128**, 12394–12395.

96 J. Klinowski, F. A. Almeida Paz, P. Silva and J. Rocha, *Dalt. Trans.*, 2011, **40**, 321–330.

97 G. H. Albuquerque and G. S. Herman, *Cryst. Growth Des.*, 2017, **17**, 156–162.

98 A. Pichon and S. L. James, *CrystEngComm*, 2008, **10**, 1839–1847.

99 M. Klimakow, P. Klobes, A. F. Thünemann, K. Rademann and F. Emmerling, *Chem. Mater.*, 2010, **22**, 5216–5221.

100 W. J. Son, J. Kim, J. Kim and W. S. Ahn, *Chem. Commun.*, 2008, 6336–6338.

101 M. Bigdeli and A. Morsali, *Ultrason. Sonochem.*, 2015, **27**, 416–422.

102 M. Li and M. Dincă, *J. Am. Chem. Soc.*, 2011, **133**, 12926–12929.

103 N. Campagnol, T. R. C. Van Assche, M. Li, L. Stappers, M. Dinca, J. F. M. Denayer, K. Binnemans, D. E. De Vos and J. Fransaer, *J. Mater. Chem. A*, 2016, **4**, 3914–3925.

104 A. Martinez Joaristi, J. Juan-Alcañiz, P. Serra-Crespo, F. Kapteijn and J. Gascon, *Cryst. Growth Des.*, 2012, **12**, 3489–3498.

105 M. Li and M. Dincə, *Chem. Mater.*, 2015, **27**, 3203–3206.

106 W. Wu, G. E. Decker, A. E. Weaver, A. I. Arnoff, E. D. Bloch and J. Rosenthal, *ACS Cent. Sci.*, 2021, **7**, 1427–1433.

107 Y. Wei, S. Han, D. A. Walker, P. E. Fuller and B. A. Grzybowski, *Angew. Chemie - Int. Ed.*, 2012, **51**, 7435–7439.

108 N. Stock and S. Biswas, *Chem. Rev.*, 2012, **112**, 933–969.

109 A. Rabenau, *Angew. Chemie Int. Ed. English*, 1985, **24**, 1026–1040.

110 R. I. Walton, *Chem. Soc. Rev.*, 2002, **31**, 230–238.

111 S. M. Moosavi, A. Chidambaram, L. Talirz, M. Haranczyk, K. C. Stylianou and B. Smit, *Nat. Commun.*, 2019, **10**, 1–7.

112 D. P. Tabor, L. M. Roch, S. K. Saikin, C. Kreisbeck, D. Sheberla, J. H. Montoya, S. Dwaraknath, M. Aykol, C. Ortiz, H. Tribukait, C. Amador-Bedolla, C. J. Brabec, B. Maruyama, K. A. Persson and A. Aspuru-Guzik, *Nat. Rev. Mater.*, 2018, **3**, 5–20.

113 O. Kwon, J. Y. Kim, S. Park, J. H. Lee, J. Ha, H. Park, H. R. Moon and J. Kim, *Nat. Commun.*, 2019, **10**, 1–8.

114 G. Avci, I. Erucar and S. Keskin, *ACS Appl. Mater. Interfaces*, 2020, **12**, 41567–41579.

115 R. Anderson and D. A. Gómez-Gualdrón, *Chem. Mater.*, 2020, **32**, 1–16.

116 Y. G. Chung, E. Haldoupis, B. J. Bucior, M. Haranczyk, S. Lee, H. Zhang, K. D. Vogiatzis, M. Milisavljevic, S. Ling, J. S. Camp, B. Slater, J. I. Siepmann, D. S. Sholl and R. Q. Snurr, *J. Chem. Eng. Data*, 2019, **64**, 5985–5998.

117 C. Duan, Y. Yu, J. Xiao, X. Zhang, L. Li, P. Yang, J. Wu and H. Xi, *Sci. China Mater.*, 2020, **63**, 667–685.

118 S. Waitschat, H. Reinsch and N. Stock, *Chem. Commun.*, 2016, **52**, 12698–12701.

119 M. Sánchez-Sánchez, N. Getachew, K. Díaz, M. Díaz-García, Y. Chebude and I. Díaz, *Green Chem.*, 2015, **17**, 1500–1509.

120 X. Feng, T. Wu and M. A. Carreon, *J. Cryst. Growth*, 2016, **455**, 152–156.

121 A. Kojtari and H. F. Ji, *Nanomaterials*, 2015, **5**, 565–576.

122 D. Banerjee, J. Finkelstein, A. Smirnov, P. M. Forster, L. A. Borkowski, S. J. Teat and J. B. Parise, *Cryst. Growth Des.*, 2011, **11**, 2572–2579.

123 S. Soni, P. Kumar Bajpai and C. Arora, *Charact. Appl. Nanomater.*, 2020, **3**, 87–106.

124 D. Saha, R. Zacharia, L. Lafi, D. Cossement and R. Chahine, *Chem. Eng. J.*, 2011, **171**, 517–525.

125 A. G. Slater and A. I. Cooper, *Science (80-.).*, 2015, **348**, 988.

126 B. Li, H. Wen, W. Zhou and B. Chen, *J. Phys. Chem. Lett.*, 2014, **5**, 3468–3479.

127 R. J. Kuppler, D. J. Timmons, Q. R. Fang, J. R. Li, T. A. Makal, M. D. Young, D. Yuan, D. Zhao, W. Zhuang and H. C. Zhou, *Coord. Chem. Rev.*, 2009, **253**, 3042–3066.

128 A. W. C. van den Berg and C. O. Areán, *Chem. Commun.*, 2008, 668–681.

129 P. P. Edwards, V. L. Kuznetsov, W. I. F. David and N. P. Brandon, *Energy Policy*, 2008, **36**, 4356–4362.

130 S. Satyapal, J. Petrovic, C. Read, G. Thomas and G. Ordaz, *Catal. Today*, 2007, **120**, 246–256.

131 H.-L. Jiang, B. Liu, Y.-Q. Lan, K. Kuratani, T. Akita, H. Shioyama, F. Zong and Q. Xu, *J. Am. Chem. Soc.*, 2011, **133**, 11854–11857.

132 A. Schoedel, Z. Ji and O. M. Yaghi, *Nat. Energy*, 2016, **1**, 16034.

133 H. W. Langmi, J. Ren, B. North, M. Mathe and D. Bessarabov, *Electrochim. Acta*, 2014, **128**, 368–392.

134 M. Dincă and J. R. Long, *Angew. Chemie - Int. Ed.*, 2008, **47**, 6766–6779.

135 X. Zhao, B. Xiao, A. J. Fletcher, K. M. Thomas, D. Bradshaw and M. J. Rosseinsky, *Science (80-.).*, 2004, **306**, 1012–1015.

136 C. Yang, X. Wang and M. A. Omary, *J. Am. Chem. Soc.*, 2007, **129**, 15454–15455.

137 L. Wang and R. T. Yang, *Energy Environ. Sci.*, 2008, **1**, 268–279.

138 D. Saha, Z. Wei and S. Deng, *Int. J. Hydrogen Energy*, 2008, **33**, 7479–7488.

139 A. U. Czaja, N. Trukhan and U. Müller, *Chem. Soc. Rev.*, 2009, **38**, 1284–1293.

140 J. R. Long, *2015 DoE Hydrog. Fuel Cells Progr. Rev.*

141 S. K. Bhatia and A. L. Myers, *Langmuir*, 2006, **22**, 1688–1700.

142 A. Goeppert, M. Czaun, G. K. Surya Prakash and G. A. Olah, *Energy Environ. Sci.*, 2012, **5**, 7833–7853.

143 A. L. Kohl and R. Nielsen, *Gas Purfication*, Elsevier, 5th edn., 1997.

144 S. M. Melnikov and M. Stein, *Phys. Chem. Chem. Phys.*, 2019, **21**, 18386–18392.

145 C.-H. Yu, H.-H. Cheng and C.-S. Tan, *Int. J. Greenh. Gas Control*, 2012, **9**, 136–147.

146 A. Sánchez-Bautista, E. M. Palmero, A. J. Moya, D. Gómez-Díaz and M. D. La Rubia, *Sustainability*, 2021, **13**, 4011.

147 S. J. Han, M. Yoo, D. W. Kim and J. H. Wee, *Energy and Fuels*, 2011, **25**, 3825–3834.

148 F. Zeman, *Environ. Sci. Technol.*, 2014, **48**, 11730–11735.

149 F. Zeman, *Environ. Sci. Technol.*, 2007, **41**, 7558–7563.

150 R. V. Siriwardane, M. S. Shen, E. P. Fisher and J. A. Poston, *Energy and Fuels*, 2001, **15**, 279–284.

151 R. V. Siriwardane, M. S. Shen, E. P. Fisher and J. Losch, *Energy and Fuels*, 2005, **19**, 1153–1159.

152 D. Cazorla-Amorós, J. Alcaniz-Monge and A. Linares-Solano, *Langmuir*, 1996, **12**, 2820–2824.

153 W. Quan, X. Jiang, X. Wang and C. Song, *ACS Sustain. Chem. Eng.*, 2020, **8**, 9998–10008.

154 M. Karimi, J. A. C. Silva, C. N. D. P. Gonçalves, J. L. Diaz De Tuesta, A. E. Rodrigues and H. T. Gomes, *Ind. Eng. Chem. Res.*, 2018, **57**, 11154–11166.

155 A. Gholidoust, J. D. Atkinson and Z. Hashisho, *Energy and Fuels*, 2017, **31**, 1756–1763.

156 A. Zhao, A. Samanta, P. Sarkar and R. Gupta, *Ind. Eng. Chem. Res.*, 2013, **52**, 6480–6491.

157 D. J. Fauth, M. L. Gray, H. W. Pennline, H. M. Krutka, S. Sjostrom and A. M. Ault, *Energy and Fuels*, 2012, **26**, 2483–2496.

158 A. D. BUCKINGHAM and R. L. DISCH, *Opt. Electr. Magn. Prop. Mol.*, 1997, 81–95.

159 A. F. Ismail, K. C. Khulbe and T. Matsuura, *Gas separation membranes: Polymeric and inorganic*, 2015.

160 P. L. Llewellyn, S. Bourrelly, C. Serre, A. Vimont, M. Daturi, L. Hamon, G. De Weireld, J. Chang, D. Hong, Y. K. Hwang and S. H. Jhung, 2008, 7245–7250.

161 L. C. Lin, J. Kim, X. Kong, E. Scott, T. M. McDonald, J. R. Long, J. A. Reimer and B. Smit, *Angew. Chemie - Int. Ed.*, 2013, **52**, 4410–4413.

162 Z. R. Herm, R. Krishna and J. R. Long, *Microporous Mesoporous Mater.*, 2012, **151**, 481–487.

163 X. Kong, E. Scott, W. Ding, J. A. Mason, J. R. Long and J. A. Reimer, *J. Am. Chem. Soc.*, 2012, **134**, 14341–14344.

164 A. R. Millward and O. M. Yaghi, *J. Am. Chem. Soc.*, 2005, **127**, 17998–17999.

165 O. M. Yaghi, *ReVision*, 2008, 939–943.

166 B. Wang, A. P. Côté, H. Furukawa, M. O'Keeffe and O. M. Yaghi, *Nature*, 2008, **453**, 207–211.

167 Y. S. Bae, B. G. Hauser, O. K. Farha, J. T. Hupp and R. Q. Snurr, *Microporous Mesoporous Mater.*, 2011, **141**, 231–235.

168 P. L. Llewellyn, S. Bourrelly, C. Vagner, N. Heymans, H. Leclerc, A. Ghoufi, P. Bazin, A. Vimont, M. Daturi, T. Devic, C. Serre, G. De Weireld and G. Maurin, *J. Phys. Chem. C*, 2013, **117**, 962–970.

169 P. Nugent, V. Rhodus, T. Pham, B. Tudor, K. Forrest, L. Wojtas, B. Space and M. Zaworotko, *Chem. Commun.*, 2013, **49**, 1606–1608.

170 S. Subramanian and M. J. Zaworotko, *Angew. Chemie Int. Ed. English*, 1995, **34**, 2127–2129.

171 P. Nugent, E. G. Giannopoulou, S. D. Burd, O. Elemento, E. G. Giannopoulou, K. Forrest, T. Pham, S. Ma, B. Space, L. Wojtas, M. Eddaoudi and M. J. Zaworotko, *Nature*, 2013, **495**, 80–84.

172 S. Xiang, Y. He, Z. Zhang, H. Wu, W. Zhou, R. Krishna and B. Chen, *Nat. Commun.*, 2012, **3**, 954.

173 J. R. Li, J. Yu, W. Lu, L. B. Sun, J. Sculley, P. B. Balbuena and H. C. Zhou, *Nat. Commun.*, 2013, **4**, 1–8.

174 T. M. McDonald, W. R. Lee, J. A. Mason, B. M. Wiers, C. S. Hong and J. R. Long, *J. Am. Chem. Soc.*, 2012, **134**, 7056–7065.

175 P. J. Milner, R. L. Siegelman, A. C. Forse, M. I. Gonzalez, T. Runčevski, J. D. Martell, J. A. Reimer and J. R. Long, *J. Am. Chem. Soc.*, 2017, **139**, 13541–13553.

176 R. W. Flaig, T. M. Osborn Popp, A. M. Fracaroli, E. A. Kapustin, M. J. Kalmutzki, R. M. Altamimi, F. Fathieh, J. A. Reimer and O. M. Yaghi, *J. Am. Chem. Soc.*, 2017, **139**, 12125–12128.

177 A. P. Gómora-Figueroa, J. A. Mason, M. I. Gonzalez, E. D. Bloch and K. R. Meihaus, *Inorg. Chem.*, 2017, **56**, 4308–4316.

178 K. Sumida, S. Horike, S. S. Kaye, Z. R. Herm, W. L. Queen, C. M. Brown, F. Grandjean, G. J. Long, A. Dailly and J. R. Long, *Chem. Sci.*, 2010, **1**, 184–191.

179 X. J. Wang, P. Z. Li, Y. Chen, Q. Zhang, H. Zhang, X. X. Chan, R. Ganguly, Y. Li, J. Jiang and Y. Zhao, *Sci. Rep.*, 2013, **3**, 1–5.

180 M. Sun, S. Yan, Y. Sun, X. Yang, Z. Guo, J. Du, D. Chen, P. Chen and H. Xing, *Dalt. Trans.*, 2018, **47**, 909–915.

181 X. J. Wang, J. Li, P. Z. Li, L. B. Xing, H. Lu, H. Wu, Y. Shi, R. Zou and Y. Zhao, *Inorg. Chem. Commun.*, 2014, **46**, 13–16.

182 R. A. Peralta, B. Alcántar-Vázquez, M. Sánchez-Serratos, E. González-Zamora and I. A. Ibarra, *Inorg. Chem. Front.*, 2015, **2**, 898–903.

183 C. A. Trickett, A. Helal, B. A. Al-Maythalony, Z. H. Yamani, K. E. Cordova and O. M. Yaghi, *Nat. Rev. Mater.*, 2017, **2**, 1–16.

184 Y. Zhou, Ed., *Eco- and Renewable Energy Materials*, Springer Berlin Heidelberg, Berlin, Heidelberg, 2013.

185 J. Liu, Y. Wang, A. I. Benin, P. Jakubczak, R. R. Willis and M. D. LeVan, *Langmuir*, 2010, **26**, 14301–14307.

186 A. Masala, J. G. Vitillo, G. Mondino, C. A. Grande, R. Blom, M. Manzoli, M. Marshall and S. Bordiga, *ACS Appl. Mater. Interfaces*, 2017, **9**, 455–463.

187 T. Y. Zhou, B. Auer, S. J. Lee and S. G. Telfer, *J. Am. Chem. Soc.*, 2019, **141**, 1577–1582.

188 X. Li, J. Wu, C. He, Q. Meng and C. Duan, *Small*, 2019, **15**, 1–26.

189 R. Limvorapitux, H. Chen, M. L. Mendonca, M. Liu, R. Q. Snurr and S. T. Nguyen, *Catal. Sci. Technol.*, 2019, **9**, 327–335.

190 J. Ye, L. Gagliardi, C. J. Cramer and D. G. Truhlar, *J. Catal.*, 2018, **360**, 160–167.

191 G. J. Chen, C. Q. Chen, X. T. Li, H. C. Ma and Y. Bin Dong, *Chem. Commun.*, 2018, **54**,

11550–11553.

192 G. Bauer, D. Ongari, X. Xu, D. Tiana, B. Smit and M. Ranocchiari, *J. Am. Chem. Soc.*, 2017, **139**, 18166–18169.

193 L. T. M. Hoang, L. H. Ngo, H. L. Nguyen, H. T. H. Nguyen, C. K. Nguyen, B. T. Nguyen, Q. T. Ton, H. K. D. Nguyen, K. E. Cordova and T. Truong, *Chem. Commun.*, 2015, **51**, 17132–17135.

194 J. Pang, S. Yuan, D. Du, C. Lollar, L. Zhang, M. Wu, D. Yuan, H.-C. Zhou and M. Hong, *Angew. Chemie*, 2017, **129**, 14814–14818.

195 Y. Ueda, H. Ito, D. Fujita and M. Fujita, *J. Am. Chem. Soc.*, 2017, **139**, 6090–6093.

196 W. Lu, D. Yuan, A. Yakovenko and H.-C. Zhou, *Chem. Commun.*, 2011, **47**, 4968–4970.

197 L. Hamidipour and F. Farzaneh, *React. Kinet. Mech. Catal.*, 2013, **109**, 67–75.

198 M. Tonigold, Y. Tu, B. Bredenkötter, B. Rieger, S. Bahnmüller, J. Hitzbleck, G. Langstein and D. Volkmer, *Angew. Chemie - Int. Ed.*, 2009, **48**, 7546–7550.

199 H. G. T. Nguyen, N. M. Schweitzer, C. Y. Chang, T. L. Drake, M. C. So, P. C. Stair, O. K. Farha, J. T. Hupp and S. T. Nguyen, *ACS Catal.*, 2014, **4**, 2496–2500.

200 Z. Li, A. W. Peters, V. Bernales, M. A. Ortuño, N. M. Schweitzer, M. R. Destefano, L. C. Gallington, A. E. Platero-Prats, K. W. Chapman, C. J. Cramer, L. Gagliardi, J. T. Hupp and O. K. Farha, *ACS Cent. Sci.*, 2017, **3**, 31–38.

201 N. Van Velthoven, S. Waitschat, S. M. Chavan, P. Liu, S. Smolders, J. Vercammen, B. Bueken, S. Bals, K. P. Lillerud, N. Stock and D. E. De Vos, *Chem. Sci.*, 2019, **10**, 3616–3622.

202 G. V. Research, *Global Hydrogen Generation Market Size, Share & Trends Analysis Report by Systems Type (Merchant, Captive), by Technology (Steam Methane Reforming, Coal Gasification), by Application, by Region, and Segment Forecasts, 2021-2028*, Grand View Research.

203 W. A. A. Arafa, M. D. Kärkäs, B. L. Lee, T. Åkermark, R. Z. Liao, H. M. Berends, J. Messinger, P. E. M. Siegbahn and B. Åkermark, *Phys. Chem. Chem. Phys.*, 2014, **16**, 11950–11964.

204 M. Blasco-Ahicart, J. Soriano-Lopez, J. J. Carbo, J. M. Poblet and J. R. Galan-Mascaros, *Nat. Chem.*, 2018, **10**, 24–30.

205 J. Soriano-López, D. G. Musaev, C. L. Hill, J. R. Galán-Mascarós, J. J. Carbó and J. M. Poblet, *J. Catal.*, 2017, **350**, 56–63.

206 S. Mukhopadhyay, R. S. Singh, A. Biswas and D. S. Pandey, *Chem. Commun.*, 2016, **52**,

3840–3843.

207 T. M. Laine, M. D. Kärkäs, R. Z. Liao, T. Åkermark, B. L. Lee, E. A. Karlsson, P. E. M. Siegbahn and B. Åkermark, *Chem. Commun.*, 2015, **51**, 1862–1865.

208 A. J. Clough, J. W. Yoo, M. H. Mecklenburg and S. C. Marinescu, *J. Am. Chem. Soc.*, 2015, **137**, 118–121.

209 J. W. Tian, M. X. Fu, D. D. Huang, X. K. Wang, Y. P. Wu, J. Y. Lu and D. S. Li, *Inorg. Chem. Commun.*, 2018, **95**, 73–77.

210 C. Wang, Z. Xie, K. E. Dekrafft and W. Lin, *J. Am. Chem. Soc.*, 2011, **133**, 13445–13454.

211 J. H. Cavka, S. Jakobsen, U. Olsbye, N. Guillou, C. Lamberti, S. Bordiga and K. P. Lillerud, *J. Am. Chem. Soc.*, 2008, **130**, 13850–13851.

212 M. J. Katz, Z. J. Brown, Y. J. Colón, P. W. Siu, K. A. Scheidt, R. Q. Snurr, J. T. Hupp and O. K. Farha, *Chem. Commun.*, 2013, **49**, 9449–9451.

213 X. F. Lu, P. Q. Liao, J. W. Wang, J. X. Wu, X. W. Chen, C. T. He, J. P. Zhang, G. R. Li and X. M. Chen, *J. Am. Chem. Soc.*, 2016, **138**, 8336–8339.

214 D. Yuan, D. Zhao, D. Sun and H. C. Zhou, *Angew. Chemie - Int. Ed.*, 2010, **49**, 5357–5361.

215 V. Brega, M. Zeller, Y. He, H. Peter Lu and J. K. Klosterman, *Chem. Commun.*, 2015, **51**, 5077–5080.

216 Q. Pang, B. Tu and Q. Li, *Coord. Chem. Rev.*, 2019, **388**, 107–125.

217 R. Wang, Q. Meng, L. Zhang, H. Wang, F. Dai, W. Guo, L. Zhao and D. Sun, *Chem. Commun.*, 2014, **50**, 4911–4914.

218 Q. Yao, A. Bermejo Gómez, J. Su, V. Pascanu, Y. Yun, H. Zheng, H. Chen, L. Liu, H. N. Abdelhamid, B. Martín-Matute and X. Zou, *Chem. Mater.*, 2015, **27**, 5332–5339.

219 N. Kobayashi and M. Kijima, *J. Mater. Chem.*, 2008, **18**, 1037–1045.

220 N. Zhu, D. Sensharma, P. Wix, M. J. Lennox, T. Düren, W. Y. Wong and W. Schmitt, *Eur. J. Inorg. Chem.*, 2016, **2016**, 1939–1943.

221 I. Kanwal, A. Mujahid, N. Rasool, K. Rizwan, A. Malik, G. Ahmad, S. A. A. Shah, U. Rashid and N. M. Nasir, *Catalysts*, 2020, **10**, 443.

222 M. Schilz and H. Plenio, *J. Org. Chem.*, 2012, **77**, 2798–2807.

223 G. M. Brown and R. Chidambaram, *Acta Crystallogr. Sect. B Struct. Crystallogr. Cryst. Chem.*, 1973, **29**, 2393–2403.

224 G. A. Craig, P. Larpent, S. Kusaka, R. Matsuda, S. Kitagawa and S. Furukawa, *Chem. Sci.*, 2018, **9**, 6463–6469.

225 L. Sarkisov, R. Bueno-Perez, M. Sutharson and D. Fairen-Jimenez, *Chem. Mater.*, 2020, **32**, 9849–9867.

226 L. D. Gelb and K. E. Gubbins, *Langmuir*, 1999, **15**, 305–308.

227 D. Alezi, I. Spanopoulos, C. Tsangarakis, A. Shkurenko, K. Adil, Y. Belmabkhout, M. O′Keeffe, M. Eddaoudi and P. N. Trikalitis, *J. Am. Chem. Soc.*, 2016, **138**, 12767–12770.

228 A. Altomare, C. Cuocci, C. Giacovazzo, A. Moliterni, R. Rizzi, N. Corriero and A. Falcicchio, *J. Appl. Crystallogr.*, 2013, **46**, 1231–1235.

229 A. Altomare, M. Camalli, C. Cuocci, C. Giacovazzo, A. Moliterni and R. Rizzi, *J. Appl. Crystallogr.*, 2009, **42**, 1197–1202.

230 H. M. Rietveld, *J. Appl. Crystallogr.*, 1969, **2**, 65–71.

231 M. A. K. and D. S. U. M. B. Shundalau, P. S. Chybirai, A. I. Komyak, A. P. Zazhogin, M. B. Shundalau, P. S. Chybirai, A. I. Komyak, A. P. Zazhogin, M. A. Ksenofontov and D. S. Umreiko, *J. Appl. Spectrosc.*, 2011, **78**, 351–361.

232 B. Smith, *Infrared Spectral Interpretation*, CRC Press, 2018.

233 G. B. Deacon and R. J. Phillips, *Coord. Chem. Rev.*, 1980, **33**, 227–250.

234 Y. Mathey, D. R. Greig and D. F. Shriver, *Inorg. Chem.*, 1982, **21**, 3409–3413.

235 D. Lin-Vien, N. B. Colthup, W. G. Fateley and J. G. Grasselli, *Handb. Infrared Raman Charact. Freq. Org. Mol.*, 1991, 277–306.

236 E. E. Crystallo-, *Eur. J. Neurol.*, 2009, **16**, 16–54.

237 S. S. Y. Chui, S. M. F. Lo, J. P. H. Charmant, A. G. Orpen and I. D. Williams, *Science (80-.).*, 1999, **283**, 1148–1150.

238 B. Chen, M. Eddaoudi, S. T. Hyde, M. O'Keeffe and O. M. Yaghi, *Science (80-.).*, 2001, **291**, 1021–1023.

239 H. Vardhan and F. Verpoort, *Aust. J. Chem.*, 2015, **68**, 707–730.

240 S. Mollick, S. Fajal, S. Mukherjee and S. K. Ghosh, *Chem. - An Asian J.*, 2019, **14**, 3096–3108.

241 J. Zhao and X. Yan, *Chem. Lett.*, 2020, **49**, 659–665.

242 B. G. Yong, X. Wang, E. V. Anokhina and A. J. Jacobson, *Inorg. Chem.*, 2005, **44**, 8265–

8271.

243 R. W. Larsen, *J. Am. Chem. Soc.*, 2008, **130**, 11246–11247.

244 N. B. Colthup and J. G. Grasselli, *The Handbook of infrared and Raman characteristic frequencies of organic molecules*, 1992, vol. 29.

245 D. B. Ninković, G. V. Janjić, D. Ž. Veljković, D. N. Sredojević and S. D. Zarić, *ChemPhysChem*, 2011, **12**, 3511–3514.

246 D. X. Xue, Y. Belmabkhout, O. Shekhah, H. Jiang, K. Adil, A. J. Cairns and M. Eddaoudi, *J. Am. Chem. Soc.*, 2015, **137**, 5034–5040.

247 J. R. Li, D. J. Timmons and H. C. Zhou, *J. Am. Chem. Soc.*, 2009, **131**, 6368–6369.

248 S. Abednatanzi, P. Gohari Derakhshandeh, H. Depauw, F. X. Coudert, H. Vrielinck, P. Van Der Voort and K. Leus, *Chem. Soc. Rev.*, 2019, **48**, 2535–2565.

249 T. K. Prasad, D. H. Hong and M. P. Suh, *Chem. - A Eur. J.*, 2010, **16**, 14043–14050.

250 C. K. Brozek and M. Dincə, *Chem. Commun.*, 2015, **51**, 11780–11782.

251 C. K. Brozek and M. Dincă, 2013, **135**, 12886–12891.

252 S. Das, H. Kim and O. Kim, *J. Am. Chem. Soc.*, 2009, **131**, 3814–3815.

253 R. Amunugama and M. T. Rodgers, *J. Phys. Chem. A*, 2001, **105**, 9883–9892.

254 H. Nose and M. T. Rodgers, *J. Phys. Chem. A*, 2014, **118**, 8129–8140.

255 A. Carné-Sánchez, J. Albalad, T. Grancha, I. Imaz, J. Juanhuix, P. Larpent, S. Furukawa and D. Maspoch, *J. Am. Chem. Soc.*, 2019, **141**, 4094–4102.

256 N. Ahmad, A. H. Chughtai, H. A. Younus and F. Verpoort, *Coord. Chem. Rev.*, 2014, **280**, 1–27.

257 V. A. Blatov, A. P. Shevchenko and D. M. Proserpio, *Cryst. Growth Des.*, 2014, **14**, 3576–3586.

258 W. Lu, Z. Wei, Z. Y. Gu, T. F. Liu, J. Park, J. Park, J. Tian, M. Zhang, Q. Zhang, T. Gentle, M. Bosch and H. C. Zhou, *Chem. Soc. Rev.*, 2014, **43**, 5561–5593.

259 F. A. A. Paz, J. Klinowski, S. M. F. Vilela, J. P. C. Tomé, J. A. S. Cavaleiro and J. Rocha, *Chem. Soc. Rev.*, 2012, **41**, 1088–1110.

260 D. Zhao, D. J. Timmons, D. Yuan and H. C. Zhou, *Acc. Chem. Res.*, 2011, **44**, 123–133.

261 Z. Guo, G. Li, L. Zhou, S. Su, Y. Lel, S. Dang and H. Zhang, *Inorg. Chem.*, 2009, **48**, 8069–8071.

262 A. G. Wong-Foy, O. Lebel and A. J. Matzger, *J. Am. Chem. Soc.*, 2007, **129**, 15740–15741.

263 L. Li, S. Zhang, L. Han, Z. Sun, J. Luo and M. Hong, *Cryst. Growth Des.*, 2013, **13**, 106–110.

264 J. A. Thomas, *Dalt. Trans.*, 2011, **40**, 12005–12016.

265 P. Y. Wang, S. C. Dai, W. F. Lin, M. F. Wu, H. B. Yang, P. Zhou, J. P. Zou, W. T. Guang and X. B. Luo, *Inorganica Chim. Acta*, 2013, **404**, 155–159.

266 G. Si, X. Kong, T. He, W. Wu, L. Xie and J. Li, *Chinese Chem. Lett.*, 2021, **32**, 918–922.

267 B. Guo, F. Li, C. Wang, L. Zhang and D. Sun, *J. Mater. Chem. A*, 2019, **7**, 13173–13179.

268 T. He, Y. Z. Zhang, X. J. Kong, X. L. Lv, L. H. Xie and J. R. Li, *Cryst. Growth Des.*, 2019, **19**, 430–436.

269 F. Wang, S. Kusaka, Y. Hijikata, N. Hosono and S. Kitagawa, *ACS Appl. Mater. Interfaces*, 2017, **9**, 33455–33460.

270 D. Yuan, D. Zhao, D. Sun and H. C. Zhou, *Angew. Chemie - Int. Ed.*, 2010, **49**, 5357–5361.

271 L. Li, J. Luo, S. Wang, Z. Sun, T. Chen and M. Hong, *Cryst. Growth Des.*, 2011, **11**, 3744–3747.

272 J. Cai, X. Rao, Y. He, J. Yu, C. Wu, W. Zhou, T. Yildirim, B. Chen and G. Qian, *Chem. Commun.*, 2014, **50**, 1552–1554.

273 G. Xu, B. Li, H. Wu, W. Zhou and B. Chen, *Cryst. Growth Des.*, 2017, **17**, 4795–4800.

274 Y. Wang, X. Wang, X. Wang, X. Zhang, W. Fan, D. Liu, L. Zhang, F. Dai and D. Sun, *Cryst. Growth Des.*, 2019, **19**, 832–838.

275 D. Zhao, D. J. Timmons, D. Yuan and H.-C. Zhou, *Acc. Chem. Res.*, 2011, **44**, 123–133.

276 M. Eddaoudi, D. B. Moler, H. Li, B. Chen, T. M. Reineke, M. O'Keeffe and O. M. Yaghi, *Acc. Chem. Res.*, 2001, **34**, 319–330.

277 D. J. Tranchemontagne, J. L. Mendoza-Cortés, M. O'Keeffe and O. M. Yaghi, *Chem. Soc. Rev.*, 2009, **38**, 1257.

278 J. K. Schnobrich, O. Lebel, K. A. Cychosz, A. Dailly, A. G. Wong-Foy and A. J. Matzger, *J. Am. Chem. Soc.*, 2010, **132**, 13941–13948.

279 D. Alezi, A. M. P. Peedikakkal, Ł. J. Weseliński, V. Guillerm, Y. Belmabkhout, A. J. Cairns, Z. Chen, Ł. Wojtas and M. Eddaoudi, *J. Am. Chem. Soc.*, 2015, **137**, 5421–5430.

280 X. L. Lv, L. Feng, L. H. Xie, T. He, W. Wu, K. Y. Wang, G. Si, B. Wang, J. R. Li and H. C.

Zhou, *J. Am. Chem. Soc.*, 2021, **143**, 2784–2791.

281 H. Furukawa, K. E. Cordova, M. O'Keeffe and O. M. Yaghi, *Science (80-.).*, 2013, **341**, 1230444.

282 B. Chen, N. W. Ockwig, A. R. Millward, D. S. Contreras and O. M. Yaghi, *Angew. Chemie - Int. Ed.*, 2005, **44**, 4745–4749.

283 T. R. Cook, Y. R. Zheng and P. J. Stang, *Chem. Rev.*, 2013, **113**, 734–777.

284 L. Feng, Z. Chen, T. Liao, P. Li, Y. Jia, X. Liu, Y. Yang and Y. Zhou, *Cryst. Growth Des.*, 2009, **9**, 1505–1510.

285 J. F. Eubank, F. Nouar, R. Luebke, A. J. Cairns, L. Wojtas, M. Alkordi, T. Bousquet, M. R. Hight, J. Eckert, J. P. Embs, P. A. Georgiev and M. Eddaoudi, *Angew. Chemie - Int. Ed.*, 2012, **51**, 10099–10103.

286 K. Zhao, Y. He, C. Shan, J. Ren, L. Wojtas, L. Wang, G. Li, Z. Song and X. Shi, *Chem. - A Eur. J.*, 2020, **26**, 16272–16276.

287 N. Zhu, M. J. Lennox, G. Tobin, L. Goodman, T. Düren and W. Schmitt, *Chem. - A Eur. J.*, 2014, **20**, 3595–3599.

288 D. Zhao, D. Yuan, D. Sun and H.-C. Zhou, *J. Am. Chem. Soc.*, 2009, **131**, 9186–9188.

289 T. Y. Kim, L. Digal, M. G. Gardiner, N. T. Lucas and J. D. Crowley, *Chem. - A Eur. J.*, 2017, **23**, 15089–15097.

290 E. T. M. Sites and P. N. W. Baxter, 2003, 5011–5022.

291 C. Song, Y. Ling, Y. Feng, W. Zhou, T. Yildirim and Y. He, *Chem. Commun.*, 2015, **51**, 8508–8511.

292 S. Urgaonkar and J. G. Verkade, *J. Org. Chem.*, 2004, **69**, 5752–5755.

293 Y. Yang, X. Chew, C. W. Johannes, E. G. Robins, H. Jong and Y. H. Lim, *European J. Org. Chem.*, 2014, **2014**, 7184–7192.

294 P. Ehlers, A. Neubauer, S. Lochbrunner, A. Villinger and P. Langer, *Org. Lett.*, 2011, **13**, 1618–1621.

295 C. Yi and R. Hua, *J. Org. Chem.*, 2006, **71**, 2535–2537.

296 D. Gelman and S. L. Buchwald, *Angew. Chemie - Int. Ed.*, 2003, **42**, 5993–5996.

297 K. Sonogashira, *J. Organomet. Chem.*, 2002, **653**, 46–49.

298 C. Glaser, *Berichte der Dtsch. Chem. Gesellschaft*, 1869, **2**, 422–424.

299 Z.-H. Xuan, D.-S. Zhang, Z. Chang, T.-L. Hu and X.-H. Bu, *Inorg. Chem.*, 2014, **53**, 8985–8990.

300 O. Alduhaish, H. Wang, B. Li, H. D. Arman, V. Nesterov, K. Alfooty and B. Chen, *Chempluschem*, 2016, **81**, 764–769.

301 G. A. Craig, P. Larpent, H. Urabe, A. Legrand, M. Bonneau, S. Kusaka and S. Furukawa, *Chem. Commun.*, 2020, **56**, 3689–3692.

302 M. Jaya Prakash, M. Oh, X. Liu, K. N. Han, G. H. Seong and M. S. Lah, *Chem. Commun.*, 2010, **46**, 2049–2051.

303 S. R. Batten, *CrystEngComm*, 2001, **3**, 67.

304 X. Liu, Z. Xiao, J. Xu, W. Xu, P. Sang, L. Zhao, H. Zhu, D. Sun and W. Guo, *J. Mater. Chem. A*, 2016, **4**, 13844–13851.

305 Y. Hu, S. Xiang, W. Zhang, Z. Zhang, L. Wang, J. Bai and B. Chen, *Chem. Commun.*, 2009, 7551–7553.

306 D. Lin-Vien, N. B. Colthup, W. G. Fateley and J. G. Grasselli, *Handb. Infrared Raman Charact. Freq. Org. Mol.*, 1991, **3**, 117–154.

307 M. O'Keeffe and O. M. Yaghi, *Chem. Rev.*, 2012, **112**, 675–702.

308 X. Lin, J. Jia, X. Zhao, K. M. Thomas, A. J. Blake, G. S. Walker, N. R. Champness, P. Hubberstey and M. Schröder, *Angew. Chemie - Int. Ed.*, 2006, **45**, 7358–7364.

309 L. Bai, H.-B. Wang, D.-S. Li, Y.-P. Wu, J. Zhao and L.-F. Ma, *Inorg. Chem. Commun.*, 2014, **44**, 188–190.

310 J. Li, G. P. Yang, S. L. Wei, R. C. Gao, N. N. Bai and Y. Y. Wang, *Cryst. Growth Des.*, 2015, **15**, 5382–5387.

311 X. Duan, R. Song, J. Yu, H. Wang, Y. Cui, Y. Yang, B. Chen and G. Qian, *RSC Adv.*, 2014, **4**, 36419.

312 C. Wang and W. Lin, 2011, 4232–4235.

313 Q. Xu, H. Li, F. Yue, L. Chi and J. Wang, *New J. Chem.*, 2016, **40**, 3032–3035.

314 J. Jiang, L. Huang, X. Liu and L. Ai, *ACS Appl. Mater. Interfaces*, 2017, **9**, 7193–7201.

315 E. A. Flügel, V. W. H. Lau, H. Schlomberg, R. Glaum and B. V. Lotsch, *Chem. - A Eur. J.*, 2016, **22**, 3676–3680.

316 S. Wang, Y. Hou, S. Lin and X. Wang, *Nanoscale*, 2014, **6**, 9930–9934.

317 Y. Liu, X. Xi, C. Ye, T. Gong, Z. Yang and Y. Cui, *Angew. Chemie Int. Ed.*, 2014, **53**, 13821–13825.

318 M. N. Ahamad, M. S. Khan, M. Shahid and M. Ahmad, *Dalt. Trans.*, 2020, **49**, 14690–14705.

319 M. Sarker and S. H. Jhung, *J. Mol. Liq.*, 2019, **296**, 112060.

320 D. P. Malenov and S. D. Zarić, *Coord. Chem. Rev.*, 2020, **419**, 213338.

321 B. Worths, *Pure Appl. Chem.*, 1977, **49**, 885–892.

322 Z. Chen, S. L. Hanna, L. R. Redfern, D. Alezi, T. Islamoglu and O. K. Farha, *Coord. Chem. Rev.*, 2019, **386**, 32–49.

323 J. Tu, X. Zeng, F. Xu, X. Wu, Y. Tian, X. Hou and Z. Long, *Chem. Commun.*, 2017, **53**, 3361–3364.

324 M. Lammert, C. Glißmann and N. Stock, *Dalt. Trans.*, 2017, **46**, 2425–2429.

325 H. Depauw, I. Nevjestić, J. De Winne, G. Wang, K. Haustraete, K. Leus, A. Verberckmoes, C. Detavernier, F. Callens, E. De Canck, H. Vrielinck and P. Van Der Voort, *Chem. Commun.*, 2017, **53**, 8478–8481.

326 D. Kim, X. Liu, M. Oh, X. Song, Y. Zou, D. Singh, K. S. Kim and M. S. Lah, *CrystEngComm*, 2014, **16**, 6391–6397.

327 G. M. Sheldrick, *Sadabs*, 1996.

328 G. M. Sheldrick, *Acta Crystallogr. Sect. A Found. Crystallogr.*, 2015, **71**, 3–8.

329 O. V. Dolomanov, L. J. Bourhis, R. J. Gildea, J. A. K. Howard and H. Puschmann, *J. Appl. Crystallogr.*, 2009, **42**, 339–341.

330 G. M. Sheldrick, *Acta Crystallogr. Sect. C Struct. Chem.*, 2015, **71**, 3–8.

331 A. L. Spek, *Acta Crystallogr. Sect. C Struct. Chem.*, 2015, **71**, 9–18.